Evaluation of a panel of 105 cytokines from human glioblastoma (GBM) tissue maintained, and treated, on a unique microfluidic platform

Amr Moursi

Thesis submitted for the degree of Doctor of Medicine

The University of Hull and the University of York

Hull York Medical School

June 2025

Abstract

GBM remains a therapeutically challenging malignancy, partly due to its complex cytokine mediated microenvironment. This study established a novel microfluidic platform to maintain patient derived GBM tissue biopsies *ex vivo* for up to 12 days, enabling the dynamic profiling of cytokine responses under treatment (1µM GSK (Glycogen Synthase Kinase) 3368715 + 10µM Temozolomide). The combination of biochemical assays (LDH activity), histological analysis (H&E staining and Immunohistochemistry (IHC) for apoptotic markers), cytokine proteome profiling and ELISA assays provides evidence that GBM tissues can be maintained in a viable state within the novel microfluidic perfusion device for at least 12 days. Cytokine profiling was performed using Proteome Profiler array for 105 different cytokines, followed by ELISA validation for seven key cytokines (VEGF, MMP9, CHI3L1, IL6, IL8, Serpin E1, and Angiopoietin-2).

Multivariate analysis showed **time** significantly influenced cytokine profiles (p = *0.0288*), with an overall **downregulation** over time. **Treatment (**temozolomide plus arginine methylation inhibitor) had **no significant global effect** on all cytokines expression level (p = *0.1977*), but did significantly affect the seven selected cytokines (p = *0.0048*). Univariate analysis confirmed **VEGF (p = *0.0004*)** and **MMP9 (p = *0.0046*)** were significantly downregulated with treatment, while **CHI3L1** was upregulated (p = *0.0088*). Additionally, **gender** (p = *0.0050*) and **age group** (<60 vs. >60 years; p = *0.0021*) were both significant covariates influencing cytokine expression. However, these findings should be interpreted with caution given the small sample size (n=13), particularly the underrepresentation of female patients (3 females vs. 10 males) and the age imbalance (4 under 60 vs. 9 over 60).

Three of the study cytokines, **VEGF, MMP9**, and **CHI3L1,** were identified as responsive biomarkers under drug treatment, supporting further exploration of these targets. The platform provides a valuable tool for preclinical therapeutic screening and biomarker discovery. With further optimisation, it could support personalised treatment strategies and contribute to the development of more effective, patient-tailored approaches for managing GBM.

Thesis Associated Publications

A- Thesis Associated Publications :

"Investigating the effects of arginine methylation inhibitors on micro-dissected brain tumour biopsies maintained in a miniaturised perfusion system." *Lab on a Chip*, 23(11), pp.2664-2682. (2023)

Antonia Barry, Sabrina F Samuel, Ines Hosni, **Amr Moursi,** Lauric Feugere, Christopher J Sennett, Srihari Deepak, Shailendra Achawal, Chittoor Rajaraman, Alexander Iles, Katharina C Wollenberg Valero, Ian S Scott, Vicky Green, Lucy F Stead, John Greenman, Mark A Wade, Pedro Beltran-Alvarez.

B- Thesis Associated Conferences :

Conference	Title	Type (oral / poster)	Date
BNOS (British Neuro Oncology Society)	Evaluation of a panel of 105 cytokines from human glioblastoma (GBM) tissue maintained, and treated, on a unique microfluidic platform	Oral presentation	22-25 June 2022
Liverpool Neuroscience Group	Real-Time Cytokine Dynamics in Living Glioblastoma Tissue on a Microfluidic Platform	Oral Presentation	6th September 2024
Brain Tumour Northwest Annual Research Retreat	Tissue maintained on a microfluidic platform uncovers persistent expression of Chitinase 3- like 1 in glioblastoma unaffected by treatment	Oral Presentation	12th to 13th December 2024
BNOS (British Neuro Oncology Society)	Persistent Expression of Chitinase 3-Like 1 in *ex vivo*-maintained Glioblastoma biopsies despite Chemotherapy: Implications for Immune Evasion	Poster Presentation	18th June 2025

List of Contents

Chapter **Page**

List of Figures

List of Tables

Abbreviations

18F-FDG	Fluorine-18 fluorodeoxyglucose
2-HG	2-hydroxyglutarate
2D	Two dimensional
3D	Three dimensional
5hmC	5-hydroxymethylcytosine
5mC	5-methylcytosine
ACZ	Acetazolamide
ADC	Apparent Diffusion Coefficient
AGT	Angiotensinogen
AICc	Corrected Akaike Information Criterion
Akt	Protein Kinase B
AKT3	RAC-gamma serine/threonine-protein kinase ()
Ang	Angiopoietin
ATRX	Alpha Thalassemia/Mental Retardation Syndrome X-Linked
BBB	Blood brain barrier
bFGF	Basic fibroblast growth factor
BTSCs	Brain tumour stem-like cells
BVZ	Bevacizumab
CAR T-cell	Chimeric Antigen Receptor T-cell
CBTRUS	Central Brain Tumor Registry of the United States
CCL	C-C Motif Chemokine Ligand
CD	Cluster of Differentiation
CDK	Cyclin-Dependent Kinase
CDKN	Cyclin-Dependent Kinase Inhibitor
CE	Contrast-enhancing
CHTOP	Chromatin Target of PRMT1
CHI3L1	Chitinase-3-like protein 1
CNS	Central Nervous System
CT	Computed tomography
CTLA-4	Cytotoxic T-Lymphocyte Antigen-4
CXCL	Chemokine (C–X–C motif) ligand
DC	Dendritic cells
Df	Degree of freedom
DMEM	Dulbecco's Modified Eagle Medium
DMSO	Dimethyl sulfoxide
DNA	Deoxyribonucleic Acid
DTI	Diffusion tensor imaging
EANO	European Association of Neuro-Oncology
ECM	Extracellular matrix
ECs	Endothelial cells
EGF	Epidermal Growth Factor
EGFR	Epidermal growth factor receptor
ELISA	Enzyme-linked immunosorbent assay
EM	Electron micrograph
EOR	Extent of resection
F	Fisher
FDA	Food and Drug Administration
FGF	Fibroblast Growth Factor
GBM	Glioblastoma

GFP	Green fluorescent protein
gp	Glycoprotein
GSC	Glioblastoma stem cells
GSK	Glycogen Synthase Kinase
Gy	Gray
H&E	Haematoxylin and eosin
H3 K27M	Histone H3 lysine 27 to methionine
H3R8me2a	Histone H3, arginine 8, asymmetric dimethylation
HGG	High-Grade Glioma
HIF1-α	Hypoxia-Inducible Factor 1-alpha
HIF1-β	Hypoxia-Inducible Factor 1-beta
HIFs	hypoxia-inducible transcription factors
H3.3G34R/V	Histone H3.3 Glycine 34 Arginine/Valine
HR	Hazard ratio
HRP	Horseradish peroxidase
hrs	Hours
HUVECs	Human umbilical vein endothelial cells
IDH	Isocitrate dehydrogenase
IFN-α	Interferon-alpha
IFN-β	Interferon-beta
IFN-γ	Interferon-gamma
IGFBP-2	Insulin-like growth factor binding protein
IHC	Immunohistochemistry
IL	Interleukin
ISF	Interstitial fluid
JAK	Janus kinase
JAK/STAT3	Janus kinase/signal transducer and activator of transcription 3
Ki-67	Kiel-67 protein
KPS	Karnofsky performance status scale
LDH	Lactate dehydrogenase
Limma	Linear Models for Microarray Data
Lip+ Lac/tCr	Lipid + lactate to total creatine
MAPK	Mitogen-activated protein kinase
MAqCI	Microfluidic Assay for Quantification of Cell Invasion
MCP	Monocyte chemoattractant protein
MDSCs	Myeloid-derived suppressor cells
MDT	Multidisciplinary team
MEK	Mitogen-activated protein kinase
MGMT	6-methylguanine-DNA methyltransferase
MHC	Major histocompatibility complex
MHC I	Major histocompatibility complex I
Ml	Millilitre
MMPs	Metalloproteinases
MPP	1-methyl-4-phenylpyridinium
MPS	Microphysiological system
MRI	Magnetic resonance imaging
mRNA	Messenger ribonucleic acid
mRNA	Messenger ribonucleic acid
MRS	Magnetic resonance spectroscopy
MTIC	(3-methyltriazen-1yl)-imidazole-4-carboxamide
mTOR	Mammalian Target of Rapamycin
NEFL	Neurofilament light polypeptide

NF1	Neurofibromatosis type 1
NHS	National health system
NICE	National Institute for Health and Care Excellence
NIHSS	National Institutes of Health Stroke Scale
NK	Natural killer
NKG2D	Natural killer group 2, member d
NKp30	Natural Killer cell p30-related protein
OS	Overall survival
OoC	Organ-on-a-Chip
P	Phosphorous
PARP	Cleaved Poly ADP-ribose polymerase
PC1	Principal component 1
PC2	Principal component 2
PC3	Principal component 3
PCA	Principal component analysis
PCNSL	Primary central nervous system lymphoma
PCR	Polymerase chain reaction
PD-1	Programmed death-1
PD-L1	Programmed death-ligand 1
PDGF	Platelet-derived growth factor
PDMS	Polydimethylsiloxane
PEGDA	Polyethylene glycol diacrylate
PET	Positron-emission tomography
PFS	Progression-free survival
pg/mL	Picograms per millilitre
pH	Potential of Hydrogen
PHDs	Hydroxylase domain enzymes
PI3K	Phosphoinositide 3-kinase
PIP2	Phosphatidylinositol (4,5)-bisphosphate
PIP3	Phosphatidylinositol (3,4,5)-triphosphate
PLS-DA	Partial least square discriminant analysis
PMMA	Polymethyl methacrylate
PpIX	Protoporphyrinogen IX
Pr	Probability
PRMT	Protein arginine methyltransferase
PS	Polystyrene
PTEN	Phosphatase and tensin homolog
Q-Q	Quantile-quantile
QOL	Quality of life
R2	R-squared
RAB21	Ras-related protein Rab-21
Ras/MAPK	Rat sarcoma viral oncogene homolog / Mitogen-Activated Protein Kinase
rCBV	Relative cerebral blood volume
RNA	Ribonucleic acid
ROS	Reactive oxygen species
RT-PCR	Reverse transcription polymerase chain reaction
Serpin E1	Serine protease inhibitor E1
siRNA	Small interfering rna
Sphero-IMPACT	Spheroid-based *In vitro* microphysiological Angiogenesis and Cancer Testing
STAT3	Signal transducer and activator of transcription 3

STING	Stimulator of Interferon Genes
SumOfSqs	Sum of Squares
SYT1	Synaptotagmin 1
T1WI	T1-weighted images
TAM	Tumour associated macrophage
tCho/tNAA	Total choline to total N-acetyl aspartate
TERT	Telomerase reverse transcriptase
TET	Ten-eleven translocation
TGF-β	Transforming growth factor-beta
TLE	Total life expectancy
TLS	Tertiary lymphatic structures
TME	Tumour microenvironment
TMZ	Temozolomide
TNF-α	Tumour necrosis factor-alpha
TP53	Tumour Protein p53
TRAEs	Treatment-related adverse events
Tregs	Regulatory T-cells
TTF	Tumour treating fields
UK	United kingdom
UK-HSA	United Kingdom Health Security Agency
VEGF	Vascular endothelial growth factor
VEGFR	Vascular endothelial growth factor receptor
VIP	Variable Importance in Projection
WHO	World health organization
XL	Extra large
α-KG	Alpha-ketoglutarate
Δ	Delta
µg	Microgram
µL	Microlitre
µM	Micromolar

Acknowledgements

I would like to express my deep thanks to *Yorkshire's Brain Tumour Charity* for funding this project.

My deepest thanks go to *Professor John Greenman*. From the first time we met at the interview, he believed in me. He has been a real role model for how a scientist should be. He didn't just support me as a supervisor but also looked after me like a father, pushing me just enough to grow, but also making sure I was never left unsupported. Without him, this work would not have been possible, especially considering the challenges I faced. I will always be grateful for the trust and care he showed me.

I also want to thank *Pedro Beltran-Alvarez*, my assistant supervisor, who kindly opened his lab for most of my experiments and stayed supportive even when the experiments didn't go as planned. His encouragement helped me stay positive and keep going.

I am extending my heartfelt thanks to *Shailendra Achawal*, for his kind supervision, constant encouragement, and continuous support throughout the work. I am extremely grateful for what he has offered me.

I want to thank the amazing staff at Hull Royal Infirmary including *Chittoor Rajaraman*, who I learned from both on the clinical level and as a person, especially in how he approached patients with empathy during the consent process. I'm also grateful to *Adam Razak* for his support in helping me access the samples needed. I want to thank the neurosurgery department consultants, colleagues, and nurses for providing a positive and encouraging environment every day.

To *Antonia*, my brilliant PhD colleague, thank you for being such a hardworking and inspiring person. Your dedication in the lab and your drive to always do more in our experiments truly motivated me.

I am also thankful to *Lauric Feugere*, who offered his biostatistical expertise and sat with me through long discussions to help me understand how to handle the many parameters and relationships in the data. Even after he moved on to a new job, he stayed in touch to help complete the work, and I truly appreciate that.

I am truly grateful to the patients I met. Despite being in one of the most vulnerable moments in their lives, they were brave, generous, and wanted to contribute to scientific work on this deadly tumour. Their families supported their loved ones' decision to donate part of their brain tumour for research.

Finally, I thank my wife, *Dr. Asmaa Elsharkawy*. Her support, patience, and even scientific discussions helped carry me through the difficult moments of this MD journey. I am lucky to have her in my life.

To my *mum and dad*, thank you for your constant emotional support, even when you didn't know all the details. You always stood by me when I needed it most.

And above all, *praise be to Allah*, the Most Gracious and the Most Merciful, who gave me the strength and ability to complete this work.

Author's declaration

I confirm that this work is original and that if any passage(s) or diagram(s) have been copied from academic papers, books, the internet or any other sources these are clearly identified by the use of quotation marks and the reference(s) is fully cited.

I certify that, other than where indicated, this is my own work and does not breach the regulations of Hull York Medical School (HYMS), the University of Hull or the University of York regarding plagiarism or academic conduct in examinations.

I have read the HYMS Code of Practice on Academic Misconduct, and state that this piece of work is my own and does not contain any unacknowledged work from any other sources.

I confirm that any patient information obtained to produce this piece of work has been appropriately anonymise

1 Introduction

1.1 Impact of Glioblastoma

The number of malignant brain tumour cases has been rising in recent years, having a devastating effect on society, not only affecting patients' lives but also their wider families. Glioblastoma is the most common primary malignant brain; unfortunately, it is also the most aggressive form.

In the United States of America, 7.08 per 100,000 people was the average annual age-adjusted incidence rate of primary malignant brain tumours over the five years of 2013 to 2017, with 81,246 deaths. These deaths accounted for an average annual mortality rate of 4.42 per 100,000 due to primary brain malignancies. The five-year relative survival rate following diagnosis of a primary malignant brain and other Central Nervous system (CNS) tumour was 36.0%. That varied between different age groups, where the best rate was in younger patients aged 0-14 years (75.4%) and worst in patients aged 40+ years (21.5 %)(Ostrom et al., 2020).

In the United Kingdom (UK), brain tumours are the 9th most common cancer, contributing approximately 3% of all new cancer cases. Every day, on average, 35 patients are diagnosed with intracranial tumours, with a total of around 12,700 annually. Unfortunately, approximately 5,500 patients with brain cancer die in the UK every year, that is 15 per day(UK, 2024) **(Figure 1.1)**. Smittenaar et al. (2016) projected that incidence rates will rise 6% in the UK between 2014 and 2035, to 22 cases per 100,000 people by 2035 due to increasing population size and the ageing population(Smittenaar et al., 2016).

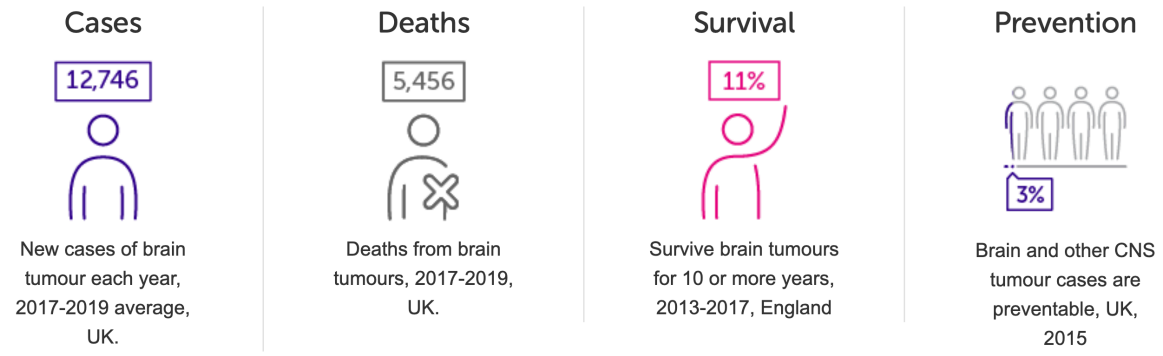

Figure 1.1: Brain, other CNS and intracranial tumours statistics

Taken from Cancer Research UK. (UK, 2024)

Globally, glioblastoma incidence is highest in North America, Australia, and Northern and Western Europe (Tan et al., 2020). The incidence rate of glioblastoma (3.23 per 100,000 population) according to the Central Brain Tumor Registry of the United States (CBTRUS). Hence, glioblastoma has the highest number of cases of all malignant tumours in the United States, with 12,800 patients projected in 2020 and almost 13,000 in 2021. Glioblastoma was the third most reported CNS histology and the most frequent malignancy overall **(Figure 1.2).** Glioblastoma was responsible for almost half (48.6%) of primary malignant brain tumours **(Figure 1.3)** (Ostrom et al., 2020).

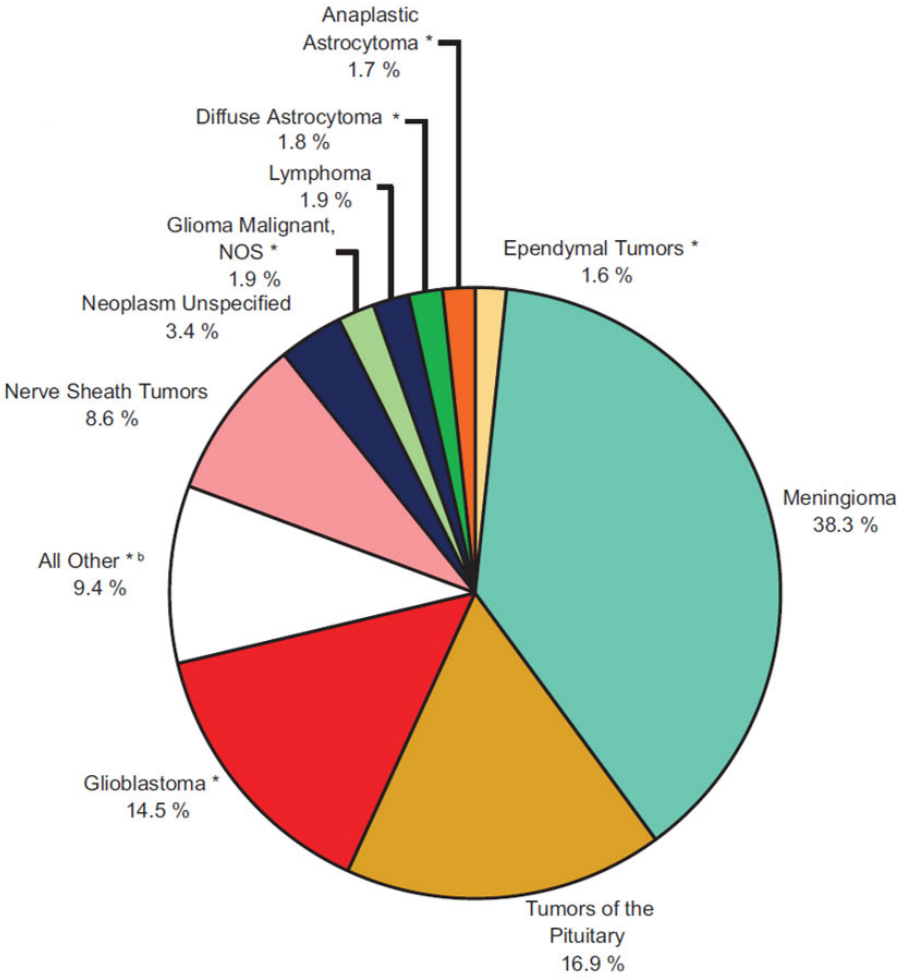

Figure 1.2: Distribution of primary brain tumours (malignant and non-malignant).
Adapted from (Ostrom et al., 2020)

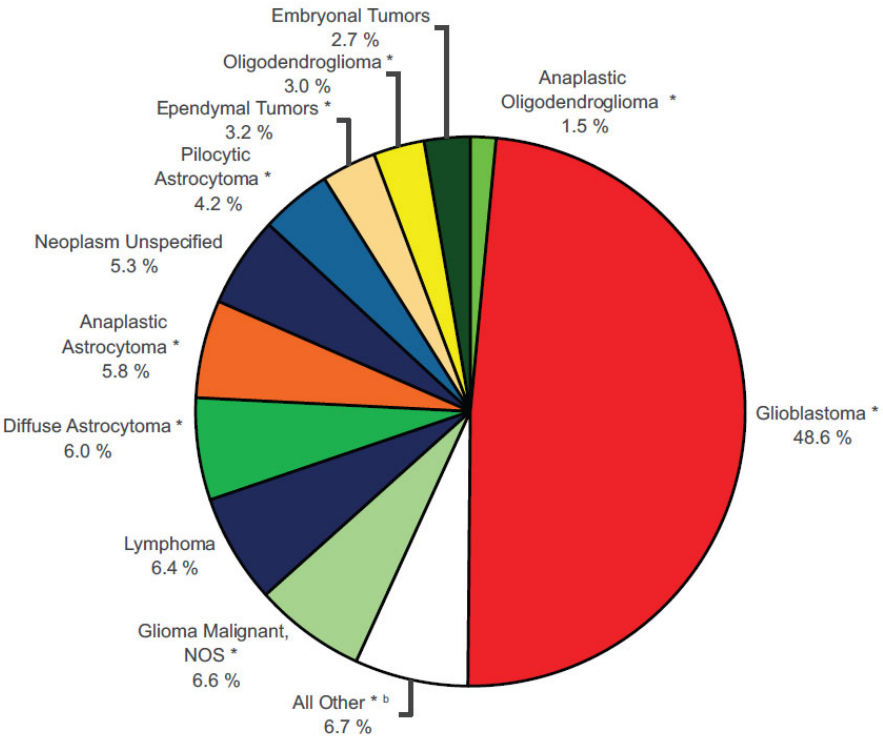

Figure 1.3: Distribution of Malignant Primary Brain and Other CNS Tumors.

Adapted from(Ostrom et al., 2020)

Similarly, in England, glioblastoma was the most common primary brain tumour registered between 1995 and 2015(Philips et al., 2018b). There were average 2530 new cases per year for period 2013-2018 with national age standardized incidence was 4.98per 100,000 per year (Le Calvez et al., 2025). The incidence rate of glioblastoma is less in the united states over period 2017-2021(3.27 per 100,000)(Price et al., 2024)

A more detailed study of the glioblastoma demographic in the United States of America showed that the incidence of glioblastoma increased with age, reaching the highest in individuals aged 75 to 84 years. That glioblastoma was twice as common in males than in females **(Figure 1.4).** Glioblastoma was also about two times higher among Whites compared to Blacks and approximately three times greater in Whites than in Asian and Pacific Islanders(Ostrom et al., 2020) **(Figure 1.5).**

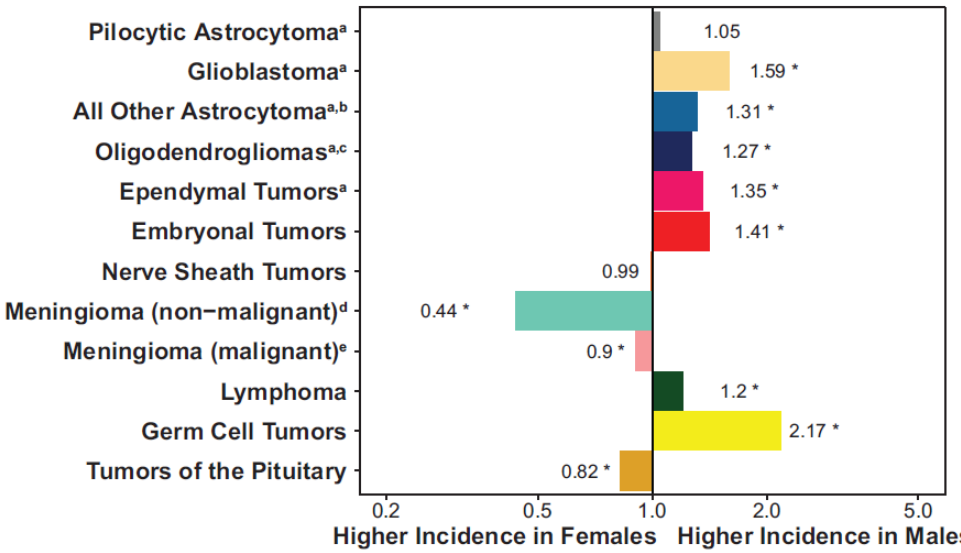

* Incidence Rate is significantly different between groups at the p<0.05 level.
a. All or some of this histology are included in the CBTRUS definition of gliomas, including ICD−O−3 histology codes 9380−9384 and 9391−9460, (Table 2).
b. ICD−O−3 Histology Codes: 9381, 9384, 9424, 9400, 9401, 9410, 9411, and 9420, all ICD−O−3 behavior codes.
c. ICD−O−3 Histology and Behavior Codes: 9450/3, 9451/3, and 9460/3.
d. ICD−O−3 Histology and Behavior Codes: 9530/0, 9530/1, 9531/0, 9532/0, 9533/0, 9534/0, 9537/0, 9538/1, and 9539/1.
e. ICD−O−3 Histology and Behavior Codes: 9530/3, 9538/3, and 9539/3.

Figure 1.4: ***Incidence rate ratios by sex (males: females) for selected primary brain and other CNS tumour histologies.***

Taken from(Ostrom et al., 2020)

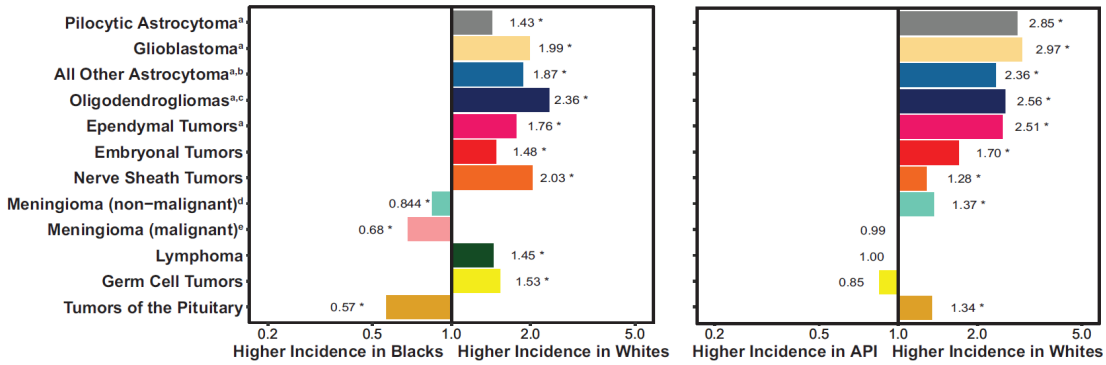

* Incidence Rate is significantly different between groups at the p<0.05 level.
a. All or some of this histology are included in the CBTRUS definition of gliomas, including ICD−O−3 histology codes 9380−9384 and 9391−9460, (Table 2).
b. ICD−O−3 Histology Codes: 9381, 9384, 9424, 9400, 9401, 9410, 9411, and 9420, all ICD−O−3 behavior codes.
c. ICD−O−3 Histology and Behavior Codes: 9450/3, 9451/3, and 9460/3.
d. ICD−O−3 Histology and Behavior Codes: 9530/0, 9530/1, 9531/0, 9532/0, 9533/0, 9534/0, 9537/0, 9538/1, and 9539/1.
e. ICD−O−3 Histology and Behavior Codes: 9530/3, 9538/3, and 9539/3.

Figure 1.5: ***Incidence Rate Ratios by Race (Whites:Blacks and Whites:Asian Or Pacific Islanders) for Selected Primary Brain and Other CNS.***

Taken from (Ostrom et al., 2020)

Likewise, in the UK, the age-standardized incidence of glioblastoma increased from 3.27 per 100,000 population per year in 1995 for males to 7.34 in 2017 and from 2.00 to 4.45 per 100,000 in females. Glioblastoma remained slightly more common in men than women, with an incidence ratio of 1.64:1.00 **(Figure 1.6).** In general, the age-specific distribution of incidence of glioblastoma remained almost the same over the period from 1995 to 2017, with increases in all ages from 40 years and being most prominent in the 60- to 79- years(Wanis et al., 2021) **(Figure 1.7).**

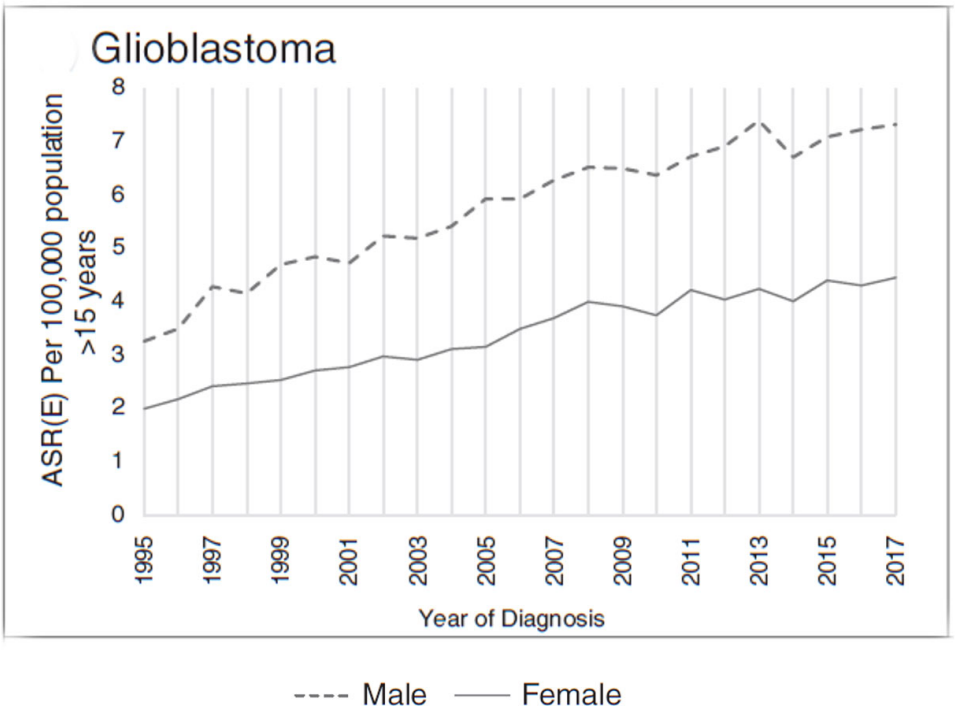

Figure 1.6: Age-standardized incidence rates of brain tumour subtypes in England, 1995-2017.

Adapted from(Wanis et al., 2021)

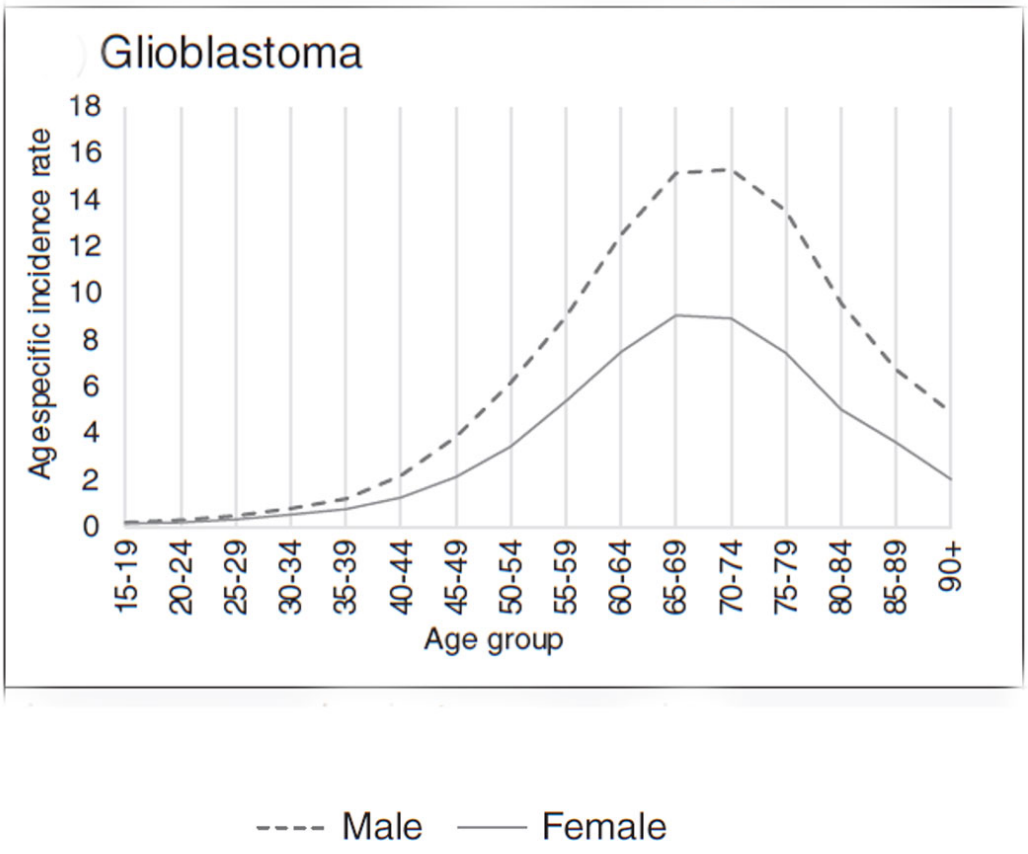

Figure 1.7: Age-specific incidence rates of brain tumour subtypes in England, 1995-2017.

Adapted from (Wanis et al., 2021)

Worldwide, the median observed survival was lowest for glioblastoma among all primary malignant brain tumours regardless of treatment(Ostrom et al., 2020) **(Table 1.1).** In elderly patients, the median survival is <4 months with best supportive care alone (Tan et al., 2020). Despite tremendous therapeutic advances, the median overall survival (OS) of GBM patients is 12–14 months. (Sareen et al., 2022). Furthermore, only 7.2% of patients diagnosed with glioblastoma survive beyond five years (Miller et al., 2021). Older adults (40+ years old), female sex, white race, poor performance status and incomplete extent of resection were well-established factors associated with poorer survival after diagnosis of glioblastoma (Ostrom et al., 2020, Tan et al., 2020).

Table 1.1: Median Survival by Histology and Age Group for Primary Malignant Brain and CNS Tumours (CBTRUS 2001–2017)

Histology	N	Deaths	Median survival (95% CI)
Pilocytic Astrocytoma	12,068	822	** (** -**)
Diffuse Astrocytoma	18,420	9,662	36 (34-38)
Anaplastic Astrocytoma	13,643	9,509	18 (17-18)
Unique Astrocytoma Variants	1,564	637	44 (36-54)
Glioblastoma	113,412	103,642	8 (8-9)
Oligodendroglioma	9,062	2,362	119 (115-124)
Anaplastic Oligodendroglioma	3,943	1,723	60 (57-64)
Oligoastrocytic Tumors	6,087	2,618	71 (68-76)
Ependymal Tumors	9,344	1,831	** (155-**)
Glioma Malignant, NOS	16,323	7,403	37 (34-42)
Choroid Plexus Tumors	310	114	77 (57-107)
Other Neuroepithelial Tumors	151	46	88 (52-**)
Neuronal and Mixed Neuronal Glial Tumors	1,907	573	93 (85-109)
Tumors of the Pineal Region	888	295	75 (68-102)
Embryonal Tumors	8,422	3,201	66 (61-73)
Nerve Sheath Tumors	467	174	95 (68-135)
Meningioma	3,807	1,771	53 (48-58)
Mesenchymal Tumors	845	337	72 (56-85)
Primary Melanocytic Lesions	140	105	11 (7-17)
Other Neoplasms Related to the Meninges	579	190	83 (70-99)
Lymphoma	15,057	10,109	13 (13-14)
Other Hemopoietic Neoplasms	392	138	84 (49-140)
Germ Cell Tumors, Cysts and Heterotopias	2,442	327	** (** -**)
Tumors of the Pituitary	343	102	139 (113-**)
All Other	72	23	133 (35-**)
Neoplasm Unspecified	8,596	7,083	2 (2-2)

** cannot be calculated
Abbreviations: CBTRUS, Central Brain Tumor Registry of the United States; NPCR, National Program of Cancer Registries; CI, confidence interval; NOS, not otherwise specified

Median survival in Months and 16-year total deaths with 95% confidence interval for primary malignant brain and other CNS tumours.
Taken from (Ostrom et al., 2020)

The United Kingdom faces a particularly challenging situation regarding glioblastoma, which is recognized as having one of the lowest five-year survival rates among all human cancers, with an average survival time of approximately one year following diagnosis (Philips et al., 2018a). Brodbelt et al. analysed the survival of 10,743 GBM cases in England over the period 2007–2011. These patients had an overall median survival of only 6.1 months, increasing to 14.9 months with maximal treatment(Brodbelt et al., 2015a) **(Figure 1.8).** Patients who underwent surgical debulking followed

by chemo-radiotherapy, were considered as having maximal treatment. One, two and five-year survivals, were 28.4%, 11.5% and 3.4%, respectively. There was a statistically significant decrease in median survival ($p < 0.0001$) with increasing age, declining from 16.2 months for the 20–44 year age group, to 7.9 months for the 45–69 years, and 3.2 months for 70+ years (Brodbelt et al., 2015a) **(Figure 1.9).**

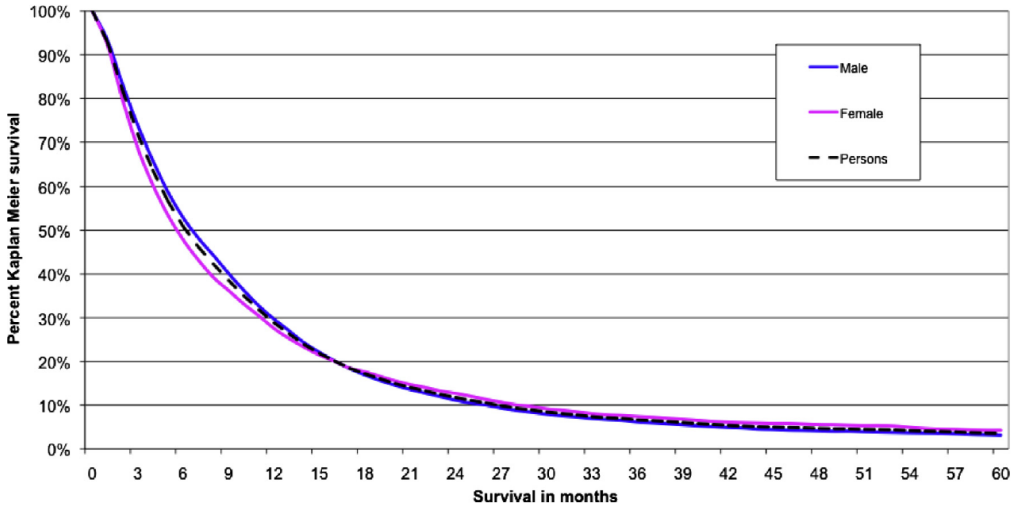

Figure 1.8: Kaplan–Meier plot showing survival for patients with a glioblastoma by gender.

Taken from (Brodbelt et al., 2015a)

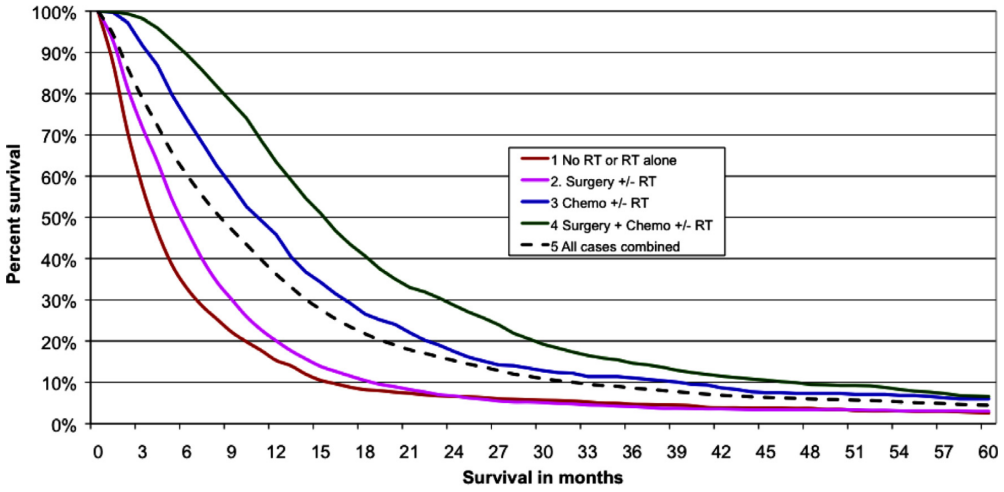

Figure 1.9: Kaplan–Meier plot demonstrating survival by treatment type for patients with glioblastoma 20–70 years of age (2007–2010).

RT: Radiotherapy. Radiotherapy data is not complete, but it is likely that most of the patients in groups 2–4 under 70 years of age received radiotherapy. Chemo: Chemotherapy. Surgery is any debulking procedure and does not include biopsy. There were significant differences between all treatment groups (p < 0_0001).

Taken from (Brodbelt et al., 2015a)

GBM has a significant health burden globally and in the UK because of its high incidence, aggressive nature and poor survival rate. Epidemiologically, it is more common in the elderly and males. Although advances in surgical and medical options have been made, survival remains limited. These statistics reinforce the urgent need for more effective diagnostic and therapeutic approaches. That started with a more precise classification of GBM, which will be explored further in the next section.

1.2 Classification of Glioblastoma

1.2.1 2021 World Health Organization (WHO) classification:

The WHO Classification of CNS Tumours' fifth edition was published in 2021, five years after the fourth edition. Advancements in molecular diagnostics have enabled the identification of new tumour entities and a more precise stratification of existing tumours. These rapid developments in our understanding of the molecular characteristics of CNS tumours led to the forming of the Consortium to Inform Molecular and Practical Approaches to CNS Tumour Taxonomy in 2017. The fifth edition of the WHO Classification of CNS Tumours incorporates the latest knowledge regarding the molecular foundations of CNS tumours while still recognising their histopathological origins. This section discusses these updates, focusing on adult-type diffuse gliomas (Louis et al., 2016, Horbinski et al., 2019, Louis et al., 2021b, Louis et al., 2017, Gonzalez Castro and Wesseling, 2021).

Before delving into specific updates, it is essential to note some general changes in the classification system. One significant change is the transition from Roman to Arabic numerals for tumour grading. In earlier versions, each tumour entity was assigned a single grade, e.g., anaplastic astrocytoma was grade III and could not be classified as grade I, II, or IV. However, the 2021 WHO classification has introduced a "within-tumour-type" grading system for most tumours. For example, astrocytoma with Isocitrate dehydrogenase (IDH) mutation can now be classified as grade 2, 3, or 4, and the term "anaplastic" is no longer used for grade 3 tumours. Furthermore, the designation of tumour grades in the 2021 classification now includes the abbreviation "CNS”, e.g., glioblastoma, CNS WHO grade 4. This change highlights the distinct grading criteria specific to CNS tumours, differentiating them from tumours in other organ systems (Louis et al., 2021b).

Before 2016, diffuse gliomas were classified primarily based on their morphological features, as these were the most information available. Tumours with specific characteristics, such as round nuclei and cytoplasmic clearing, were classified as oligodendrogliomas, while those with clumped chromatin and angulated nuclei were categorised as astrocytomas. However, the 2016 classification edition revolutionised the glioma classification process, including the establishment of molecular features. The presence of IDH mutation and 1p/19q co-deletion became essential criteria for diagnosing specific types of gliomas. In the 2021 classification, it has been recognised that molecular subgrouping is more effective than histopathologic grading for risk stratification, especially in the case of diffuse astrocytomas. Consequently, hybrid entities like oligoastrocytomas, which often get reclassified as other tumour types when molecular testing is conducted, have been eliminated from the new system (Louis et al., 2007, Louis et al., 2021b, Brat et al., 2018).

Before discussing the 2021 WHO classification of adult gliomas, the most important molecular markers will be reviewed, focusing on IDH mutations due to their importance. The European Association of Neuro-Oncology's (EANO) latest guidelines (March 2022) consider eleven different molecular features to diagnose diffuse gliomas of adulthood (Weller et al., 2022, Weller et al., 2021) **(Table 1.2)**.

Table 1.2: Molecular markers for the diagnosis and management of gliomas.

Molecular marker	Biological function of affected genes	Diagnostic roles
IDH1 R132 or IDH2 R172 mutation	Gain-of-function mutation.	Distinguishes diffuse gliomas with IDH mutation from IDH-wild-type glioblastomas and other IDH-wild-type gliomas.
1p/19q codeletion	Inactivation of putative tumour suppressor genes on the short arm of chromosome 1 **and** the long arm of chromosome 19.	Distinguishes oligodendro-glioma, IDH- mutant and 1p/19q co-deleted from astrocytoma, IDH- mutant.
Loss of nuclear ATRX	Cell proliferation and promotion of cellular longevity by alternative lengthening of telomeres	Loss of nuclear ATRX in an IDH-mutant glioma is diagnostic for astrocytic lineage tumours.
Histone H3 K27M mutation	Mutation affects epigenetic regulation of gene expression.	Defining molecular feature of diffuse midline glioma, H3 K27M- mutant.
Histone H3.3 G34R/V mutation	Mutation affecting epigenetic regulation of gene expression.	Defining molecular feature of diffuse hemispheric glioma, H3.3 G34- mutant.
MGMT promoter methylation	DNA repair.	A predictive biomarker of benefit for alkylating chemo-therapy in patients with IDH- wild-type glioblastoma.
Homozygous deletion of CDKN2A/CDKN2B	Encodes cyclin-dependent kinase inhibitors 2A and 2B and tumour suppressor ARF, which function as regulators of Rb1 and p53- dependent signalling.	A marker of poor outcome and WHO grade 4 diseases in IDH-mutant astrocytomas.
EGFR amplification	Cell proliferation, invasion and resistance to induction of apoptosis.	EGFR amplification occurs in ~40–50% of glioblastoma, IDH wild type Molecular marker of glioblastoma, IDH wild type, WHO grade 4.
TERT promoter mutation	Cell proliferation; promotes cellular longevity by increasing TERT expression.	TERT promoter mutation occurs in ~70% of glioblastoma, IDH wild type and >95% of oligodendro-glioma, IDH- mutant and 1p/19q- co-deleted Molecular marker of glioblastoma, IDH wild type, WHO grade 4.
+7/–10 cytogenetic signature	Gain of chromosome 7 (harbouring genes encoding PDGFA and EGFR) combined with a loss of chromosome 10 (harbouring genes including PTEN and MGMT).	A molecular marker of glioblastoma, IDH wild type, WHO grade 4.
BRAFV600E mutation	Oncogenic driver mutation leading to MAPK pathway activation	Rare in adult diffuse gliomas but amenable to pharmacological intervention

** IDH1 R132 or IDH2 R172 mutation: Isocitrate dehydrogenase 1 (R132) or Isocitrate dehydrogenase 2 (R172) mutation, 1p/19q codeletion: Co-deletion of the short arm of chromosome 1 (1p) and the long arm of chromosome 19 (19q), ATRX: Alpha-thalassemia X-linked mental retardation, Histone H3 K27M mutation: Histone H3 lysine 27 to methionine mutation, Histone H3.3 G34R/V mutation: Histone H3.3 glycine 34 to arginine/valine mutation, MGMT promoter methylation: O6-methylguanine-DNA methyltransferase promoter methylation, CDKN2A/CDKN2B homozygous deletion: Cyclin-dependent kinase inhibitor 2A/2B homozygous deletion, EGFR amplification: Epidermal growth factor receptor amplification, TERT promoter mutation: Telomerase reverse transcriptase promoter mutation,+7/–10 cytogenetic signature: Gain of chromosome 7 and loss of chromosome 10, BRAFV600E mutation: B-Raf proto-oncogene, serine/threonine kinase V600E mutation, PDGFA: Platelet-Derived Growth Factor Subunit A.*
Adapted from (Weller et al., 2021).

IDH

It is essential to state that determination of the mutational status of IDH is the most impactful change in recent WHO classification. It is crucial for differentiating GBM and Astrocytoma grade 4 (Louis et al., 2021a). IDH1 and IDH2 are metabolic enzymes that participate in the tricarboxylic acid cycle by catalysing the oxidative carboxylation of isocitrate to α-ketoglutarate and carbon dioxide (Kaminska et al., 2019).

Mutations in the IDH1 and IDH2 genes result in a single amino acid substitution of arginine residues at codon 132 of the IDH1 gene, and codons 140 or 172 of the IDH2 gene. In addition to losing their normal catalytic activity, the mutant IDH enzymes gain the function of producing 2-hydroxyglutarate (2-HG). 2-HG is widely believed to function as an oncometabolite primarily due to its role in competitively inhibiting the enzymatic activities of Alpha-ketoglutarate dependent dioxygenases. As a result, there is an increase in Deoxyribonucleic Acid (DNA) and histone hypermethylation, which is a prominent mechanism contributing to the development of tumours (Solomou et al., 2023, Sharma et al., 2023a) **(Figure 1.10).**

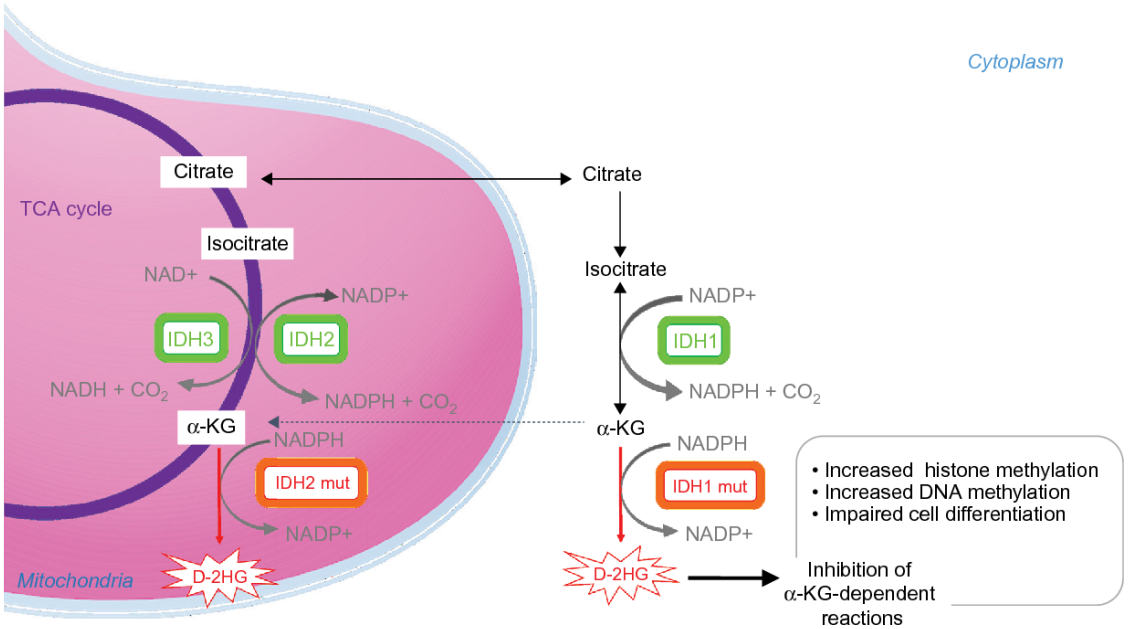

Figure 1.10: Enzymatic activities of wild type and mutated IDH enzymes.

Notes: The IDH family of enzymes comprises three proteins located in the cytoplasm and peroxysomes (IDH1), and mitochondria (IDH2 and IDH3). IDH1 and IDH2 catalyze the reversible NADP+-dependent oxidative decarboxylation of isocitrate to αKG. IDH3 catalyzes the NAD+-dependent conversion of isocitrate to αKG in the TCA cycle. IDH1 and IDH2 mutant enzymes gain neomorphic enzymatic activity, converting NADPH and αKG to NADP+ and D-2-hydroxyglutarate (D-2HG). D-2HG acts as a weak competitive inhibitor of αKG-dependent dioxygenases. αKG-dependent dioxygenases are involved in various cellular processes such as hypoxia, angiogenesis, maturation of collagens of the extracellular matrix, and regulation of epigenetics. Excess of D-2HG is associated with increased histone and DNA methylation, altering cancer cells differentiation. Abbreviations: αKG, alpha ketoglutarate; D-2HG, D-2-hydroxyglutarate; IDH, isocitrate dehydrogenase; DNA, deoxyribonucleic acid; mut, mutated; NAD, nicotinamide adenine dinucleotide; NADP, nicotinamide adenine dinucleotide phosphate; TCA cycle, tricarboxylic acid cycle.

Taken from (Mondesir et al., 2016)

IDH wildtype GBM:

In the latest WHO classification, glioblastoma is a diffuse astrocytic glioma with no mutations in IDH genes or histone H3 genes. It is characterised by microvascular proliferation, necrosis and/or specific molecular features, including Telomerase Reverse Transcriptase (TERT) promoter mutation, Epidermal growth factor receptor (EGFR) gene amplification and/or a +7/–10 cytogenetic signature. Additional common genetic events include mutations or deletion of phosphatase and tensin homolog (PTEN), BRAF V600E mutation and TP53 mutations; however, it retains a normal Alpha Thalassemia/Mental Retardation Syndrome X-Linked (ATRX) protein, as determined by immunohistochemistry. O6-Methylguanine-DNA Methyltransferase (MGMT) promoter methylation status is important, as it predicts response to alkylating chemotherapeutic drugs such as temozolomide (TMZ). GBM tend to occur in older adults and are rare below the age of 55 (Ostrom et al., 2019), (Weller et al., 2022) **(Figure 1.11).**

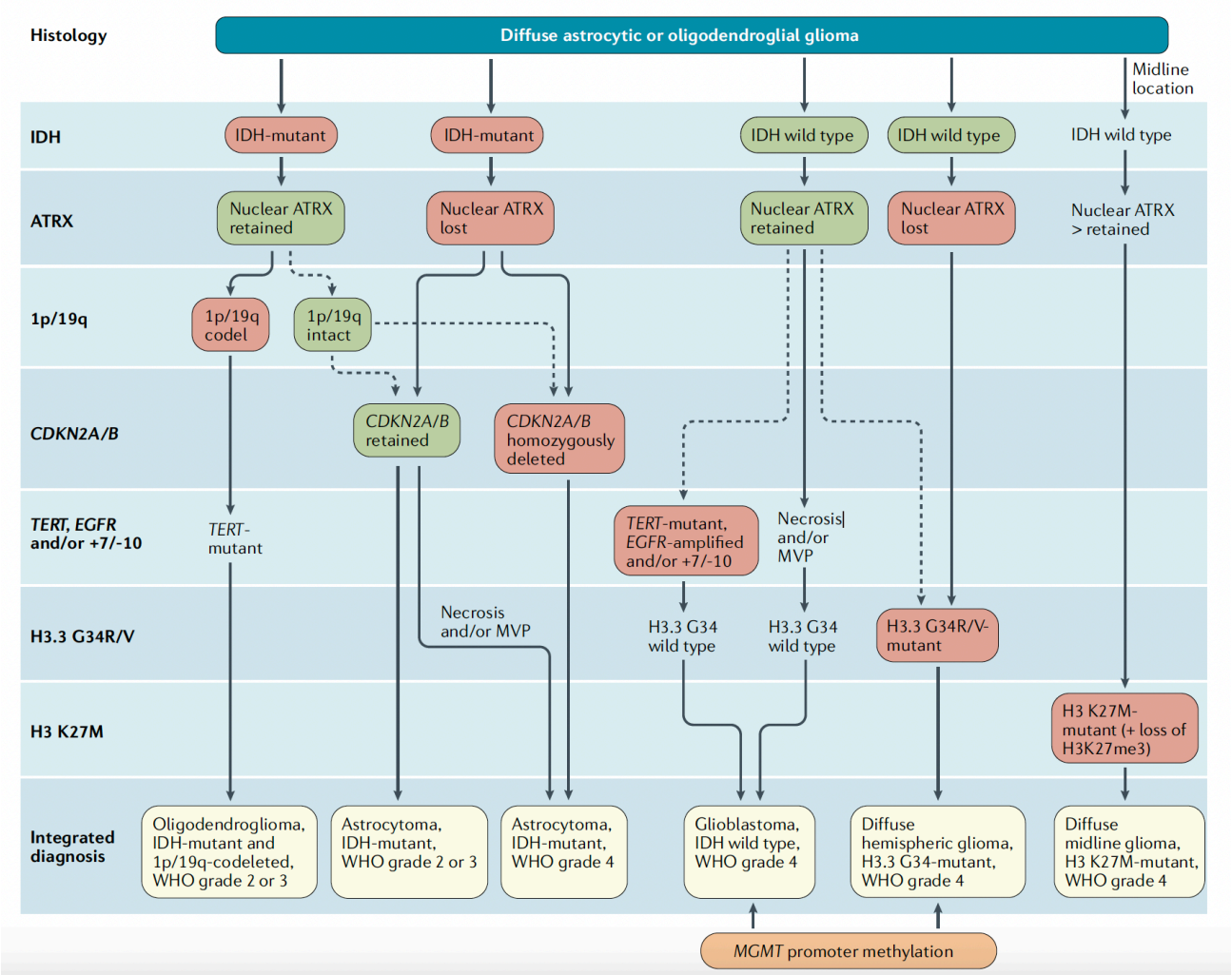

Figure 1.11: Diagnostic algorithm for the integrated classification of the major diffuse gliomas in adults.

** MVP: microvascular proliferation.*

Taken from Weller et al (Weller et al., 2021).

Astrocytoma IDH-mutant:

Astrocytoma, IDH-mutant, is defined by a mutation in either IDH1 or IDH2 resulting in overproduction of the oncometabolite D-2-hydroxyglutarate, which acts as an inhibitor of enzymes that use α-ketoglutarate as a cofactor, resulting in genomic Cytosine-phosphate-Guanine (CpG) hypermethylation and suppression of differentiation (could one of the references go here?). These tumours most often occur in younger adults (median age 38 years) and are rarely diagnosed in adults over 55. Most IDH-mutant astrocytomas also have Tumour Protein p53 (TP53) alterations resulting in substantial nuclear accumulation of abnormal p53 in >50% of tumour cell nuclei. About 90% of supratentorial IDH-mutant astrocytomas also have ATRX mutations that result in loss of normal ATRX expression in the tumour cells. Therefore, p53 and ATRX are immunohistochemistry markers that are useful as part of a panel when working on diffuse gliomas. IDH-mutant astrocytoma grades range from 2 to 4, based on the presence of anaplasia, mitotic activity, necrosis, microvascular proliferation, and homozygous CDKN2A/B deletion (Mondragon-Soto et al., 2022) (van den Bent et al., 2021).

It is observed that high-grade IDH-mutant astrocytomas are less aggressive than their IDH-wildtype counterparts. PFS (Progression-Free Survival) and OS were examined, revealing significant statistical differences between two groups of patients based on their mutation status: mutated IDH (total life expectancy (TLE) 18.9 months and survival gross (SG) 24 months) compared with IDH wild type (TLE 12 months and SG 14 months) (Mondragon-Soto et al., 2022) **(Figure 1.12).** Nevertheless, the current recommended standard of therapy for high-grade IDH mutant gliomas remains similar to that for IDH-wildtype GBM, given that it the most effective approved treatment (van den Bent et al., 2021).

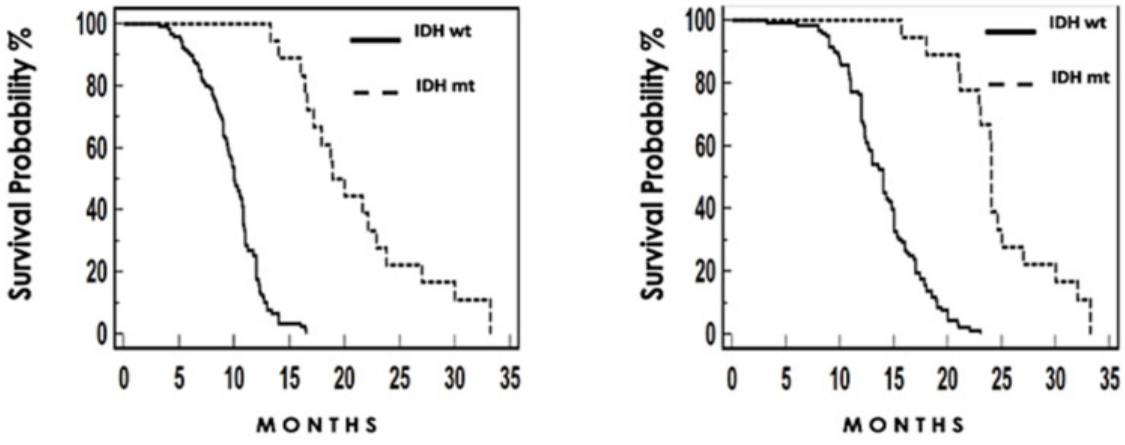

Figure 1.12: Clinical experience based on IDH 1 mutation.
Left: Progression. Right: Overall survival.
Taken from ***(Mondragon-Soto et al., 2022).***

Diffuse hemispheric glioma:

In the presence of Histone H3.3 Glycine 34 Arginine/Valine (histone H3.3 G34R/V) mutations should be assessed by immunohistochemistry or DNA sequencing to identify H3.3 G34- mutant diffuse hemispheric gliomas. Patient data demonstrate a median age at diagnosis of 15.8 years (interquartile range [IQR]: 13–22 years). Most frequently, the disease presents in only a single lobe, the most common being the frontal lobe. The most described co-mutations are the ATRX mutations and TP53. The median survival time for patients diagnosed with H3 G34-mutant tumours was 17.3 months (Crowell et al., 2022, Lucas et al., 2021)

Diffuse midline glioma:

H3 K27M- mutant (Histone H3 lysine 27 to methionine mutation), WHO grade 4 diffuse gliomas located in midline structures, such as the thalamus, pons, brainstem and spinal cord. These malignancies carry mutations in the histone proteins H3.3 or H3.1, with a lysine-to-methionine substitution at position 27 on the histone tail (K27M).H3 K27M- mutant diffuse midline gliomas are typically positive for nuclear immunostaining of H3 K27M with the corresponding loss of nuclear staining for K27-trimethylated histone H3 (H3K27me3), which together serve as immunohistochemical markers of this tumour type (Weller et al., 2021). The median age of diagnosis is 6-7 years old, with a near-zero survival rate. Only radiation therapy provides marginal survival benefit; however, the median survival time remains less than a year. Historically, the infiltrative nature and sensitive tumour location rendered surgical removal and biopsies difficult (Pachocki and Hol, 2022, Coleman et al., 2023).

Oligodendroglioma:

Both 1p/19q co-deletion and IDH mutations are essential for diagnosing oligodendroglioma. In addition to IDH mutations and 1p/19q co-deletion, most oligodendrogliomas also have TERT promoter mutations (Eckel-Passow et al., 2015). In contrast to IDH mutant astrocytomas, oligodendrogliomas tend to retain ATRX expression because 1p/19q co-deletion is mutually exclusive with TP53 and ATRX gene alterations. Some oligodendrogliomas have CDKN2A/B deletion, which predicts more aggressive behaviour when present (Mohile et al., 2022, Bou Zerdan and Assi, 2021).

1.2.2 Genetic classification

A widely adopted approach for molecular subclassification of GBM, as proposed by Verhaak et al. (2010), involves the identification of four distinct subtypes: Proneural, Neural, Classical, and Mesenchymal. These subtypes are determined based on specific molecular characteristics associated with each subtype (Verhaak et al., 2010) **(Figure 1.13).**

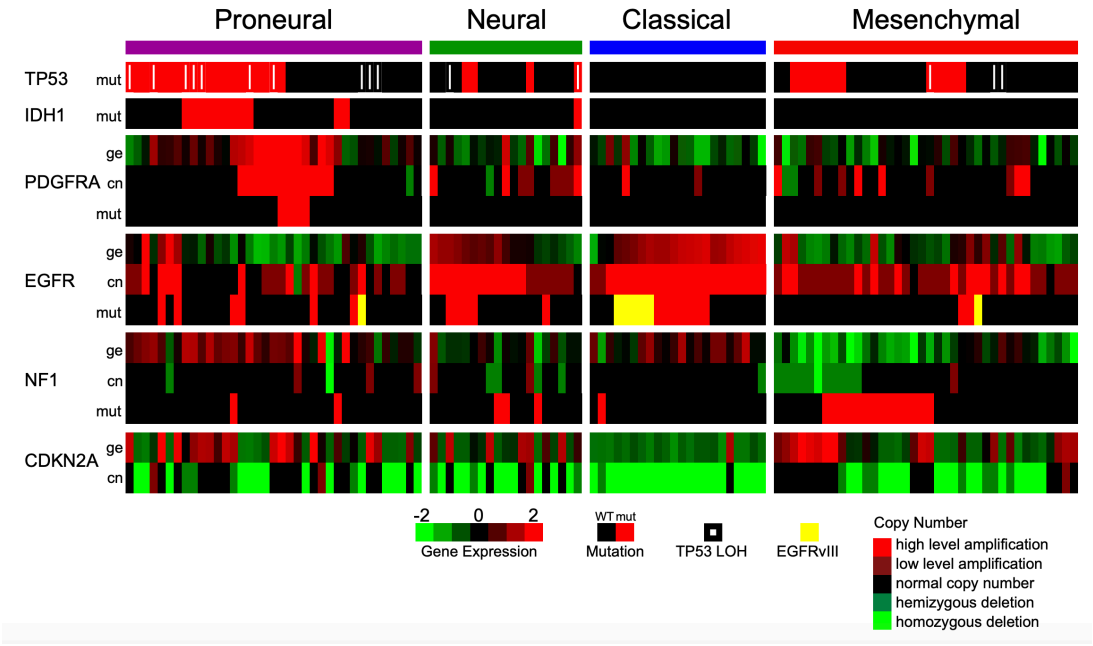

Figure 1.13: Integrated View of Gene Expression and Genomic Alterations across Glioblastoma Subtypes

Gene expression data (ge) were standardised (mean equal to zero, standard deviation equal to 1) across the 202 data set; data are shown for the 116 samples with both mutation and copy number data. Mutations (mut) are indicated by a red cell, a white pipe indicates loss of heterozygosity, and a yellow cell indicates the presence of an EGFRvIII mutation. Copy number events (cn) are illustrated by bright green for homozygous deletions, green for hemizygous deletions, black for copy number neutral, red for low-level amplification, and bright red for high-level amplifications. A black cell indicates no detected alteration

Taken from (Verhaak et al., 2010).

The Proneural subtype of glioblastoma is commonly observed in younger patients and is characterised by elevated expression of the PDGFRA gene and frequently an IDH1 mutation. Patients with this subtype may exhibit relatively better survival outcomes than those with other subtypes (proneural 17, classical 14.7 and mesenchymal 11.5 months). The proneural subtype demonstrates the characteristics typically associated with oligodendroglial cells described above (Zhang et al., 2020b, Verdugo et al., 2022).

The Neural subtype of glioblastoma exhibits relatively few gene changes. This subtype is known to be more responsive to radiation and chemotherapy treatments than other types. The neural subtype originates from both astrocytes and oligodendrocytes. Glioblastomas classified as the Neural subtype often express neural markers such as SYT1 (Synaptotagmin 1), SLC12A5 (Solute carrier family 12 member 5), GABRA1 (Gamma-aminobutyric acid type A receptor alpha1), and Neurofilament light polypeptide (NEFL) (Zhang et al., 2020b, Verdugo et al., 2022).

The Classical subtype of GBM is characterised by CDKN2A homozygous deletion and EGFR amplification (Ah-Pine et al., 2023). Furthermore, the activation of Sonic Hedgehog pathways involving SMO (Smoothened homolog), GAS1 (Growth arrest-specific protein 1), and GLI2 (Growth arrest-specific protein 2) is observed in this subtype. It exhibits the characteristics of astrocytic gliomas. Importantly, patients with the Classical subtype experience a significant reduction in mortality when treated with aggressive radiotherapy and chemotherapy (Zhang et al., 2020b, Verdugo et al., 2022).

The Mesenchymal subtype of glioblastoma is characterised by extensive necrosis and inflammation, upregulation of interstitial and angiogenesis genes, deletion of tumour suppressor genes P53, PTEN, and Neurofibromatosis type 1 (NF1), and high expression of genes in the tumour necrosis factor superfamily and the NF-κB pathway. Although Mesenchymal subtypes show responsiveness to aggressive radiotherapy and chemotherapy, they have the worst prognosis among all subtypes (Median survival is 11.5 months). The Mesenchymal subtype exhibits a high expression of genes such as *VEGF-A* (Vascular endothelial growth factor A), *VEGF-B*, Angiopoietin-1 (Ang-1), and *Ang-24* that are involved in angiogenesis and vascular endothelial growth. Chitinase-3-like protein 1**(**CHI3L1) is a specific biomarker overexpressed in the mesenchymal glioblastoma subtype, distinguishing it from other molecular subtypes. The malignant cells typically exhibit astrocyte-like features (Zhang et al., 2020b, Verdugo et al., 2022).

In conclusion, the 2021 WHO classification of gliomas significantly advances our understanding of tumours, integrating molecular and genetic criteria with traditional histopathological appearance. The central role of IDH mutation status in differentiating glioblastoma subtypes highlights the importance of molecular diagnostics in guiding diagnosis and treatment (Weller et al., 2021). Additionally, the genetic classification provides further insight into the molecular heterogeneity of glioblastoma, with each subtype demonstrating unique genetic alterations and potential therapeutic vulnerabilities (Verhaak et al., 2010). These advancements pave the way for developing personalised treatment strategies tailored to the specific molecular profile of each patient's tumour, ultimately improving patient outcomes and quality of life.

1.3 Diagnosis of Glioblastoma

Unfortunately, only 2% of GBM is diagnosed by a general practitioner in England. Almost 50% of the patients are first diagnosed after presenting to the Accident & Emergency (A&E) department (McKinnon et al., 2021). Thus, accurate and rapid methods for their diagnosis and follow-up are essential for giving patients a chance for maximum treatment options. Diagnosis of GBM currently depends on a clinical picture combined with an appropriate imaging modality.

Most patients' clinical presentations result from increased intracranial pressure from the mass effect of the tumour itself and affected adjacent brain structures. The symptoms and signs vary according to the anatomical location of the tumour, e.g. a frontal lesion can cause contralateral weakness, or an occipital lesion can cause visual deficit. Hence, they are not specific to glioblastoma and can be found in other brain tumours or some brain lesions that share the exact intracranial location. Headache is the most frequent symptom, but patients can present with vomiting, nausea, weakness, seizure, visual problems, memory difficulty, speech difficulty, drowsiness, significant confusion and even impaired consciousness (Gilard et al., 2021, McKinnon et al., 2021) **(Figure 1.14).** Therefore, clinical examination alone is insufficient to diagnose; imaging is essential.

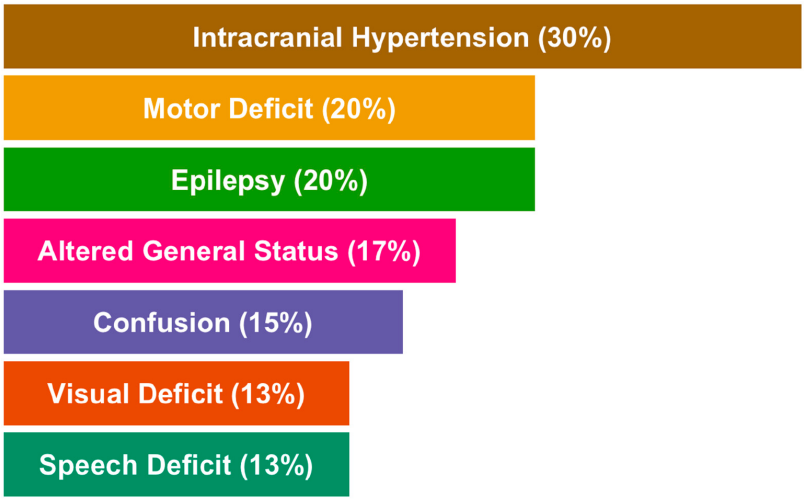

Figure 1.14: Overview of the main reported clinical features in glioblastoma
Taken from (Gilard et al., 2021).

A computed tomography (CT) scan is the first investigation when a patient presents at A&E. However, the modality of choice is magnetic resonance imaging (MRI) with gadolinium contrast agent, which enhances tumour vasculature and helps identify areas of active tumour growth by disrupting the blood-brain barrier in GBM. The tumour typically appears on MRI as an irregular, ill-defined mass surrounded by vasogenic oedema. Enhancement occurs after contrast injection around the rim of the tumour, while the central area remains non-enhanced. This distribution picture of enhancement is explained as the actively growing part of glioblastoma at the periphery is where neo-angiogenesis is occurring, and the dye can localise, while the central part is more necrotic (Henssen et al., 2022, Al-Okaili et al., 2007) **(Figure 1.15).** The expected location of the glioblastoma is mainly in the supratentorial, namely the frontal lobe (24.9%), and the temporal lobe (21.8%), with other brain areas being affected less frequently (Brodbelt et al., 2015b).

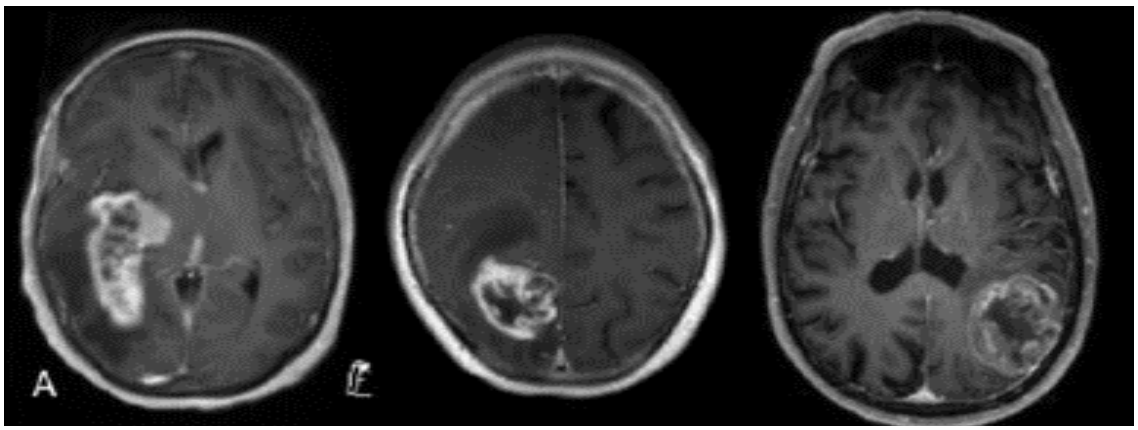

Figure 1.15: Different examples of glioblastoma appearance using Conventional brain MRI with contrast.

Adapted from (Henssen et al., 2022).

Despite conventional MRI remaining the cornerstone, more advanced imaging techniques are needed due to the aggressive infiltration nature of GBM to identify the tumour margins for more precise treatment and follow-up. Therefore, perfusion MRI, Magnetic Resonance Spectroscopy (MRS), Diffusion tensor imaging (DTI) and 18F-fluoroethylthyrosine-positron emission tomography (FET-PET) will be discussed further in this section(Shukla et al., 2017).

Perfusion MRI measures regional blood flow within the brain, which is an early indicator of malignant transformation in low-grade gliomas to higher grades. There is some evidence that perfusion may be able to detect the true progression and the transforming anaplastic foci within low-grade gliomas (Henssen et al., 2022, Danchaivijitr et al., 2008, Tournier et al., 2011). Serial MR perfusion of low-grade glioma can reveal a progressive increase in relative cerebral blood volume (rCBV) over time, warning of increasing tumour vascularity and transformation to high-grade. Therefore, perfusion MRI can be a valuable tool to identify early transformation of low-grade gliomas (Danchaivijitr et al., 2008) **(Figure 1.16).**

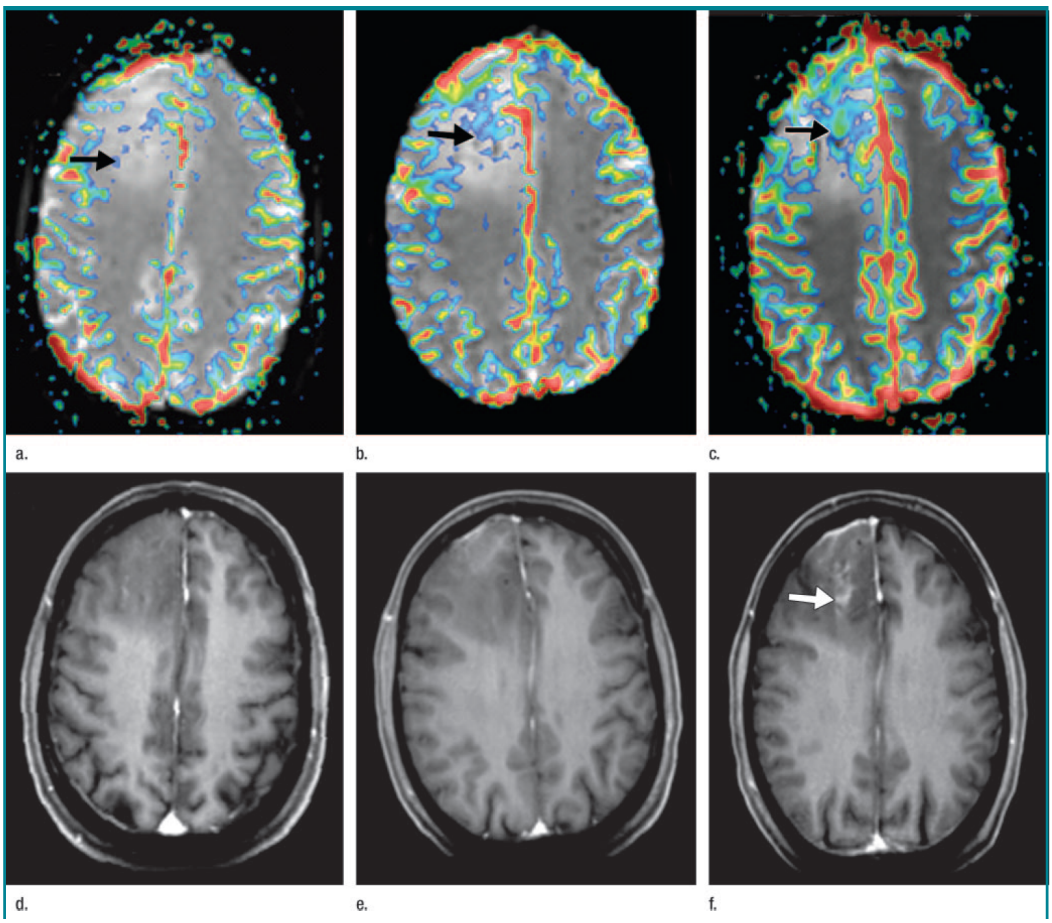

Figure 1.16: Images from serial MR perfusion studies in a 30-year-old patient with low-grade glioma that showed progression to high-grade tumour 18 months after study entry.

(a-c) (rCBV)overlay images. (d–f) post-contrast-enhanced volumetric T1-weighted sequence. The rCBV map at baseline shows a small area of elevated rCBV (a - arrow) measuring up to 4.52 units. At six months, the rCBV map (b) before the transformation to a higher-grade tumour shows a larger blood volume (arrow) area, measuring up to 8.32. (c) rCBV map at transformation shows a further increase in area with elevated rCBV (arrow), reaching a maximum value of 12.04. (d) A baseline contrast-enhanced T1-weighted image shows a hypointense tumour without pathologic enhancement. (e) There is no evidence of pathologic intratumoral enhancement six months before transformation, despite a markedly increased rCBV. (f) At transformation, there is an irregular enhancement in the centre of the tumour (arrow); the area of pathologic enhancement is much smaller than the region of increased rCBV. Taken from (Danchaivijitr et al., 2008).

MRS can measure tumour metabolites in an area of interest. Glioblastoma has a typical pattern which reflects its metabolism. It usually has a decreased N- acetyl aspartate (a marker of white matter integrity), a rise in total choline (a quality of membrane turnover) and signals for lipids and lactate (due to necrosis) compared with normal brain tissue. MRS can help in cases where the diagnosis is in doubt, as in pseudoprogression (Henssen et al., 2022, Bulik et al., 2015) (Figure 1.17). Pseudoprogression, often caused by radiation-induced inflammation and cell death, leading to ambiguous changes in standard gadolinium-enhanced T1-weighted images (T1WI) following surgical and chemoradiotherapy. That can confuse the treatment team whether these changes are representing true recurrence and progression or radiation induced inflammation. MRS aids in this

distinction by providing metabolic information: high tCho/tNAA (total choline to total N-acetyl aspartate) and Lip + Lac/tCr (lipid + lactate to total creatine) ratios, indicative of increased cell membrane turnover and necrosis, respectively, are associated with relapse, whereas lower ratios are seen in pseudoprogression. Another way of differentiation is using Apparent Diffusion Coefficient (ADC) maps, which measure water molecule movement within tissues, reveal lower values in active tumour growth (relapse) areas due to increased cellular density. By combining these imaging modalities, clinicians can make more informed decisions regarding the need for further treatment or just continue surveillance (Bulik et al., 2015).

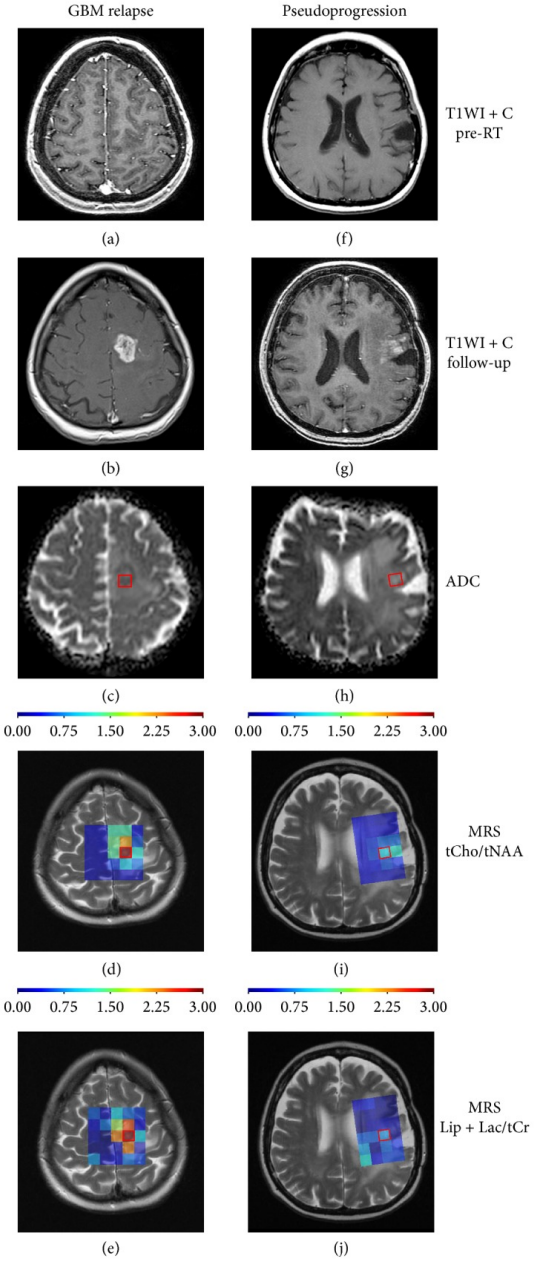

Figure 1.17: Using MRS and ADC to differentiate between glioblastoma relapse and pseudoprogression

(a) + (f) shows T1WI with gadolinium after surgical resection before radiotherapy, (b) + (g) shows follow-up T1WI with gadolinium after three months of radiotherapy, (c) + (h) show ADC, a low value in GBM relapse and an elevated ADC value in pseudoprogression due to cell death. (d) + (i) show proton MR spectroscopy maps focused on tCho/tNAA ratio with high ratio in GBM relapse and low

in pseudoprogression), (e) + (j) show proton MR spectroscopy maps focused on Lip + Lac/tCr ratio with high in GBM relapse and low in pseudoprogression). Adapted from (Bulik et al., 2015).

DTI is an extension of DWI imaging and is sensitive to the directional diffusion of water molecules (Price et al., 2006, Tournier et al., 2011). The water molecules tend to diffuse more freely along the direction of white matter tracts as compared to the tumour tissue, and it can be used to assess the disruption of white matter tracts close to the tumour (Price et al., 2006, Tournier et al., 2011). To further help clinicians, three-dimensional (3D) reconstruction of those white tracts can be done; this is called fibre tractography (FT). That leads to better surgical planning and a more accurate expectation of possible neurological deficits (Price et al., 2006, Tournier et al., 2011) **(Figure 1.18).**

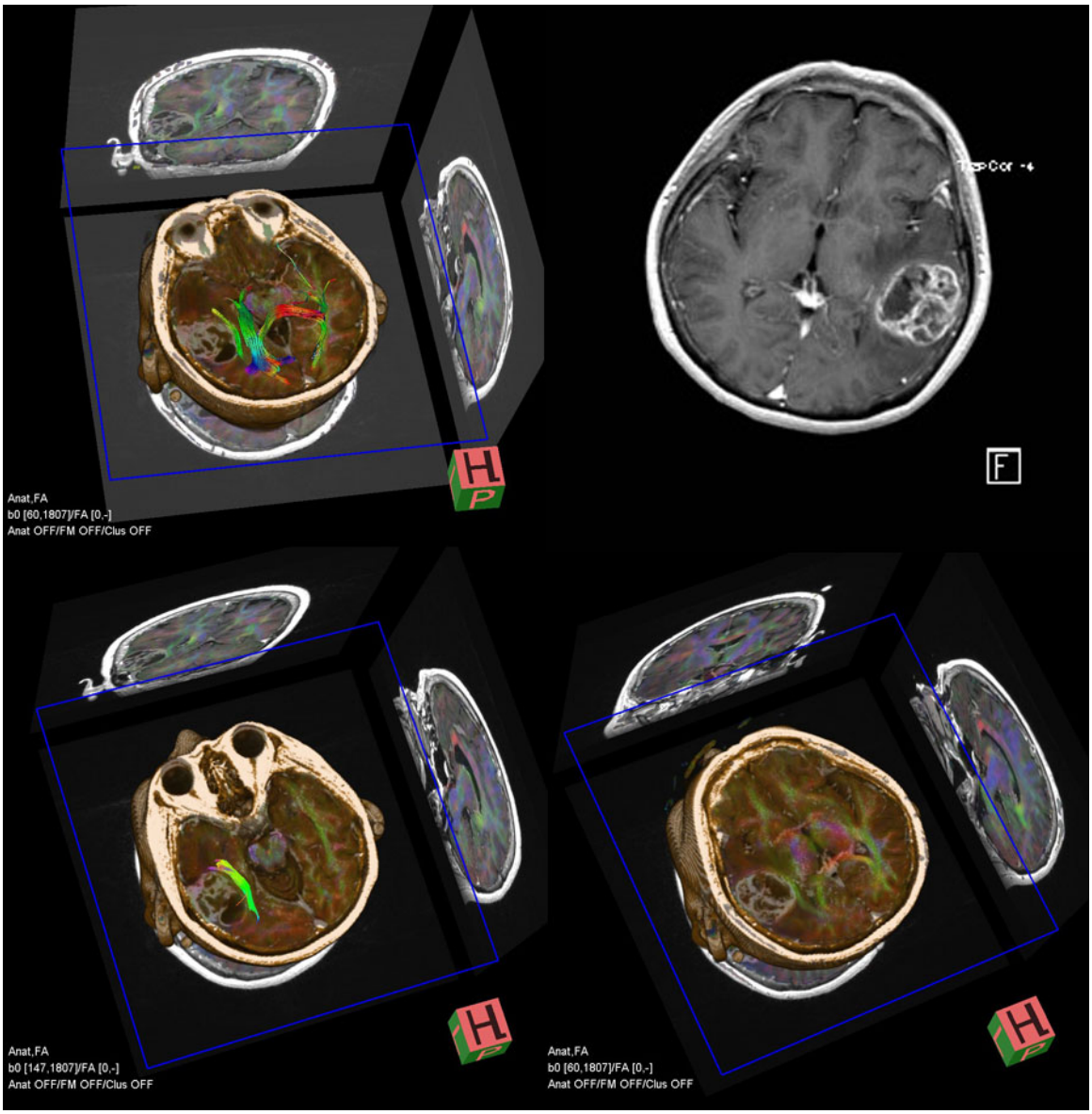

Figure 1.18: Post-contrast MR shows a necrotic mass in the left temporal lobe.

Taken from (Bhuta, 2011)

Fluorine-18 fluorodeoxyglucose (18F-FDG) PET is a molecular imaging technique based on that glucose analogue which can across the blood-brain barrier (BBB) into the brain and become trapped in tumour cells (Quartuccio et al., 2020). Increased accumulation of 18F-FDG directly reflects glucose hypermetabolism compared to the normal cortex (Quartuccio et al., 2020). Some evidence has shown that using PET to direct image-guided biopsies results in better diagnostic outcomes from biopsies (Levivier et al., 1995), which can facilitate identifying the area for surgical removal (Pirotte et al., 2009, Quartuccio et al., 2020). Additionally, it can differentiate between glioblastoma and some other lesions like low-grade glioma and primary central nervous system lymphoma (PCNSL) (Quartuccio et al., 2020) **(Figure 1.19).**

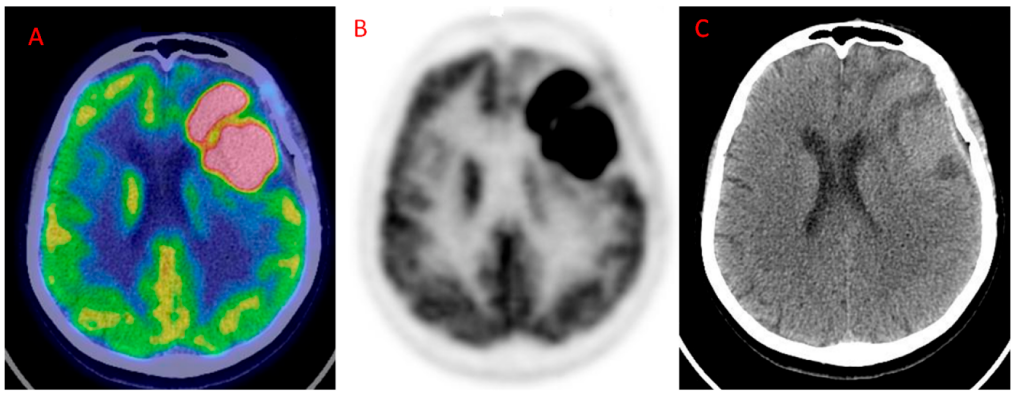

Figure 1.19: Primary Central Nervous System Lymphoma (PCNSL) in the left frontal cortex showing high 18F-FDG uptake.

(A) Axial fused 18F-FDG PET/ CT; (B) 18F-FDG PET; (C): CT.

Taken from (Quartuccio et al., 2020).

Finally, despite previously mentioned advanced diagnostic tools, there is a requirement for new methods to provide earlier diagnosis and to monitor tumour progression, regression, and recurrence. That is why an enormous amount of ongoing work is searching for biomarkers as potential diagnostic or prognostic indicators in GBM (Sareen et al., 2022). Many potential biomarkers have been studied in malignant tissues or body fluids such as serum or plasma, including DNA, Ribonucleic Acid (RNA), enzymes, cytokines, metabolites, transcription factors, and cell surface receptors (Wu and Qu, 2015). However, most biomarkers lack reliability and demand more pre-clinical and clinical studies before being them in the current clinical practice (Sareen et al., 2022). This work is part of those efforts.

1.4 Treatment of Glioblastoma

Despite recent advancements in diagnosis and treatment, the prognosis for glioma patients remains relatively poor in overall survival. This thesis section will critically examine the current approaches, including medical management, surgical interventions, chemotherapy and radiotherapy. Followed by a concise overview of promising therapeutic modalities such as targeted molecular therapies, antiangiogenic therapy, immunotherapy, and tumour treating fields.

1.4.1 Treatment decision making:

Due to the absence of current curative treatments, selecting an appropriate treatment modality poses a significant challenge for patients and medical professionals. Developing a personalised treatment plan is crucial, and various factors need to be considered, including the patient's functional status, the risk-benefit ratio associated with different interventions, and the prognostic implications specific to each patient. As per the most recent guidance from the U.K. National Institute for Health and Care Excellence (NICE), the decision-making process for treating GBM necessitates the involvement of a multidisciplinary team (MDT) in collaboration with the patient (Excellence, 2021). Typically, the MDT consists of neurosurgeons, neuro-oncologists, specialist nurses specialising in neuro-oncology, and neuroradiologists. Treatment options may encompass a spectrum ranging from conservative approaches to surgical intervention and subsequent adjuvant therapy. The primary objective of glioma management is to achieve an accurate diagnosis and extend progression-free survival. Factors such as Karnofsky's performance status (KPS) and age are crucial in determining each individual's most appropriate treatment approach (Excellence, 2021) **(Figure 1.20).**

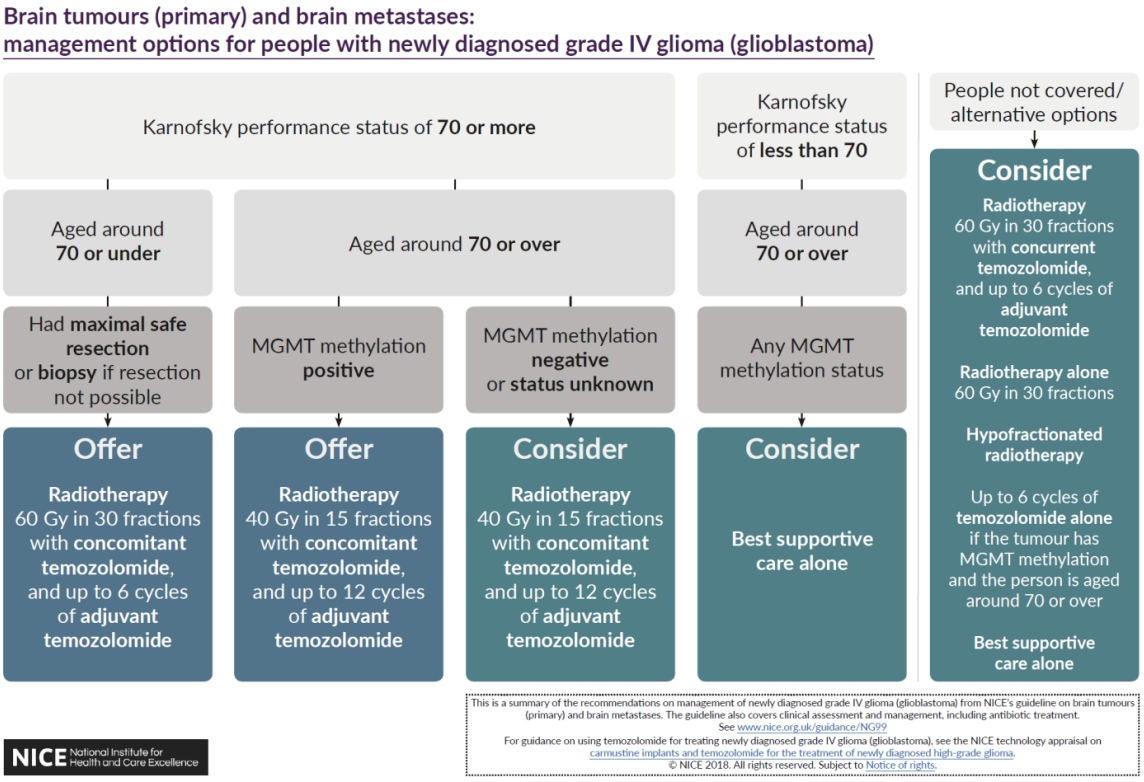

Figure 1.20: NICE Recommendations on management of newly diagnosed grade IV glioblastoma
Taken from (Nice, 2021)

KPS was developed in the late 1940s (Timmermann, 2013). It is widely utilised for assessing the functional status of cancer patients as one of the essential factors in decision-making. It employs an 11-point rating scale from normal functioning (100) to death (0). This scoring system quantitatively evaluates the patient's overall ability to perform ordinary tasks and activities of daily life. It serves as a valuable tool in assessing the ability of the patient to undergo specific therapies and their overall prognosis (Mor et al., 1984) **(Figure 1.21).**

KARNOFSKY PERFORMANCE STATUS SCALE DEFINITIONS RATING (%) CRITERIA

Able to carry on normal activity and to work; no special care needed.	100	Normal no complaints; no evidence of disease.
	90	Able to carry on normal activity; minor signs or symptoms of disease.
	80	Normal activity with effort; some signs or symptoms of disease.
Unable to work; able to live at home and care for most personal needs; varying amount of assistance needed.	70	Cares for self; unable to carry on normal activity or to do active work.
	60	Requires occasional assistance, but is able to care for most of his personal needs.
	50	Requires considerable assistance and frequent medical care.
Unable to care for self; requires equivalent of institutional or hospital care; disease may be progressing rapidly.	40	Disable; requires special care and assistance.
	30	Severely disabled; hospital admission is indicated although death not imminent.
	20	Very sick; hospital admission necessary; active supportive treatment necessary.
	10	Moribund; fatal processes progressing rapidly.
	0	Dead

Figure 1.21: Karnofsky performance status score.

Taken from (Mor et al., 1984).

Sometimes, the best supportive care is the most suitable approach for patients. For instance, surgical intervention may not be viable for individuals with a KPS below 70, particularly those aged 70 years or older. In such situations, providing high-quality palliative and supportive care becomes paramount. Focusing on alleviating symptoms, enhancing comfort, and addressing the patient's psychosocial needs becomes crucial in optimising their overall well-being(Nice, 2021).

Conversely, patients aged 70 years or below who exhibit a high-performance status score of 70 or higher are typically considered ideal candidates for an aggressive treatment approach involving maximal safe surgical resection followed by chemoradiotherapy. In these cases, the goal is to achieve the maximum surgical removal, followed by a combination of chemotherapy and radiotherapy to target any remaining cancer cells and minimise the risk of recurrence (Excellence, 2021), (Stupp et al., 2005) Since Stupp protocol in 2005, no significant breakthroughs or fundamental changes in the treatment approach for GBM have emerged (Excellence, 2021).

1.4.2 Medical management:

Dexamethasone:

Upon diagnosis of glioblastoma, symptomatic patients are typically given dexamethasone at 16 mg/day as a starting dose. Dexamethasone is crucial in alleviating cerebral vasogenic oedema associated with GBM, leading to significant and rapid improvement in presenting symptoms such as headache, weakness, and speech difficulties. However, it is essential to note that this intervention is temporary as the tumour grows and symptoms are likely to reoccur. Nonetheless, this temporary relief provides valuable time to complete necessary investigations and facilitate effective communication between the medical team, the patient, and their relatives during this life-changing event (Kotsarini et al., 2010).

Dexamethasone is administered to decrease symptomatic peritumoral vasogenic oedema due to its potent anti-inflammatory properties and minimal mineralocorticoid effects (Lim-Fat et al., 2019b). The efficacy of dexamethasone in reducing oedema suggests their involvement in BBB disruption mechanisms. Analysis of the blood-tumour barrier using gadolinium-diethylenetriamine penta-acetic acid (Gd DTPA) in patients with primary and secondary brain tumours confirms this. Some studies have demonstrated a radiologically noticeable reduction in cerebral oedema following seven days of dexamethasone treatment, which correlates with a decrease in the transport rate across the blood-tumour barrier (Andersen et al., 1994). The available evidence suggests that dexamethasone may reduce BBB permeability, although the precise mechanism of action has yet to be fully understood. One suggested mechanism involves the decreased expression of VEGF, a factor that significantly enhances permeability (Kim et al., 2008, Kaur and Thomas, 2023) **(Figure 1.22).**

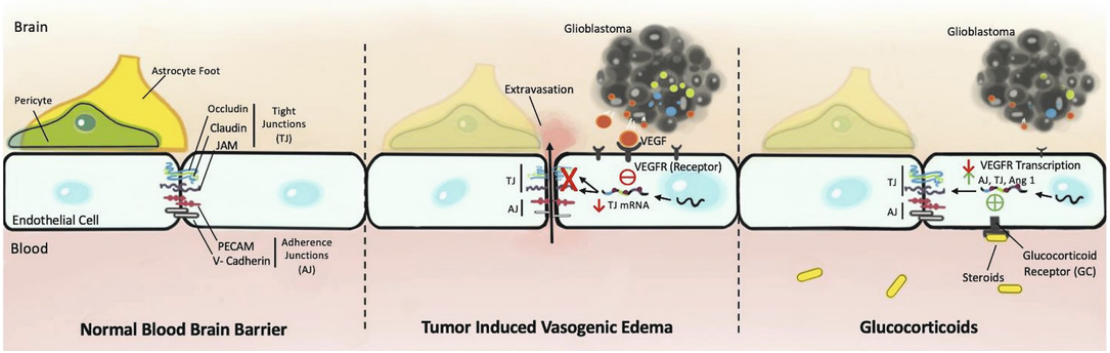

Figure 1.22: Glucocorticoid Pathophysiology.

Taken from (Kaur and Thomas, 2023).

Dexamethasone has a half-life of 36-54 hours (hrs). This prolonged activity allows for sustained therapeutic effects after the initial high-dose administration. Furthermore, clinical observations indicate that a significant proportion (75%) of patients exhibit noticeable neurological improvement within 24-72 hrs of initiating dexamethasone treatment (Ryan et al., 2012). By starting with a high dose and then gradually tapering it over two weeks, the regimen maximises the beneficial effects of dexamethasone during the critical initial phase when rapid neurological improvement is observed. At the same time, gradual tapering helps reduce potential toxicity by minimising the cumulative dose and duration of corticosteroid exposure (Lim-Fat et al., 2019a, Lee and Wen, 2016). Overall, this approach aims to optimise the therapeutic benefits of dexamethasone while minimising the risks of adverse effects.

1.4.3 Surgical management

Up to 80% of patients experience their first GBM recurrence near the site of surgical resection. Despite this high local relapse rate, extensive surgical resection has been demonstrated to extend survival (Wach et al., 2023).

The impact of the extent of resection (EOR) on improving survival in GBM patients is well established (Ius et al., 2020). Gross total resection can be assessed by measuring the residual tumour volume following surgery. The relationship between residual tumour volume and overall survival supports the principle of maximum safe resection. This relationship can be demonstrated by employing log-logistic regression models, where predicted OS and residual tumour volume are single predictors. Both curves exhibit a continuous, nearly linear relationship, running parallel (Skardelly et al., 2021) **(Figure 1.23)**.

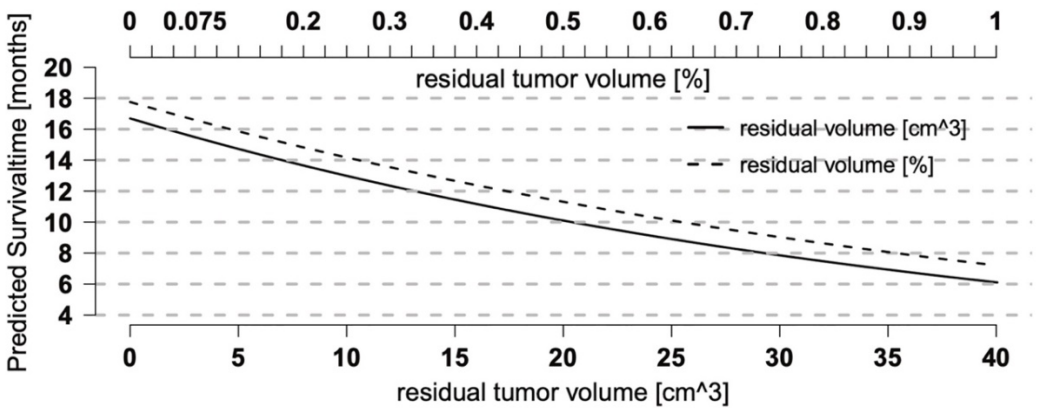

Figure 1.23: Relationship between residual tumour volume and overall survival.
Taken from (Skardelly et al., 2021).

A recent meta-analysis suggests that resection, as opposed to biopsy, is associated with improved OS and PFS in elderly patients with newly diagnosed GBM. However, postoperative complications are more common with resection (Pichardo-Rojas et al., 2024). Interestingly, the first multi-institutional randomised clinical trial comparing biopsy with resection of surgically accessible GBM in the elderly shows that while PFS and quality of life (QOL) were improved by resection, it did not translate to improved OS. There was no statistically significant difference in median survival between the surgery (9.37 months) and the biopsy (8.96 months, $p = 0.36$). However, the surgery group had an increased PFS (5.06 vs 4.02 months; $p = 0.034$) adjusted hazard ratio (HR) 0.50, 95% CI 0.32–0.78, $p = 0.002$). Less deterioration of quality of life and KPS score evolution than in the biopsy group was (Laigle-Donadey et al., 2023).

The Response Assessment in Neuro-Oncology group tried to go beyond the gross total resection term to supramaximal resection. Supramaximal resection, which involves removing non-contrast-enhancing (non-CE) tumour tissue beyond the contrast-enhancing (CE) borders, provides a substantial survival advantage. Specifically, patients who underwent supramaximal resection demonstrated a median overall survival of 29 months, compared to 20 months for those with only complete CE resection, translating to a 9-month survival benefit (Karschnia et al., 2022). Currently, recruitment is underway for the SUPRAMAX study, a prospective multicentre prospective cohort study to evaluate not only OS but also morbidity using National Institutes of Health Stroke Scale(Gerritsen et al., 2024).

Secondly, 5-aminolevulinic acid fluorescence guidance (5-ALA) offers a way to identify tumours under a blue light (405 nm) microscope. 5-ALA is internalised by cells and undergoes enzymatic conversion within mitochondria, forming Protoporphyrinogen IX (PpIX), which subsequently transforms into heme. However, dysfunction of the ferrochelatase enzyme in GBM cells causes the accumulation of PpIX. When exposed to 405-633nm light, PpIX becomes photosensitised, leading to the observed fluorescence under a microscope (Traylor et al., 2021, Harada et al., 2022) **(Figure 1.24, 1.25)**.

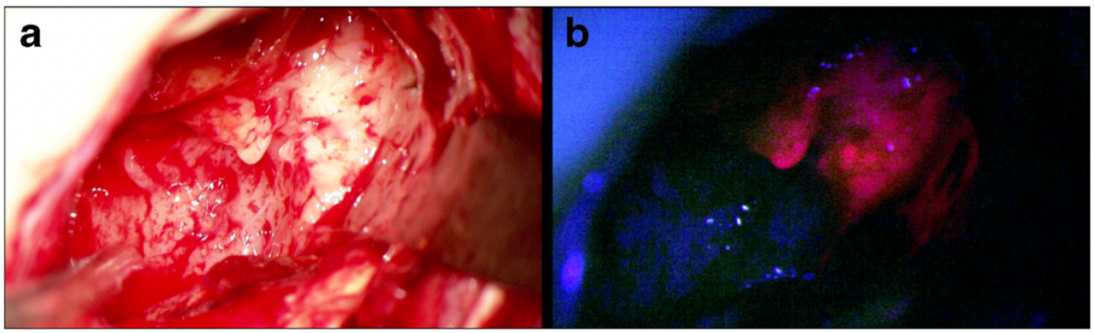

Figure 1.24: Fluorescence-guided surgery with ALA in a patient with GBM.

Demonstrating the intraoperative view of glioblastoma under white-light microscopy and PpIX fluorescence with blue 405 filters.

Taken from Molina et al (Suero Molina et al., 2019).

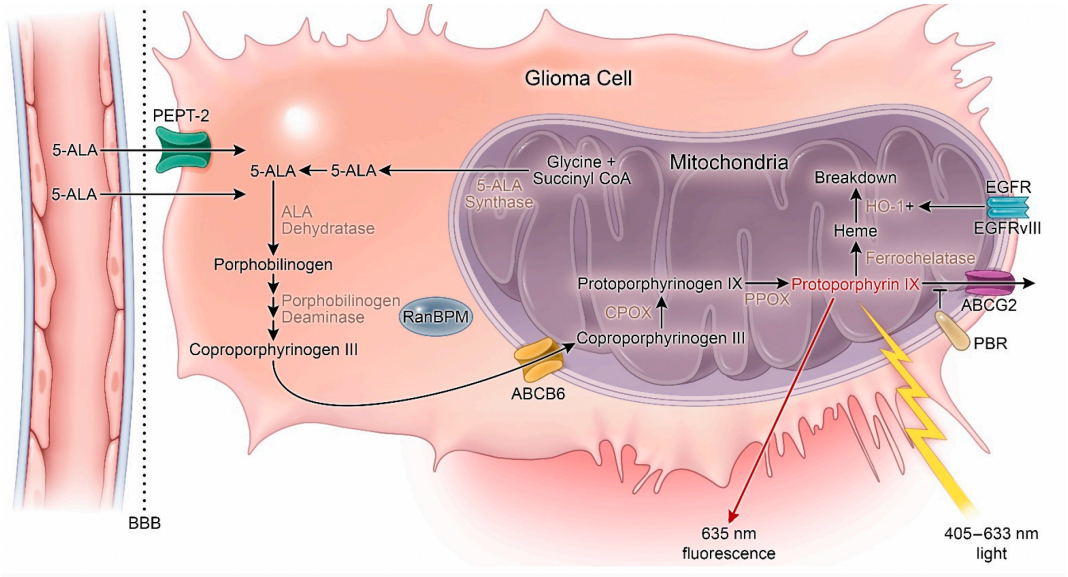

Figure 1.25: Heme synthesis 5-ALA fluorescence mechanism.

5-ALA: 5-aminolevulinic acid; ABCG2: ATP-binding cassette G2; ABCB6: ATP-binding cassette B6; BBB: Blood–brain barrier; CPOX: Coproporphyrinogen oxidase; HO-1: Heme-oxygenase 1; PBR: Peripheral benzodiazepine receptor; PPOX: Protoporphyrinogen oxidase. + = increased activity.

Taken from (Traylor et al., 2021).

Although imaging techniques can estimate tumour margins, gliomas often exhibit microscopic, finger-like projections undetectable by preoperative or intraoperative imaging (Kircher et al., 2012). 5-ALA facilitates better resections of contrast-enhancing tumours, resulting in improved progression-free survival. Studies by Stummer et al. (2006) demonstrated a 29% increase in complete resection rates in the 5-ALA group compared to the white light group. Furthermore, the 5-ALA group exhibited higher 6-month progression-free survival rates than the white light group (Suero Molina et al., 2019, Stummer et al., 2006).

Finally, emerging techniques such as intraoperative mapping and awake surgery have emerged as valuable tools to address the challenge of maximising resection while minimising neurological deficits (Bonosi et al., 2023). The relationship between EOR and QoL forms the foundation for prioritising preserving cortico-subcortical functions over traditional oncological margins (Bonosi et al., 2023). Implementing these new techniques has significantly reduced postoperative neurological deficits (Staub-Bartelt et al., 2024). Available evidence indicates that the utilisation of awake craniotomy for the resection of supratentorial glioblastoma is linked to a low incidence of persistent neurological deficits while still achieving an acceptable rate of gross total resection (Zhang et al., 2020a).

1.4.4 Chemotherapy

Systematic Chemotherapy:

Before temozolomide (TMZ) become the standard of care, the adjuvant chemotherapy regimen for GBM was Procarbazine, lomustine, and vincristine. This nitrosourea-based chemotherapy demonstrated a modest survival advantage, with a 5% increase in 2-year survival rates (Group, 2002).

TMZ alone is non-inferior to radiotherapy alone in treating elderly patients with GBM (Wick et al., 2012). However, the combined treatment of temozolomide and radiation significantly improves the prognosis of GBM. In a multicentre trial by Stupp et al. (2005), it was demonstrated that the median survival at a median follow-up of 28 months was 14.6 months in the radiotherapy plus temozolomide group, compared to 12.1 months with radiotherapy alone. The 2-year survival rate was 26.5% versus 10.4%, and a 5-year review of the same population revealed a 5-year survival rate of 9.8% in the temozolomide group compared to 1.9% in the radiotherapy group (Stupp et al., 2005, Stupp et al., 2009). These findings represent an improvement in survival outcomes for GBM compared to previous statistics **(Figure 1.26)**.

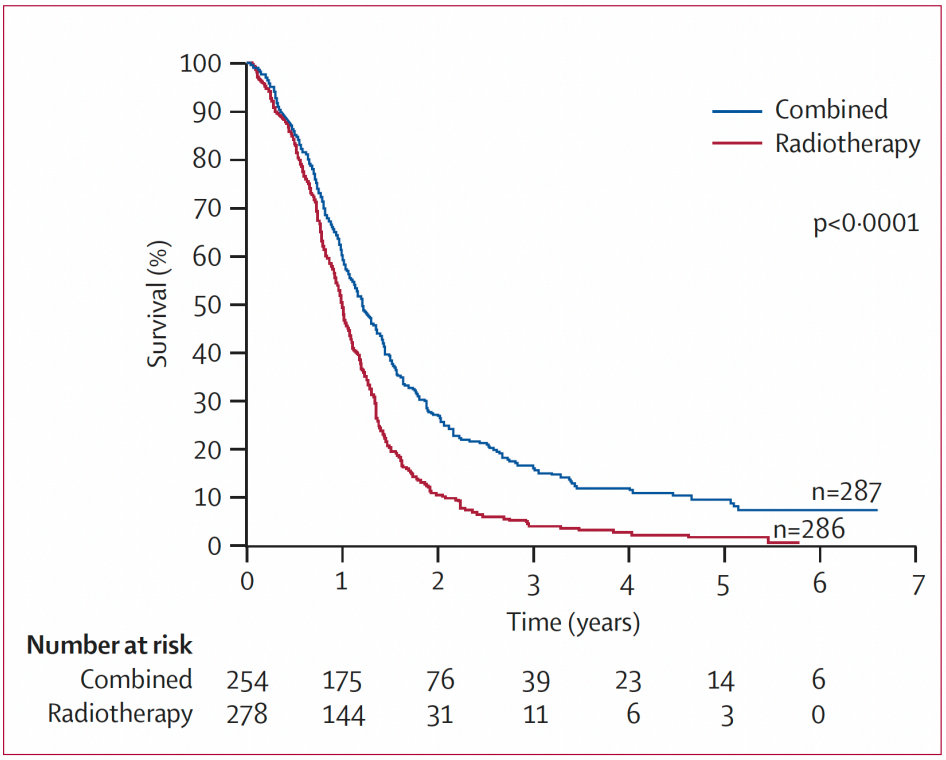

Figure 1.26: Kaplan-Meier estimates of overall survival by treatment group.

The combined treatment group received radiotherapy plus Temozolomide. Taken from (Stupp et al., 2009).

TMZ has obtained U.K. marketing authorisation for multiple indications. It is approved for treating newly diagnosed glioblastoma in combination with radiotherapy, followed by monotherapy. Additionally, temozolomide is authorised to treat recurrent or progressive malignant glioma after standard therapy (Excellence, 2007).

TMZ is a lipophilic prodrug that undergoes rapid metabolism to its active form, 3-methyl-(triazen-1-yl) imidazole-4-carboxamide (MTIC), at normal physiological Potential of Hydrogen (pH). MTIC acts by inhibiting cell division through disruption of DNA replication. Specifically, it adds a methyl group to the O6 position of guanine in DNA, leading to the incorporation of a thymine residue instead of a cytosine during DNA replication. This abnormal guanine-thymine pair triggers cell cycle arrest and activates the DNA mismatch repair pathway. Apoptosis occurs if the repair mechanism fails to keep pace with the DNA damage (Roos et al., 2007, Hammond et al., 1999) **(Figure 1.27)**.

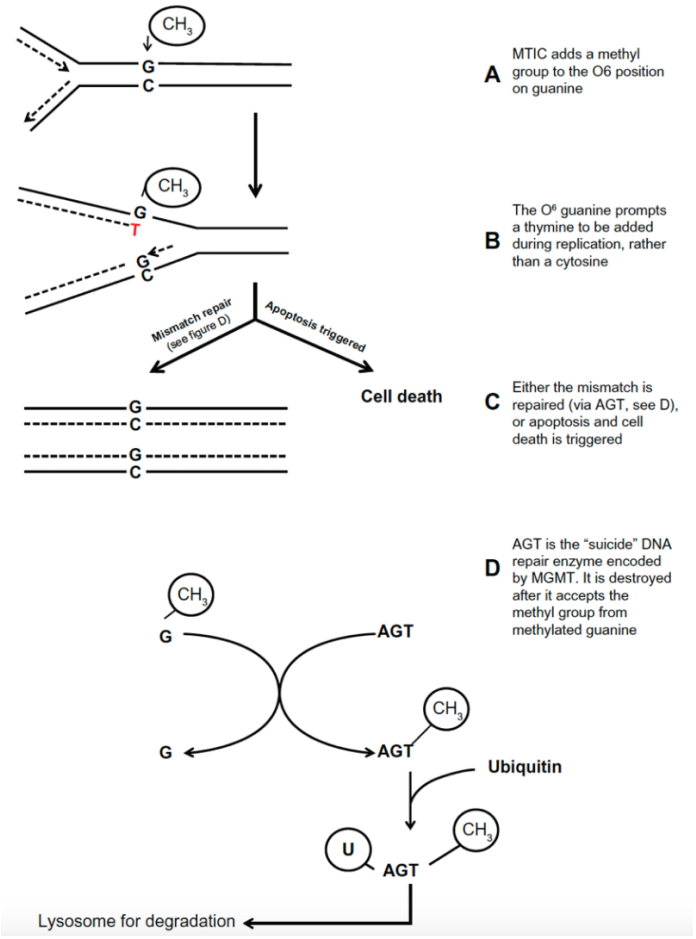

Figure 1.27: Mechanism of TMZ-induced DNA damage and MGMT repair pathway.

MTIC, the active metabolite of TMZ, adds a methyl group to guanine, which causes a base pair mismatch. Abbreviations: AGT, O6-alkylguanine-DNA alkyl transferase; MGMT, O6-methylguanine-DNA methyltransferase; MTIC, 5-(3-methyltriazen-1yl)-imidazole-4-carboxamide; TMZ, temozolomide.
Taken from (Thomas et al., 2012).

TMZ is available in both oral and intravenous formulations, but the oral formulation is predominantly used in clinical practice due to its high bioavailability. The bioavailability of the oral formulation is nearly 100%, allowing for rapid and complete absorption (Ortiz et al., 2021). TMZ serum half-life is about two hrs, and its peak concentration can reach 28.4 (micromolar)µM (5.5 microgram per millilitre (µg/mL)) in the serum and 3.2 µM (0.6 µg/mL) in the brain interstitium and peritumoral concentration after an oral dose of 150 mg/m^2 (Beltzig et al., 2021). Once TMZ is in the plasma, it undergoes a nonenzymatic chemical degradation process to convert into its active metabolite, MTIC. This conversion occurs independent of liver metabolism, allowing TMZ to avoid potential interactions with other medications. MTIC is further degraded into 4-amino-5-imidazole-carboxamide and a methyl diazonium cation. The methyl diazonium cation transfers its methyl group to DNA, forming abnormal DNA structures (Newlands et al., 1997, Ortiz et al., 2021).

The MGMT status has been identified as the most significant predictive biomarker for the response to alkylating agents. The MGMT gene produces the Angiotensinogen (AGT) enzyme, which is responsible for repairing damage caused by TMZ. AGT is considered a "suicide enzyme" because it can only remove one alkyl molecule per molecule of AGT, rendering itself inactive (Hegi et al., 2008). The hypermethylation of the MGMT promoter region leads to reduced expression of MGMT, which in turn enhances the response to alkylating agents by suppressing DNA repair. Consequently, MGMT promoter methylation is associated with a significantly increased median survival following treatment with TMZ, with reported median OS: 14.11 and 24.59 months for unmethylated and methylated GBM, respectively (Staub-Bartelt et al., 2024) **(Figure 1.28)**. Despite the association between MGMT promoter methylation and improved response to TMZ, current UK NICE guidance does not significantly differ between positive and negative MGMT methylation status due to the absence of alternative superior treatment options (Excellence, 2021).

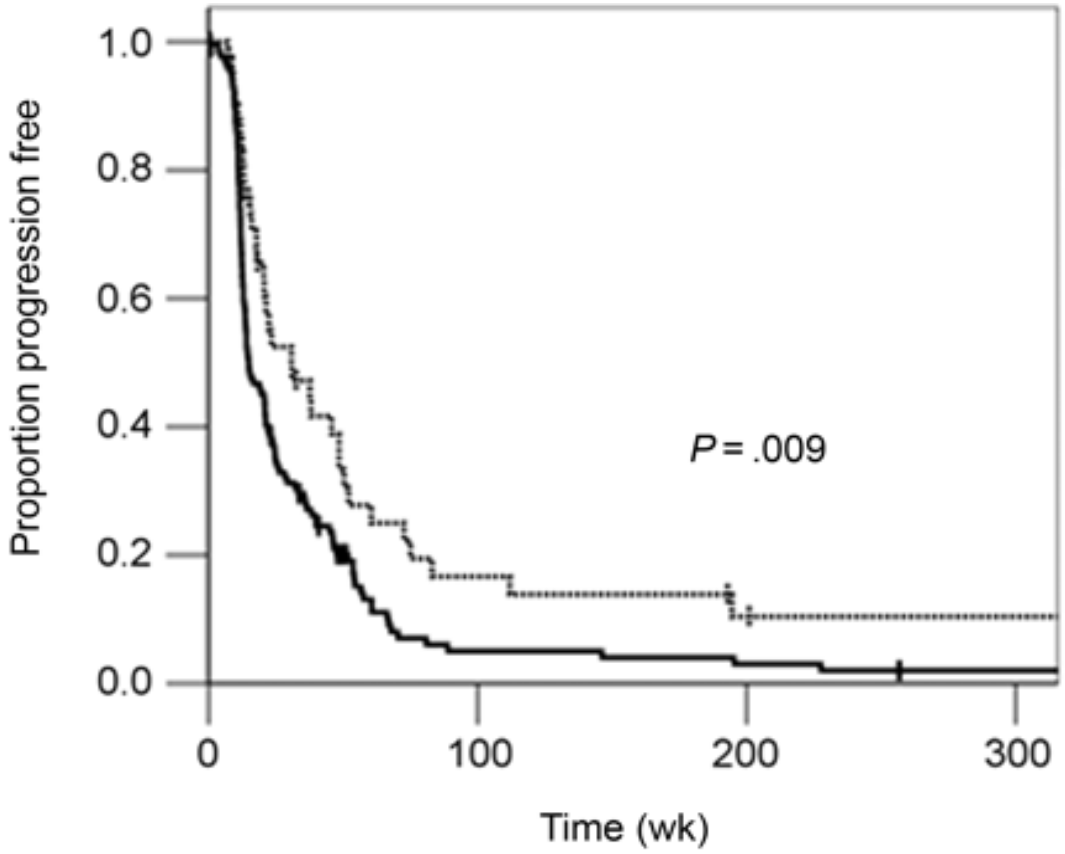

Figure 1.28: Progression-free survival and MGMT promoter methylation status.
Kaplan–Meier curves showing progression-free survival for patients with methylated (dotted line) vs unmethylated (solid line) tumours. Taken from (Rivera et al., 2009).

TMZ is generally well-tolerated but may cause adverse effects such as anorexia, constipation, fatigue, headache, lymphopenia, nausea, neutropenia, thrombocytopenia, and vomiting (Excellence, 2007).

Temozolomide is administered at a dose of 75 mg/m2 per day for six weeks, along with radiotherapy (60 Gray (Gy) in 30 fractions). It is then continued as monotherapy at a dose of 150-200 mg/m2 per day for five days, followed by a 23-day treatment-free period for a maximum of six cycles (Excellence, 2007)**(Figure 1.29).**

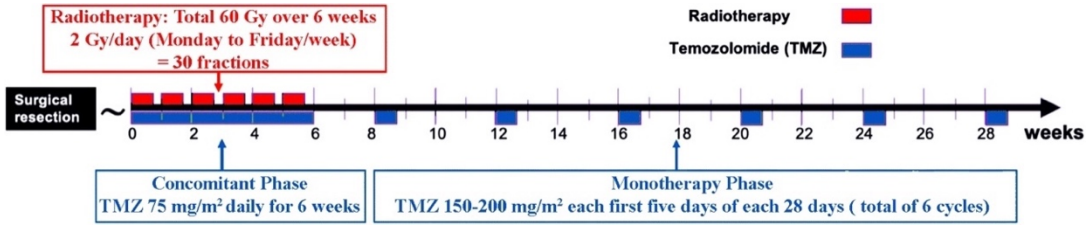

Figure 1.29: A schematic timeline of the standard treatment for newly diagnosed GBM patients (Stupp protocol)
Adapted from (Alghamdi et al., 2021).

1.4.5 Radiotherapy:

Radiotherapy allows for precise tumour targeting, minimising damage to surrounding healthy tissue and improving outcomes. It has long been used to improve local control and survival rates for gliomas and remains a crucial technique in their management (Le Rhun et al., 2017). The commonly used radiotherapy regimen involves delivering a total dose of 60 Gy over 30 daily fractions (2 Gy per day)(Excellence, 2021).

1.4.6 Future therapies:

Despite significant efforts to explore novel approaches, managing glioma patients has not undergone fundamental changes in the last 20 years. However, ongoing trials toward potentially revolutionising glioma treatment are eagerly anticipated. There is a wide range of promising new therapies, and some of them will be briefly reviewed.

Targeted molecular therapies:

Targeted molecular therapies aim to disrupt oncogenic pathways in GBM by inhibiting specific receptors or downstream targets. A recent systematic review analysed 166 studies involving 2,526 patients with GBM to evaluate current molecular targeted therapies (Begagić et al., 2023). The most frequently targeted molecular mechanisms were Protein Kinase Pathways, with EGFR as the most common target. Other significant targets included the Mammalian Target of Rapamycin (mTOR), VEGF, and Mitogen-Activated Protein Kinase (MEK). The review found that combination therapies were more effective than monotherapies. Clinical outcomes varied widely, with some targeted therapies showing promise, such as the combination of bevacizumab (targets VEGF) with Cediranib (targets Vascular endothelial growth factor receptor (VEGFR)) and Gefitinib (targets EGFR), which improved PFS to 3.6 months (Begagić et al., 2023) **(Figure 1.30)**.

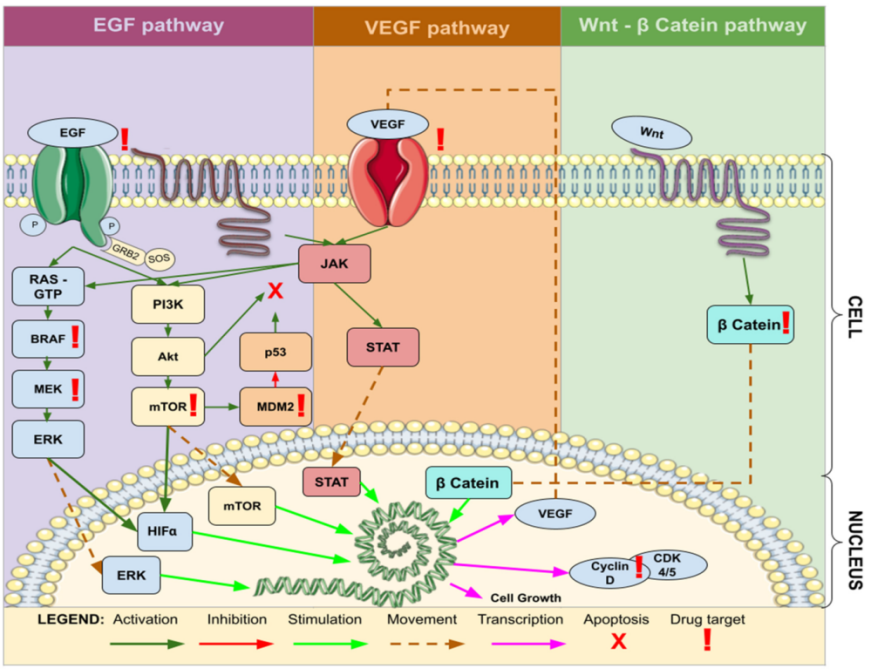

Figure 1.30: Common molecular pathways associated with target therapy of GBM.
Legend: EGF—Epidermal Growth Factor; VEGF—Vascular Endothelial Growth Factor; JAK—Janus Kinase; STAT—Signal Transducer and Activator of Transcription; Wnt—Wingless-Related Integration Site; Cyclin—Regulatory proteins involved in cell cycle progression; β Catenin—Beta-Catenin; RAS—Rat Sarcoma; GTP—Guanosine Triphosphate; BRAF—B-Raf Proto-Oncogene; MEK—Mitogen-Activated Protein Kinase Kinase; ERK—Extracellular Signal-Regulated Kinase; PI3K—Phosphatidylinositol 3-Kinase; Akt—Protein Kinase B; mTOR—Mammalian Target of Rapamycin; HIFa—Hypoxia-Inducible Factor-alpha; CDK—Cyclin-Dependent Kinase; MDM2—Mouse Double Minute 2 Homolog.
Taken from (Begagić et al., 2023).

Antiangiogenic therapies:

Bevacizumab (BVZ), a humanised monoclonal antibody, targets VEGF-A, a key mediator in the angiogenesis process, which is crucial for the growth of GBM. By preventing VEGF from binding to its receptors on endothelial cells, BVZ effectively inhibits the formation of new blood vessels, thereby slowing tumour growth and potentially enhancing the efficacy of radiotherapy and chemotherapy (Fu et al., 2023b, Xie et al., 2023a). Recent clinical trials found that while BVZ improves PFS, it does not necessarily extend OS (Fu et al., 2023a, Xie et al., 2023a). BVZ is associated with an increased risk of adverse events, particularly hypertension and proteinuria, underscoring the need for careful management of these side effects in clinical practice (Xie et al., 2023a). BVZ has received approval for use in GBM in the United States. However, the European Medicines Agency and UK NICE guidance have not approved BVZ due to concerns about the validity of the demonstrated outcome and true clinical benefit in GBM(Excellence, 2021, Smolenschi et al., 2023).

Immunotherapy:

Immunotherapy, which has revolutionised treatment in various cancers, is being explored in GBM with mixed results. The primary immunotherapeutic approaches include immune checkpoint inhibitors, oncolytic viruses, therapeutic vaccines, and Chimeric Antigen Receptor T-cell (CAR T-cell) therapies. Immune checkpoint inhibitors, such as those targeting programmed death-1/ programmed death-ligand 1(PD-1/PD-L1) and Cytotoxic T-Lymphocyte Antigen-4 (CTLA-4), aim to restore the ability of T cells to recognise and attack tumour cells by blocking inhibitory signals that allow cancer cells to evade immune detection. Oncolytic viruses selectively infect and destroy cancer cells while stimulating a robust anti-tumour immune response, thus potentially transforming the immunosuppressive tumour microenvironment into an immunocompetent one. Therapeutic vaccines, including peptide-based, cell-based, and Messenger Ribonucleic Acid (mRNA) vaccines, elicit a targeted immune response against specific GBM antigens, enhancing the body's natural ability to combat the tumour. Lastly, CAR T-cell therapies involve engineering T cells to express receptors that specifically recognise and eliminate GBM cells, offering a highly personalised approach to treatment (Tiwari and Han, 2024, Maccari et al., 2023) (**Figure 1.31)**.

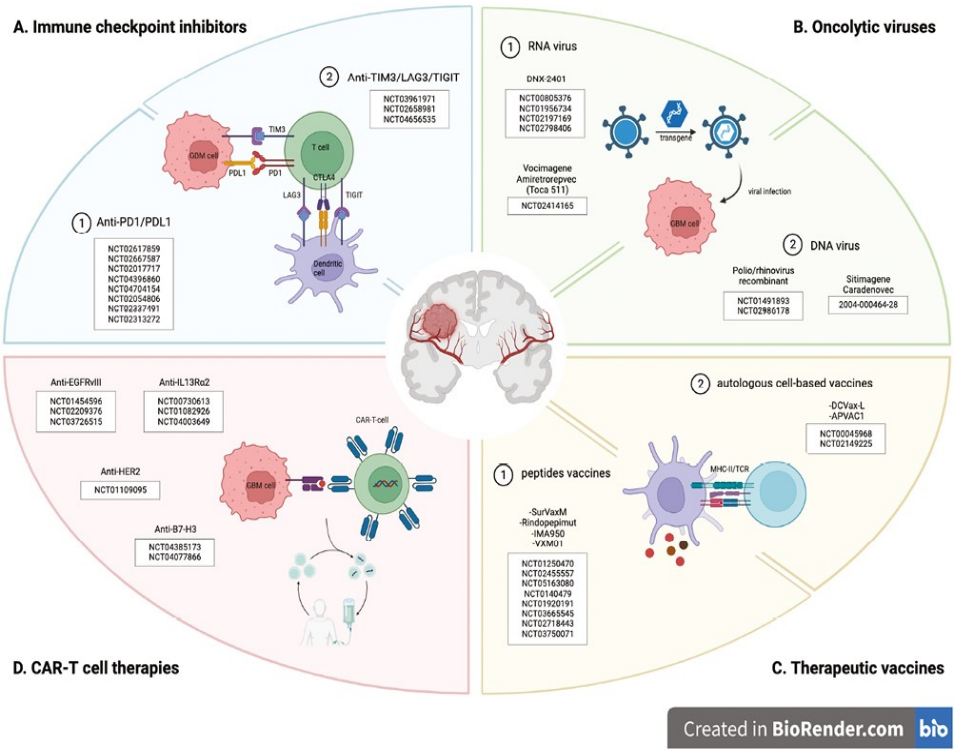

Figure 1.31: Overview of the current landscape of immunotherapy strategies in GBM and related clinical trials.

A. Immune checkpoint inhibitors are specific antibodies that block PD1/PDL1 or CTLA4 pathways and TIM3, LAG3, and TIGIT coinhibitory molecules. B. Oncolytic viruses are RNA or DNA viruses that selectively infect and kill cancer cells. C. Therapeutic vaccines are peptide or "autologous" cell-based vaccines that activate T cells to target tumour antigens. D. CAR T-cell therapies target GBM-associated or GBM-specific antigens, including EGFRvIII, IL13Rα2, HER2, and B7-H3. Image created in BioRender.com Taken from (Maccari et al., 2023).

Despite the significant advancements in immunotherapy, its effectiveness in treating glioblastoma remains limited and challenging. Clinical trials for immune checkpoint inhibitors in GBM, such as those involving nivolumab and pembrolizumab, have shown modest results, often failing to improve overall survival rates significantly. Oncolytic viruses and CAR T-cell therapies have demonstrated potential in early-phase trials, with some patients experiencing prolonged survival. However, these approaches are often met with the challenge of the blood-brain barrier, which limits the delivery of therapeutic agents and the tumour's ability to develop resistance through immune escape mechanisms. While immunotherapy offers hope, its current application in GBM is constrained by these significant biological and physiological barriers, necessitating the development of combination strategies and novel approaches to overcome these obstacles (Tiwari and Han, 2024, Maccari et al., 2023).

Tumour treating fields (TTF):

TTF are portable medical devices that produce low intensity alternating electric fields. These electric fields affect cancer cells through altering DNA repair, membrane permeability, and immune responses. TTF exert antimitotic effects that specifically target rapidly dividing cells. By disrupting critical proteins involved in cell division, TTF can reduce cell proliferation, induce mitotic catastrophe, and ultimately cause cell death. TTF therapy offers a unique approach to treating cancer by utilising the selective effects of electric fields on tumour cells (Slavkov et al., 2023) **(Figure 1.32).**

Figure 1.32: The Optune system.
Left: The Optune TTF delivery system consists of four transducer arrays, a field generator and a power source. Right: a patient wearing the Optune system. Taken from (Slavkov et al., 2023).

A recently published phase III study has demonstrated a substantial improvement in survival when utilising TTF therapy during the adjuvant phase of chemotherapy for GBM. As a result, TTF has gained approval in the United States as part of adjuvant therapy for glioblastoma (Stupp et al., 2015), (Wen et al., 2020). However, the UK NICE guidance committee has recommended against using TTF based on health economic evidence, suggesting it may not be a cost-effective use of NHS resources (Excellence, 2021).

1.5 The GBM microenvironment

It is essential to understand the microenvironment of GBM to explore the potential use of the immune system against cancerous cells and how resistance to current and emerging treatments develops.

The tumour microenvironment (TME) comprises a complex network of interactions involving immune, nervous, and chemical components (Sharma et al., 2023b). From a tumour perspective, this interaction's primary objective is to establish a highly immune-suppressive state that facilitates tumour growth (Sharma et al., 2023b) **(Figure 1.33).**

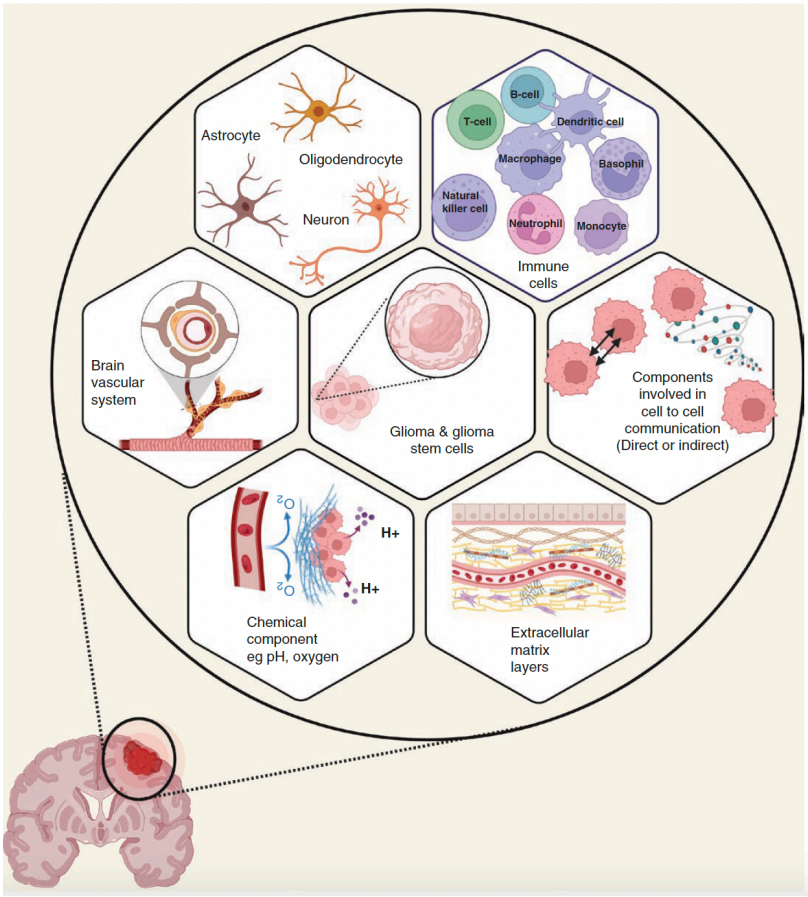

Figure 1.33: Schematic representation of the glioma tumour microenvironment components.
The glioma tumour microenvironment is a complex, heterogeneous, and interactive system consisting of glioma stem cells, immune cells, nervous system, brain vascular system, and extracellular matrix layers. The factors involved in direct and indirect cell communication and chemical tumour microenvironment, such as pH and oxygen, also play a significant role in modulating the glioma tumour microenvironment.
Adapted from (Sharma et al., 2023b).

1.5.1 Immune components:

Immune cells comprise a significant portion of the tumour cellularity, accounting for up to 50% of the mass of some tumours. These immune cells principally include tumour-associated macrophage (TAM), microglia, natural killer (NK) cell, and tumour-infiltrating lymphocyte(Pombo Antunes et al., 2021, Klemm et al., 2020).

1.5.1.1 BBB:

The endothelial cells of the BBB are connected by tight junctions, which regulate the barrier's permeability. In normal conditions, these tight junctions are well-controlled. However, these junctions become less tightly connected during inflammatory conditions like GBM, resulting in a "leaky" environment. The compromised blood-brain barrier permits the infiltration of myeloid-derived immune cells, where a significant portion of the immune cells consists of microglia and monocytes that eventually differentiate into macrophages (Abels et al., 2020, Engelhardt, 2008).

In addition to the endothelium, the BBB comprises a two-layered basement membrane consisting of pericytes and perivascular astrocytes. These components play a crucial role in regulating the functions of the endothelium and structurally strengthening the barrier. Together with the extracellular matrix and cytokine, these components control the permeability of the BBB (Wolburg et al., 2009) **(Figure 1.34).**

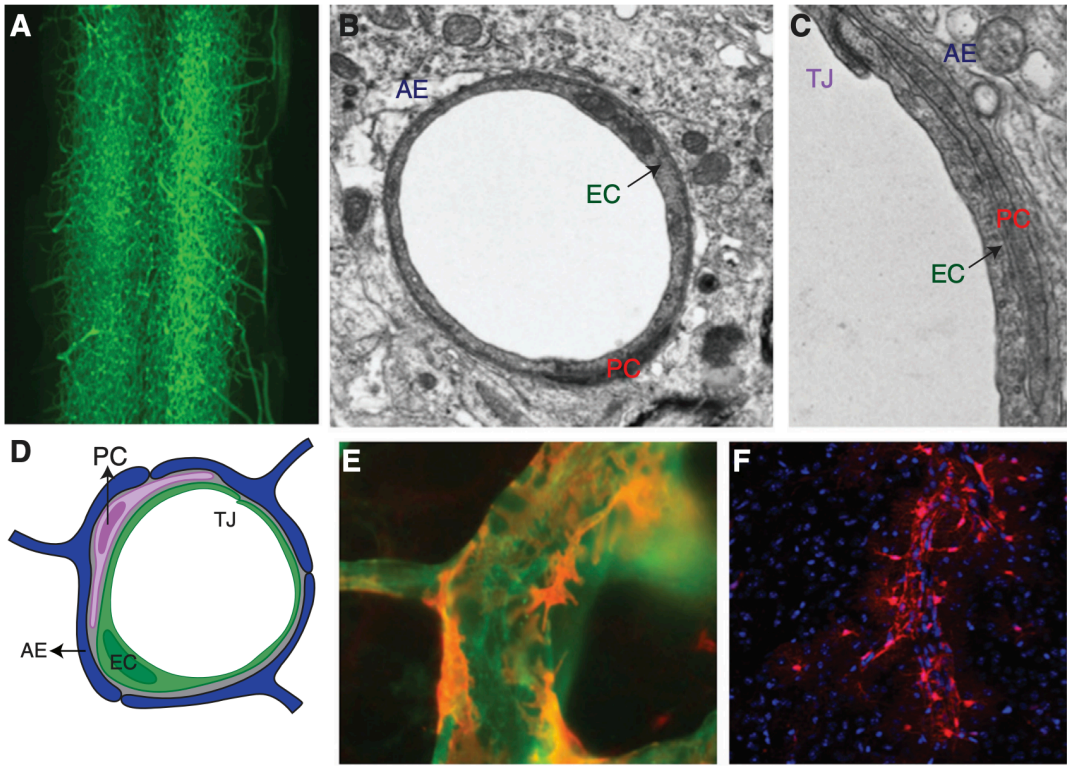

Figure 1.34: Components of the BBB.
(A) Vascular cast of a spinal cord showing the density of the CNS vascular network. (B) Electron micrograph (EM) of a cross-section of a CNS vessel depicting a relationship among endothelial cells (ECs), pericytes (PCs), and astrocytes. (C) Magnified EM of ECs depicting a relationship among ECs (with tight junctions [TJ]), PCs, basement membranes (BMs), and astrocyte endfeet (AE). (D) Schematic representation of the cell types within the neurovascular unit.
(E) Immunofluorescence micrograph depicting the relationship of PCs (red) with ECs (green). (F) Micrograph depicting astrocytes' relationship (red-labelled with GFAP-cre; Rosa-tdTomato) with blood vessels (unstained). Astrocytes extend processes that ensheath the blood vessels, such that the outline of the blood vessels can be visualised by the end feet of these processes.
Taken from (Daneman and Prat, 2015).

The brain has traditionally been viewed as an immune-privileged organ because it was considered not to have a direct connection with the lymphatic system, and the fact the BBB selectively controls the entry of immune cells into the brain (Sampson et al., 2017). Nevertheless, this conventional understanding has recently been questioned in light of recent findings of a metabolic waste clearance pathway called the glymphatic system, which includes a meningeal lymphatic compartment, as well as the drainage of lymphatic fluid from CNS to cervical lymph nodes (Ding et al., 2023) **(Figure 1.35)**.

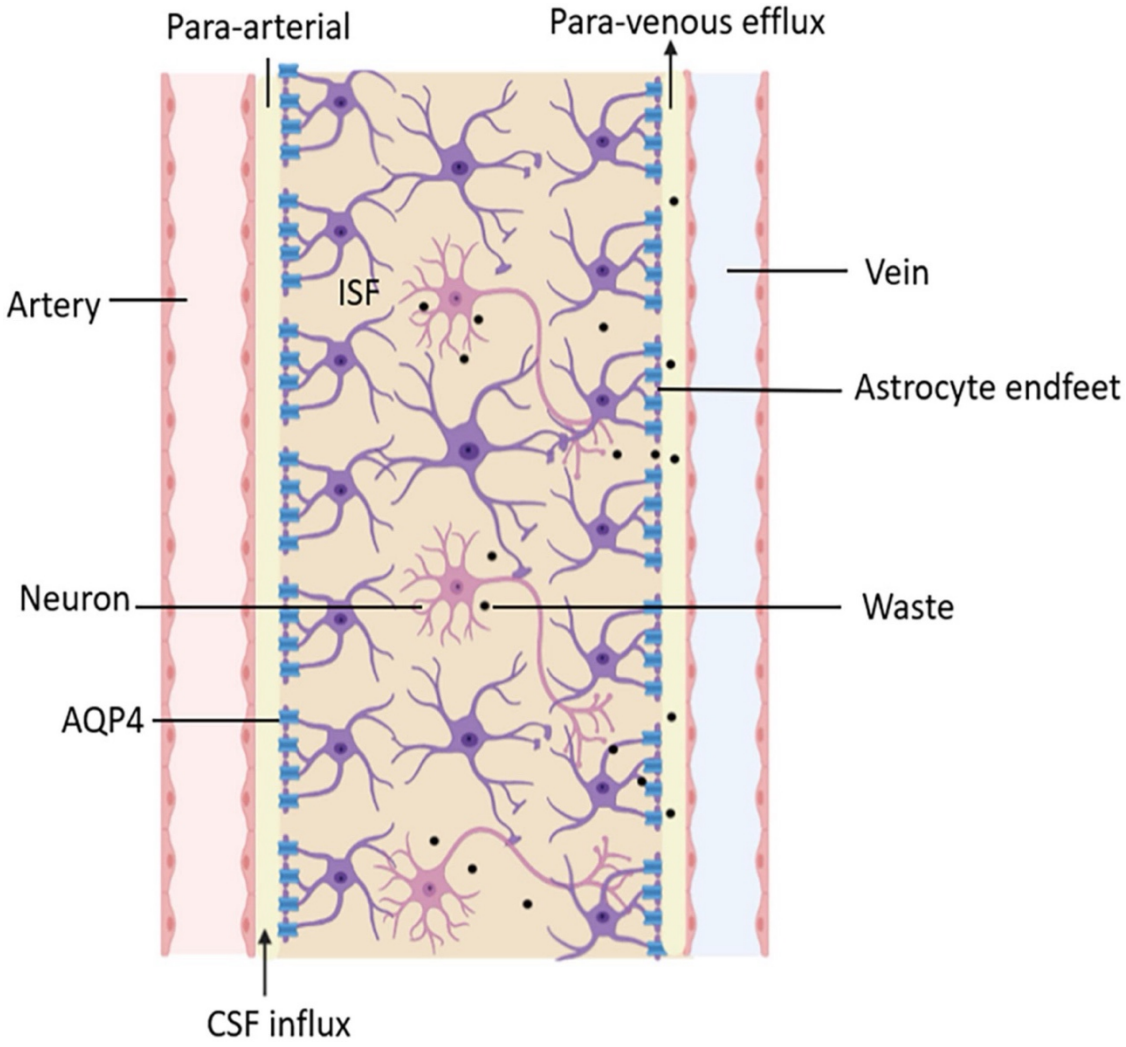

Figure 1.35: Functional diagram of the glymphatic system.
The glymphatic system is a brain-wide perivascular pathway driven by Aquaporin-4 (AQP4) on astrocytic end feet. CSF delivers nutrients and neuroactive substances to the brain parenchyma through the peri-arterial spaces pathway and mixes with interstitial fluid (ISF) in the brain parenchyma. The mix of CSF and ISF removes metabolic wastes through peri-venous clearance routes.
Adapted from (Ding et al., 2023).

These discoveries provide a new basis for the involvement of adaptive immunity in CNS inflammation and certain neurodegenerative diseases (Louveau et al., 2015, Ding et al., 2023). That leads to speculations about the potential involvement of the meningeal lymphatic system in the immune response of GBM. Subsequent studies conducted in mouse models of brain tumours have provided evidence supporting this hypothesis (Song et al., 2020, Hu et al., 2020b). Besides the meningeal lymphatic system, additional lymphatic structures called tertiary lymphatic structures (TLS) have been discovered within brain tumours. TLS is an alternative location for activating T-cells and is currently the only known pathway for lymphocyte infiltration other than across the BBB (Hu et al., 2020b).

1.5.1.2 TAM

Microglia, which are tissue-resident macrophages, are the most abundant immune cells in the brain (Ajami et al., 2007). Microglia are immune cells originating from a progenitor in the yolk sac (Ismailov et al., 2025). An additional source of phagocytic cells in the brain is the peripheral blood monocytes, which can be attracted to the brain, crossing the BBB when compromised (Lund et al., 2018). A prominent feature of the GBM microenvironment is the elevated abundance of TAM, which typically constitutes a substantial proportion, ranging from 30% to 50%, of the tumour mass (Matias et al., 2018).

TAM in glioblastoma can adopt different phenotypes, namely the anti-tumour M1 phenotype or the pro-tumour M2 phenotype, which has been described for other malignancies, for example, in breast cancer (Erices et al., 2023). M1 macrophages display enhanced expression of surface molecules involved in antigen presentation and recognition, secrete proinflammatory cytokines, and engage in target phagocytosis. In contrast, M2 macrophages contribute to immune suppression and facilitate tumour invasion (Kennedy et al., 2013). Glioblastoma cells typically release interleukin-10 (IL-10), transforming growth factor-beta (TGF-β), and glucocorticoids. These substances contribute to the expansion of the M2 population of TAM within the microenvironment. The M2 TAM, in turn, enhance the growth and proliferation of tumour cells, creating a positive feedback loop that sustains tumour progression (Komai et al., 2018, Zhang et al., 2016) **(Figure 1.36).**

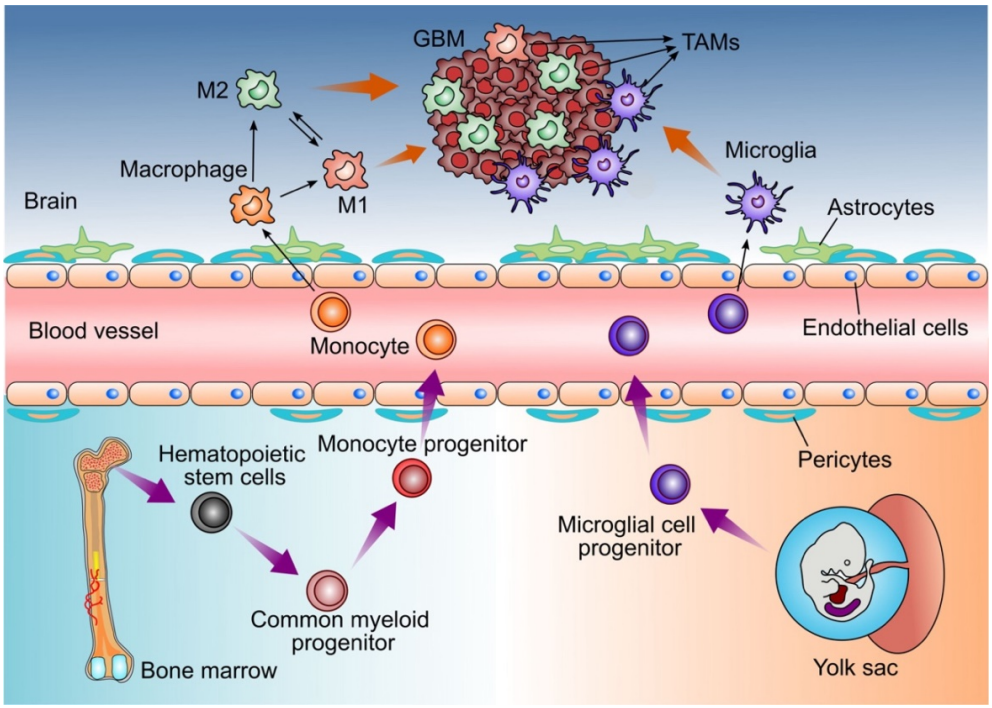

Figure 1.36: Distinct origins of Glioblastoma-associated Microglia and macrophages.
Microglia derive from the embryonic yolk sac progenitors, while peripheral macrophages are the monocytes deriving from the hematopoietic stem cells in bone marrow. Both cell populations enter the CNS and could be recruited by GBM cells, called tumour-associated microglia and macrophages (TAM).
Taken from (Wang et al., 2022).

1.5.1.3 Myeloid-derived suppressor cells (MDSCs):

MDSCs are a diverse group of immature myeloid cells at various stages of differentiation, originating in the bone marrow. Under normal physiological conditions, these immature myeloid cells mature into macrophages, granulocytes, and dendritic cells in proportions required to maintain cells at the correct relative concentrations. However, the presence of pathological states, such as in GBM, causes disruption that leads to the generation, recruitment, expansion, and activation of MDSCs, not only within the tumour microenvironment but also systemically in the peripheral blood (Del Bianco et al., 2022, Lakshmanachetty et al., 2021).

The mechanisms by which MDSCs are recruited and activated in GBM involve a complex interplay of signals from glioma cells, T cells, microglia, and macrophages. Glioma cells overexpress various factors such as Cluster of Differentiation 200 (CD200), Indoleamine 2,3-Dioxygenase 1 (IDO1), and secrete chemokines like C-C Motif Chemokine Ligand 20 (CCL20) and CCL2 to attract MDSCs. The hypoxic conditions within the tumour upregulate factors like VEGF and Hypoxia-Inducible Factor 1-alpha (HIF1α), further promoting MDSC accumulation and activation. Once recruited, MDSCs are expanded and activated through cytokines (IL-6, IL-10, TGF-β) and chemokines (C-C Motif Chemokine Receptor 2 (CCR2)), which enhance their immune-suppressive functions. These activated MDSCs then contribute to the immunosuppressive environment by different mechanisms, for example, the expression of PD-L1, activation of signal transducer and activator of transcription 3 (STAT-3), and producing enzymes like arginase 1 and reactive oxygen species (ROS), ultimately aiding in tumour survival and growth **(Figure 1.37)**.

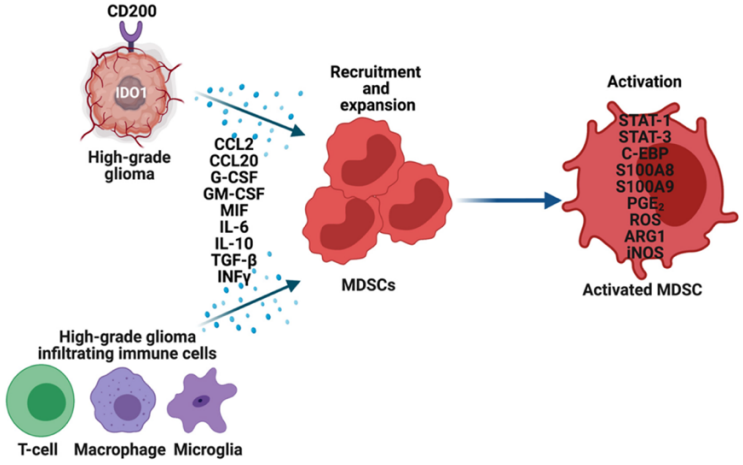

Figure 1.37: Recruitment, expansion, and activation of MDSCs in HGG.
Glioma cells, T-cells, Macrophages, and Microglia in the tumour microenvironment overexpress multiple genes and secrete various cytokines, chemokines, and other factors to recruit and expand MDSCs. These factors also activate MDSCs through multiple mechanisms, which perform their immune-suppressive functions in HGG. Taken from (Lakshmanachetty et al., 2021).

1.5.1.4 Dendritic cells (DC)

DC are a crucial component of the immune system, primarily known for their role as professional antigen-presenting cells. These cells are distributed throughout the body, with specific populations in tissues such as the skin, mucosal surfaces, and lymphoid organs, where they monitor for pathogens or abnormal cells. Upon encountering antigens, DCs process and present these on their surface using major histocompatibility complex (MHC) molecules, which are then recognised by T cells, initiating an adaptive immune response. In healthy brain tissue, DCs are mostly absent from the parenchyma but are found in border regions like the meninges and choroid plexus, where they are thought to contribute to immune surveillance (Dapash et al., 2021, Conarroe and Bullock, 2023).

Paradoxically in the context of GBM, DC infiltrates the TME and contributes to tumour progression rather than elimination. Within the immunosuppressive TME of GBM, DC are commonly exposed to various factors that impair their ability to present antigens and activate T cells effectively. For example, glioblastoma cells and other immune cells within the TME secrete cytokines like TGF-β, IL-10, and VEGF, inhibiting DC maturation and promoting an immunosuppressive status. This results in DCs that are less capable of initiating strong anti-tumour immune responses, instead contributing to T cell anergy or the expansion of regulatory T cells (Tregs), further suppressing immune activity. Additionally, the hypoxic conditions prevalent in GBM can skew DC function towards supporting tumour growth and survival (Conarroe and Bullock, 2023) **(Figure 1.38).**

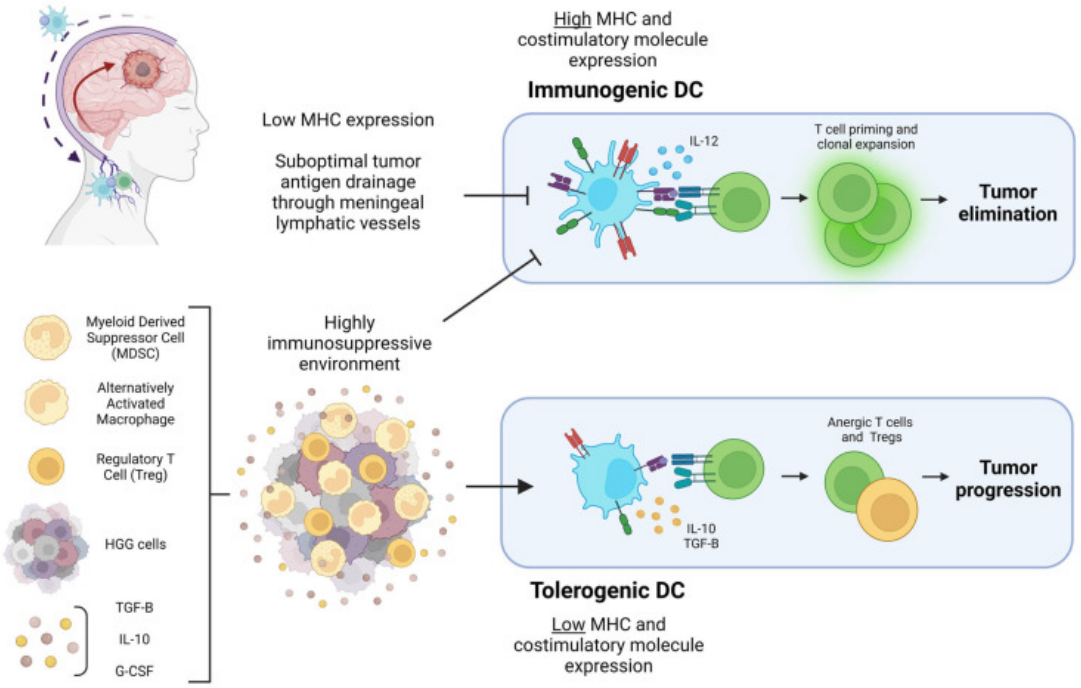

Figure 1.38: Diagram of the HGG-associated factors that can lead to tumour elimination or progression through DC polarisation.
Pictured in the top left corner is a diagram of HGG (High-Grade Glioma) antigen drainage through meningeal lymphatic vessels to draining cervical lymph nodes mediated by DC. Suboptimal tumour antigen drainage prevents T cell priming and clonal expansion in the cervical lymph nodes. The highly immunosuppressive HGG TME at the bottom left prevents DC from expressing the costimulatory molecules necessary for immunogenic T cell priming. Cytokines and immunosuppressive cells within the TME result in DC with a tolerogenic character that ultimately prime anergic T cells and Tregs, contributing to tumour progression. Taken form (Conarroe and Bullock, 2023).

1.5.1.5 Tumour infiltrating lymphocytes:

Cytotoxic T cells typically carry the PD-1 receptor on their surface. PD-1 acts as a checkpoint to prevent the immune system from attacking the body's cells, helping maintain tolerance and avoid autoimmunity. However, in GBM, the tumour used this pathway to evade the immune response. When PD-1 on cytotoxic T-cells binds to its ligand PD-L1 expressed on the GBM cells, it sends an inhibitory signal that reduces the T-cells' ability to attack the tumour. This suppresses the immune response, allowing the tumour to grow unchecked. Additionally, GBM patients show higher activity of Tregs with support of TGF-β and IL-10, which further suppresses the activity of cytotoxic T-cells (Mormino and Garofalo, 2022, Tripathy et al., 2024, Trevisi and Mangiola, 2023, Caldwell et al., 2017). Finally, NK cells, part of the innate immune system, can directly identify and destroy tumour cells without needing previous exposure. However, their activity is inhibited by TGF-β, which reduces the expression of crucial receptors like Natural Killer cell p30-related protein (NKp30) and Natural Killer Group 2, Member D (NKG2D) that are essential for activating NK cells (Mormino and Garofalo, 2022, Sharma et al., 2023b) **(Figure 1.39).**

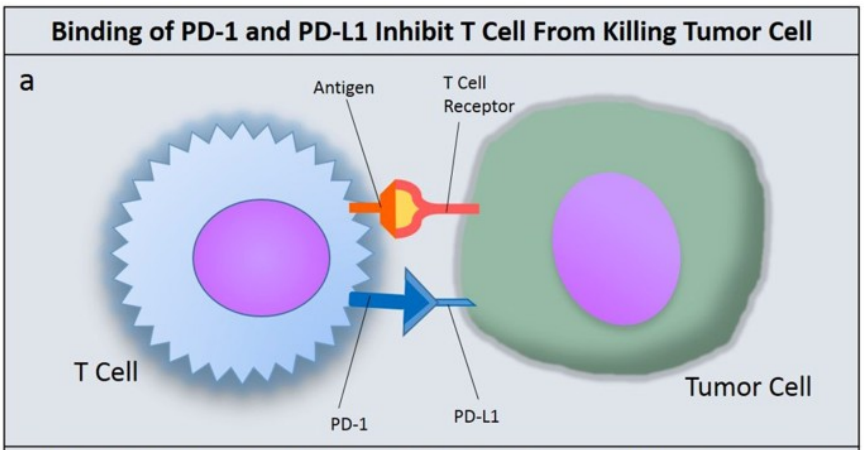

Figure 1.39: Blocking of PD-1 or PD-L1 Restores Host T-Cell Function.
*(**a**) Binding of PD-L1 to PD-1 will inhibit host T cell from killing the tumor cell. Taken from (Caldwell et al., 2017).*

1.5.2 Nervous components:

Glioblastoma stem cells (GSCs) exhibit stem cell properties that allow them to differentiate into different cell types, possess the self-renewal ability and potentially contribute to tumour growth and treatment resistance (Mondragon-Soto et al., 2022, Hawly et al., 2024). These cells have developed mechanisms to evade immune responses, such as downregulating the expression of MHC class I molecules and preventing the activation and lysis by cytotoxic T cells. A limited number of Major histocompatibility complex I (MHC I) molecules are preserved on the GSCs surface to avoid detection by NK cells (Bischof et al., 2017, Hawly et al., 2024) **(Figure 1.40).**

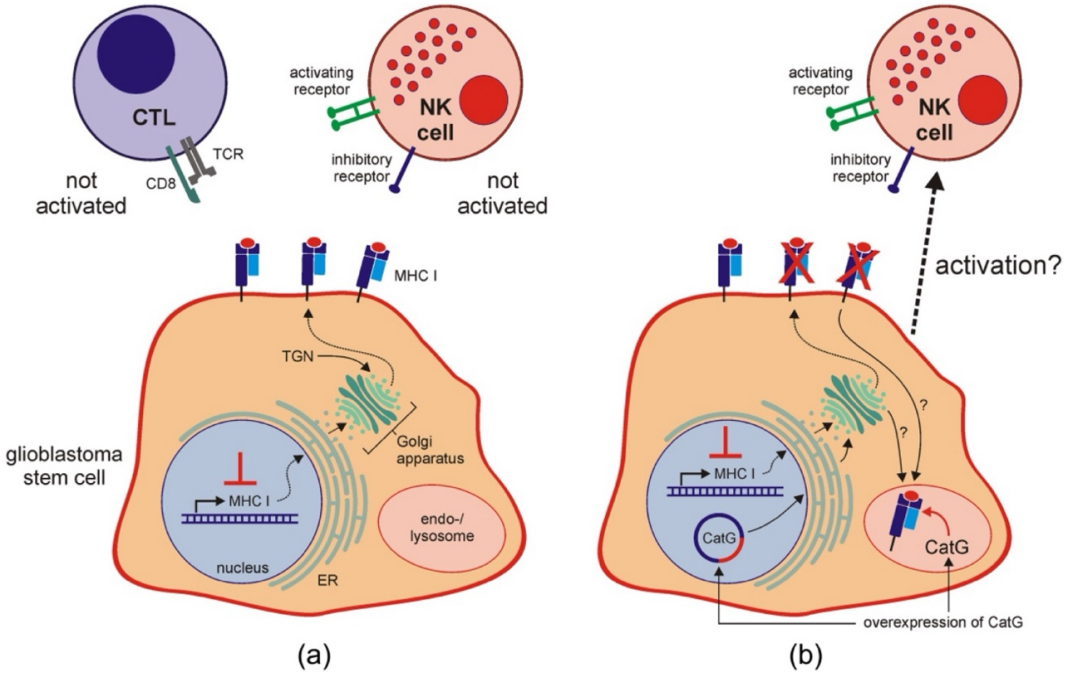

Figure 1.40: Immune evasion mechanism of glioblastoma stem cells.
Invading glioblastoma stem cells reduces surface expression of MHC I to diminish tumour-associated antigen presentation and evade recognition by CTLs. A limited set of cell surface MHC I molecules is maintained to escape recognition by NK cells. CatG: cathepsin G; CD8: cluster of differentiation 8; CTL: cytotoxic T lymphocyte; ER: endoplasmic reticulum; MHC I: major histocompatibility complex I; NK cell: natural killer cell; TCR: T cell receptor; TGN: trans-Golgi network.
Adapted from (Bischof et al., 2017).

Another important escape mechanism involves the presence of PD-L1 on extracellular vesicles released by GBM cells, which inhibits the T-cell receptor and reduces the activation and proliferation of any invasive CD4+ and CD8+ T cells (Hersh et al., 2022, Hawly et al., 2024). GSCs also avoid immune responses by promoting the production and infiltration of T reg cells and increasing the TGF-β levels produced by TAM. The increased TGF-β further down-regulates MHC II molecules and impairs the antigen processing mechanism, leading to T-cell anergy. Finally, GSC attracts TAM by secretion cytokines like CCL2 and promotes their polarisation towards an immunosuppressive M2 state (DeCordova et al., 2020, Hawly et al., 2024).

1.5.3 Chemical component (acidosis and hypoxia)

1.5.3.1 Acidosis:

Acidosis, a well-known characteristic of cancer, refers to the acidic environment found in tumour tissues compared to healthy tissues. The extracellular pH of tumours is typically lower, around 6.5, compared to the normal physiological value of 7.4. This acidity is primarily attributed to various processes occurring within tumour cells, including oxidative stress, nutrient deprivation, hypoxia, and higher rates of anaerobic glycolysis. These processes increase lactic acid carbonic acid production and decrease perfusion due to the dysregulated blood supply (Martins et al., 2023).

Tumour acidosis influences the TME and plays a role in developing GSC characteristics. Acidosis promotes the expression of GSC markers and stimulates tumour growth by releasing angiogenic factors regulated by hypoxia-inducible transcription factors (HIFs), specifically HIF-1α. Additionally, acidosis enhances autophagic activity, which is associated with tumour cell survival and aggressiveness. The acidic conditions also impair the function of CD8 T lymphocytes, causing them to become anergic and reducing the secretion of IL-2 and T-cell receptor signalling. Acidosis also hampers the cytotoxic effects of NK cells while promoting the accumulation of MDSC that also actively inhibits NK cell-mediated cytotoxicity (Martins et al., 2023).

The ongoing Phase I clinical trial "Study of Acetazolamide (ACZ) With Temozolomide in Adults With Newly Diagnosed or Recurrent Malignant Glioma" (NCT03011671) is exploring the safety and tolerability of combining ACZ, a pH-balancing inhibitor, with the standard chemotherapy drug TMZ. This trial is based on the emerging therapeutic strategy of targeting tumour acidosis to improve treatment outcomes. By adding ACZ to TMZ, researchers aim to counteract the acidic tumour environment, potentially enhancing the effectiveness of the standard-of-care therapy. The trial's primary focus is monitoring adverse events and dose-limiting toxicities, while secondary objectives include evaluating tumour response rates, progression-free survival, and overall survival. The trial recruits participants, with an estimated enrolment of 60 patients and final data collection expected by October 2026 (2017, Sharma et al., 2023b).

1.5.3.2 Hypoxia:

Under normal oxygen conditions, HIF-1α is hydroxylated by prolyl hydroxylase domain enzymes (PHDs), which marks it for degradation by the proteasome. However, the rapid proliferation of tumour cells coupled with the chaotic vasculature of GBMs often results in regions of the tumour experiencing significant oxygen deprivation. In hypoxic conditions, the activity of PHDs is inhibited, allowing HIF-1α to accumulate and translocate to the nucleus, where it dimerises with HIF-1β. This complex then binds to hypoxia-response elements (HREs) in the DNA, initiating the transcription of various genes that facilitate adaptation to hypoxia, including those involved in angiogenesis, metabolism, and survival (Sharma et al., 2023b, Zhao et al., 2022, Shi et al., 2023a).

The activation of HIF under hypoxia triggers a cascade of downstream effects that significantly contribute to GBM progression. A key consequence of HIF activation is the upregulation of VEGF, a potent stimulator of angiogenesis. VEGF leads to the formation of new blood vessels, which, although often abnormal and leaky, provide a route for increased nutrient and oxygen delivery to the tumour, thus fuelling its growth. Additionally, HIF induces the expression of genes associated with cell invasion and migration, including matrix metalloproteinases (MMPs) that degrade the extracellular matrix, allowing tumour cells to invade surrounding brain tissue. This invasive capacity, along with the stimulation of angiogenesis, makes GBMs particularly challenging to treat surgically.

Furthermore, HIF also drives metabolic reprogramming in GBM cells, promoting a shift towards glycolysis even in the presence of oxygen (known as the Warburg effect). This metabolic adaptation enables GBM cells to generate energy efficiently under hypoxic conditions (Shi et al., 2023a, Park and Lee, 2022, Tamai et al., 2022). Currently, there are two ongoing clinical trials (NCT04874506 and NCT02974738) investigating the use of MBM-02 (Tempol) and belzutifan to inhibit HIFs in GBM patients (Sharma et al., 2023b) **(Figure 1.41).**

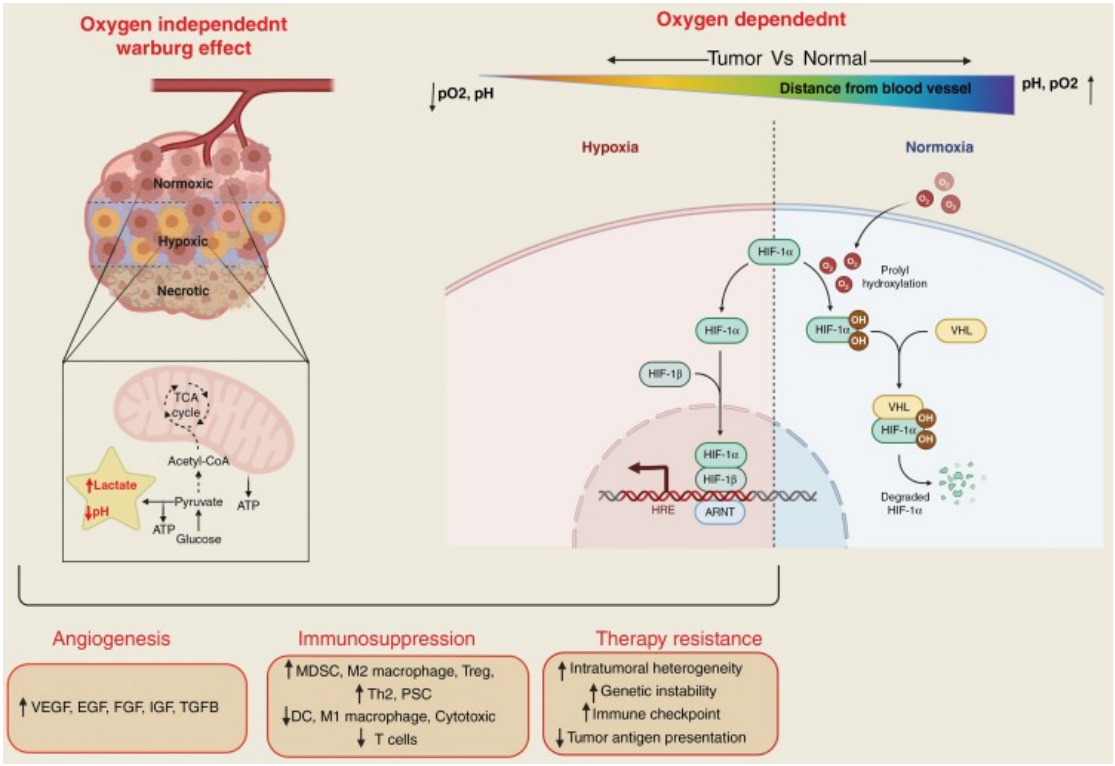

Figure 1.41: ***The role of oxygen-dependent (HIF1-α mediated) and independent (Warburg effect), chemical tumor microenvironment in glioma angiogenesis, immunosuppression, and therapy resistance.***
ARNT, aryl hydrocarbon receptor nuclear translocator; EFG, epidermal growth factor; FGF, fibroblast growth factor; HIF1-α, hypoxia-inducible factor 1-α; HIF1-β, hypoxia-inducible factor 1-β; HRE, hypoxia response element; IGF, insulin-like growth factor; VEGF, vascular endothelial growth factor; VHL, Von Hippel–Lindau; TGFB, transforming growth factor β.Taken from (Sharma et al., 2023b).

In summary, the extensive interactions and relationships between different cells in the glioblastoma microenvironment work together to achieve a state of immune suppression. The specific roles of cytokines, crucial in facilitating communication and coordination among other cells, will be explored further in the next section.

1.6 Cytokines with a major impact on Glioblastoma cytokines

Major Glioblastoma-Associated Cytokines

The relationship between glioma cells and the immune system is a dynamic process where a wide variety of cytokines shape both the tumour microenvironment and the broader immune response. Cytokines, signalling molecules almost always smaller than 70 kDa, regulate immune cells' activities, movement, viability and many other cell populations. Their impact on tumorigenesis is mixed, exhibiting either pro-growth in IL-10, IL-4, VEGF, IL-8 and IL-6 or inhibitory effects like cytokines IL-2, IL-12, IL-13 and Interferon-alpha (IFN-α), Interferon-beta (IFN-β), and Interferon-gamma (IFN-γ). A comprehensive understanding of the cytokine functions within glioma biology and in response to treatment is essential to take advantage of the power of the immune system against malignancies (Mellinghoff et al., 2005, Kim et al., 2021) **(Figure 1.42)**.

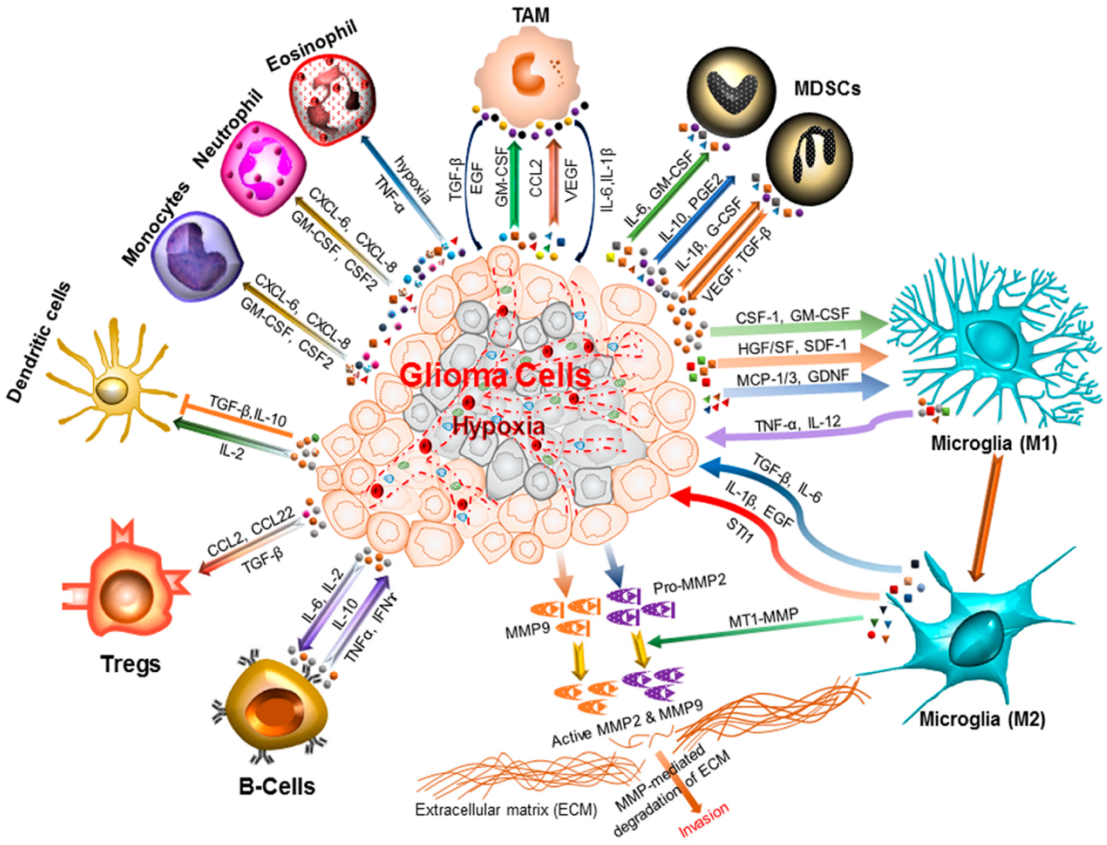

Figure 1.42: Inflammatory microenvironment prevalent in brain cancers.
The glioma microenvironment is heavily infiltrated with different inflammatory cells, including microglia, macrophages, neutrophils, eosinophils, monocytes, dendritic cells, T-cells B-cells, and myeloid-derived suppressor cells (MDSCs). These cells release various mediators that promote cancer cell proliferation, survival, migration and invasion upon activation. These include pro-inflammatory and cytotoxic cytokines, growth factors, bioactive lipids, hydrolytic enzymes, matrix metalloproteinases, reactive oxygen intermediates, and nitric oxide. The cell types involved and the cytokines produced are shown. CCL: C–C Motif Chemokine Ligand 2/monocyte chemoattractant protein 1 (MCP1); TNF-α: Tumor necrosis factor-alpha; CXCL: Chemokine (C–X–C motif) ligand; INF-ɣ: Interferon-gamma; TAM: Tumor-associated macrophages; Tregs: Regulatory T-cells; IL-1β: Interleukin 1 beta; IL-2/6/10/12: Interleukin 2/6/10/12; CSF-1: Colony stimulating factor 1; GM-CSF: Granulocyte-macrophage colony-stimulating factor; HGF/SF: Hepatocyte growth factor or scatter factor; SDF-1: Stromal cell-derived factor 1; MCP-1/3: Monocyte chemoattractant protein 1 or 3; GDNF: Glial cell-derived neurotrophic factor; TGF-β: Transforming growth factor beta; EGF: Epidermal growth factor; STI1: Stress inducible protein 1; MT1-MMP: Membrane type 1-matrix metalloproteinase; MMP2/9: Matrix metalloproteinase 2 or 9.
Taken from (Mostofa et al., 2017).

1.6.1 IL-6:

Multiple cell types secrete IL-6, most prominently the GBM cells themselves, TAMs, and the endothelial cells associated with the tumour *(Kim et al., 2021).*

IL-6 is essential in activating the Janus kinase/signal transducer and activator of the transcription 3 (JAK/STAT3) pathway in GBM, contributing significantly to tumour progression and immune evasion. The IL-6 signalling pathway is initiated when IL-6 binds to the membrane-bound IL-6 receptor (IL-6R, also known as glycoprotein (gp)80), which is expressed in various immune cells. This IL-6/IL-6R complex subsequently associates with the expressed membrane-bound gp130, forming an activated receptor complex that triggers intracellular signalling. IL-6 can also signal through a trans-signalling pathway, where it binds to soluble IL-6R and then to gp130 on cells that lack membrane-bound IL-6R, broadening the range of target cells. Both classic and trans-signalling pathways activate JAKs and STATs, particularly STAT3, which is crucial in modulating cellular responses. In the context of GBM, IL-6-induced STAT3 activation promotes several oncogenic processes, including inhibiting apoptosis and enhancing cell cycle progression. (Kim et al., 2021, Cho et al., 2021, Yeo et al., 2021, Grochans et al., 2022, Torrisi et al., 2022, Hersh et al., 2022) **(Figure1.43)**. The activation of STAT3 by IL-6 not only enhances the proliferative and invasive capabilities of GBM cells but also increases the expression of PD-L1 in immunosuppressive myeloid cells, facilitating immune evasion and contributing to the chronic inflammatory environment that supports GBM progression (Zhao et al., 2022, DeCordova et al., 2020).

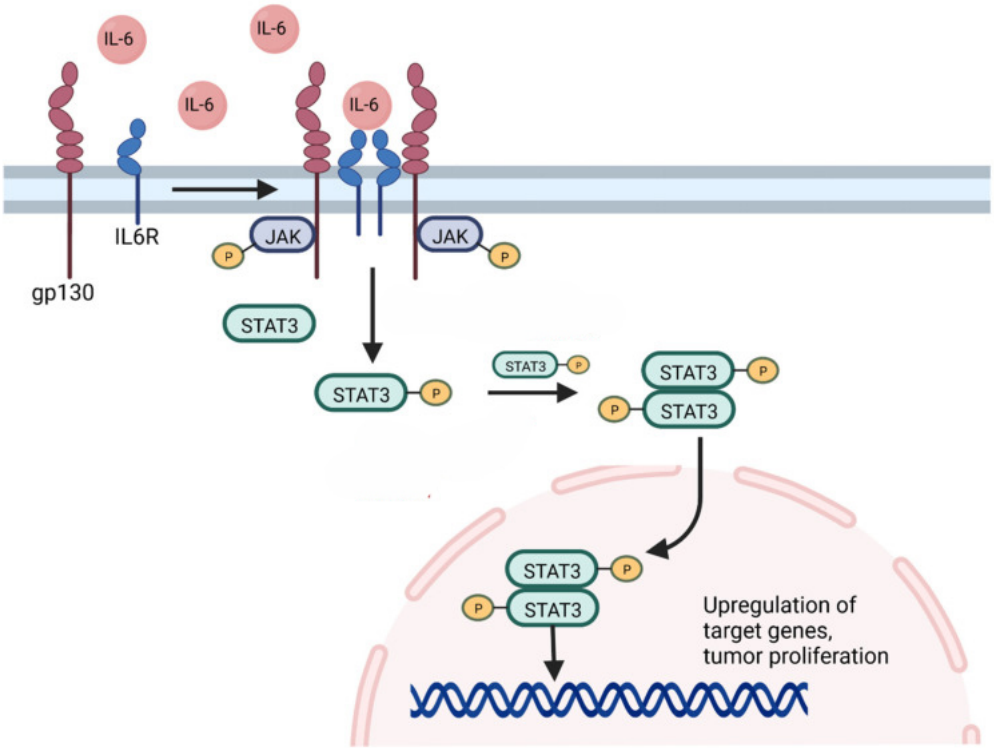

Figure 1.43: STAT3 signaling pathway.
The IL-6 cytokine triggers dimerisation and activation of the IL6 receptor with its gp130 subunit. JAK phosphorylation results in STAT3 phosphorylation, which dimerises and translocates to the nucleus to upregulate target genes associated with stemness and GSC survival. Adapted from (Hersh et al., 2022).

Multiple studies have established the value of IL-6 as a prognostic marker in GBM. Serum IL-6 levels in glioma patients are markedly elevated compared to healthy controls, with a direct correlation observed between IL-6 levels and tumour grade (Kim et al., 2021, Cho et al., 2021, Shan et al., 2015). Moreover, surgical resection of the tumour leads to a significant reduction in serum IL-6, reinforcing its association with tumour burden, and that the malignancy is a major source of the cytokine (Shan et al., 2015).

1.6.2 VEGF:

The most recognised regulators of angiogenesis in glioblastoma progression include VEGF, basic fibroblast growth factor (bFGF), hepatocyte growth factor (HGF), PDGF, as well as TGF-β, MMPs, and angiopoietins (Angs) (Ahir et al., 2020).

VEGF is the primary mediator of angiogenesis in response to hypoxia, a common feature within the glioblastoma microenvironment (Mosteiro et al., 2022). VEGF-A exerts its effects by binding to specific receptor tyrosine kinases on the surface of endothelial cells, namely VEGFR-1, VEGFR-2, and VEGFR-3. Upon binding to its receptors, VEGF induces receptor dimerisation and transphosphorylation, activating downstream signalling pathways such as the Rat sarcoma viral oncogene homolog / Mitogen-Activated Protein Kinase (Ras/MAPK) and Phosphoinositide 3-Kinase / Protein Kinase B (PI3K/Akt) pathways. These cascades promote endothelial cell proliferation, migration, and survival, essential to forming new blood vessels. Additionally, VEGF signalling enhances the secretion of MMPs by endothelial cells, which degrade the extracellular matrix (ECM), allowing endothelial cells to invade the surrounding tissue and form new vascular structures (Ahir et al., 2020, Zhang et al., 2023, Berro et al., 2024) **(Figure 1.44).**

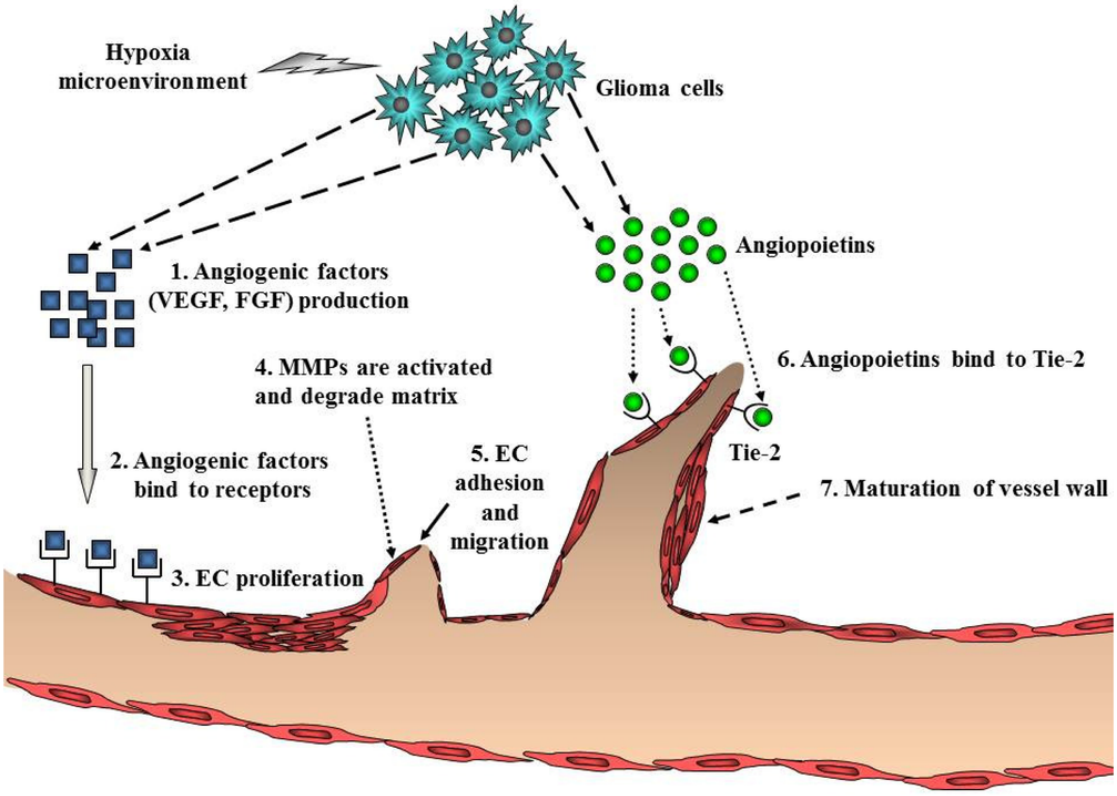

Figure 1.44: A schematic diagram of angiogenesis in gliomas.
Angiogenesis is initiated by angiogenic factors, which are released from glioma cells in the hypoxic glioma microenvironment. Major angiogenic factors include VEGF and FGF. Upon binding to their cognate receptors on endothelial cells, angiogenic factors trigger endothelial cell proliferation and migration. After the degradation of ECM, endothelial cells are assembled into a tubular lumen. The final process is a maturation of the vessel wall, which is constructed by recruiting pericytes to assemble along the endothelial cells outside the new vessel. Taken from (Nakada et al., 2011).

In GBM, the upregulation of VEGF drives the formation of new blood vessels and results in abnormal, dysfunctional vasculature development. The hypoxic conditions within the tumour further exacerbate VEGF expression through hypoxia-inducible factor-1α (HIF-1α), which binds to hypoxia response elements in the VEGF gene promoter, enhancing its transcription. Furthermore, glioblastoma cells frequently harbour genetic alterations in the RTK/Ras/PI3K signalling pathway, which independently promotes VEGF production even in non-hypoxic conditions. This continuous upregulation of VEGF leads to the formation of leaky and inefficient blood vessels, which not only facilitate tumour growth and invasion but also create a barrier to effective drug delivery (Ahir et al., 2020, Zhang et al., 2023, Berro et al., 2024)

Bevacizumab, a humanised monoclonal antibody targeting VEGF-A, has become a cornerstone in managing recurrent GBM since its FDA approval in 2009. This approval was initially based on phase II trials demonstrating a reduction in tumour size, prolonged PFS, and alleviation of cerebral oedema, which translated into improved neurological function for patients. However, despite these benefits, the phase III EORTC 26101 trial revealed that whilst bevacizumab significantly

extended PFS and reduced the need for corticosteroids, it did not offer a substantial OS advantage compared to chemotherapy alone. Bevacizumab exerts its effects by binding to VEGF-A, thereby inhibiting the angiogenic signalling crucial for glioblastoma's highly vascularised nature. This action results in decreased microvascular growth and blood supply to the tumour, which helps manage symptoms like brain oedema but falls short of significantly enhancing patient survival. However, its use is accompanied by significant adverse effects, including gastrointestinal perforations, haemorrhage, and arterial thromboembolism, which necessitate careful patient selection and monitoring during treatment (Zhang et al., 2023, Berro et al., 2024).

The initial promise of anti-VEGF therapies in treating glioblastoma was rooted in the rationale that inhibiting angiogenesis would starve the tumour of its blood supply. However, the clinical outcome is little to no significant increase in overall survival. This resistance to anti-VEGF therapy can be attributed to the glioblastoma's ability to activate alternative pro-angiogenic pathways and adapt metabolically to hypoxic conditions induced by such treatments. For instance, bevacizumab has been shown to trigger compensatory mechanisms, such as the upregulation of Proto-oncogene tyrosine-protein kinase Src, a key mediator of tumour invasion and enhancement of glycolytic pathways through upregulated glucose transporter 3, promoting a Warburg effect-mediated resistance. Additionally, the hypoxic environment resulting from VEGF inhibition can paradoxically stimulate further angiogenesis by recruiting bone marrow-derived cells (BMDCs) and promoting the expression of other pro-angiogenic factors like bFGF. These adaptive responses highlight the complexity of glioblastoma's vascularisation mechanisms and suggest that future therapeutic strategies should simultaneously focus on combination therapies that target multiple angiogenic pathways (Torrisi et al., 2022, Zhang et al., 2023).

1.6.3 IL-8:

IL-8 is a pro-inflammatory chemokine synthesised by various cell types, including monocytes and macrophages, and it plays a key role in directing leukocytes, such as neutrophils, basophils, and T lymphocytes, to sites of infection or injury (Masood et al., 2020, Mellinghoff et al., 2005). IL-8 has been associated with increased migration of myeloid-origin neutrophils and suppressor cells, facilitating a pro-tumorigenic environment (Masood et al., 2020).

IL-8 is highly overexpressed and exerts its pro-angiogenic effects primarily through the C-X-C motif containing chemokine receptor, CXCR2, on brain endothelial cells. This interaction promotes endothelial cell migration and survival. It increases vascular permeability, contributing to the formation of abnormal, highly permeable blood vessels/ Moreover, IL-8 is known to induce the production of MMPs, particularly MMP-2 and MMP-9, which are crucial for the degradation of the

ECM. This degradation is a key step in enabling the invasion of glioblastoma cells along pre-existing blood vessels, a process known as vascular co-option. The elevated levels of IL-8 observed at the tumour resection margins, as compared to lower levels in the peritumoral regions, suggest its role in facilitating angiogenesis and the invasive behaviour of GBM. (Masood et al., 2020, Strepkos et al., 2020, Mellinghoff et al., 2005, Mostofa et al., 2017, Mosteiro et al., 2022, Testa et al., 2022). Moreover, IL-8 is implicated in upregulating stem cell marker expression in GSCs and activating various signalling pathways associated with tumorigenesis, including STAT3, PI3K, and MAPK (Masood et al., 2020, Testa et al., 2022, McCoy et al., 2019).

Multiple studies have increasingly recognised and supported the role of IL-8 as a diagnostic biomarker in GBM. Immunohistochemical studies demonstrate that approximately 65% of primary and secondary GBM samples exhibit elevated IL-8 expression, which is directly correlated with the induction of angiogenesis and invasion (Jarmuzek et al., 2023). Additionally, IL-8 levels in plasma were significantly higher in GBM patients compared to healthy controls ($p < 0.001$), emphasising its potential as a diagnostic marker (Jarmuzek et al., 2023). Furthermore, a large cohort study involving 158 glioma patients (WHO grade II-IV) found that High plasma IL-8 (HR = 1.52; P =.0077) were associated with short progression-free survival and high plasma IL-8 (HR = 1.40; P =.044) and were associated with short OS in newly diagnosed patients with GBM. These findings underline IL-8 role in the tumour microenvironment and solidify its utility as a potential prognostic biomarker in GBM (Holst et al., 2021).

A recent study showed targeting IL-8 can enhance the effectiveness of anti-PD-1 therapy in GBM. It was found that IL-8-producing CD4+ T cells play a significant role in the glioblastoma microenvironment by promoting MDSC infiltration and angiogenesis, which impairs anti-PD-1 treatment efficacy. Specifically, anti-PD-1 therapy alone did not significantly alter tumour growth, but when combined with Anti-IL-8 treatment, it substantially reduced tumour size and improved survival. (Li et al., 2023) **(Figure 1.45)**

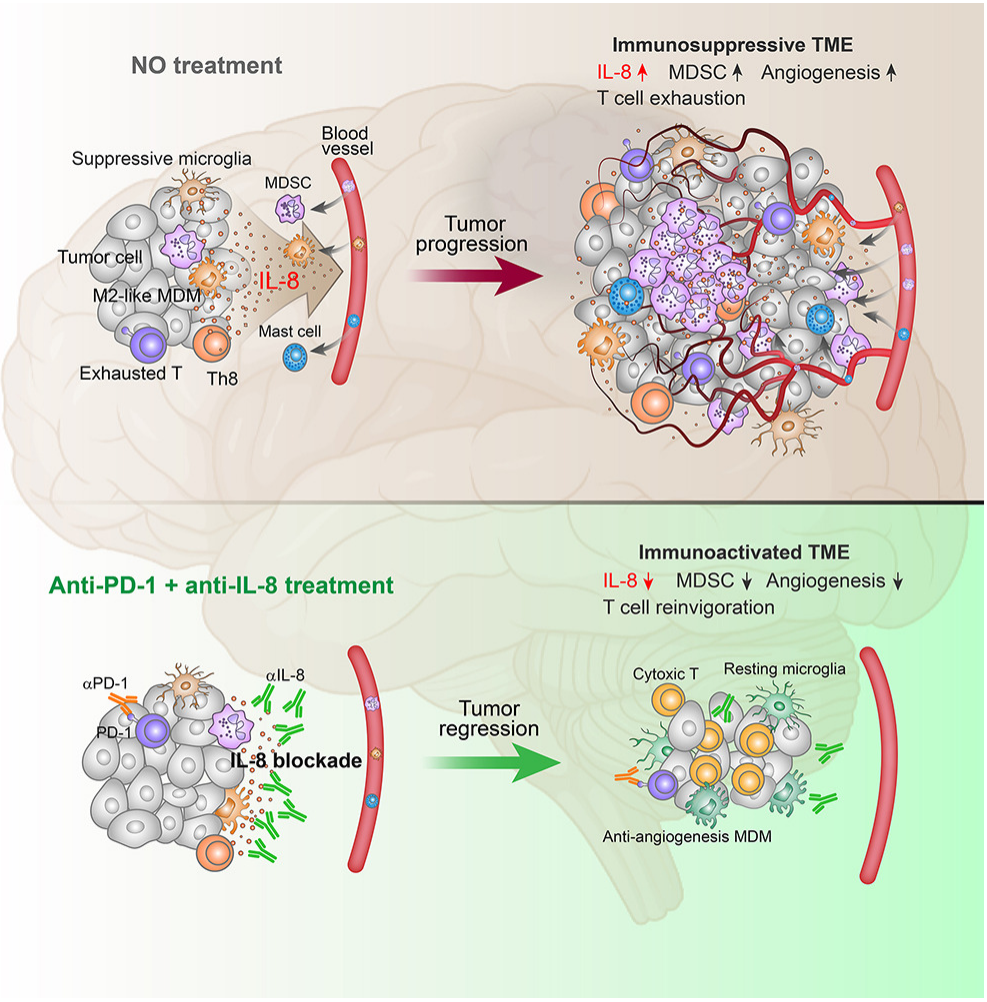

Figure 1.45: ***Effect of combining Anti-IL-8 and Ant-PD-1 in glioblastoma***
Taken from (Li et al., 2023).

Cytokines are key players in the GBM microenvironment through immune cell recruitment, angiogenesis, invasion and escaping the body's immune system. Known cytokines such as IL6, VEGF and IL8 promote GBM growth and progression. They can serve as biomarkers or therapeutic targets. In addition to cytokines, epigenetic regulators such as protein arginine methyltransferases (PRMTs) have emerged as crucial players in GBM behaviour. That provides new ways to conduct therapeutic interventions. These will be explored further in the next section.

1.7 PRMTs role in glioblastoma

1.7.1 Overview of PRMTs

The PRMT family comprises nine members regulating transcription, translation, splicing, and cell signalling. PRMTs facilitate transferring one or two methyl groups to the guanidine nitrogen atoms of arginine, commonly on the histone tail (Stitzlein et al., 2024).

PRMTs are categorised into three main types based on the methylation pattern they produce: Type I enzymes (PRM1, 2, 3, 4, 6, and 8) catalyse asymmetric dimethylarginine or monomethylarginine, Type II enzymes (PRMT5 and 9) produce symmetric dimethylarginine or monomethylarginine, and PRMT7, the only Type III enzyme, generates monomethylarginine only. Dysregulation of PRMT activity has been implicated in various diseases, particularly cancer, where abnormal PRMT expression and function contribute to tumorigenesis, progression, and resistance to therapy (Bryant et al., 2021a, Samuel et al., 2021, Barry et al., 2023b) **(Figure 1.46).**

This section will present the most relevant PRMT in glioblastoma and recent clinical trials using PRMT inhibitors.

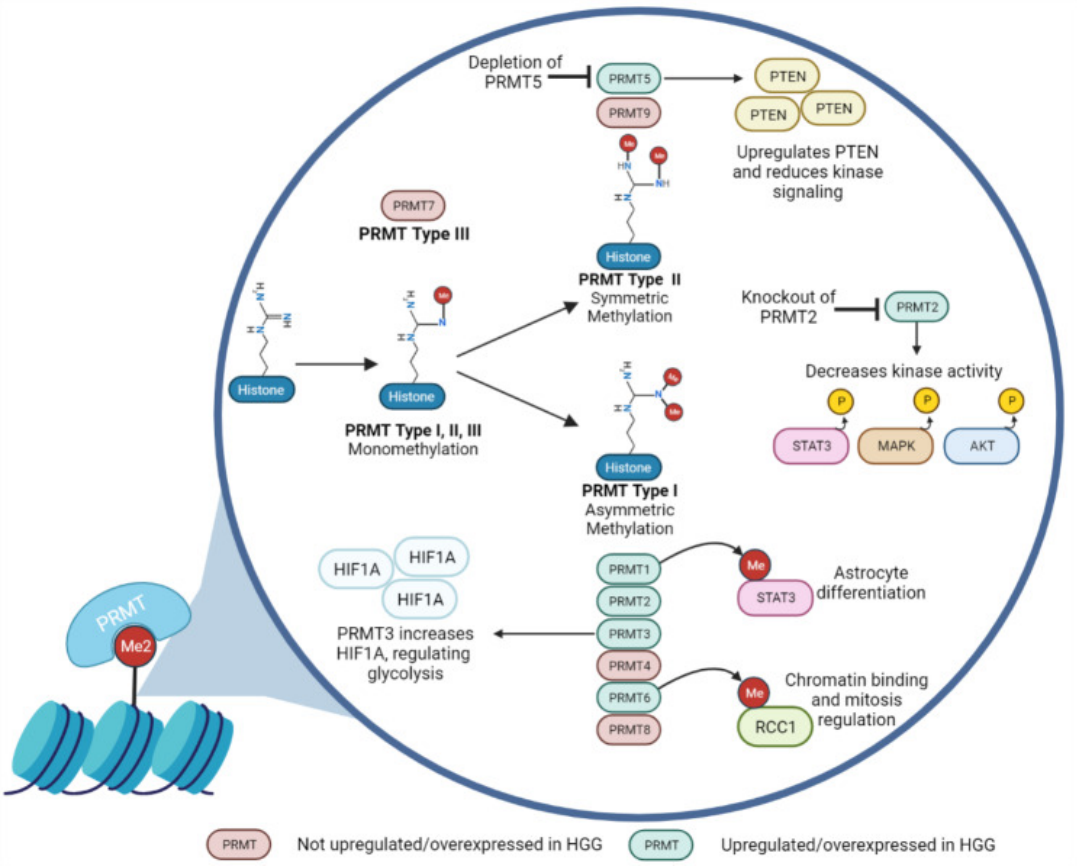

Figure 1.46: Patterns of PRMT Methylation.

Taken from (Stitzlein et al., 2024).

1.7.2 PRMT1 in Glioblastoma

PRMT1 regulates the differentiation of neural stem cells into astrocytes by methylating arginine residues on STAT3. STAT3 activation can occur through phosphorylation or methylation. As a non-histone target of PRMT1, the methylation of STAT3 leads to its enhanced activation (Bryant et al., 2021a, Samuel et al., 2021, Stitzlein et al., 2024) **(Figure 1.47).**

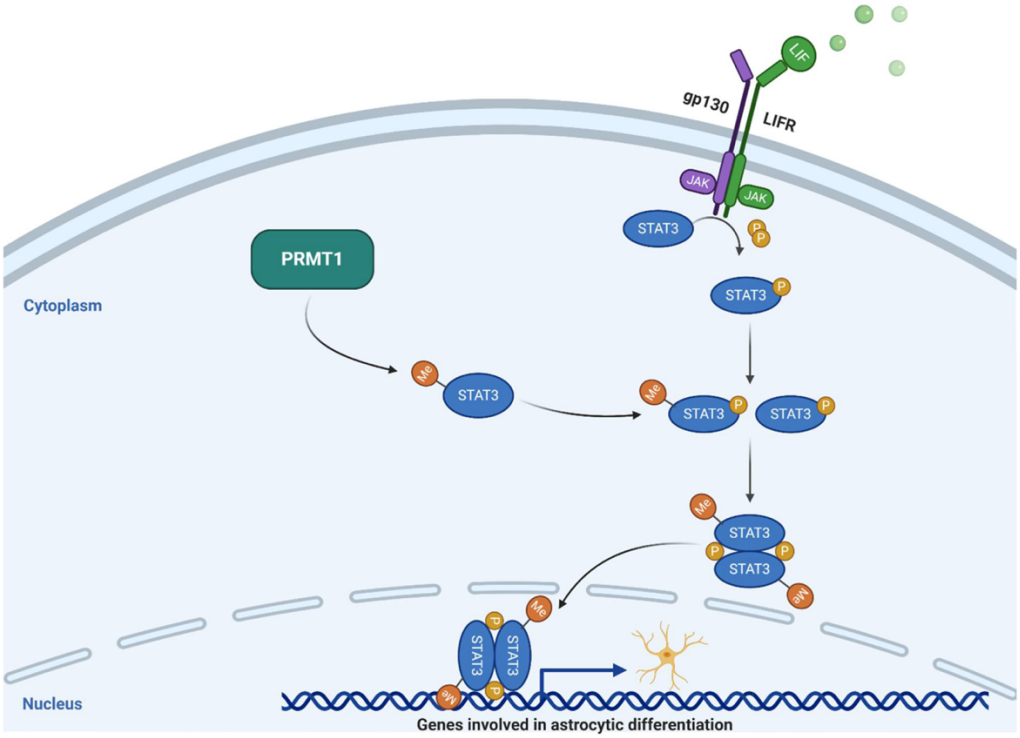

Figure 1.47: Schematic drawing of the PRMT1-STAT3 axis.
JAK = Janus kinase; LIFR Leukemia inhibitory factor receptor; Me = Methyl; P = Phosphorous; PRMT1 = protein arginine methyltransferase 1; STAT3 = Signal transducer and activator of transcription 3. Adapted from "PI3K/Akt, RAS/MAPK, JAK/STAT Signaling" by BioRender.com (2020). Retrieved from ***https://app.biorender.com/biorender-templates****. Taken from (Bryant et al., 2021a).*

The hyperactivation of the JAK/STAT3 pathway contributes to tumour growth, therapeutic resistance, invasion, and immune suppression in GBM. This pathway is triggered when extracellular signalling molecules bind to specific receptors on GBM cells, leading to the activation of JAK enzymes. Activated JAKs phosphorylate receptor tyrosine residues, creating docking sites for STAT3 proteins. These STAT3 proteins subsequently bind, undergo phosphorylation, dimerise, and translocate to the nucleus, where they regulate the transcription of genes involved in cell survival, proliferation, invasion, angiogenesis, and immune evasion. Activated STAT3 facilitates the recruitment of immunosuppressive cells such as myeloid- MDSCs, M2-like TAMs, and Tregs into the GBM microenvironment through cytokines including IL-6, IL-10, and TGF-β. In addition,

STAT3 also promotes the accumulation of other immune cells such as T cells, DCs, and NK cells at the tumour site. Radiotherapy further influences the immune landscape. Radiation-induced DNA damage activates and recruits NK cells, M1-like TAMs, CD8+ T cells, and other cytotoxic immune cells. Concurrently, activation of the stimulator of interferon genes (STING) pathway leads to excessive stimulation of the PD1/PD-L1 immune checkpoint and reduces arginine levels in the tumour microenvironment. Together, these mechanisms exhibit both synergistic and antagonistic effects on immune responses. Ultimately, they contribute to the development of a profoundly immunosuppressive microenvironment in GBM.(Ou et al., 2021, Fu et al., 2023b).

Building upon the understanding of PRMT1's role in glioblastoma, the Chromatin Target of PRMT1 (CHTOP) protein binds to 5-hydroxymethylcytosine (5hmC) and is part of an arginine methyltransferase complex known as the methylosome. This complex facilitates the PRMT1-mediated methylation of arginine three on histone H4 (H4R3) in genes implicated in the development of glioblastoma, such as EGFR, RAC-gamma serine/threonine-protein kinase **(**AKT3), Cyclin-Dependent Kinase 6 (CDK6), Cyclin D2 (CCND2), and BRAF. This suggests that 5hmC is crucial in glioblastoma formation (Samuel et al., 2021, Takai et al., 2014, Izumikawa et al., 2018).

The generation of 5hmC from 5-methylcytosine (5mC) is catalysed by the ten-eleven translocation (TET) family of enzymes. However, mutations in IDH enzymes lead to 2-hydroxyglutarate, an oncometabolite that inhibits TET activity and consequently impedes the conversion of 5mC to 5hmC. This observation suggests that the presence of mutant IDH, despite its oncogenic role, may indirectly suppress tumorigenesis by hindering the 5hmC-dependent recruitment of the CHTOP-methylosome complex, thus potentially accounting for the improved prognosis observed in glioblastoma patients with IDH mutations (Samuel et al., 2021, Takai et al., 2014) **(Figure 1.48).**

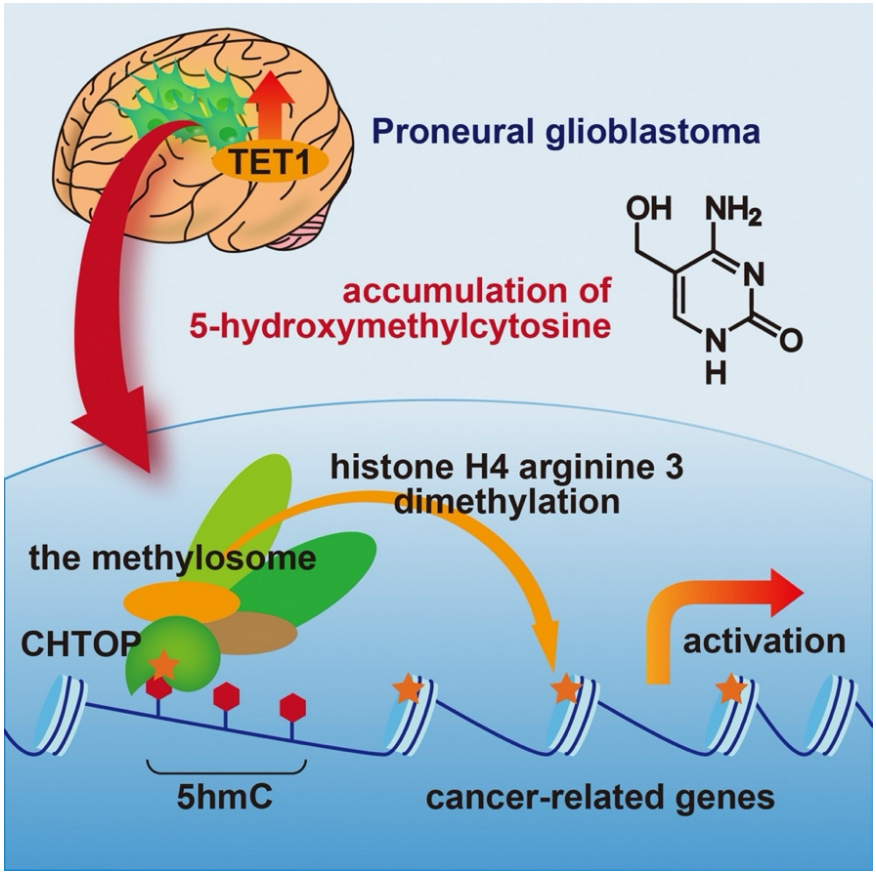

Figure 1.48: TET1/5hmC pathway recruits the CHTOP–methylosome complex to activate cancer-related genes in GBM.
Glioblastoma cells contain elevated levels of 5hmC, and TET1 TET1-mediated production of 5hmC is required for glioblastomagenesis 5hmC recruits the CHTOP-methylosome complex. The CHTOP-methylosome complex methylates H4R3 and transactivates cancer-related genes.
Taken from (Takai et al., 2014)

A recent study investigated the therapeutic potential of targeting PRMT1 in GSC. The study found furamidine, a PRMT1 inhibitor, significantly reduced the proliferation and tumorsphere formation of U87MG-derived GSCs by causing cell cycle arrest at the G0/G1 phase and activating the intrinsic apoptotic pathway. Additionally, furamidine strongly suppressed the *in vivo* tumour growth of U87MG GSCs in a chick embryo model. This inhibitory effect was linked to the downregulation of STAT3 (Yuk and Jung, 2024).

1.7.3 PRMT2 in Glioblastoma

Histone modifications serve as critical epigenetic regulators of gene transcription in eukaryotic cells. Among these modifications, histone arginine methylations have emerged as pivotal players in modulating transcriptional processes. PRMT2, a histone methyltransferase, specifically catalyses the asymmetric dimethylation of histone H3 at arginine 8 (H3R8me2a) (Dong et al., 2018).

H3R8me2a emerges as a critical player in glioblastoma pathogenesis. By facilitating the recruitment of PRMT2 to specific gene promoters, B-cell lymphoma 2 (Bcl-2). H3R8me2a enhances the accessibility of STAT3, leading to increased expression of genes promoting cell proliferation and survival (Stitzlein et al., 2024, Rosenthal et al., 2020, Cura and Cavarelli, 2021) **(Figure 1.49).**

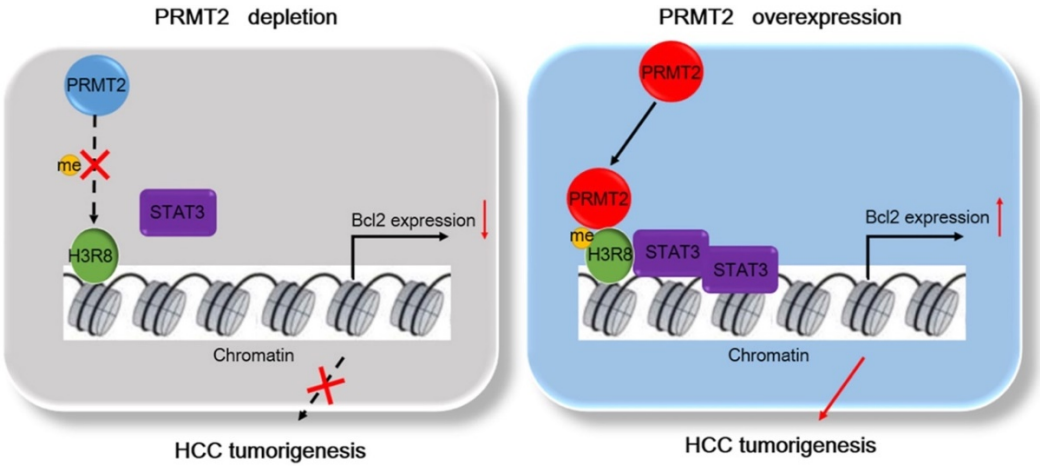

Figure 1.49: The mechanism of PRMT2 in tumorigenesis
Taken from (Hu et al., 2020a).

In addition to *in vitro* findings, the Dong et al study showed that knocking down PRMT2 in GBM cells led to decreased tumour growth *in vivo,* as seen in orthotopic mouse models. PRMT2 depletion reduced tumour volume and invasiveness and extended the survival of mice with GBM. These results suggest that targeting PRMT2 could be a potential therapeutic strategy for treating GBM (Dong et al., 2018, Stitzlein et al., 2024).

1.7.4 PRMT3 in Glioblastoma

Studies demonstrate PRMT3 overexpression in GBM is associated with poorer patient survival (Liao et al., 2022). Functionally, PRMT3 promotes tumour growth by regulating glycolysis through its interaction with HIF1α. The glycolytic program is the metabolic pathway favoured by cancer cells for energy production. Furthermore, the knockdown of PRMT3 in GSCs induces cell cycle arrest and apoptosis. These findings suggest PRMT3 as a potential therapeutic target by disrupting the HIF1α-mediated glycolytic pathway in GBM (Stitzlein et al., 2024, McCornack et al., 2023).

1.7.5 PRMT5 in Glioblastoma

The PTEN/Akt pathway is a signalling pathway that regulates cell growth, survival, and metabolism. It begins with PI3K activation when growth factors (EGFR and PDGFR) bind to receptors on the cell surface, converting the membrane phospholipid from phosphatidylinositol 4,5-bisphosphate (PIP2) into Phosphatidylinositol (3,4,5)-trisphosphate (PIP3). Activated Akt promotes cell growth and survival by phosphorylating various targets, inhibiting apoptotic pathways, and stimulating protein synthesis and

glucose metabolism. PTEN (phosphatase and tensin homolog) acts as a tumour suppressor by converting PIP3 back to PIP2, reducing Akt activation, and preventing excessive cell proliferation. In GBM, the loss or mutation of PTEN leads to overactivation of Akt, contributing to uncontrolled cell growth and resistance to apoptosis (Deng et al., 2022, Kim and Ronai, 2020). PRMT5 plays a role in this pathway by methylating proteins involved in Akt signalling, enhancing Akt activation. (Bryant et al., 2021b, Banasavadi-Siddegowda et al., 2017) **(Figure 1.50)**.

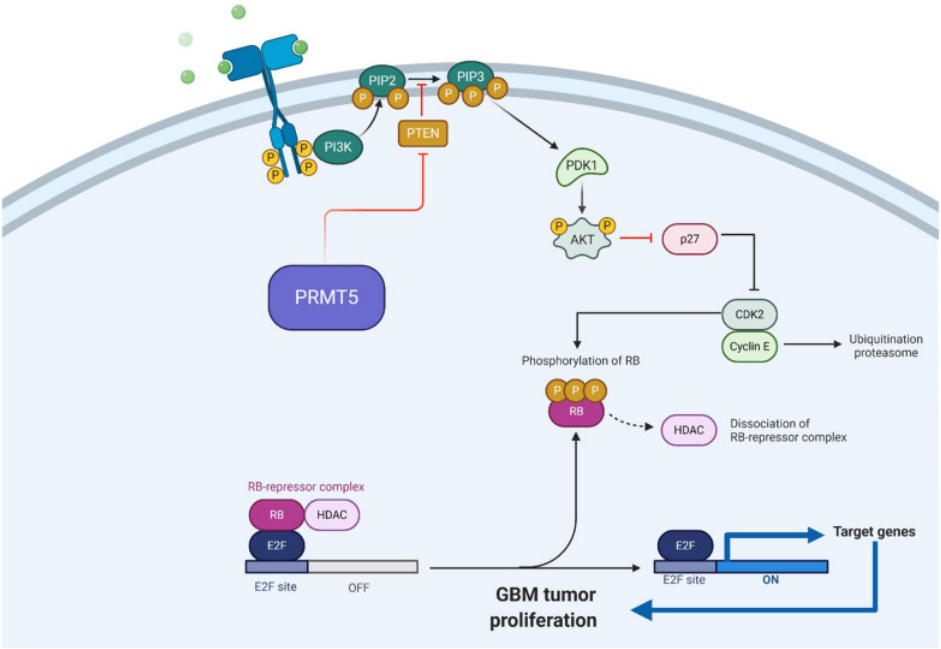

Figure 1.50: Schematic drawing of PRMT5-PTEN axis.
Akt = Protein kinase B; CDK2 = Cyclin-dependent kinase 2; GBM = Glioblastoma; HDAC = Histone deacetylase; PIP2 = Phosphatidylinositol (4,5)-bisphosphate; PIP3 = Phosphatidylinositol (3,4,5)-triphosphate; P = Phosphorous; PTEN = Phosphatase and tensin homolog; PI3K = Phosphoinositide-3-kinase; PRMT5 = Protein arginine methyltransferase 5; RB = Retinoblastoma. Adapted from "G1/S Checkpoint", by BioRender.com (2020). Retrieved from https://app.biorender.com/biorender-templates. Taken from (Bryant et al., 2021b).

A study using two different inhibitors of PRMT5, GSK591 and LLY-283, demonstrates that blocking PRMT5 activity reduces the growth of 46 patient-derived glioblastoma (GBM) stem cell cultures, with the proneural subtype being more sensitive to treatment (Sachamitr et al., 2021). Another recent study investigated the combined use of trametinib, an FDA-approved MEK inhibitor, and PRMT5 inhibition to treat GBM. The study found that PRMT5 inhibition enhanced trametinib's antitumor efficacy in glioblastoma animal models (Banasavadi-Siddegowda et al., 2022).

1.7.6 PRMT8 in Glioblastoma

PRMT8 is a member of the Type I PRMT family and is primarily expressed in the neurons of the CNS. It is closely related to PRMT1 but has a distinctive N-terminal domain. This domain includes a myristoylation site at the N-terminus, which allows it to anchor to the plasma membrane. Additionally, PRMT8 possesses phospholipase activity, making it the only PRMT with both methyltransferase and phospholipase activities. These dual enzyme functions enable PRMT8 to perform various roles in neurons. Unlike other PRMTs, PRMT8 is downregulated in GBM. (Dong et al., 2021, Samuel et al., 2021, Simandi et al., 2015) **(Figure 1.51)**.

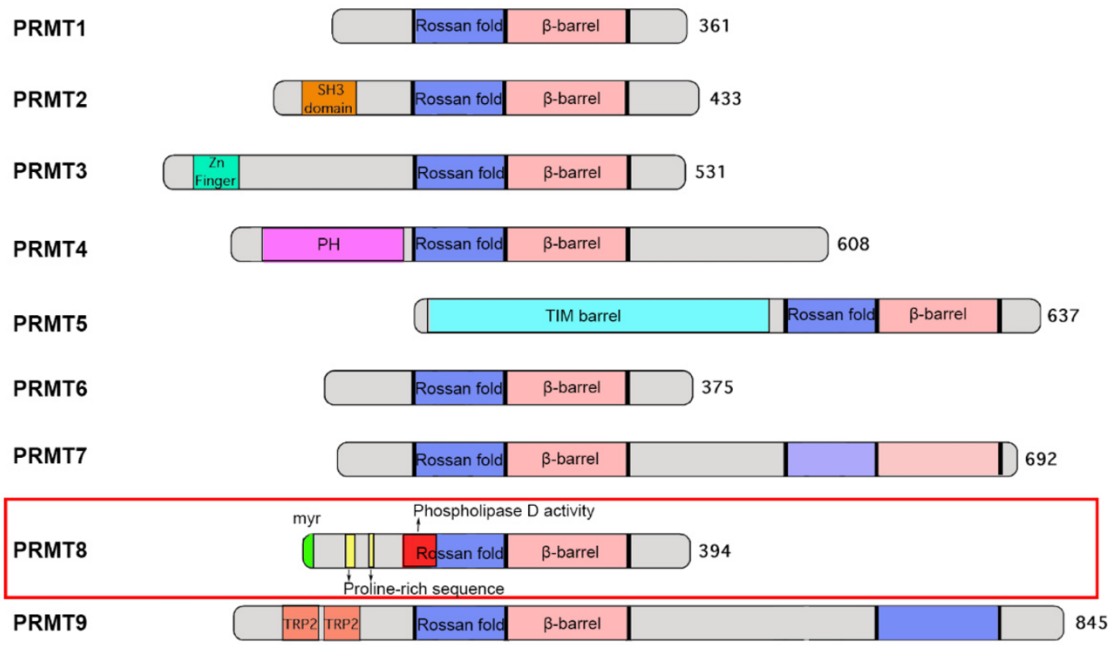

Figure 1.51: Schematic diagram illustrating the domain architecture of various PRMTs. *Taken from (Dong et al., 2021).*

1.7.7 Recent Clinical Trials of PRMT Inhibitors in GBM

The METEOR-1 (NCT02783300) using GSK3326595

The METEOR-1 study (NCT02783300), a phase I open-label trial, aimed to evaluate the safety, pharmacokinetics, pharmacodynamics, and clinical activity of GSK3326595, a PRMT5 inhibitor, in patients with advanced solid tumours, including glioblastoma, and non-Hodgkin's lymphoma. (ClinicalTrials.gov, 2023).

Despite early termination, the trial showed modest efficacy, with partial responses in patients with adenoid cystic carcinoma and breast cancer and complete responses in two non-Hodgkin lymphoma patients. The trial indicated that GSK3326595 had a tolerable safety profile consistent with other PRMT5 inhibitors. Treatment-related adverse events (TRAEs) were reported in 95% of patients, with grade 3 TRAEs in 46% and grade 4 in 7%. Serious TRAEs occurred in 19% of

participants, with significant rates of dose reductions and treatment interruptions due to adverse effects. The results demonstrated potential efficacy but highlighted challenges in balancing benefit and risk (OncLive, 2023).

NCT04089449 trial using PRT811

The clinical trial NCT04089449 aimed to evaluate the safety and effectiveness of a drug called PRT811, which is a PRMT5 inhibitor. This first phase of the clinical trial was an early stage focused on determining a safe dosage and assessing potential drug side effects. The trial included patients with various advanced cancers, including GBM, and recruited participants who had exhausted all other available treatment options. PRT811 was given orally to the participants throughout the study.

The clinical trial concluded in April 2023. Although detailed results are not yet available on ClinicalTrials.gov, data presented at a major oncology conference (American Society of Clinical Oncology) showed PRT811 appeared well-tolerated by patients and offered early signs of effectiveness in specific groups. In particular, the drug showed potential for treating IDH-muted recurrent high-grade gliomas (Monga et al., 2023, ClinicalTrials.gov, Updated April 5, 2023).

1.8 Microfluidic platforms used in GBM research

GBM poses a significant clinical challenge due to treatment resistance and poor prognosis, which is still not adequately addressed. Traditional research models often fail to capture the complexities of the tumour microenvironment, hindering drug discovery or therapeutic development. Microfluidics offers a revolutionary approach, enabling the creation of sophisticated ex vivo models that mimic key aspects of GBM biology better than static two-dimensional (2D) systems (Thenuwara et al., 2024).

This section briefly reviews the potential of microfluidics in GBM research, highlighting applications in drug delivery, cell-cell interactions, and personalised medicine. Additionally, it discusses the advantages and limitations of microfluidic platforms, outlining future directions for their development and application.

1.8.1 The Need for Advanced Models in Glioblastoma Research

The shortcomings of existing therapeutic strategies are compounded by the high failure rates in clinical trials, primarily due to imperfect models that impede accurate predictions of efficacy and toxicity in humans. This issue is especially evident in glioblastoma, where no effective treatment has significantly enhanced survival since Temozolomide was introduced two decades ago (Bi et al., 2020, Mariappan et al., 2021). GBM remains a complex challenge in oncology, characterised by its aggressive

growth, high recurrence rates, and resistance to therapy. The TME is pivotal in GBM progression, including interactions between diverse cell types, extracellular matrix components, and soluble factors (De Fazio et al., 2024). Conventional 2D and 3D cell culture models have been insufficient in replicating the dynamic and complex characteristics of the GBM TME, limiting the understanding of disease mechanisms and the ability to develop effective treatments. This inadequacy has led to the advancement of sophisticated *in vitro* models, particularly organ-on-a-chip (OoC) platforms based on microfluidic technology, which provide a more physiologically relevant and controllable setting for studying GBM (Thenuwara et al., 2024, Slika et al., 2023, Alves et al., 2022).

1.8.2 Advantages of Microfluidic Models Over Traditional Cell Culture Methods

While 2D cell cultures offer an easy, simple, and well-studied platform for cancer cells, they fail to replicate the complexity of the GBM TME. Approximately 97% of oncology preclinical trials have not secured FDA approval because 2D *in vitro* and animal *in vivo* platforms cannot accurately mimic the tumour microenvironment (Regmi et al., 2022). Microfluidic systems can incorporate multiple cell types, such as GBM, endothelial and immune cells along with extracellular matrix (ECM) components, which are essential in glioblastoma pathophysiology. These elements establish a bidirectional and complex interaction with GBM cells, regulating several cellular processes that promote tumour cell proliferation, invasion, and resistance. Consequently, microfluidics allows for testing tissues within their complex niche rather than as isolated cells, leading to more effective and reliable clinical results (Xie et al., 2023a, Cai et al., 2020b) **(Figure 1.52)**.

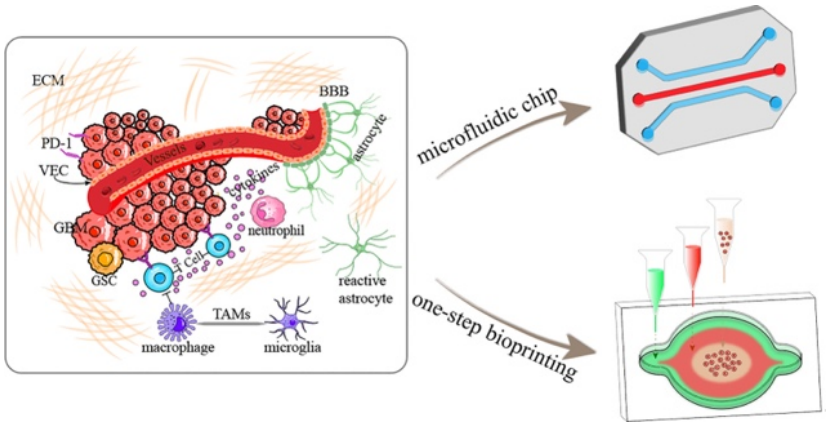

Figure 1.52: Schematic diagram illustrating the GBM tumour microenvironment and construction of GBM-on-a-chip based on microfluidics and one-step bioprinting. *ECM, extracellular matrix; BBB, blood-brain barrier; PD-1, programmed cell death protein 1; VEC, vascular endothelial cell; GSC, glioma stem cell; TAMs, tumour-associated microglia and macrophages. Taken from (Xie et al., 2023b).*

While 2D cell cultures consist of a monolayer, microfluidic systems can maintain cells in correct 3D arrangements. This 3D structuring, including 3D culture scaffolds and perfusable vascular networks, is essential as it replicates the *in vivo* organisation of TME. This allows for a more accurate study of the spatial and functional interactions between different cell types (Cai et al., 2020a, Cauli et al., 2023, Jensen and Teng, 2020, Habanjar et al., 2021).

Microfluidic platforms offer precisely controlled environments where small devices host living cells in microchambers that are perfused through hollow microchannels. These channels create gradients of oxygen, nutrients, and growth factors, reflecting the heterogeneity and dynamic nature of the GBM TME. This setup enables studying complex interactions between tumour cells and biochemical and biophysical stimuli, closely resembling tissue functions. It provides valuable insights into tumour growth, invasion, and response to therapy (Thenuwara et al., 2024, Slika et al., 2023, Straehla et al., 2022, Ko et al., 2022).

More sophisticated 3D *in vitro* models, such as spheroids and organoids, have been developed to meet the need for a 3D physiological structure. However, these models still lack essential features like flow and mechanical cues like shear stress. Microfluidic platforms address this by replicating and controlling human-like physiological cues, such as perfusion, through pumps that facilitate the movement of the medium inside designed channels. Introducing flow and shear stress in microfluidic channels more accurately mimics physiological conditions, allowing for studying cell migration, invasion, and drug response under more realistic circumstances. This is especially relevant for GBM, where tumour cells interact with blood vessels and the blood-brain barrier (Straehla et al., 2022, Wong et al., 2021b, Cauli et al., 2023) **(Figure 1.53).**

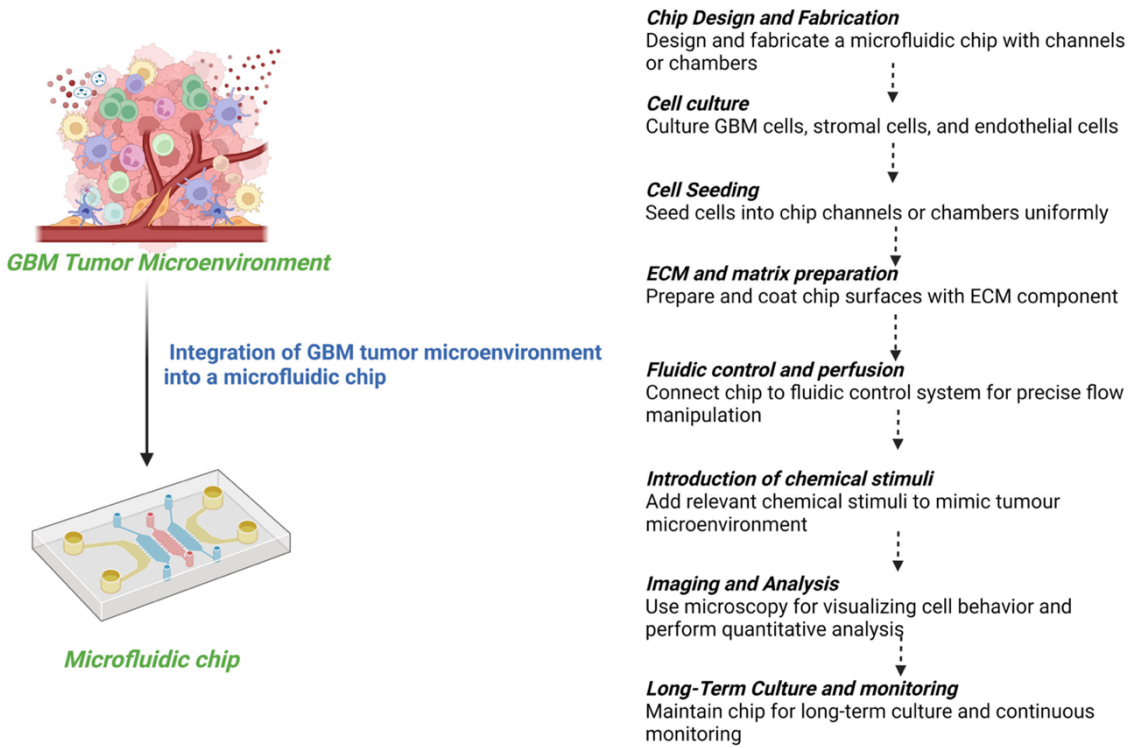

Figure 1.53: Workflow for creating a glioblastoma tumour microenvironment in microfluidic chips.
This figure illustrates the step-by-step process for preparing a glioblastoma tumour microenvironment using traditional microfluidic chips. From chip design and fabrication, the workflow progresses through cell culture, seeding, preparation of ECM, fluidic control, introduction of chemical stimuli, imaging, analysis, and long-term culture and monitoring. Each step is crucial for accurately mimicking the complex tumour microenvironment, enabling researchers to study tumour biology, drug responses, and therapeutic interventions in a controlled laboratory setting.
Taken from (Thenuwara et al., 2024).

Real-time monitoring capabilities represent a significant advantage of microfluidic GBM models. Integration with imaging and sensor technologies allows for continuous, non-invasive monitoring of cellular behaviour, drug responses, and molecular changes in real time. This provides valuable insights into the dynamic processes occurring within the tumour and its response to treatment (Thenuwara et al., 2024, Straehla et al., 2022). In OoC systems, sensors with various outputs, such as temperature, pH, and oxygenation, can be integrated to monitor and control the microenvironment and perform real-time measurements. For instance, sensors have been used to regulate and measure physical characteristics like flow, temperature, and pH (Kim et al., 2021, Lopez-Muñoz et al., 2022, Zhao et al., 2021, Meghani et al., 2020). When combined with imaging instruments, OoC systems enable real-time monitoring of changes in cell biology, allowing for observing alterations in cell behaviour during disease states and in response to drugs (Thenuwara et al., 2024).

These systems allow for real-time, in situ, and dynamic maintenance and monitoring of various biological parameters, including shear stress, pH, oxygen levels, cytokines, and chemokines. Additionally, they enable downstream and off-chip analyses of molecular signatures, and tissue pathology using

traditional analytical tools such as enzyme-linked immunosorbent assay (ELISA), polymerase chain reaction (PCR), and single-cell mRNA sequencing (Ma et al., 2021).

Crucially, microfluidic platforms enable real-time in situ detection of secreted proteins, exosomes, and other biomarkers produced during cellular physiological processes. Monitoring biomarkers in living cells at different life stages and under varying microenvironments is essential for investigating cellular processes. This capability enhances our understanding of cellular life processes (Lou et al., 2024).

Microsystems primarily use polydimethylsiloxane (PDMS), a type of silicone rubber, which has facilitated research groups' widespread adoption of microfluidic platforms. It has become the preferred material for manufacturing microfluidic devices, replacing more expensive and time-consuming materials like glass and silicon. The PDMS model can be covalently bonded to a glass substrate using a simple plasma process, resulting in a sealed microfluidic system (Cauli et al., 2023, Roy et al., 2016, Borók et al., 2021) **(Figure 1.54).**

The deformability of PDMS allows for leak-proof fluidic connections and the inclusion of valves in biological studies. The PDMS device is gas permeable, allowing gas to flow freely between the cells without external air. Furthermore, its air permeability may be easily adjusted by modifying its composition. Its transparency aids in on-chip imaging as well (Lamberti et al., 2014, Regmi et al., 2022).

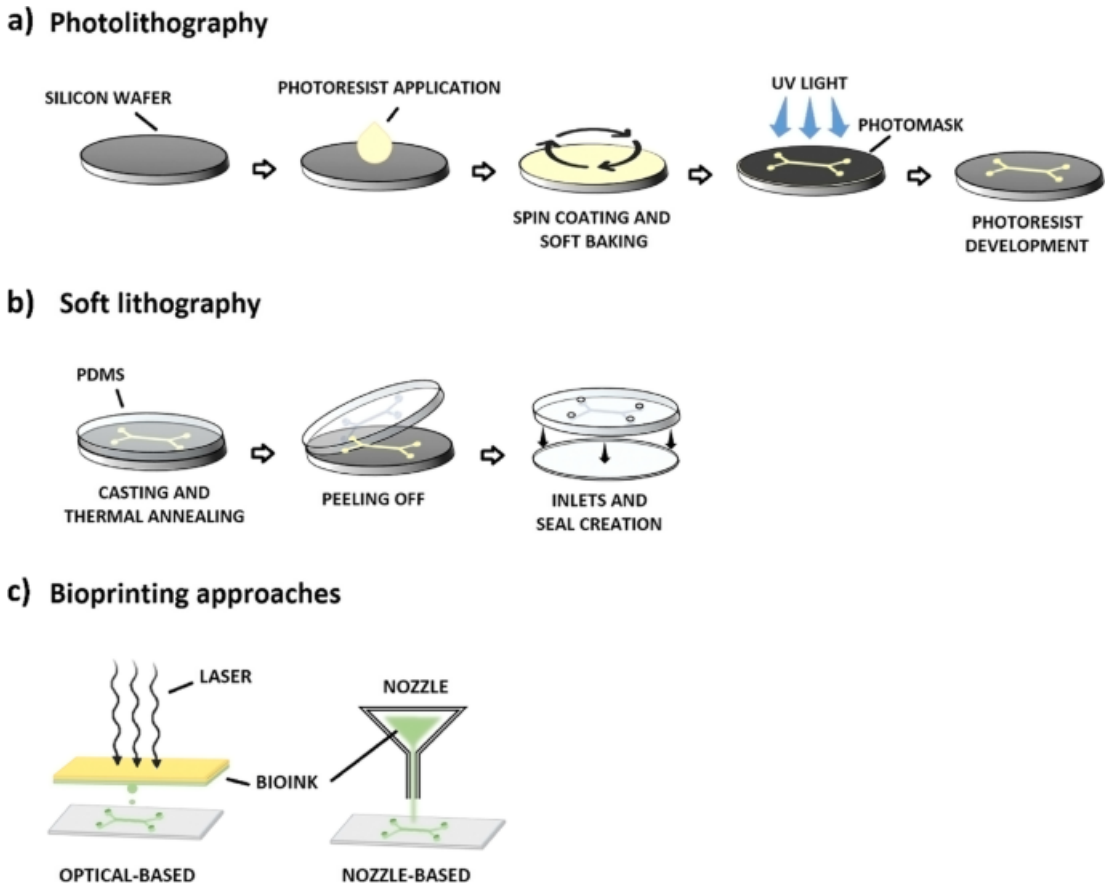

Figure 1.54: The two main microfabrication techniques used to generate organs-on-chip. *Photolithography is the core microfabrication technique that transfers micro- and nanoscale patterns to photosensitive materials by optical radiation. A silicon wafer supports the photosensitive material, which is generally called photoresist. After its application on the wafer's surface, the wafer is spin-coated to obtain a thin, uniform film of the photoresist. It is then brought in contact with a photomask that reproduces the desired pattern. The photoresist crosslinks in the parts exposed to high-intensity ultraviolet (UV) light while a chemical agent removes the covered photoresist. The negative design of the mask is now reproduced on the silicon master.* ***b*** *Soft lithography allows the fabrication of elastomeric moulds using a replica moulding technique. The PDMS is cast against the bas-relief pattern of the silicon master photoresist. After a thermal phase, the resulting substrate is peeled off, showing the 3D pattern of the original master. The microfluidic device is then generated by creating the needed features, e.g., the inlets, and bonding it to a PDMS or glass slab.* ***c*** *3D bioprinting constructs microfluidic devices using a fast and automated process. In the bioprinting nozzle-based approach, the bioink is extruded through a nozzle moved by a computer-controlled arm to create 3D shapes. Superior resolutions are obtained using optical-based approaches where laser exposure solidifies the bioink through a crosslinking reaction. Taken from (Cauli et al., 2023).*

Poly methyl methacrylate (PMMA) is an alternative material to PDMS that can be used to fabricate the microfluidic platforms. It is known for its optical transparency, mechanical strength, biocompatibility, and low permeability to small molecules, making it suitable for long-term culture and real-time imaging in microfluidic systems (Raman et al., 2024, Mishra et al., 2025). PMMA devices allow precise and cost-effective fabrication (Mishra et al., 2025).

However, PMMA exhibits some limitations. It is relatively low gas permeability and autofluorescence may interfere with oxygen exchange and high-sensitivity imaging, respectively (Cao et al., 2023).

Patient-derived cells can be directly cultured within the platform, providing a precise tool for investigating the biological mechanisms underlying cancer development and identifying the most suitable patient-specific drug therapies during clinical trials. (Caballero et al., 2020, Regmi et al., 2022). Additionally, GBM-on-a-chip platforms enhanced with biosensors provide a valuable tool for drug screening and personalised medicine. By continuously monitoring cellular responses to pharmacological agents, these biosensors can help determine optimal drug dosages, treatment regimens, and drug combinations that effectively target specific pathways or vulnerabilities within the glioblastoma TME. This dynamic and personalised approach to drug testing has the potential to improve the efficacy of therapeutic interventions and reduce the likelihood of drug resistance. (Xie et al., 2023a, Deng et al., 2023). The pressing need for patient-specific precision therapeutic strategies and tailored approaches for enhancing overall survival rates and the quality of life for the GBM patients (Xie et al., 2023b) **(Figure 1.55).**

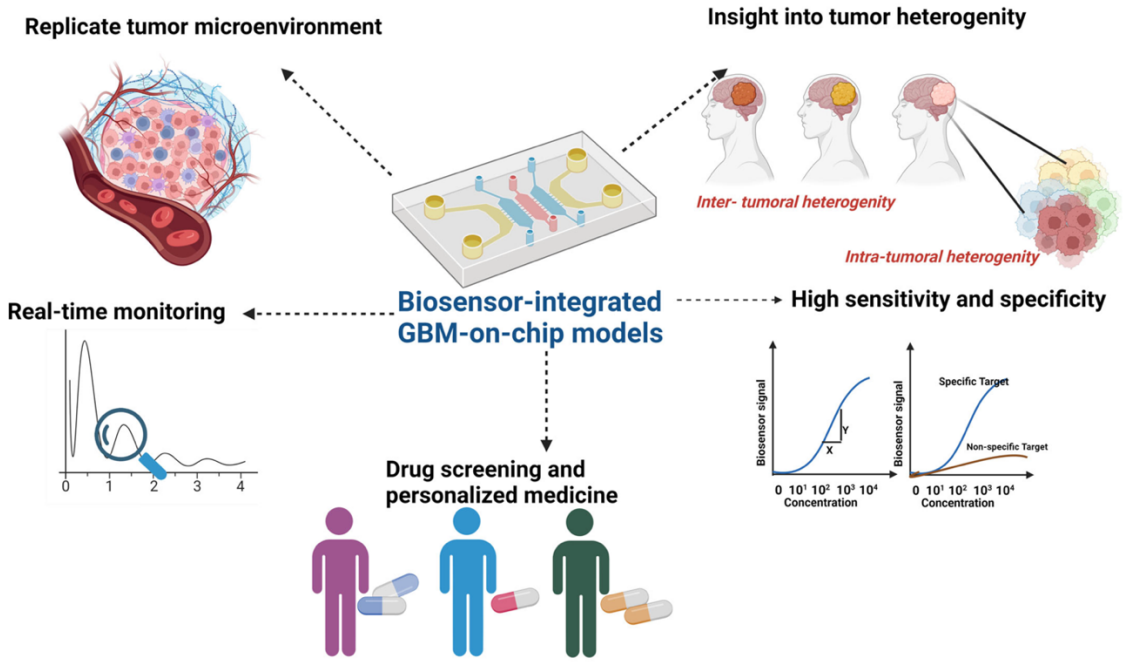

Figure 1.55: ***Integrated biosensors in GBM-on-chip models revolutionise glioblastoma research by enabling real-time monitoring of tumour dynamics and treatment responses.***
This schematic illustrates the multifaceted benefits of biosensor-integrated GBM-on-chip models, including the replication of tumour microenvironmental cues, real-time monitoring of biomarker expression and cellular responses, high sensitivity and specificity in biomarker detection, facilitation of drug screening and personalised medicine approaches, insights into tumour heterogeneity, and reduced reliance on animal models for preclinical studies. These advancements pave the way for an improved understanding of GBM biology and for developing more effective therapeutic strategies (created with Biorender).
Taken from (Thenuwara et al., 2024).

1.8.3 Limitation of Microfluidic Models

On one hand, Microfluidic platform versatility is a significant factor driving the adoption of the technology to develop reliable and robust organ mimicking models. On the other hand, integrating sensors can increase the complexity of these platforms, making them not easily accessible to those without the necessary expertise or facility (Cauli et al., 2023).

Overall, OoC microfluidic based systems are more challenging to offer higher throughput implementation than other 3D models, such as spheroids (Bassi et al., 2021).

PDMS is the most used material for producing microfluidic, has limitation of nonspecific absorption of small hydrophobic molecules, including certain drugs. Therefore, it is not ideal for drug testing (Shakeri et al., 2021, Mair et al., 2022, Sønstevold et al., 2023).

The small scale and complexity of microfluidic platforms make them vulnerable to minor factors like air bubbles, which can disrupt their operation by interfering with controls and features. Researchers have explored various methods to prevent bubble formation, offering insights into channel design and strategies for effectively eliminating bubbles (Pereiro et al., 2019, He et al., 2021, Zhao et al., 2022) **(Figure 1.56).**

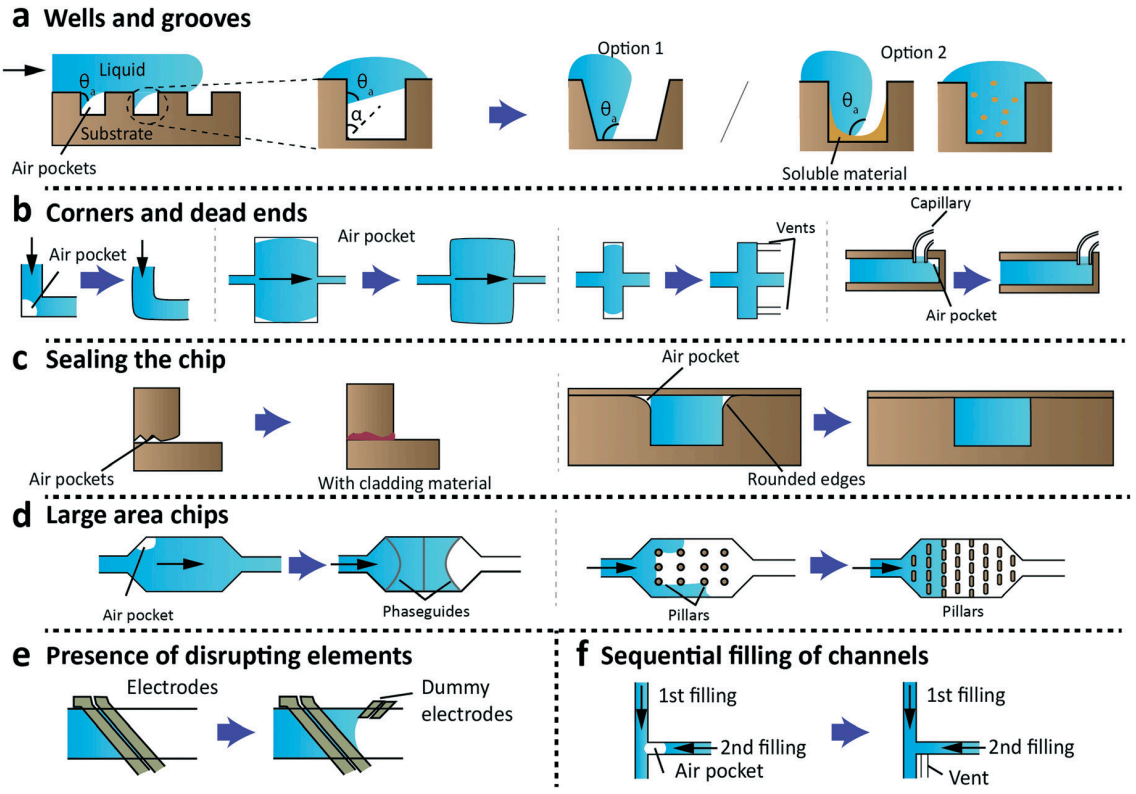

Figure 1.56: Examples of structures contributing to bubble formation on a chip.
(a) Microwells and grooves on a device substrate. (b) Corners, dead ends, and solutions through corner rounding, venting, and capillary location. (c) Increased reliability of chip sealing with the use of cladding materials and avoidance of rounded edges. (d) Difficulties filling chambers with a high width-to-height aspect ratio, helped by phase guides and adequate pillar geometry. (e) The presence of elements in channels, e.g. electrodes, disrupts front uniformity and is compensated by added channel features. (f) Bubble formation by non-synchronised liquid filling at junctions.
Taken from (Pereiro et al., 2019).

Users typically develop their own fabrication and cell culturing methods without standardised guidance. This results in microfluidic systems that vary in both technological and biological aspects. Consequently, this lack of standardisation hinders the transition from microscale results to potential macroscale applications (Ko et al., 2022) **(Figure 1.57).**

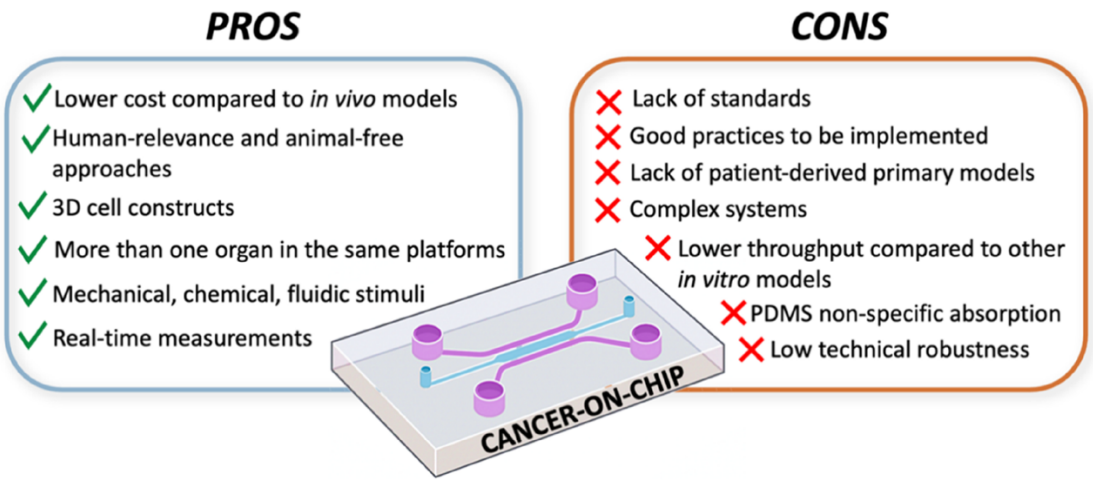

Figure 1.57: Summary of pros and cons of cancer-on-chips.
Many pros have been identified for cancer-on-chip technology compared to conventional in vitro and in vivo models. However, accepting cancer-on-chip as a preclinical tool has several drawbacks that must be solved.
Taken from (Cauli et al., 2023).

1.8.4A Examples of Specific Applications in Glioblastoma Research: BBB

Microfluidic models of BBB offer a unique opportunity to evaluate drug delivery systems. This complex barrier often impedes drug transport to the brain, posing a significant challenge in treating GBM, as mentioned in section 1.5. Microfluidic platforms enable researchers to assess how effectively drugs and delivery systems, such as nanoparticles, can cross this barrier. By providing a realistic representation of the BBB, these platforms aid in the development of innovative therapeutic strategies that can successfully overcome this obstacle and deliver essential treatments to the brain (Straehla et al., 2022, Zakharova et al., 2020, Noorani et al., 2021).

OoC systems that integrate Microfluidic BBB into GBM OoC setup to replicate the brain's distinct vascular characteristics and study drug transport dynamics across the BBB. By culturing brain endothelial cells within microfluidic devices with integrated perfusable channels, researchers can examine how BBB dysfunction affects GBM progression and assess innovative drug delivery methods for targeted therapy. These models offer valuable insights into the challenges of delivering therapeutic agents to GBM tumours and aid in developing more effective treatment strategies (Thenuwara et al., 2024).

In 2023, Shi and colleagues highlighted the urgent need for preclinical models that effectively incorporate the complexity of the tumour microenvironment and the BBB structure and function for glioma treatment. Since most anti-glioma drug candidates have difficulty permeating the BBB, developing such models is essential. The researchers developed an *in vitro* BBB-glioma microfluidic chip model to address this need. This model included primary human brain microvascular endothelial cells, pericytes, astrocytes, and glioma cells, successfully replicating the high barrier function characteristic of the human BBB and the glioma microenvironment (Shi et al., 2023b).

1.8.5B Examples of Specific Applications in Glioblastoma Research: chemotherapy efficacy using Temozolomide alone or in combination

Microfluidic platforms allow for the investigation of single-agent and combination therapies, providing insights into drug responses under conditions that closely resemble the *in vivo* tumour microenvironment.

In the case of TMZ, the first-line chemotherapy drug for GBM (Section 1.4.4), microfluidic models have been used to assess its impact on tumour cell invasion and programmed cell death. Samiei et al. created a multi-compartment microfluidic device to demonstrate TMZ-induced autophagy and apoptosis in GBM cells while reducing invasiveness (Samiei et al., 2020). Ozturk et al. employed a bioprinted microfluidic platform to examine the long-term effects of TMZ, revealing that some GBM cells can develop resistance and regain invasiveness even after prolonged treatment (Ozturk et al., 2020). Zhang et al. focused on the impact of TMZ on single-cell adhesion in GBM cells, highlighting the importance of considering cell adhesion in drug evaluations (Zhang et al., 2020c).

Beyond single-agent TMZ, microfluidic platforms have been instrumental in evaluating TMZ-based combination therapies. Akay et al. utilised a GBM-on-a-chip platform to assess the combined effect of TMZ and bevacizumab, demonstrating enhanced efficacy compared to TMZ alone (Akay et al., 2018b). Jie et al. developed a bionic intestine-liver-GBM system to evaluate the combined effect of irinotecan and TMZ, showing a marked improvement in efficacy compared to single-drug treatments (Jie et al., 2017).

These examples highlight the potential of microfluidic models in advancing our understanding of chemotherapy drug responses in GBM. By providing a more physiologically relevant platform for drug evaluation, these models can aid in developing personalised treatment strategies and identifying novel drug combinations that may improve patient outcomes.

1.8.6A Recent Advances: Biosensor Integration in Microfluidics

Incorporating biosensors into microfluidic systems marks a notable progression in glioblastoma research. These biosensors are capable of real-time detection and quantification of diverse biomarkers, including proteins, nucleic acids, and metabolites, within the microfluidic setting. This capability facilitates the ongoing monitoring of cellular reactions to pharmaceuticals, the discovery of potential diagnostic and prognostic biomarkers, and the evaluation of mechanisms related to drug resistance (Thenuwara et al., 2024, Cauli et al., 2023).

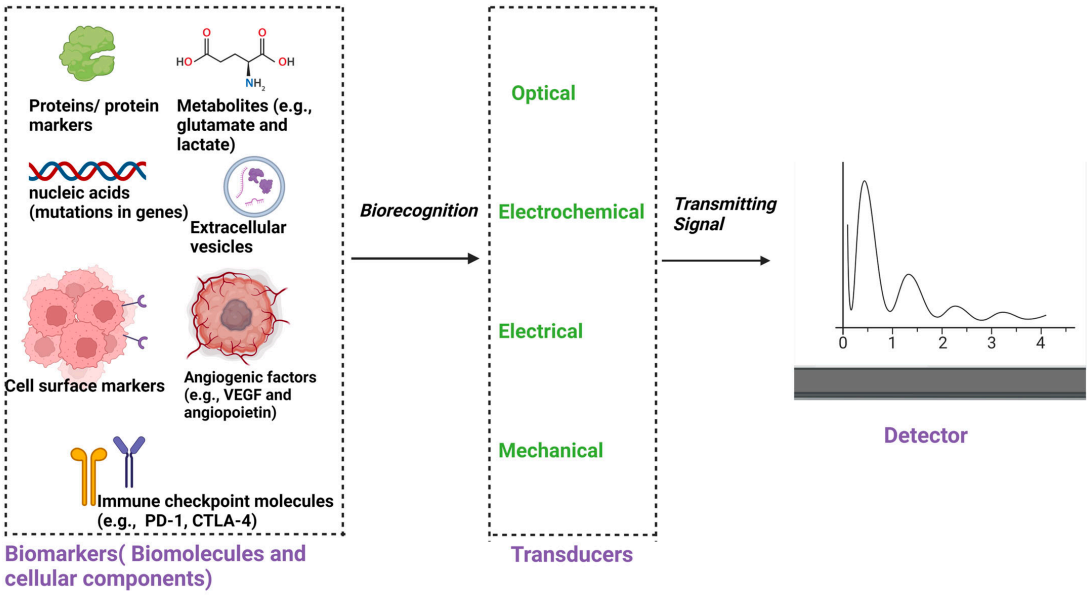

Figure 1.58 Biosensor detection of GBM biomarkers: sequential process.
The process by which biosensors detect biomarkers associated with GBM begins with recognising specific biomarkers present within the GBM microenvironment. These biomarkers include proteins, nucleic acids, metabolites, extracellular vesicles, cell surface markers, angiogenic factors, and immune checkpoint molecules. Following biorecognition, a signal is either generated or modulated, which subsequently undergoes transmission and detection by the biosensor system. This systematic sequence of events, involving biorecognition, signal transmission, and detection, facilitates identifying and quantifying GBM biomarkers. Ultimately, this process yields valuable insights into GBM tumour biology, aiding in assessing diagnosis, prognosis, and treatment response (created with Biorender).
Taken from (Thenuwara et al., 2024).

Depending on the transduction principle, various biosensing technologies, such as optical, electrochemical, and electrical biosensors, have demonstrated significant potential for cancer diagnosis. Evaluating cancer biomarkers and drug-resistant mutations in real time enables physicians to employ precision medicine, which may enhance patient survival rates. Different biosensing technologies, including optical, electrochemical, and electrical biosensors, hold significant promise for cancer diagnosis due to their real-time ability to detect cancer biomarkers and drug-resistant mutations. This capability supports precision medicine approaches, potentially improving patient survival. Optical biosensors utilise changes in optical properties for detection, while electrochemical biosensors convert biochemical activity into electrical signals using a system of three electrodes, each with specific functions (Saha et al., 2023, Vatankhahan et al., 2024) **(Figure 1.59).**

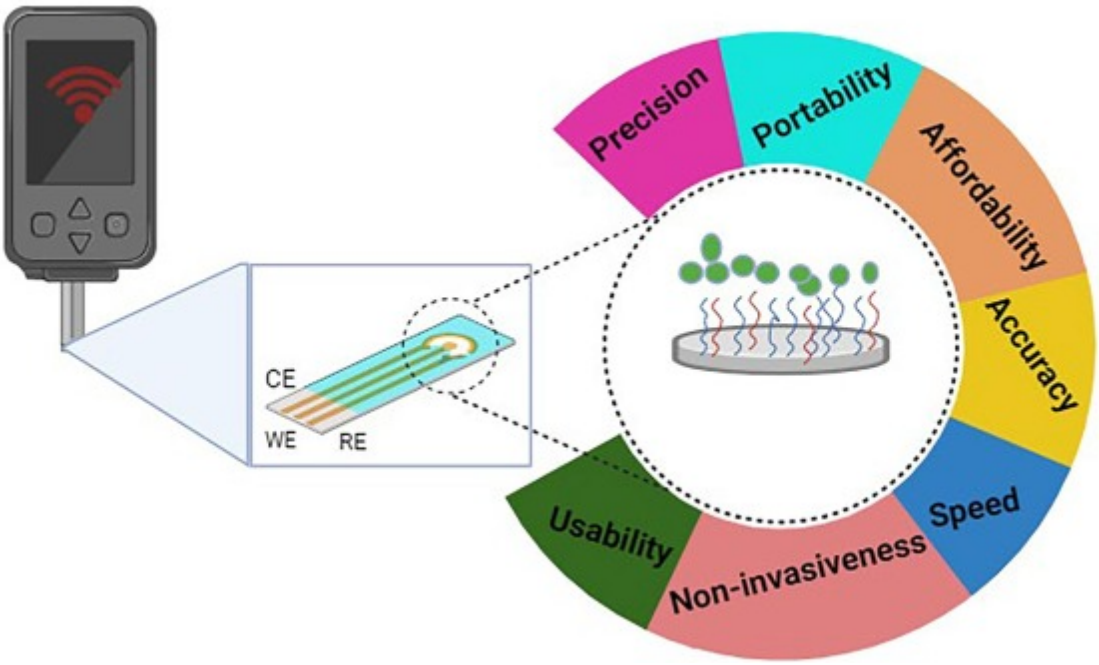

Figure 1.59: Key Features of the Electrochemical Biosensor.
This biosensor exhibits several advantageous characteristics: (A) Precision, ensuring high-quality results; (B) Portability, due to its compact size, allowing easy integration into wearable devices; (C) Affordability, enabled by low-cost mass production; (D) Speed, providing quick results for timely decision-making; (E) Sensitivity, through its selective and sensitive nature; (F) Usability, with a user-friendly design that can be used even by minimally trained individuals; (G) Non-invasiveness, due to its non-invasive nature; and (H) Accuracy, enhanced by precise signal detection. Taken from (Vatankhahan et al., 2024).

1.8.7B. Recent Advances: 3D bioprinting microfluidic-based platforms

In addition to microfluidics, bioprinting can be utilised to create sophisticated GBM-on-a-chip models. This technology enables the simultaneous 3D printing of specific components, such as different cell types and ECM-like materials, directly onto a substrate compatible with cells. This substrate can be used to develop vascular networks and replicate the heterogeneous TME (DePalma et al., 2022).

Moreover, researchers can obtain cells from GBM patients to create *in vitro* tumour-on-a-chip models that mimic the biochemical and biophysical characteristics of GBM. These models replicate the structure and genetics of their *in vivo* counterparts. Recently, GBM models bioprinted using a unique combination of cells and bioinks have been increasingly utilised to explore the biological mechanisms of GBM and conduct preclinical studies on GBM therapies. For instance, a GBM tumour was bioprinted within a hydrogel system containing macrophages using extrusion-based bioprinting to create a bionic GBM tumour microenvironment. This model is used to study how infiltrating immune cells influence GBM cell behaviour and drug responses (Xie et al., 2023b, Tang et al., 2020).

Conclusion

Microfluidic technology has revolutionised GBM research by providing a more physiologically relevant and versatile platform for studying tumour biology, drug screening, and personalised medicine. By overcoming the limitations of traditional cell cultures, microfluidic models hold great promise for accelerating the development of effective GBM therapies and ultimately improving patient outcomes.

2 Aims and Objectives

Overarching Aim

To identify the cytokine profile released by GBM tissue, maintained in a novel microfluidic device, and to identify altered patterns in response to current (temozolomide) and emerging (arginine methylation inhibitors) drugs; evaluating potentially diagnostic or prognostic value.

It is hypothesised that GBM biopsies treated with drugs will firstly have an altered effluent cytokine profile with time on microfluidic device and secondly, that this profile will alter when tissue is treated with drugs.

Specific Objectives:

1. To optimize a simple screening method for detection of cytokines in GBM effluents using a Proteome Profiler 105 cytokine antibody array. This will involve determining the optimal sample incubation times, effluent pre-treatment, and detection methods to ensure accurate and reliable quantification of cytokines
2. It is planned initially to collect effluent at days 2, 4, 8 and 12 days when appropriate to study cytokine release over time alone, or TMZ and arginine methylation inhibitor.
3. To verify a selected cohort of cytokines using enzyme-linked immunosorbent assay across all time point to give a quantitative assessment of cytokine levels.

3 Materials and Methods

3.1 Patient tissue samples preparation

Sample recruitment starts when the accident and emergency department in Hull University Teaching Hospital (HUTH) NHS Trust refers potential candidates to the neurosurgery on-call registrar. All suspected GBM cases are reviewed in the multidisciplinary meetings in the presence of neurosurgery, neuroradiology, neuro-oncology, and neuropathology consultants. Patients selected for surgery due to history, clinical examination and imaging suggesting a GBM tumour, will be seen in a clinic or hospital where informed consent for surgery is obtained. Patients are seen before surgery and the patient information sheet for the research project is explained. After answering any raised concerns, patients sign written permission to use a part of their resected tumour for the research project. Ethics approval was gained from the Yorkshire & The Humber - South Yorkshire Research Ethics Committee (Research Ethics Committee reference: 13/YH/0238 Amendment 5,01 February 2021, IRAS project ID: 131630). A copy of the ethical consent remains in the patient's file. Copies of the ethical committee approval, patient information sheet and consent forms are available (Appendix 7.1, 7.2 and 7.3, respectively).

Patients included in the study are aged 18 years or above and undergoing planned tumour resection where a sample of brain tumour tissue is expected to be taken by the surgeon while the principal diagnosis is suspected of being GBM. During surgery, the neurosurgery consultant makes their best judgment to choose a non-necrotic part of the resected GBM tumour. They depend on 5 ALA, high magnification operating microscope, brain lab guide and their clinical experience **(Figure 3.1)**.

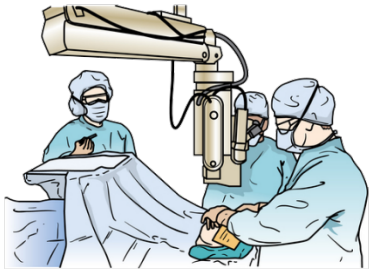

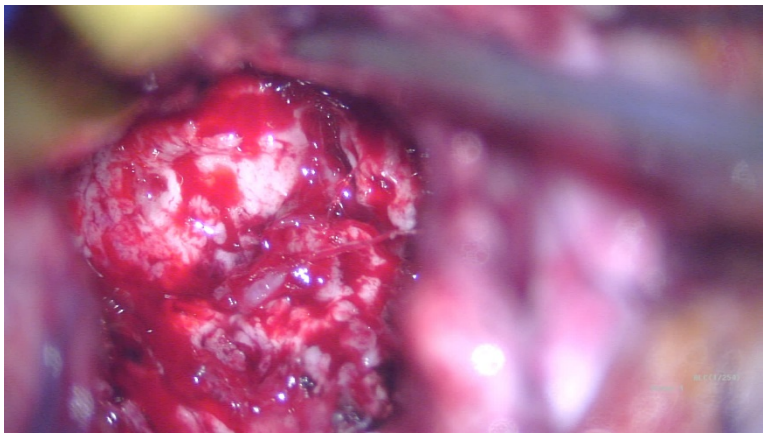

The Intraoperative image under the operating microscope

The Intraoperative image under the blue light microscope using 5-ALA

Figure 3.1: GBM tumour appearance intraoperatively

During surgery, tumour samples were freshly taken and placed in a 15 ml centrifuge tube filled with complete Dulbecco's Modified Eagle Medium (DMEM). Complete DMEM contains 10% (v/v) Foetal bovine serum (FBS; Sigma) and antibiotic/antimycotic solution (100 units/mL penicillin / 0.1 mg/mL streptomycin, 0.25 µg/mL amphotericin B (Sigma).

Samples varied in size ranging from 0.25 g to 2.5 g. The tube containing tissue was stored in a tissue transportation box and taken to the Hull University laboratory and processing started within 60 minutes. In the laboratory, the sample was dissected into multiple small sections (avoiding any blood clots), with an average weight of 20 mg (+/- 0.4 mg) **(Figure 3.2)**. Each tissue section was inserted into a microfluidic chip **(Figure 3.3)**. All tissue handling was conducted within a Class II Biosafety cabinet to ensure the sterility of the tissue.

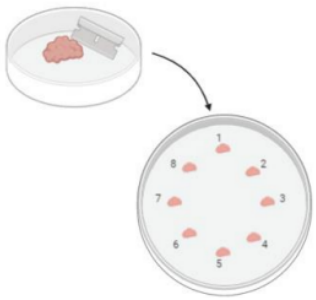

Figure 3.2: Sample dissection
Samples were around 3 mm in diameter (an approximate volume of 14 mm^3)

3.2 Microfluidic Chip setup

The microfluidic chip used in this study was fabricated in-house from three layers of PMMA, laser-cut and solvent-bonded using chloroform (Akhil et al., 2016). The final device measured approximately 30 mm in length and comprised three main compartments: an inlet chamber (12 × 15 mm), a semipermeable central barrier ("frit") measuring 3 × 15 mm with 37 pores of 100 µm diameter, and an outlet chamber (15 × 15 mm). A circular pocket of 4 mm diameter in the inlet chamber was designed to hold the micro-dissected tumour biopsy (~3 mm diameter) (Barry et al., 2023b) **(Figure 3.3)**

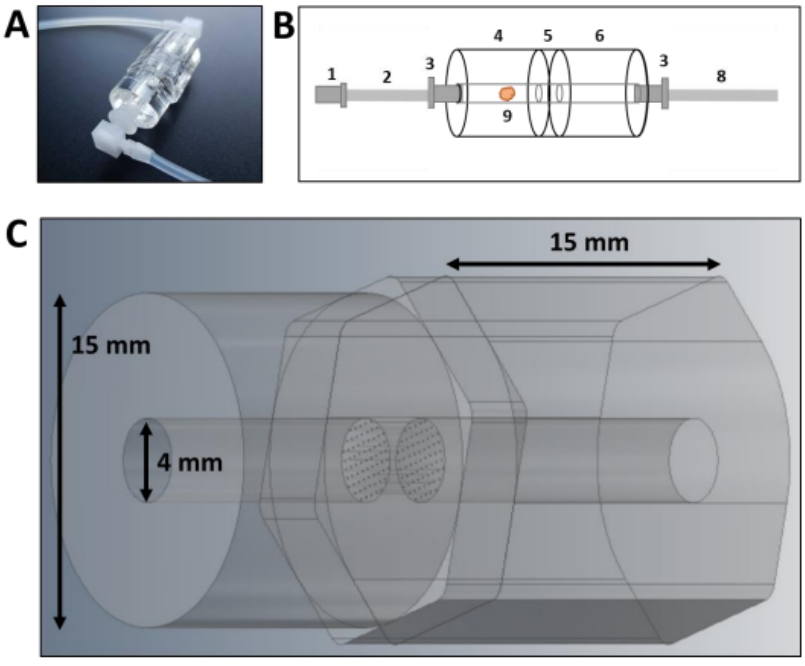

Figure 3.3: The miniature chip used in microfluidic experiments.

(A)Photograph of the microfluidic device used in patient sample incubations (B) schematic of the microfluidic device: 1- female connector 2- inlet tubing 3- male connector 4- inlet chamber 5- perforated chamber 6- outlet chamber 8- outlet tubing 9- tissue sample (C) 3D rendering of the microfluidic device including measurements.

Flow connections were established using 1/32″ Tygon 66 silicone tubing (Cole-Parmer), attached to Luer connectors (Ibidi). Assembled chips were sterilised with 70% ethanol, rinsed, and connected to syringes containing either control or treatment media. The syringe, tubing, and chip were mounted onto a Harvard Apparatus PHD-ULTRA syringe pump and maintained at 37 °C in a humidified incubator **(Figure 3.4)**.

A

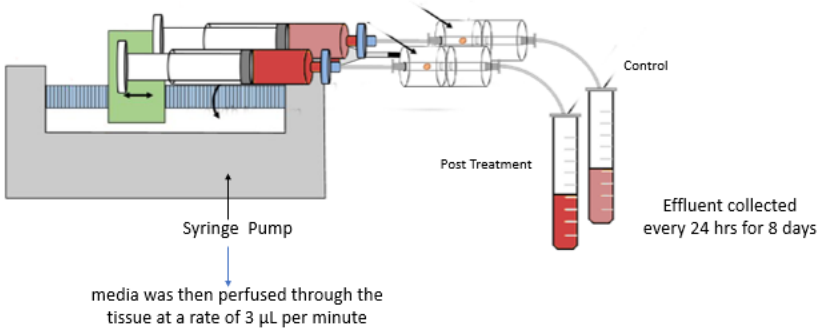

B

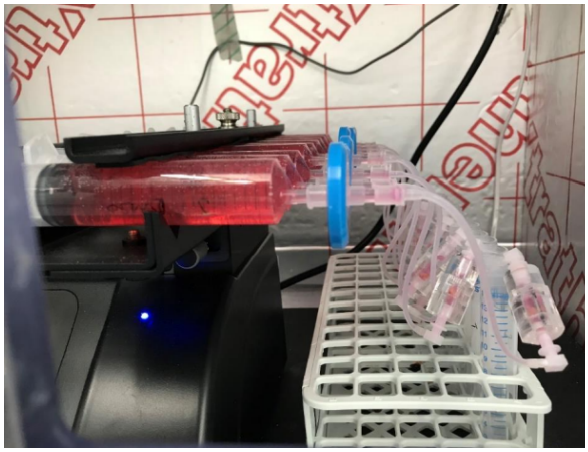

Figure 3.4: Microfluidic setup.
(A) schematic image. (B) Photograph.

Media was perfused through the device at a **constant flow rate of 3 µL min⁻¹**, a rate chosen to mimic physiological interstitial flow and maintain tissue viability. The **flow velocity (u)** within the chamber was estimated using the relationship:

$$u = \frac{Q}{A}$$

where Q is the volumetric flow rate and A the cross-sectional area of the chamber. Based on the 4 mm channel diameter, this corresponded to a mean velocity of approximately **2.6×10^{-6} m s⁻¹**.

To assess flow behaviour, the **Reynolds number (Re)** was calculated using:

$$Re = \frac{\rho u d}{\mu}$$

where ρ is the density of the medium, d the channel diameter, and μ the dynamic viscosity. The calculated value (**Re ≈ 0.005**) confirmed that the flow was **laminar**, as expected in microfluidic systems. This stable flow regime ensures even nutrient distribution and minimal shear stress on the tissue sample.

Two chips were used for control conditions and perfused with Dulbecco's Modified Eagle Medium (DMEM) containing 0.02% (v/v) DMSO, equivalent to the solvent concentration in treated samples. Two additional chips received treatment media containing **1 µM GSK3368715 + 10 µM TMZ**. Perfusion was maintained for either 8 or 12 days, during which **effluent was collected every 24 hours**. Samples from three time points (8-day model) or four time points (12-day model) were used for downstream cytokine analysis by proteome profiler array or ELISA. Effluent was stored at –80 °C until analysis **(Figure 3.5)**.

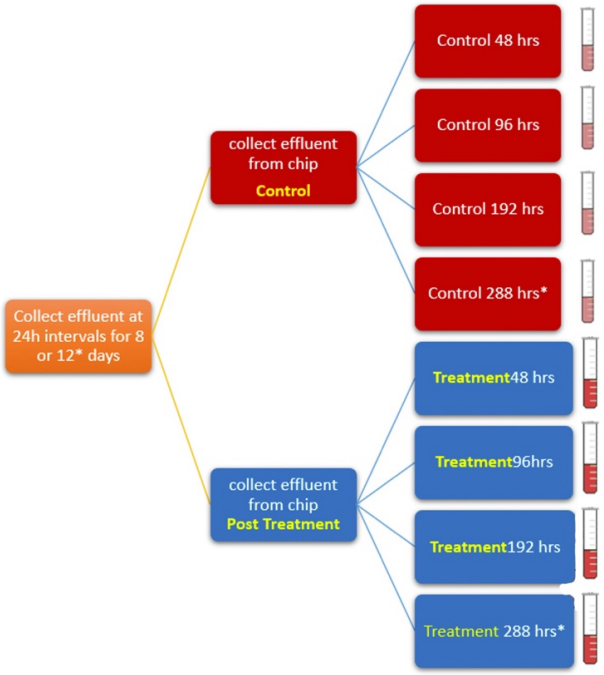

Figure 3.5: The chosen time points for effluent analysis.
**Only in the twelve-day model.*

3.3 Proteome Profiler

3.3.1 Proteome profiler principle

The Proteome Profiler Human Extra Large (XL) Cytokine Array Kit (R&D systems) is a membrane-based sandwich immunoassay for the parallel determination of the relative levels of selected human cytokines and chemokines. It has been validated by the company for analyte detection in cell culture supernatants, cell lysates, tissue lysates, serum, plasma, human milk and saliva. The effluent from the microfluidic devices is a form of cell supernatant and thus is suitable for analysis. See Appendix 7.4, for list of 105 cytokines included in this array.

Determining the expression of multiple cytokines in a single sample can be expensive, time-consuming, and require specialised equipment. Using a multiplex antibody array to detect multiple cytokines in a single sample is cost- and time-effective as compared with multiple western blots. In addition, less sample is required in comparison with 10-12 western blots.

Each Profiler Array Kit has 4 membranes with the 105 capture antibodies spotted in duplicate in a known array that bind to their specific target proteins if present in the sample (Figure 3.6). Captured proteins are then detected with biotinylated detection antibodies and visualised using chemiluminescent detection reagents. The signal produced is proportional to the amount of analyte bound.

3.3.2 Proteome Profiler Protocol Steps:

3.3.2.1 Proteome Profiler Kit Contents

Rectangular 4-Well multi-dish 4 Human XL Cytokine Array nitrocellulose membranes spotted with 105 different antibodies to human cytokines, Array Buffer 4, Array Buffer 6, Chemi Reagent 1, Chemi Reagent 2, Detection Antibody Cocktail, Human XL Cytokine Array, Streptavidin-Horseradish Peroxidase (HRP), Transparency Overlay Template, Wash Buffer Concentrate (25X). The kits were stored in a refrigerator at 2–8 °C and were used before the manufacturer's expiry date.

3.3.2.2 Reagent Preparation

All reagents were brought to room temperature before use. Lab coats and gloves were used to protect kit reagents from contamination. A flat-tipped tweezer was used to remove Human XL Cytokine Array membrane from the protective sheets. The membranes were handled with gloved hands and flat-tipped tweezers only. The detection Antibody Cocktail was reconstituted in 200 µL of distilled water. Each Array Buffer 4 and 6 was mixed well before use because they may contain a precipitate. Four ml of Array Buffer 4 was added to each 8 ml of Array Buffer 6 to make a buffer 4/6 mixture. Wash Buffer bottles were warmed to room temperature until crystals were dissolved entirely. Forty mL of Wash Buffer Concentrate was added to 960 mL of distilled water to prepare 1000 ml of Wash Buffer. Chemi Reagents 1 and 2 were mixed in equal volumes within 15 minutes of use and protected from light. One ml of the resultant mixture is required per membrane. Streptavidin-HRP was diluted in Array Buffer 6 immediately before use and according to the vial label for dilution factor.

3.3.2.3 Array Procedure

All reagents were prepared as directed in the previous section. Effluent tubes were brought from the – 80oC freezer to be at room temperature. Two ml of Array Buffer 6 was pipetted into each well

of the 4-well multi-dish. Array Buffer 6 serves as a block buffer. Each membrane was placed in a separate well. The number on the membrane was facing upward. Upon contact with Array Buffer 6, the blue dye from the spots disappeared, but the capture antibodies remained in their specific locations. The 4-well multi-dish was incubated for 1 hour on a rocking platform shaker. The 4-Well multi-dish was oriented so that each membrane rocked end to end in its well. While the arrays were blocking, effluent fluid samples were prepared by diluting the desired quantity to a final volume of 1.5 mL with Array Buffer 6. Seven hundred µL of each sample (Effluent) was mixed with 800 µL of buffer 6 to make 1.5 ml of the mixture per each sample. Array Buffer 6 was aspirated from the wells of the 4-Well Multi-dish. Each prepared mixture was added to one of the wells in the dish. The lid was placed on the 4-Well Multi-dish. It was incubated overnight at 2-8°C on a rocking platform shaker to ensure optimal sensitivity. Carefully each membrane was removed and placed into individual plastic containers with 20 mL of Wash Buffer. The 4-Well multi-dish was rinsed with deionised water and dried thoroughly. Each membrane was washed with Wash Buffer for 10 minutes on a rocking platform shaker three times in total. For each array, 30 µL of Detection Antibody Cocktail was added to 1.5 mL of Buffer 4/6 mixture. The diluted Detection Antibody Cocktail (1.5 mL) was pipetted into the 4-Well Multi-dish. Carefully each array was removed from its wash container. Excess Wash Buffer was allowed to drain from the array. The array was returned to the 4-Well Multi-dish containing the diluted Detection Antibody Cocktail and covered with the lid. Then it was incubated for 1 hour on a rocking platform shaker. Each array was washed three times, as described before (Systems, 2024).

Two ml of Streptavidin-HRP was pipetted into each well of the 4-Well Multi-dish. Each membrane was removed from its wash container and excess wash Buffer was drained. The membrane was returned to the 4-Well Multi-dish containing the Streptavidin-HRP then was incubated for 30 minutes at room temperature on a rocking platform shaker. Each array was washed three times, as described before. The remaining steps were completed without interruption. Each membrane was finally removed from its wash container and excess Buffer was allowed to drain from the membrane by blotting the lower edge onto paper towels. Each membrane was placed on the bottom sheet of the plastic sheet protector with the identification number facing up. One ml of the prepared Chemi Reagent Mix was pipetted evenly onto each membrane, covering the whole membrane surface. Any air bubbles were gently smoothed out, and Chemi Reagent Mix was spread evenly to all corners of each membrane and was incubated for one minute. The membranes were placed with the identification numbers facing up in the plastic containers (Systems, 2024). Membranes were visualised using the ChemiDoc™ Imaging system (Bio-Rad), and the length of exposure was monitored to ensure optimal image quality and to prevent over-saturation by maintaining exposure time within the linear range **(Figure 3.6).**

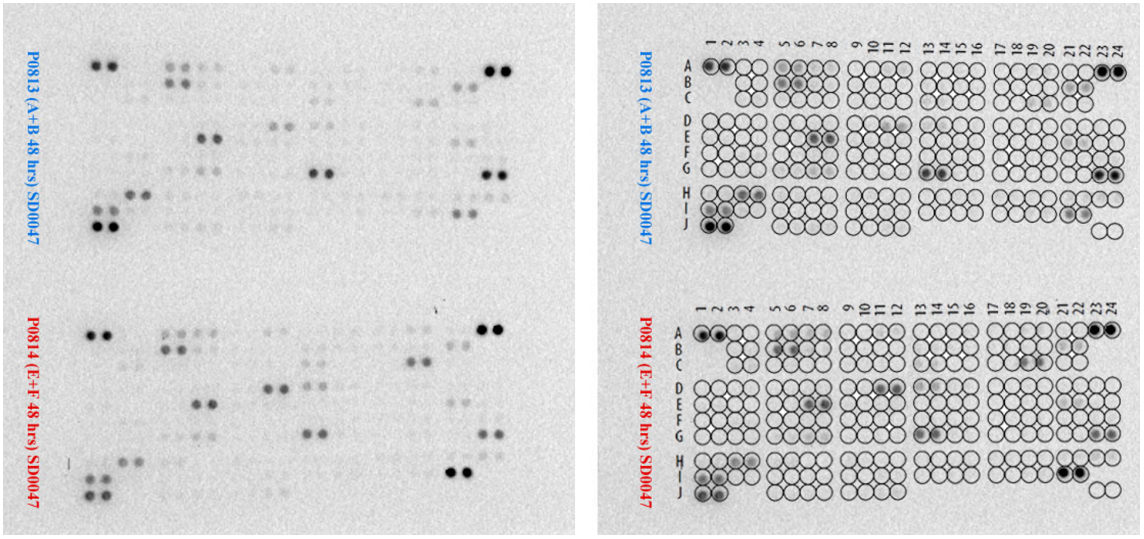

Figure 3.6: Applied example of two membranes visualised by ChemiDoc.

3.3.2.4 Data Analysis

The positive signals were seen on the developed image, which QuickSpots Software can identify. QuickSpots is an OptimEyes-powered solution that enables users to process Proteome Profiler™ antibody arrays from R&D Systems accurately (IdealEyes, 2024). It generates a detailed analysis of the results provided by the antibody arrays **(Figure 3.7)**.

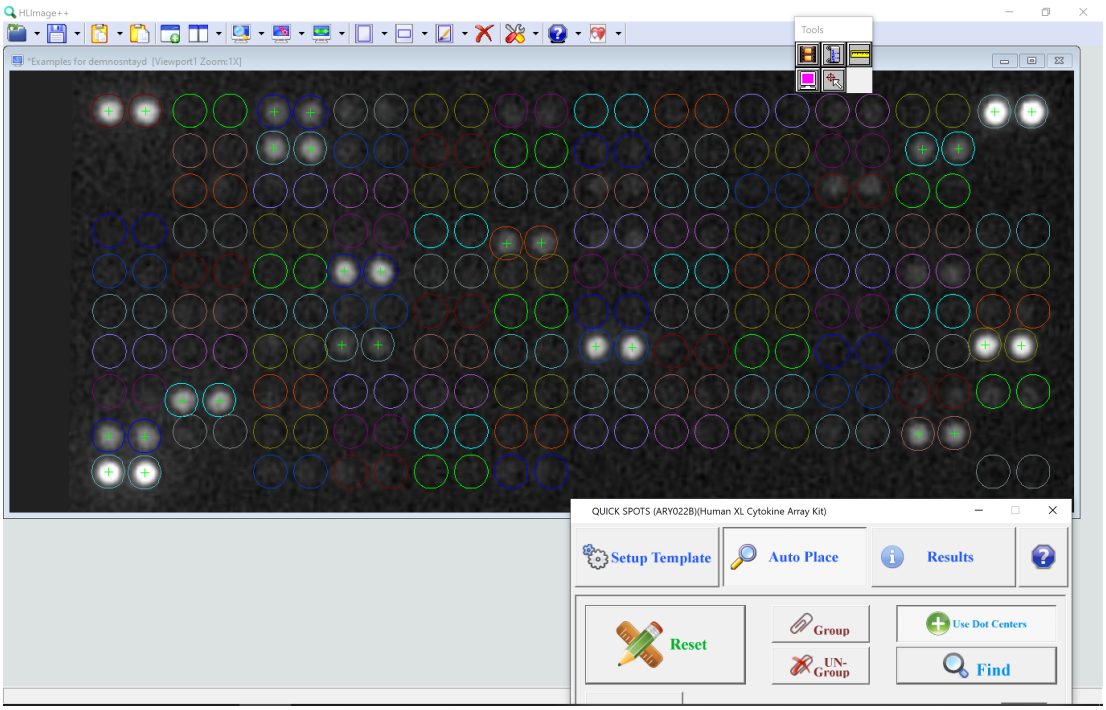

Figure 3.7: Applied example analysis of relative density value of cytokines detected in one membrane by QuickSpots Software.

The average signal (pixel density) of the pair of duplicate spots representing each cytokine was calculated. The signal from the negative control spots was used as a background value which was subtracted from the averaged value for each spot. Finally, each cytokine's relative value was calculated as a percentage of the average value of three duplicate positive controls. The relative values of each cytokine ranged from 0 to 1. A cut-off value of 5% above the average pixel density of the duplicate negative control was used. Any cytokine value below that cut-off value was considered zero.

3.4 ELISA

3.4.1 Reagents required for individual assays

Each kit contained a specific set of paired antibodies (capture and detection) for a specific human cytokine. The provided standard is used to create a 2-fold serial dilution series as advised by the manufacturer's protocol using reagent diluent **(Table 3.1)**. Section 2.4.4 explains how the absorbance of the known standards is used to calculate the cytokine concentration in the effluent samples. The accurate preparation of the standard dilution series is paramount for reliable concentrations of the samples. Solutions were prepared guided by the DuoSet Ancillary Reagent Kit (R&D Systems, DY008) and in house formulations as detailed in Appendix 7.5.

Table 3.1: Concentration ranges of standards for each cytokine assay.

Cytokine studied	Concentration Range for Serial Dilution (pg/mL)
IL-8	31.2 – 2000
IL-6	9.38 – 600
VEGF	31.2 – 2000
Angiopoietin-2	93.8 – 6000
CHI3L1	31.2 – 2000
Serpin E1	312 – 20,000
MMP9	31.2-2000

picograms per millilitre (pg/mL)

3.4.2 ELISA protocol

Sandwich ELISAs for IL-8, IL-6, VEGF, Angiopoietin-2, CHI3L1, Serine protease inhibitor E1 (Serpin E1) and MMP9 (R&D Systems) were conducted to quantify the released cytokine in the effluents collected from previous microfluidic experiments. The manufacturer's protocol was followed throughout.

Each well was washed twice with the prepared wash buffer using the ASYS Atlantis microplate washer (Biochrom, G021101) after each step unless stated otherwise. A 96-well maxisorp ELISA plate (Thermo-scientific) was coated with 100 µL of the capture antibody and incubated overnight at room temperature. In the morning the antibody was removed and wells were blocked with 300 µL reagent diluent at room temperature and left for at least 1 hour. The standard or sample (100 µL) was pipetted in duplicate on the plate in a standardised manner **(Figure 3.8)**. The plate was then covered and incubated for 2 hrs at room temperature; antigens present within the standard/sample became bound by the immobilised capture antibody on the surface of the wells. After washing the biotinylated detection antibody (100 µL) was added to each well and incubated for 2 hrs at room temperature. This detection antibody binds to any antigen immobilised specifically on the well surface. Streptavidin-HRP (100 µL) was added to each well and incubated for 20 minutes at room temperature, avoiding direct sunlight. Substrate solution (100 µL) was finally added to each well and incubated for 20 minutes, avoiding direct sunlight, to become cleaved by the bound enzyme resulting in a yellow colour. The wells were not washed as previously described instead the stop solution (1N sulfuric acid; 50 µL) is added to each well which stops the reaction, turning the sample from blue to yellow. The end colour is directly proportional to the amount of cytokine in the sample (Nemzek et al., 2001). The colour was immediately measured using a spectrophotometer plate reader (Synergy HTX Microplate Reader (BioTek)) at 450-540 nm. The above process was repeated on effluents from each patient biopsy (Technologies, 2024) **(Figure 3.9).**

Plate X MMP9												
	1	2	3	4	5	6	7	8	9	10	11	12
A	1000 standard	1000 standard	SD050 AB 192 hrs	SD050 AB 192 hrs	SD056 JI 96 hrs	SD056 JI 96 hrs	SD057 AB 288 hrs	SD057 AB 288 hrs	SD060 AB 288 hrs	SD060 AB 288 hrs	SD066 BH48 hrs	SD066 BH 48 hrs
B	500 standard	500 standard	SD050 EF 48 hrs	SD050 EF 48 hrs	SD056 JI 192 hrs	SD056 JI 192 hrs	SD057 JI 288 hrs	SD057 JI 288 hrs	SD060 JI 288 hrs	SD060 JI 288 hrs	SD066 BH 96 hrs	SD066 BH 96 hrs
C	250 standard	250 standard	SD050 EF 96 hrs	SD050 EF 96 hrs	SD057 AB 48 hrs	SD057 AB 48 hrs	SD060 AB 48 hrs	SD060 AB 48 hrs	SD065 AB 48 hrs	SD065 AB 48 hrs	SD066 BH 192 hrs	SD066 BH 192 hrs
D	125 standard	125 standard	SD050 EF 192 hrs	SD050 EF 192 hrs	SD057 AB 96 hrs	SD057 AB 96 hrs	SD060 AB 96 hrs	SD060 AB 96 hrs	SD065 AB 96 hrs	SD065 AB 96 hrs	SD066 EF 48 hrs	SD066 EF 48 hrs
E	62.5 standard	62.5 standard	SD056 AB 48 hrs	SD056 AB 48 hrs	SD057 AB 192 hrs	SD057 AB 192hrs	SD060 AB 192 hrs	SD060 AB 192 hrs	SD065 AB 192 hrs	SD065 AB 192 hrs	SD066 EF 192 hrs	SD066 EF 192 hrs
F	31.3 standard	31.3 standard	SD056 AB 96 hrs	SD056 AB 96 hrs	SD057 JI48 hrs	SD057 JI 48 hrs	SD060 JI 48 hrs	SD060 JI 48 hrs	SD065 JI 48 hrs	SD065 JI 48 hrs	SD066 EF 48 hrs	SD066 EF 48 hrs
G	15.6 standard	15.6 standard	SD056 AB 192 hrs	SD056 AB 192 hrs	SD057 JI 96 hrs	SD057 JI 96 hrs	SD060 JI 96 hrs	SD060 JI 96 hrs	SD065 JI 96 hrs	SD065 JI 96 hrs	backup	backup
H	Negative control*	Negative control*	SD056 JI 48 hrs	SD056 JI 48 hrs	SD057 JI 192hrs	SD057 JI 192 hrs	SD060 JI 192 hrs	SD060 JI 192 hrs	SD065 JI 192 hrs	SD065 JI 192 hrs	DMEM media	DMEM media

Figure 3.8: Example layout of ELISA plate for standards and samples.
2-fold dilution series of standards prepared for cytokine according to manufacturer's protocol using reagent diluent as the diluting liquid. The highest concentration (i.e. 1000 pg/mL) in the top wells of the plate (indicated in orange), followed by the lowest concentration (i.e. 15.6 pg/mL). Reagent diluent controls the standards in the bottom two wells (indicated in pink). Columns 3 to 12 correspond to different samples with different time points and ID numbers. Each sample is run in duplicate, starting from 96 hrs to 192 hrs and sometimes to 288hrs as well. The last two wells contained only DMSO in the media, as a control.

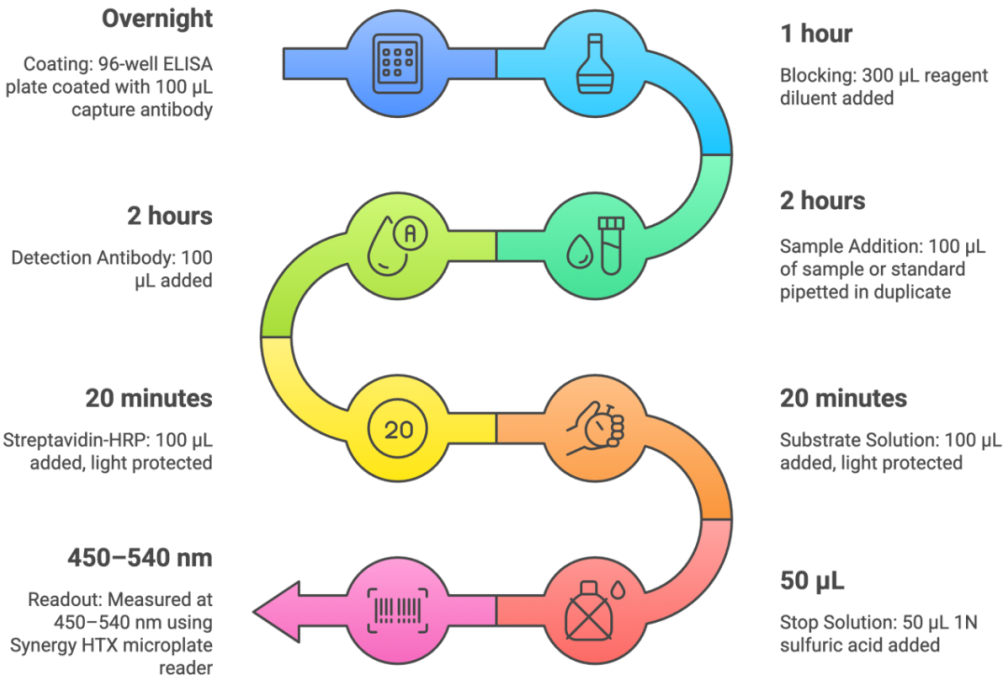

Figure 3.9: ELISA Protocol Timeline.

3.4.3 Concentration calculation and data analysis

An applied example of how the concentration of the cytokine (in this case, MMP9) **(Figure 3.10).**

MMP9 1	1	2	3	4	5	6	7	8	9	10	11	12	
A	1.551	1.337	0.208	0.205	0.079	0.08	0.233	0.296	0.009	0.004	0.029	0.035	dual wavelength
B	0.266	0.196	0.381	0.364	0.088	0.084	0.165	0.129	0.19	0.166	0.016	0.022	dual wavelength
C	0.138	0.096	0.484	0.436	0.184	0.224	0.258	0.219	0.15	0.155	0.024	0.031	dual wavelength
D	0.062	0.043	0.314	0.317	0.152	0.18	0.238	0.218	0.156	0.123	0.066	0.092	dual wavelength
E	0.035	0.016	0.263	0.288	0.171	0.161	0.206	0.15	0.136	0.125	0.076	0.085	dual wavelength
F	0.017	0.015	0.089	0.126	0.14	0.168	0.252	0.192	0.096	0.071	0.051	0.072	dual wavelength
G	0.015	0.004	0.052	0.074	0.239	0.237	0.336	0.32	0.064	0.055	0.021	0.094	dual wavelength
H	0.001	-0	0.122	0.229	0.162	0.121	0.26	0.286	0.118	0.123	0.016	0.02	dual wavelength

Figure 3.10: MPP 9 plate as an example.

First, all the data generated by the spectrophotometer was inputted into Microsoft Excel, and

the average of the duplicate absorbances for the standards and reagent diluent was calculated. The average of the reagent diluent was subtracted from each average absorbance for all standards. The average standard absorbance minus the average reagent diluent absorbance is then Log10 transformed as is the known concentration of the standard using the 10 =Log10 (number) equation.

The log-transformed absorbances (Y-axis) and concentrations (X-axis) are then plotted, and a line of best fit is drawn. The closer the R-squared (R^2) number of the standard curve is to 1.00, the more reliable the data generated based on the standard curve; it also demonstrates an accurate pipetting technique **(Figure 3.11).**

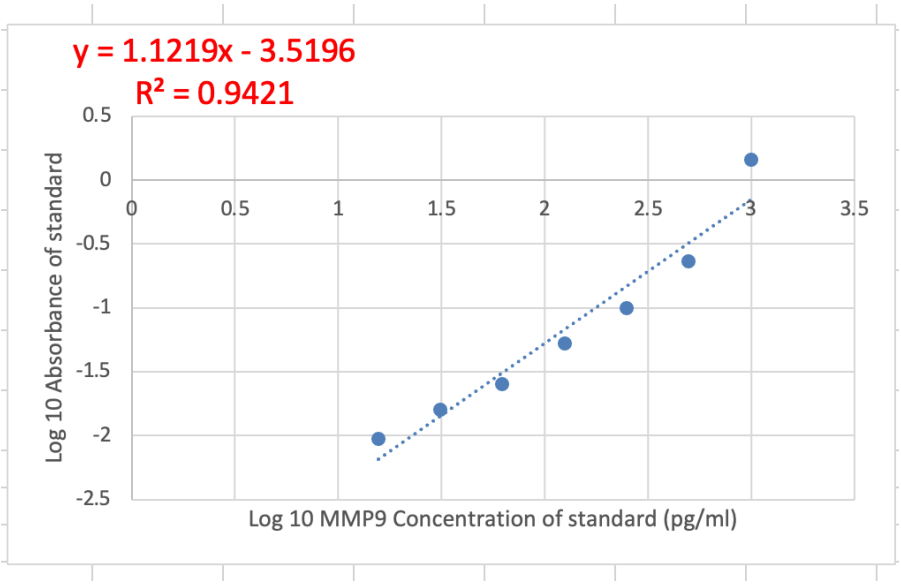

Figure 3.11: Generation of a standard curve using known concentrations of provided standard.

The standard curve was generated using the data. The Log10 transformed data is reported on the X axis and logged absorbance on the Y axis.
The average absorbance of the duplicate results for each effluent was calculated for each patient sample. The average absorbance of the reagent diluent is then subtracted from the data.

The next step was to inverse log (=10^(number)) all the data generated after using the trend equation; this gave the cytokine concentration in the samples. All cytokine concentrations for each time point recorded into a Microsoft Excel spreadsheet, which was then used for statistical analysis.

3.5 Statistical analysis:

The data analysis was performed in R version 4.3.0, using RStudio 2023.03.0 Build 386. Graphs were built using ggplot2 (Kassambara, 2020). The raw cytokine data was square-root normalised and range-scaled using MetaboAnalystR v4.0.0 R package (Pang et al., 2020). No outliers were detected when combining a visual method (samples outside the 95% confidence interval) with a Henze-Zirkler's test from the MVN v5.9 R package (Korkmaz et al., 2014).

The normality and equal variance of the cytokine expression were verified with Shapiro-Wilk's and Levene's tests, respectively, using the rstatix v0.7.2 R package (Kassambara, 2023). The multicollinearity was tested using the corrplot v0.92 R package (Wei and Simko, 2021). The dispersion of the multivariate data was compared with the permutest function on the Euclidean distance obtained from the vegdist and betadisper functions from the vegan v2.6-4 R package (Oksanen et al., 2022).

The multivariate analysis was conducted via non-parametric Permutational Analyses of Variance (PERMANOVAs) using the vegan R package v2.6-4 (Oksanen et al., 2020). Pairwise comparisons between groups of interest were computed using the pairwiseAdonis v0.4.1 R package (Martinez Arbizu, 2017).

The linear model was fitted using the Linear Models for Microarray Data (Limma) v3.56.2 R package (Ritchie et al., 2015). The effect of treatment on the cytokine expression was visualised using the EnhancedVolcano v1.18.0 R package (Blighe et al., 2020).

4 Results

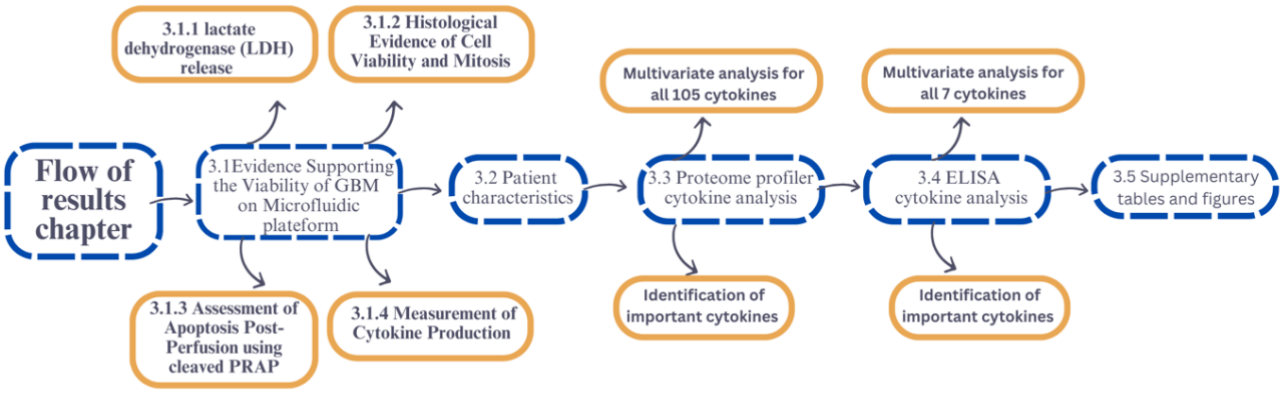

Figure 4.1: Diagrammatic overview of the results chapter.

4.1 Evidence Supporting the Viability of GBM Tissue Maintained in the Microfluidic Perfusion Device for 8-12 Days

Before analysing the cytokines detected in the effluents from the microfluidic perfusion device, it was essential to first establish that GBM tissue remains viable whilst on the chip, for the periods of perfusion used in this study. The initial viability testing procedures described below were primarily performed by PhD student Antonia Barry. All the cytokine measurements were carried out independently by the author. The aim was to provide robust evidence that GBM tissues could be maintained alive within the device for up to 12 days, setting the foundation for detailed analyses in the following sections.

4.1.1 Cellular viability assessed by lactate dehydrogenase (LDH) release at 8 days and 12 days on chip

To evaluate whether GBM tissues remain viable in the microfluidic perfusion device LDH colorimetric assays were performed on effluents collected every 24 hrs from the chips; the flow rate was 3 µL/min based on previous work (Barry et al., 2023a). The assay measures the absorbance at 495 nm which is directly proportional to LDH present in the effluent sample. LDH is an enzyme released upon cellular stress or damage, and its a ctivity in the effluent serves as a marker for cellular viability and stress levels (Kaja et al., 2017).

For the 8-day analysis, 12 different samples were used. Initial LDH levels were high most likely due to stress from tissue extraction and handling but decreased significantly over the first 48 hrs, stabilising at low levels (0.021–0.025 AU mg^{-1}) for the remaining days, as has been seen by others in the laboratory (Olubajo et al., 2020, Hattersley et al., 2008). Statistical analysis showed no significant fluctuations in LDH activity over the 8-day period ($F = 1.11$, $df = 7$, $p = 0.37$), indicating minimal cellular stress and suggesting that the tissues remained viable in the perfusion device. After the 8 day period, the samples were lysed to quantify any retained LDH, which was a significantly larger amount compared to baseline expression.

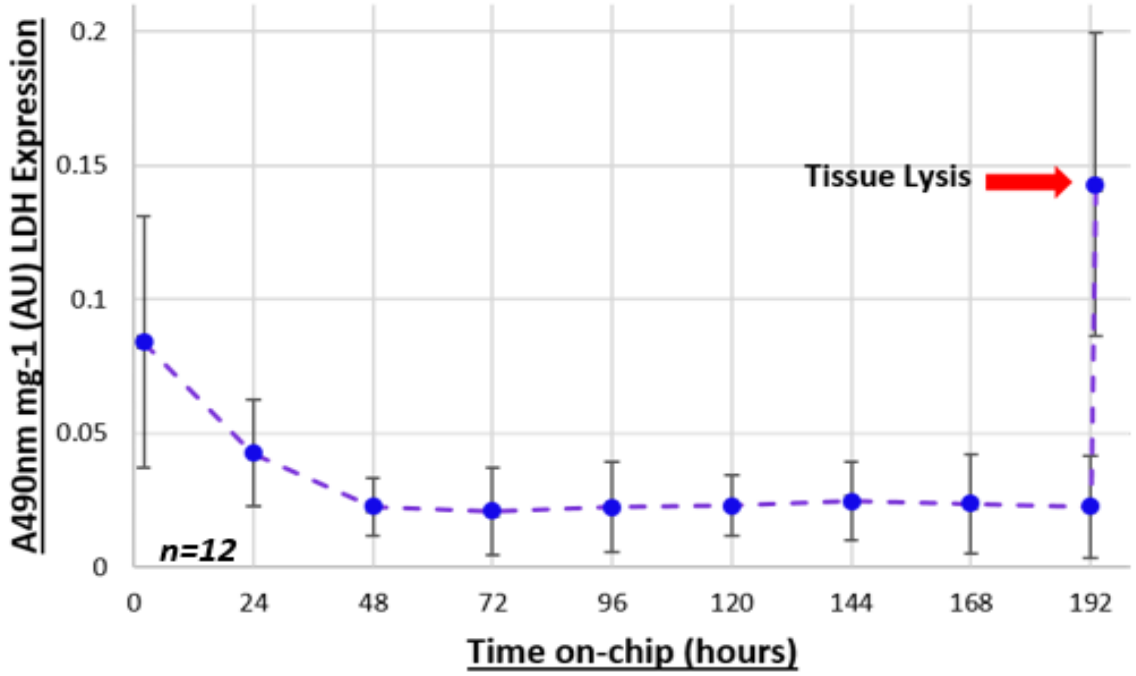

Figure 4.2: Lactate dehydrogenase expression of GBM (n=12) over 8 days.
LDH activity was measured in the effluent, collected every 24 hrs over 8 days, via *absorbance at 490 nm* (A_{490nm}) (n = *12, LDH activity decreased to 0.023 AU (absorbance units)/mg ± 0.011 at 48 hrs and fluctuated minimally (*F = *1.11, df = 7,* p = *0.37) between 0.021–0.025 AU* mg^{-1} *for the remaining 6 days. One-way ANOVA performed using R 4.2.0 after data transformation. After 8 days, tissues were lysed to assess remaining LDH within the biopsies (*n= *10), (indicated by red arrow) (*t= *-6.64, df = 97,* p = 1.80×10^{-9}*, compared to baseline expression).*

Similarly, for the 12-day analysis, but with a smaller sample size (n=4), LDH activity decreased over the first 48 hrs and then remained stable (0.023–0.032 AU mg^{-1}) over the full period of time. Again, no significant fluctuations were observed (F = 1.38, df = 11, p = 0.22) **(Figure 4.3).**

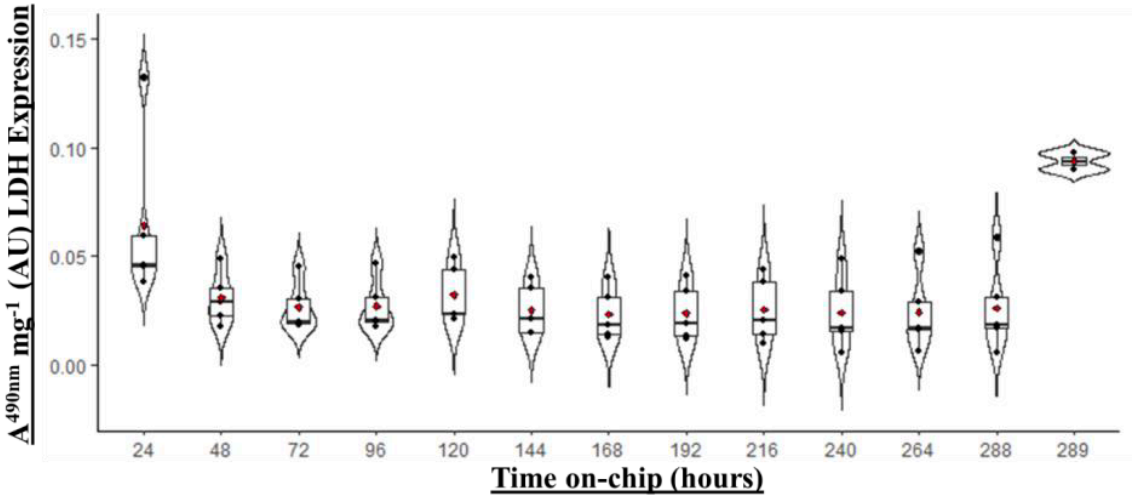

Figure 4.3: Lactate Dehydrogenase expression in GBM tissue (n=4), over 12 days
LDH activity was measured in the effluent, collected every 24 hrs over 12 days, via absorbance at 490 nm (A_{490nm}). LDH activity decreased to 0.031 AU (absorbance units)/mg ± 0.012 at 48 hrs and fluctuated (F =1.38, df =11, p =0.22) between 0.023–0.032 AU mg^{-1} for the remaining 10 days, One-way ANOVA performed using R 4.2.0 after data transformation. After 12 days, tissues were lysed to assess remaining LDH within the biopsies, leading to a peak reading at 0.094 AU mg^{-1} ± 0.005 (indicated by red arrow) (t = -7.08, df =55, p =2.81 × 10^{-9}, compared to baseline expression).

Both 8- and 12-day LDH measurement showed not only that GBM tissue remained in low stress level during the time in the chip but also at the end of incubation period significant amount LDH enzyme retained inside the cells. That confirming the viability of the GBM tissue while on the chip throughout the 8 to12 day period in the chip.

4.1.2. Histological Evidence of Cell Viability and Mitosis

Haematoxylin and eosin (H&E) staining was performed on both pre- and post-perfused GBM tissues after 8 and 12 days to assess cellular morphology and the presence of mitotic figures, indicative of cell division and viability **(Figure 4.4)**.

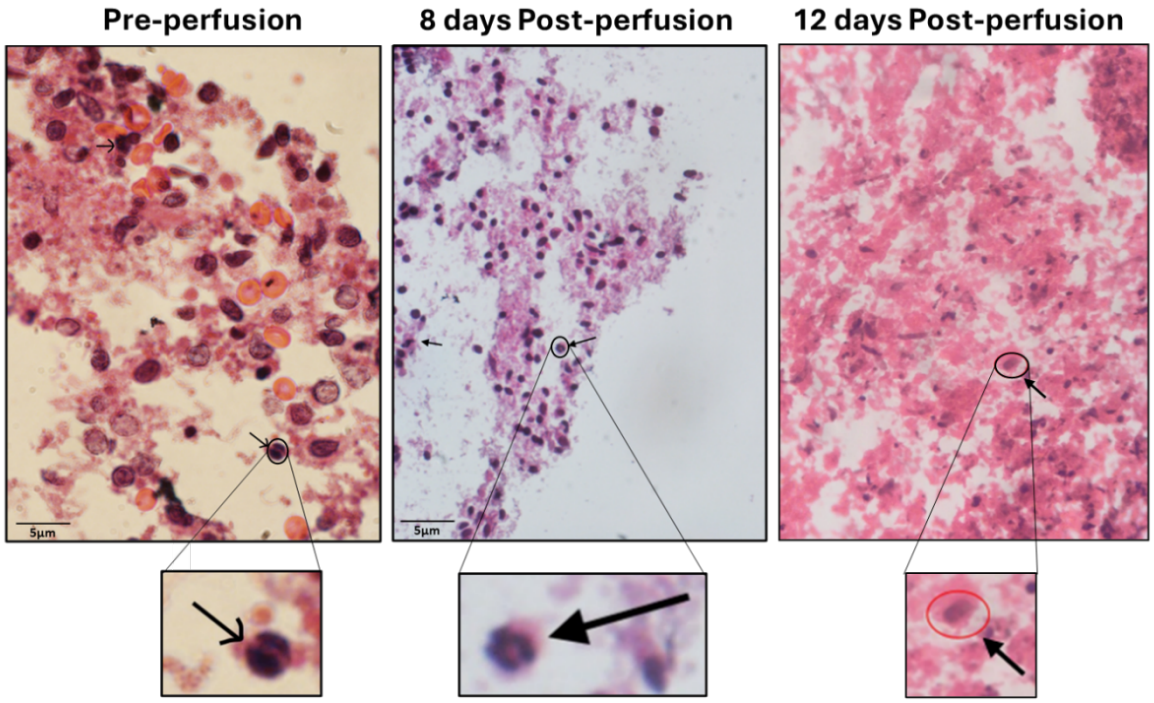

Figure 4.4: Representative H&E staining of GBM tissue pre-, 8 days and 12 days post-perfusion. *Haematoxylin (purple) stains nuclear aspects of cells and eosin stain highlights cytosolic cellular fractions. Arrows on both images highlight mitotic figures, with inset showing magnified images. Images at x40 magnification were taken on an Olympus IX71 inverted fluorescence microscope using CellSens software 1.18 and assessed together with Consultant Neuropathologist Dr. Ian Scott.*

Microscopic examination revealed mitotic figures in both pre- and post-perfused tissues, demonstrating that GBM cells remained capable of division after perfusion on a device. The presence of uneven mitosis and chromatin distribution further confirmed that these were tumour cells actively proliferating, rather than non-tumour contaminant cells. This histological evidence supports the conclusion that GBM tissues maintained their viability and proliferative capacity within the perfusion device over the experimental period (Barry et al., 2023b).

4.1.3 Assessment of Apoptosis Post-Perfusion using cleaved Poly ADP-ribose polymerase (PARP)

To ascertain whether the perfusion process itself induced apoptosis in GBM tissues, expression of the apoptotic markers cleaved PARP and Annexin V were compared between pre and post-perfused tissues at both 8-day and 12-day time points. Cleaved PARP expression was measured using immunohistochemistry with automated counting by Cell Profiler pipeline which was validated by technical replicates and manual counting (Bressenot et al., 2009) **(Figure 4.5)**.

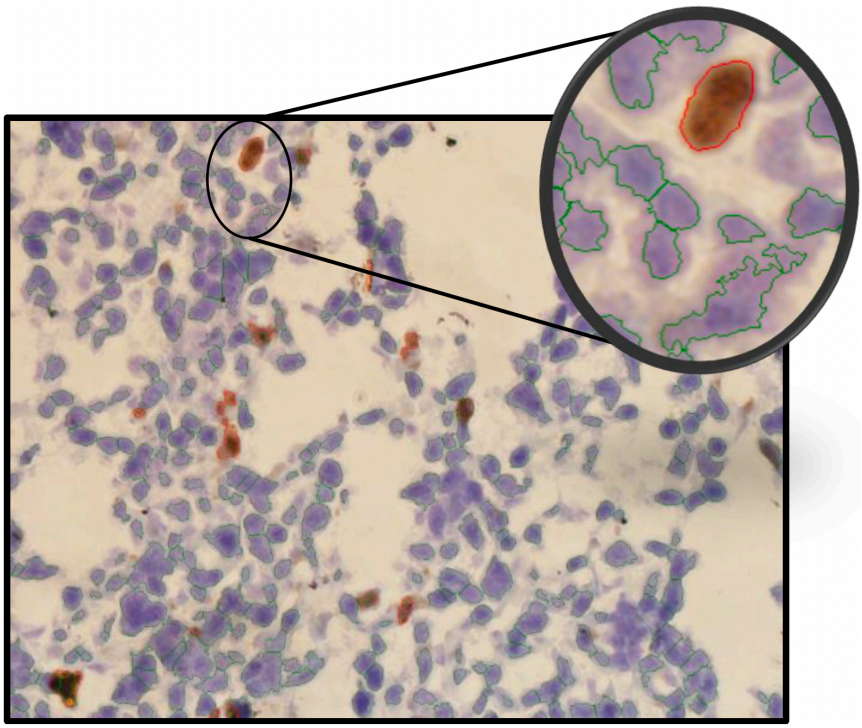

Figure 4.5: Detection of cleaved PARP-positive cells using Cell Profiler on IHC-stained GBM tissue.
Cell Profiler output image, haematoxylin stains cell nuclei blue, whilst 2'2'-diaminobenzidine (DAB) stains cleaved PARP expressing cells brown. Images at x40 magnification were taken on an Olympus IX71 inverted fluorescence microscope using Cell Sens software 1.18. Green outlines highlight blue haematoxylin-stained cells, which do not appear to be expressing the protein for which is being probed. Red outlines highlight brown DAB-stained cells, which do appear to be expressing the protein of interest.

For cleaved PARP, no statistically significant difference was observed between the two tissues at 8 days (mean pre-: 0.61 ± 0.47; post-perfusion: 1 ± 0.73; $p = 0.151$) or 12 days (mean pre-: 0.82 ± 0.78; post-perfusion: 1 ± 0.48; $p = 0.71$). Similarly, Annexin V staining showed no significant changes in apoptosis between pre- and post-perfused tissues at 8 days (mean pre-: 0.99 ± 0.58; post-perfusion: 1 ± 0.39; $p = 0.95$).

These results indicate that the microfluidic perfusion device did not induce apoptosis in the GBM tissues over the duration of the experiments, further supporting tissue viability.

4.1.4 Measurement of Cytokine Production from GBM Tissue on Microfluidic Devices over time.

An important piece of evidence for the viability of GBM tissue on the microfluidic devices is the continuous detection of cytokines secreted into the effluents at time points up to 12 days. Using proteome profiler and ELISA assays, it was observed that the GBM tissues consistently produced and released a variety of cytokines throughout the entire period they were on the chip (Please see Chapter 2 Materials and Methods). This sustained cytokine production strongly suggests that the tissues remained metabolically active and functional, capable of synthesising new cytokines over the duration of the experiment (Xie et al., 2023b). Detailed figures and tables showing cytokines detected using proteome profiler and ELISA assays are presented in section 4.3 Proteome profiler cytokine analysis and 4.4 ELISA cytokine analysis.

Conclusion

The combination of biochemical assays (LDH activity), histological analysis (H&E staining and IHC for apoptotic markers), cytokine proteome profiling and ELISA assays provides evidence that GBM tissues can be maintained in a viable state within the novel microfluidic perfusion device for at least 12 days. The tissues exhibited low cellular stress, active cell division, minimal apoptosis, and stable cytokine secretion profiles, confirming the device's effectiveness in preserving GBM tissue viability *ex vivo*. This establishes the perfusion device as a valuable platform for extended studies on GBM biology and therapeutic testing in the author’s hands.

4.2 Patient characteristics

Thirteen glioblastoma patients were included in this study, with varying ages, genders, MGMT status, and survival outcomes **(Figure 4.6)** and **(Table 4.1)**.

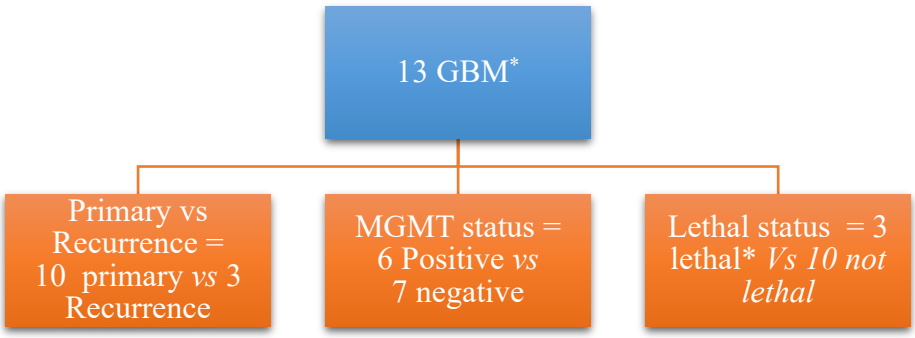

Figure 4.6: ***Classification of 13 Glioblastoma Patients Based on Tumour Status, MGM Promoter Methylation Status, and Survival Outcome***
**Lethality is scored positive if patient died within 6 months of their operation date*

Table 4.1: Clinical and Demographic Characteristics of the 13 Glioblastoma Patients Analysed.

	ID	Sex	Age	Primary /Recurrence status	MGMT status	Lethal = survival less 6 months
1	SD0043	male	56	primary	negative	Not lethal
2	SD0044b	male	67	recurrent	positive	Not lethal
3	SD0045	male	75	primary	positive	lethal
4	SD0046	male	67	recurrent	negative	lethal
5	SD0047	female	50	primary	negative	Not lethal
6	SD0048	male	71	primary	negative	Lethal
7	SD0050	male	72	recurrent	negative	Not lethal
8	SD0056	female	74	primary	negative	Not lethal
9	SD0057	female	73	primary	positive	lethal
10	SD0060	male	67	primary	positive	Not lethal
11	SD0065	male	58	primary	positive	Not lethal
12	SD0066	male	58	primary	negative	Not lethal
13	SD0067	male	76	primary	positive	Not lethal

4.3 Proteome profiler cytokine analysis

To investigate the cytokine profiles associated with glioblastoma and treatment effects, effluents from treated and control biopsies at multiple time points were initially analysed using a proteome profiler assay covering 105 cytokines to assess a large panel of cancer-related molecules (see Appendix 7.4). Results were analysed in two ways: the major body of work was studied at four time points: 48, 96, and 192 hrs, as a complete data set existed (n=13), and secondly the data at 288 hrs was analysed for the 3 patients for which full data were available (n=3) **(Figure 4.7).**

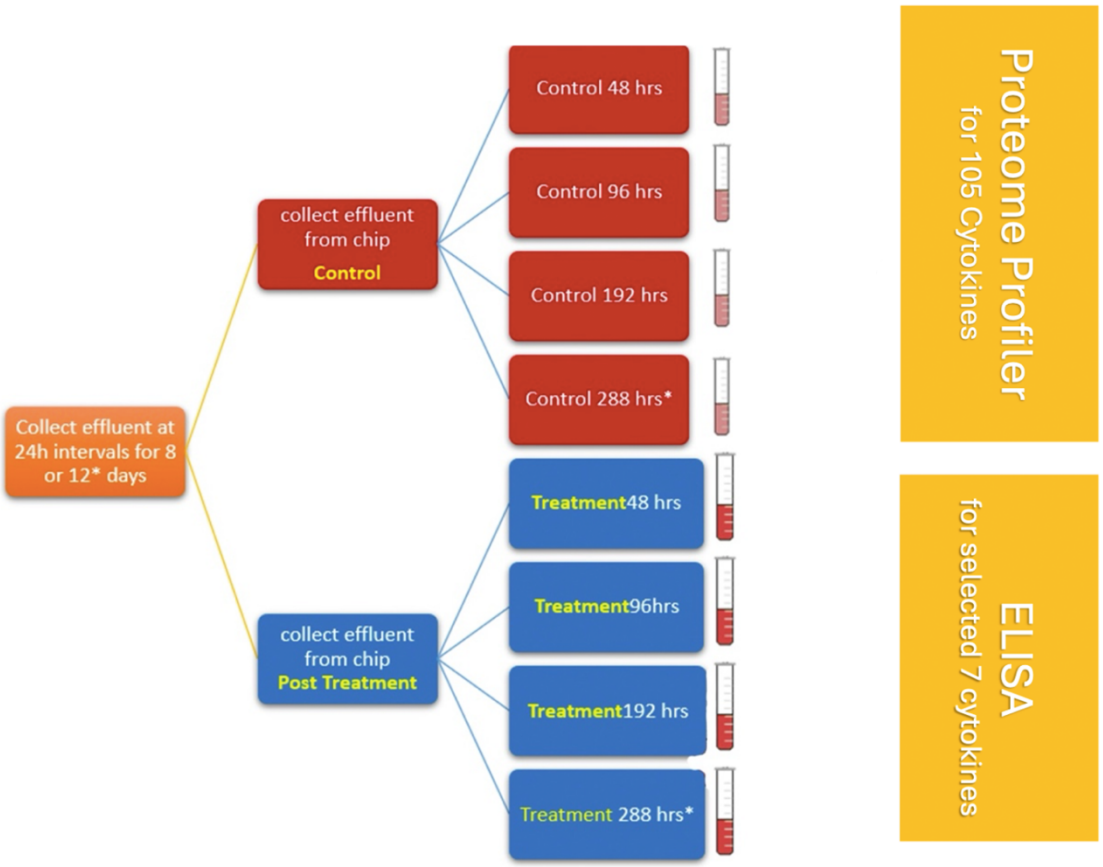

Figure 4.7: Experimental Timeline for Effluent Collection from Control and Treated GBM Biopsies

**Only 3 samples (SD0057, SD0060 and SD0067) were analysed up to 288 hrs (12 days).*

4.3.1 Methods:

Given the complexity of the data generated and multiple time points, advice was taken from a biostatician Dr. Lauric Feugere. A list of models with the different variables (Treatment, Time) and covariates (Patient, Age, Gender, MGMT status, Survival at 6 months, Recurrence status) were obtained and compared using the make_model and fit_model functions, respectively, within the AICcPermanova v0.0.2 R package (Corcoran, 2023). To identify any cytokines with differences between the treated and control biopsies, two methods were combined: a Partial Least Square Discriminant Analysis (PLS-DA) and moderated t-test model. First, the PLS-DA identified the cytokines that contributed the most to the discrimination between treated and control biopsies using the mixOmics v6.24.0 R package (Rohart et al., 2017, Welham et al., 2012). However, since PLS-DA tends to overfit the data, this analysis was combined with a linear model comparing the treated and control biopsies with covariate adjustment identified from the Corrected Akaike Information Criterion (AICc) model selection method that will be explained below in further details.

4.3.2 Data Structure:

To investigate the impact of the treatment on cytokine expression, it was crucial to first examine the structure and distribution of the cytokine dataset derived from the proteome profiler assay. Understanding the data's characteristics ensured that the most appropriate statistical methods for analysis could be selected. This preliminary assessment focused on identifying any data skewness due to zero expression values and detecting outliers that might unduly influence the results. By addressing these aspects, the reliability of subsequent multivariate analyses will be enhanced, thereby ensuring that the findings accurately reflect the biological effects of the treatment.

The data were scaled and normalised using MetaboAnalyst R, which made them more suitable for subsequent statistical analyses. Next, the dataset was screened for the presence of outliers using the Mahalanobis distance (Pang et al., 2020, Pang et al., 2024, Chong and Xia, 2018). Given that there were more than 100 response variables, the outliers were first screened using the two components of spectral decomposition. This statistical detection of outliers was combined with a visual inspection using the 95% confidence interval of the principal component analysis. This showed that there were no outliers that were both outside of the 95% confidence interval and significant outliers according to the Henze-Zirkler's test on the Mahalanobis Distance. The resulting dataset contains 78 effluent samples, representing the total numbers of controlled and treated sample for each 13 patients across the three time points (48, 96, 192 hrs). (78=13 patients X 2 (control and treated group) X 3 (three time points)) **(Figure 4.8).**

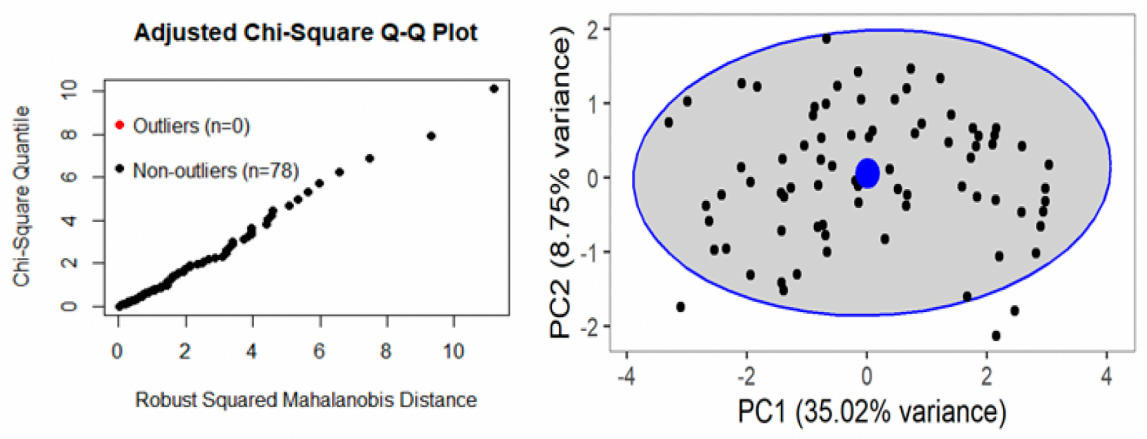

Figure 4.8: ***Detection of outliers.***
Left: detection of outliers using the statistical method from a Henze-Zirkler's test on the Mahalanobis Distance. Right: visual method showing the 95% confidence interval (ellipse) around the centroid (large blue point).

4.3.3 Multivariate analysis for all cytokines:

The multivariate analysis was conducted using data from all 105 cytokines. Before performing the analysis, key statistical assumptions were assessed to determine the suitability of the chosen approach.

4.3.3.1 Assumption Assessment

One key requirement for multivariate analysis is that response variables should be independent. However, this assumption is likely to be violated in this dataset because many cytokines are biologically related biomarkers. A correlation matrix confirms significant correlations between many cytokines, demonstrating interdependence. Additionally, **Figure 4.9** illustrates the presence of multicollinearity, as the histogram of p-values from correlation tests shows that most cytokines are significantly correlated ($p < 0.05$, indicated by the green line).

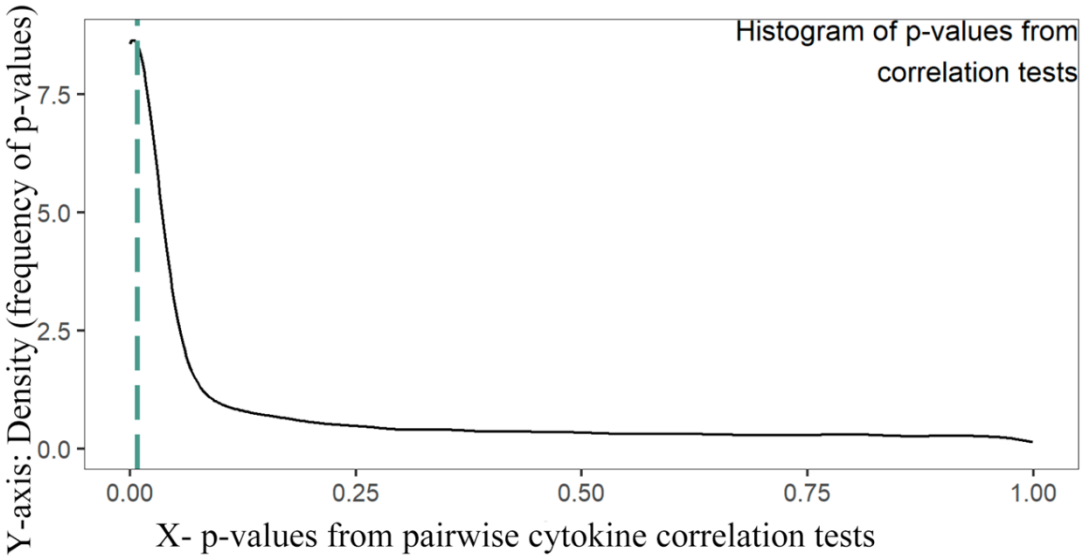

Figure 4.9: Histogram showing multicollinearity in the cytokine data.
Histogram of distribution of p-values from correlation tests between cytokines. The green line shows the median value below $p < 0.05$.
Another consideration is the sample size. Ideally, the number of observations should exceed the number of response variables; however, this criterion is not met, as the dataset includes 78 samples but 105 response variables.

Multivariate normality is generally respected across the dataset, though some individual cytokines deviate from normality. On the other hand, the assumption of homogeneity of variance is met, as demonstrated by beta-dispersion analysis (Table 4.2). The results indicate no significant differences in dispersion across treatment groups: treatment (F = 0.03, $P = 0.87$), time (F = 0.34, $P = 0.71$), and time × treatment interaction (F = 0.22, $P = 0.95$). This confirms that any differences detected in the PERMANOVA are due to shifts in the centroids of cytokine profiles rather than variance differences.

Table 4.2: Summary of dispersion tests.

Term	Df	Sum Sq	Mean Sq	FF	P	Dispersion test for:
Treatment	1	0.01	0.01	0.03	0.8708	Treatment
Residuals	76	24.84	0.33	-	-	Treatment
Time in hrs	2	0.23	0.12	0.34	0.7073	Time
Residuals	75	25.51	0.34	-	-	Time
Subgroups	5	0.40	0.08	0.22	0.9542	Treatment × _Time
Residuals	72	26.08	0.36	-	-	Treatment × _Time

Permutation tests on beta-dispersion tests. "Group" represents the time × _Treatment subsets. Df: degree of freedom. Sq: square. All permutation tests were conducted with 9999 permutations to ensure robust estimation of p-values.

Given the presence of multicollinearity and given sample size is smaller than number of variables, PERMANOVA was selected as the preferred analytical approach over MANOVA. While MANOVA, which needs traditional assumptions to be met, namely independent variables and a larger sample size, PERMANOVA is a more robust non-parametric alternative that accommodates the assumptions violations. This approach ensures a more reliable interpretation of cytokine expression patterns.

4.3.3.2 Model selection

Different models were compared to determine the best to examine cytokine expression whilst accounting for Treatment as the main variable of interest. AICc was used, as it helps identify the best-fitting. Lower AICc values indicate a better model fit, balancing accuracy with simplicity (fewer parameters). Because the sample size is relatively small compared to the number of parameters, AICc was used to avoid bias (Corcoran, 2023).

The interaction model ("Treatment × Time") did not improve model fit compared to the additive model ("Treatment + Time"), as indicated by a difference in AICc greater than 2 (ΔAICc = 3.44) *(Δ means delta which is the difference between AICc of the suggested model and the best (lowest) AICc value model in the comparison).* This suggests that the effect of Treatment can be considered independently of Time, as there was no significant interaction between the two variables. Therefore, the simpler "Treatment + Time" model was preferred since it provided nearly the same explanatory power without unnecessary interaction terms.

Among the tested models, several had ΔAICc values of less than 2, meaning they essentially as good as best model and had similar fits. In such cases, the model with fewer explanatory variables is preferred for interpretability. The model that best balanced accuracy and simplicity was **"**Treatment + Time + Gender + Age."

Further analysis revealed two distinct age groups: patients aged >60 and patients aged <60. To improve clarity, the age variable was converted into a binary category **(Figure 4.10)**. When comparing this binary age model to the original model with age as a continuous variable, there was no difference in AICc. Therefore, the binary age variable was chosen for simplicity, allowing for clearer representation in multivariate analyses and graphic visualisations.

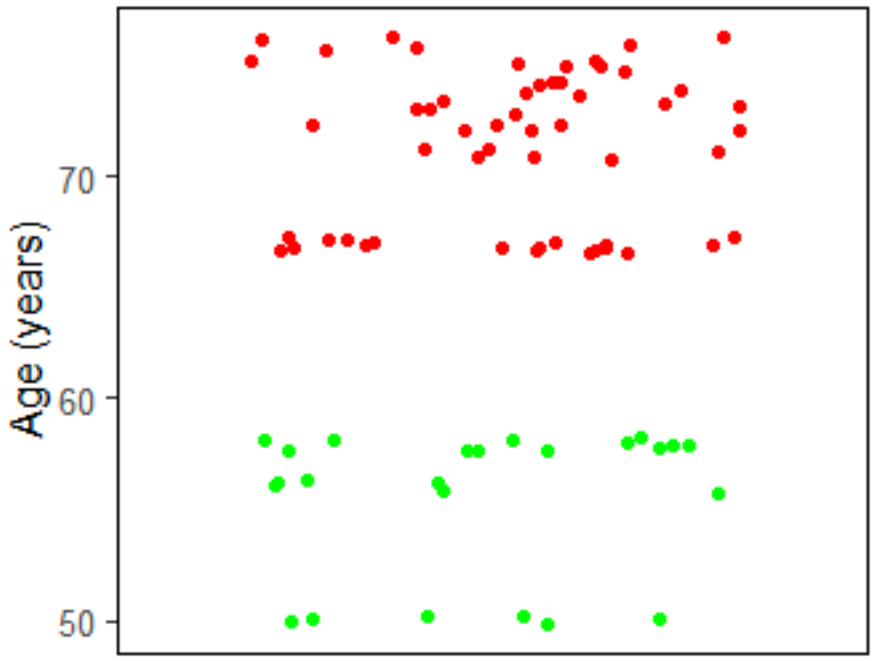

Figure 4.10: Age stratification of patients into two groups: under 60 and over 60 years.

Based on AICc scores and balanced selection, the model used for downstream analyses was: "Treatment + Time + Age (binary) + Gender" **(Table 4.3)**.

Table 4.3: Model selection for PERMANOVAs.

	AICc	**ΔAICc**
Treatment + Time + Age + Gender	167.29	0.00
Treatment + Time + Age2 + Gender	167.91	0.62
Treatment + Time + all covariates	168.07	0.79
Treatment + Time	171.03	3.75
Treatment x Time + covariates	171.97	4.68
Treatment x Time	174.47	7.18

AICc:Akaike Information Criterion with correction for small sample size. ΔAICc: delta AICc compared to the model with the lowest AICc value. Age2 is the age as a binary variable for >60 and <60 age groups. The preferred model is shown in bold Terms.

The selected model demonstrated that, across all conditions and considering all cytokines, Treatment had no significant effect on cytokine levels (F = 1.28, p = 0.1977). In contrast, Time (F = 1.91, p = 0.0288), Gender (F = 3.32, p = 0.0050), and Age (F = 4.21, p = 0.0021) showed significant effects, indicating that cytokine expression varied over time and differed between genders and age groups **(Table 4.4)**.

4.3.3.3 Summary of Multivariate model for all cytokines using PERMANOVA and Principal component analysis (PCA)

Table 4.4: Summary of PERMANOVA analyses

	Df	Sum of Squares (SumOfSqs)	R^2	**F**	***P***
Treatment	1	10.05	0.02	1.28	0.1977
Time in hrs	2	30.02	0.05	1.91	**0.0288**
Gender	1	26.13	0.04	3.32	**0.0050**
Age (binary)	1	33.18	0.05	4.21	**0.0021**
Residual	72	567.00	0.85	NA	NA
Total	77	666.38	1.00	NA	NA

Further analysis of the cytokine profiles revealed significant effects of incubation time, patient gender, and age on cytokine expression levels. As illustrated in Figure **7.5 in Appendix 7.6**, cytokine expression was generally downregulated over time, with notable decreases observed between the 48-hour and 192-hour time points. This temporal decline suggests a reduction in cytokine production and/or release as the incubation period extends, which may reflect changes in cellular activity or viability over time. There is an exploratory analysis of 288hrs conducted in 4.3.5 section.

Gender differences were also noticed in the cytokine expression patterns. **Figure 7.6 in Appendix 7.6** demonstrates that cytokine levels were upregulated in female patients compared to male patients, except for MMP9 and Osteopontin, which did not follow this trend. These differences could have implications for understanding gender-related disparities in glioblastoma progression and/or treatment efficacy (Lee et al., 2022a, Barnett et al., 2024).

Age emerged as another significant factor influencing cytokine expression. As shown in Supplementary **Figure 7.7 in Appendix 7.6**, patients aged less than 60 years exhibited increased cytokine expression across most cytokines, with the exception of eight specific cytokines (Osteopontin, MMP9, Kallilkein.3, CHI3L1, Resistin, VGEF, Insulin-Like Growth Factor Binding Protein (IGFBP-2), IL17-A).

PCA was performed to visualise the variance in cytokine expression and assess the effects identified in the PERMANOVA **(Figure 4.11)**. The first two principal components (PC1 and PC2) did not show a clear separation between treatment groups, aligning with the PERMANOVA results, which indicated no significant effect of treatment on cytokine expression.

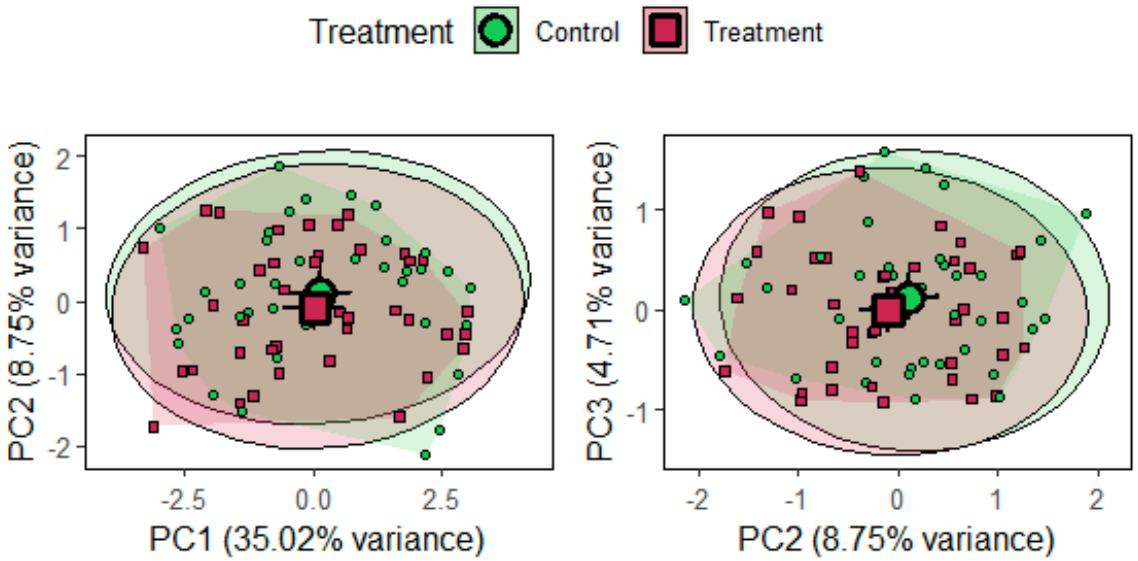

Figure 4.11: ***2D PCA of treatment effect for 105 cytokines using proteome profiler.***
Left: PC1 and PC2 axes. Right: PC2 and PC3 axes. Large shapes show the centroids (± 95% confidence intervals). Small shapes show individual data points. Ellipses show the 95% confidence intervals. Polygons show the maximal dispersion between outermost points for each group.

In contrast for other covariates namely, Time, Age, Gender, Recurrence, and MGMT status where PCA revealed distinct separation in Principal component 1(PC1) and Principal component 2 (PC2) which support PERMANOVA analysis **(Figure 4.12)**. The separation was less pronounced along PC2 and Principal component 3 (PC3) **(Figure 4.13)**. Additionally, survival at six months did not exhibit a clear separation along the first three principal components, suggesting that cytokine expression patterns were not strongly associated with short-term survival outcomes.

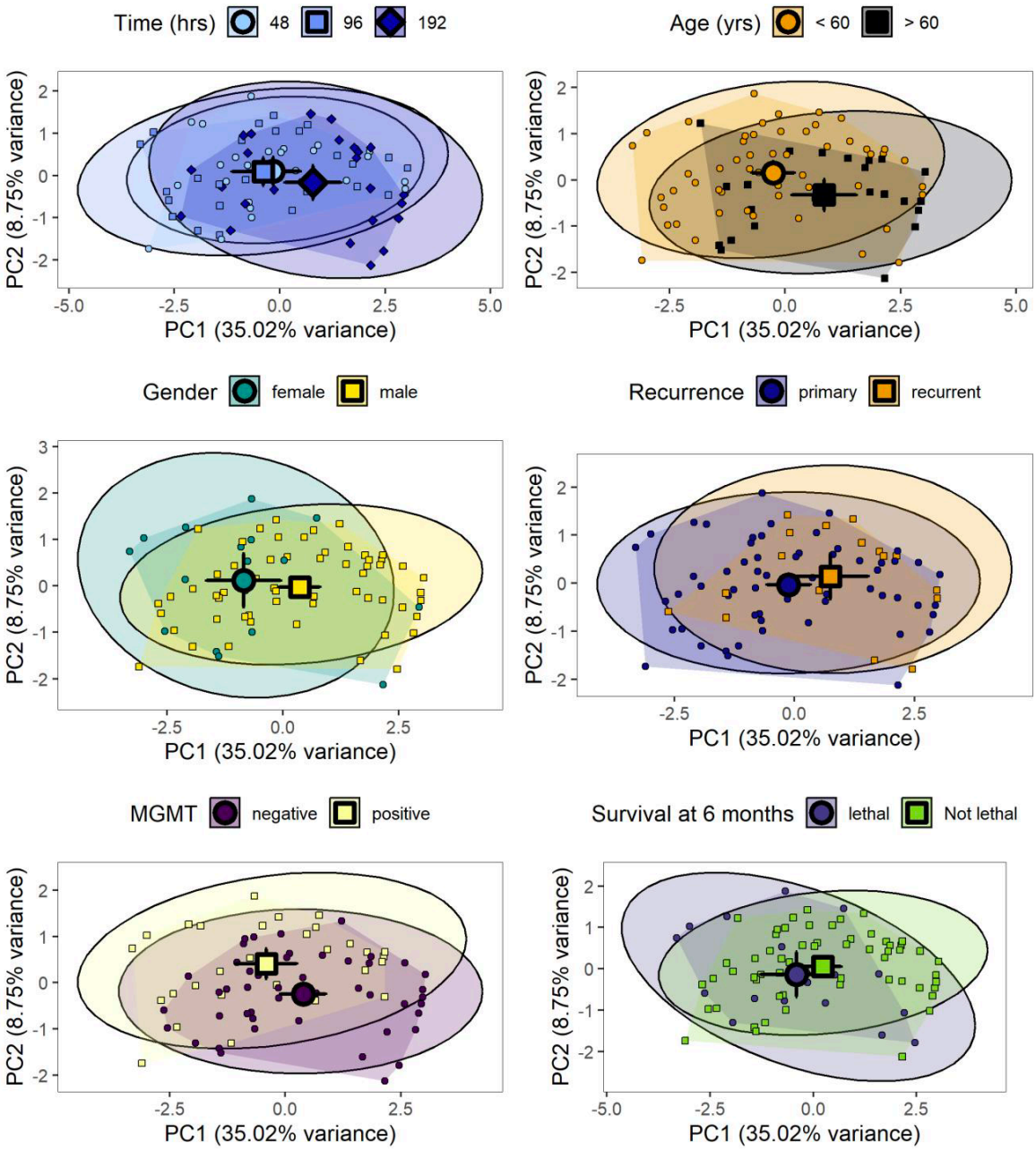

Figure 4.12: 2D PCA of covariate effects for all cytokines (PC1 and PC2).
Large shapes show the centroids (± 95% confidence intervals). Small shapes show individual data points. Ellipses show the 95% confidence intervals. Polygons show the maximal dispersion between outermost points for each group of a variable.

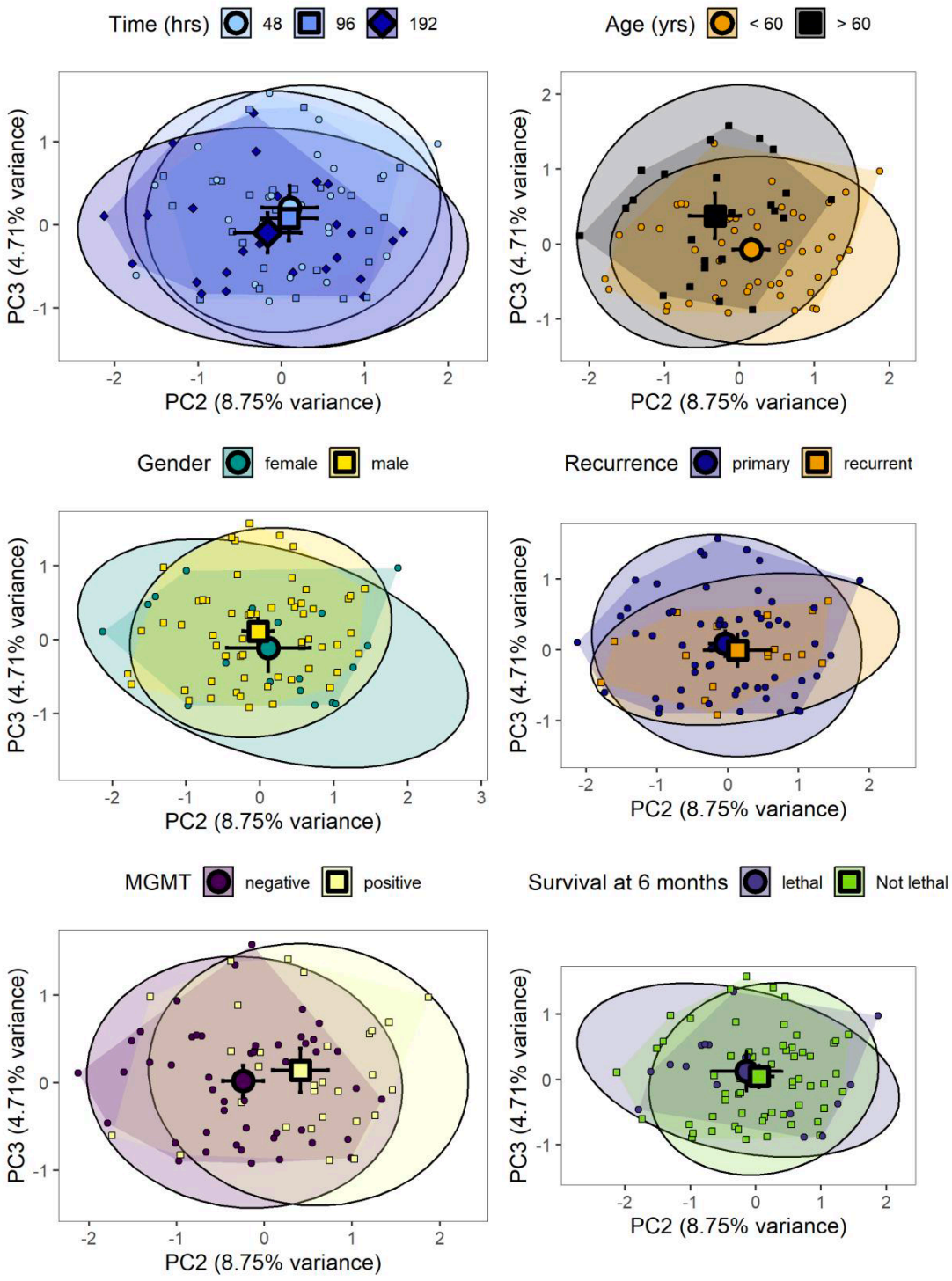

Figure 4.13: 2D PCA of covariate effects for all cytokines (PC2 and PC3).
Large shapes show the centroids (± 95% confidence intervals). Small shapes show individual data points. Ellipses show the 95% confidence intervals. Polygons show the maximal dispersion between outermost points for each group of a variable.

A pairwise PERMANOVA comparing the different time groups showed that the 192-hr time point was significantly different from 48 hrs (F = 2.09, $p = 0.0381$) and 96 hrs (F = 3.09, $p = 0.0117$) time points **(Table 4.5).** This suggests that the cytokine profile is maintained up to 96 hrs but varies after 192 hrs.

Table 4.5: Summary of pairwise PERMANOVA for the time effect.

	Df	**SumOfSqs**	R^2	Fisher's **(F)**	Probability **(Pr)(>F)**
48 hrs. vs 96 hrs.					
Time	1	5.03	0.01	0.63	0.8465
Treatment	1	9.05	0.02	1.13	0.2593
Gender	1	27.10	0.06	3.38	0.0054
Age (binary)	1	19.00	0.04	2.37	0.0269
Residual	47	377.00	0.86	NA	NA
Total	51	437.17	1.00	NA	NA
48 hrs. vs 192 hrs.					
Time	1	17.01	0.04	2.09	**0.0381**
Treatment	1	6.62	0.02	0.81	0.5630
Gender	1	10.46	0.02	1.28	0.1879
Age (binary)	1	13.54	0.03	1.66	0.0919
Residual	47	382.71	0.89	NA	NA
Total	51	430.33	1.00	NA	NA
96 hrs. vs 192 hrs.					
Time	1	22.99	0.05	3.09	**0.0117**
Treatment	1	9.22	0.02	1.24	0.2137
Gender	1	21.41	0.05	2.88	0.0143
Age (binary)	1	46.97	0.10	6.31	0.0003
Residual	47	349.66	0.78	NA	NA
Total	51	450.25	1.00	NA	NA

The significant differences between time groups are shown in bold. The pairwise PERMANOVAs are corrected for the effect of covariates.

Building on these results, it was decided to focus on the most frequently detected and abundant cytokines to further explore their roles in treatment response.

4.3.4 Identification of important cytokines

4.3.4.1 Univariate analysis of cytokines in function of treatment

A combination of PLS-DA and Limma was used to identify key cytokines. PLS-DA identified 27 cytokines that differentiated the treatment groups. The Limma method, using a linear model with the formula "Treatment + Time + Age (binary) + Gender", identified cytokines that showed significant differences between treated and control biopsies while accounting for covariates (Time, Age, and Gender) **(Figure 4.14)**.

Among these, seven cytokines were consistently identified by both methods, reinforcing their potential relevance in distinguishing treatment effects. Analysis of the direction of change in these cytokines showed that all were upregulated under the effect of treatment, except for MMP9, which was downregulated. However, after *p*-value adjustment for multiple testing, only three cytokines (Angiopoietin 2, Apolipoprotein A I, and BDNF) remained statistically significant and upregulated, as shown in the volcano plot **Table 4.6; Figure 4.15).**

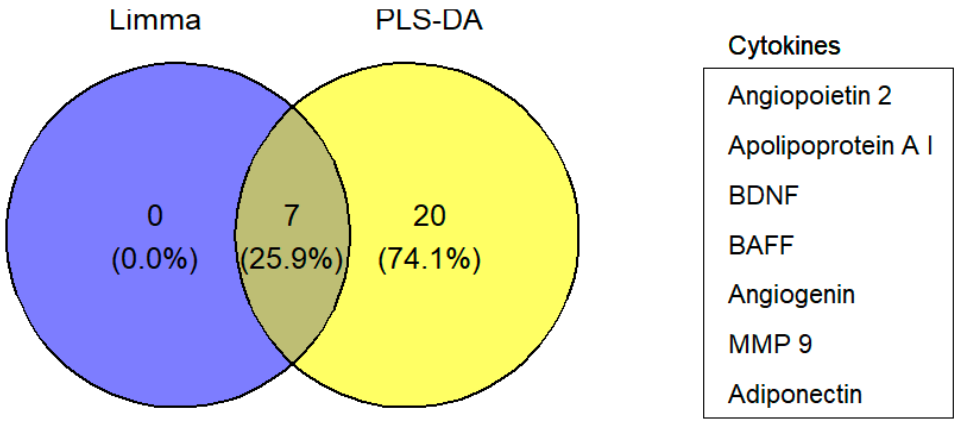

Figure 4.14: Cytokines influenced by treatment identified by PLS-DA and Limma methods.

4.3.4.2 Multivariate analysis of cytokines altered by treatment.

To validate the findings from the univariate approaches, a multivariate linear model was applied to assess cytokine expression while adjusting for potential confounders, including time, age, and gender. This analysis allowed for a more refined measurement of treatment-associated changes in cytokine levels. The results, summarised in Table 4.6 and visualised in Figure 4.15, further support the identification of Angiopoietin 2, Apolipoprotein A I, and BDNF as key cytokines significantly altered by treatment.

Table 4.6: Differential cytokine expression between treated and control GBM biopsies based on proteome profiler analysis.

No.		logFC	AveExpr	t	P.Value	adj.P.Val	B
1	**Angiopoietin 2**	**0.24**	**0.00**	**3.58**	**0.0006**	**0.0386**	**-0.37**
2	**Apolipoprotein A I**	**0.17**	**0.01**	**3.50**	**0.0007**	**0.0386**	**-0.60**
3	**BDNF**	**0.21**	**-0.01**	**3.30**	**0.0014**	**0.0493**	**-1.17**
4	BAFF	0.17	-0.02	2.57	0.0119	0.3132	-3.03
5	Angiogenin	0.14	0.01	2.46	0.0158	0.3313	-3.27
6	MMP 9	-0.11	0.04	-2.06	0.0421	0.5118	-4.09
7	Adiponectin	0.07	-0.03	2.00	0.0486	0.5118	-4.21

Cytokine expression was compared between treated and control biopsies whilst adjusting for Time, Age, and Gender. Significant cytokines after p-value correction are shown in bold. ***logFC*** *= log_2-fold change in treated biopsies relative to control. adj.P.Val = adjusted p-value.*

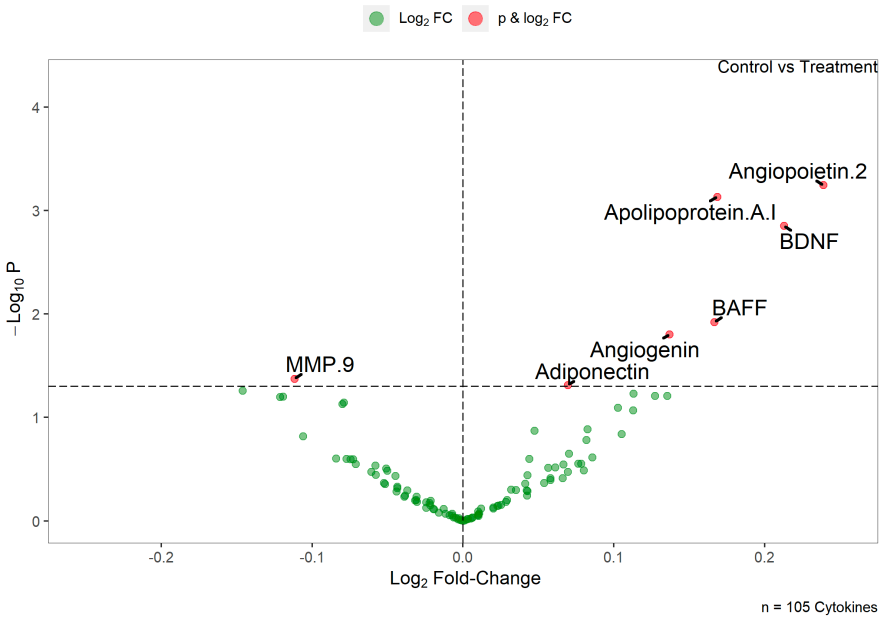

Figure 4.15: Volcano plot of the cytokine expression between treated and control biopsies. *The expression is adjusted for the time, age, and gender. Raw p-values are shown. Annotated points show the significant cytokines with raw p-values < 0.05.*

A PERMANOVA analysis was conducted on the subset of cytokines that were identified as distinguishing treatment vs. control groups by both PLS-DA and Limma methods. AICc model selection indicated that the most suitable model, i.e., the model with ΔAICc < 2, was best explained by Treatment and Age as the key factors.

The results showed a significant effect of Treatment (F = 8.47, p = 0.0002) and Age (F = 2.96, p = 0.0267) on cytokine expression **(Table 4.7)**. This suggests that treatment strongly influenced cytokine levels, while age also had a measurable but smaller effect. These differences were further visualised using PCA, which showed clear separation between treated and control biopsies when focusing on cytokines most affected by treatment **(Figure 3.16)**.

Table 4.7: Summary of PERMANOVA for the selected cytokines.

	Df	SumOfSqs	R^2	F	Pr(>F)
Treatment	1	3.80	0.10	8.47	**0.0002**
Age	1	1.33	0.03	2.96	**0.0267**
Residual	75	33.63	0.87	NA	NA
Total	77	38.75	1.00	NA	NA

Significant terms are shown in bold.

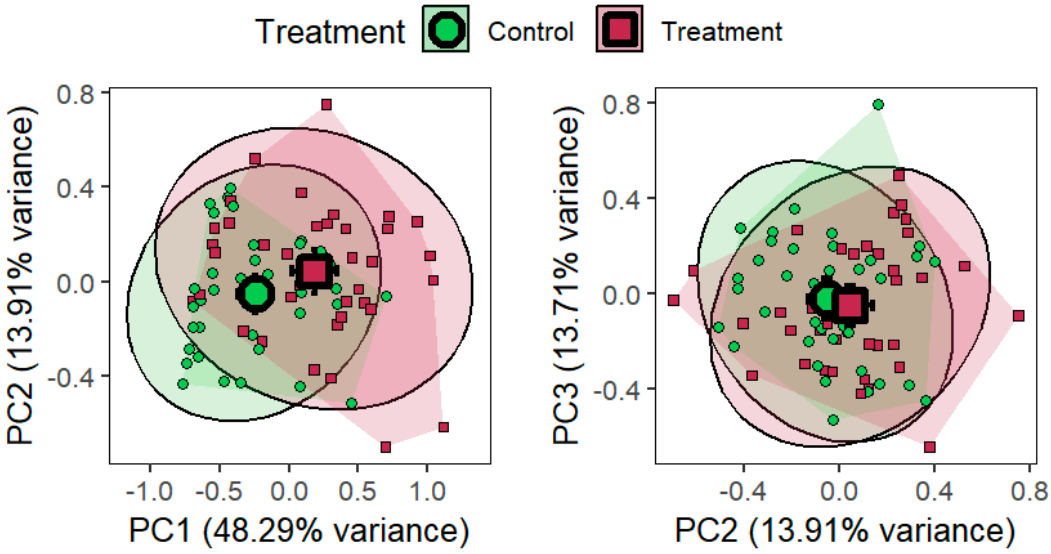

Figure 4.16: Principal Component Analysis of the effect of treatments for all times for cytokines of interest.
Large shapes show the centroids (± 95% confidence intervals). Small shapes show individual data points. Ellipses show the 95% confidence intervals. Polygons show the maximal dispersion between outermost points per treatment. Treatment = GSK+TMZ. Control = DMSO.

4.3.4.3 The most frequent and most abundant cytokines

Across the cytokines examined, the top five most frequently detected across all samples - irrespective of time point or treatment - were CHI3L1, IL-8, and Osteopontin, followed by CCL2/MCP-1, and finally Serpin E1. This high frequency suggests that these cytokines are continually expressed and may play key roles in the GBM related processes in the study population (Table 4.8).

Table 4.8: Top five most frequently detected cytokines

Cytokine	Percentage of detection in all samples
CHI3L1	98.8%
IL8	98.8%
Osteopontin (OPN)	98.8%
CCL2/MCP-1	97.6%
Serpin E1	96.4%

The most highly expressed cytokines in the cohort were identified by calculating their mean relative expression levels across all samples, based on pixel density analysis from QuickSpots Software. Each cytokine's relative expression value was normalised to the average of three duplicate positive controls, resulting in values ranging from 0 to 1. A value of 1 indicates expression equal to the average positive control, while lower values represent lower relative expression. The average expression values for each cytokine visualised in **(Figure 4.17)**, and the top six most abundant cytokines are listed in **(Table 4.9)**.

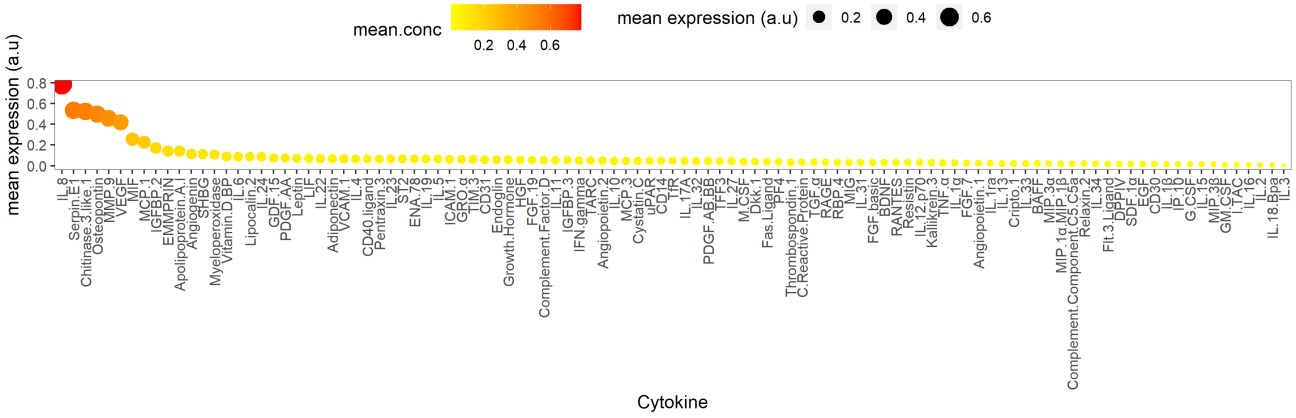

Figure 4.17: Graph showing mean expression of cytokines in all samples.

Table 4.9: Mean Expression Levels of the Top Six Cytokines.

Cytokine	Mean relative expression (a.u)
IL.8	0.78
Serpin.E1	0.53
CHI3L1	0.52
Osteopontin	0.49
MMP.9	0.45
VEGF	0.41

a.u.: arbitrary units.

4.3.5 Exploratory analysis of the 288-hrs group

To evaluate long-term cytokine expression changes, an exploratory analysis was conducted on samples collected at 288 hrs. This analysis showed a strong effect of covariates, possibly due to the low number of samples (n = 3). Despite this limitation, cytokine expression in the 288-hour group was significantly different from earlier time points **(Table 4.10)**. The data suggested greater variability in cytokine responses at 288 hrs, as indicated by increased dispersion **(Figure 4.18)**. However, a formal dispersion test did not detect a statistically significant difference in variance between time groups (F= 0.4962, p = 0.6892).

Pairwise comparisons between time points revealed that cytokine profiles at 288 hrs differed significantly from those at 48 hrs (p = 0.0298), 96 hrs (p = 0.0423), and 192 hrs (p = 0.0049), with the most pronounced shift occurring after 192 hrs. These changes suggest a progressive alteration in cytokine expression over time, which becomes more evident at 288 hrs **(Figure 4.18).**

Table 4.10: Exploratory analysis of the 288-hrs group.

	Df	SumOfSqs	R^2	F	Pr(>F)
48 vs 288	1	20.55	0.07	2.26	**0.0298**
96 vs 288	1	18.11	0.06	2.21	**0.0423**
192 vs 288	1	30.37	0.10	3.62	**0.0049**

The significant differences between time groups are shown in bold. The model was adjusted for the covariates but only the time effect is shown.

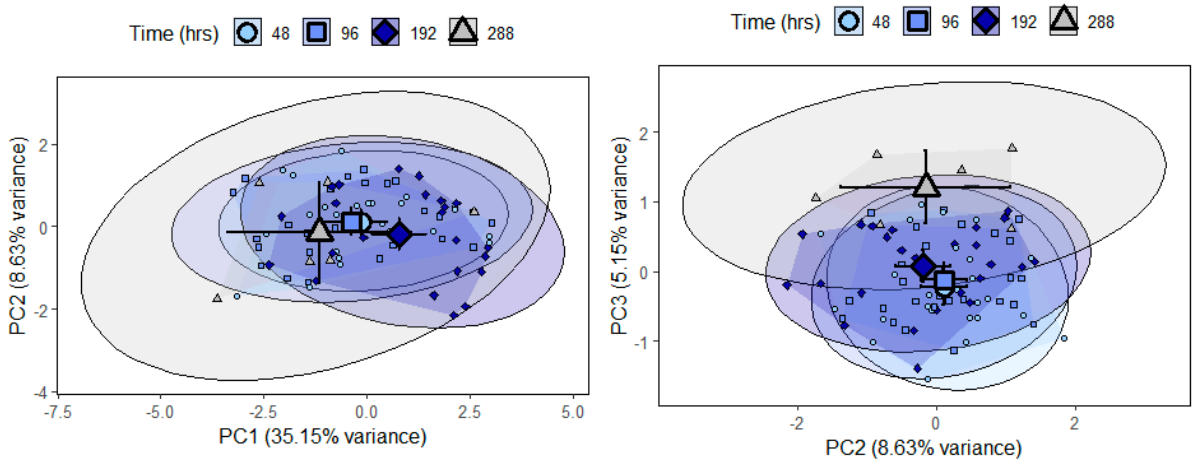

Figure 4.18: Principal Component Analysis of the effect of time for all cytokines. *Large shapes show the centroids (± 95% confidence intervals). Small shapes show individual data points. Ellipses show the 95% confidence intervals. Polygons show the maximal dispersion between outermost points per treatment. The data indicates that cytokine profiles shift progressively after 192 hrs and even more substantially at 288 hrs.*

4.4 ELISA cytokine analysis

Based on the results of the proteome profiler, seven cytokines were selected for quantitative analysis using ELISA: Angiopoietin-2, MMP9, Serpin E1, CHI3L1, IL-8, and VEGF **(Table 4.11)**. IL6 was chosen due to previous research conducted within the host laboratory.

Table 4.11: Rational behind choosing individual cytokines for ELISA analysis.

	Cytokine	Rationale
1	Angiopoietin-2	Most significantly **upregulated** cytokine following treatment.
2	MMP9	The only significantly **downregulated** cytokine with combined treatment **and** one of the most abundant cytokines.
3	Serpin E1	Among the most frequently detected **and** abundant cytokines in all effluents.
4	CHI3L1	Highly frequent **and** abundant across all effluents.
5	IL-6	Selected on basis of previous work in the host laboratory.
6	IL8	Among the most frequently detected **and** abundant cytokines in all effluents.
7	VEGF	One of most abundant cytokines across all effluents.

4.4.1 Methods

The data analysis was again performed in R version 4.3.0, using RStudio 2023.03.0 Build 386, and graphs were built using ggplot2 (Kassambara, 2020). The raw cytokine data was cube-ronormalisedsed and range-scaled using MetaboAnalystR v4.0.0 with the "CrNorm" and "RangeNorm" arguments, respectively (Pang et al., 2020). In order to remove unwanted noise from covariates, the data was then fitted to a mixed-effect linear model using the *lmm2met* v1.0 R package (Wanichthanarak et al., 2019).

Twelve outliers were detected when combining a visual method (samples outside the 95% confidence interval) with a Henze-Zirkler's test from the MVN v5.9 R package on the first two principal components of the spectral decomposition obtained by the *prcomp* R function (Korkmaz et al., 2014). Despite being associated with two patients only, these outliers were not removed from the data as they were not associated with a particular condition or covariate across the two patients. The main data set was analysed for the data that contained entries for time points: 48, 96, and 192 hrs. The normality and homoscedasticity of the cytokine expression were verified with Shapiro-Wilk's and Levene's tests, respectively, using the *rstatix* v0.7.2 R package (Kassambara, 2023). The multicollinearity was tested using the *corrplot* v0.92 R package (Wei and Simko, 2021). The dispersion of the multivariate data was compared with the *permutest* function on the Euclidean distance obtained from the *vegdist* and *betadisper* functions from the *vegan* v2.6-4 R package (Oksanen et al., 2022).

The list of models with the different variables (Treatment, Time) and covariates (Age, Gender, MGMT status, Survival at 6 months, Recurrence status) were obtained and compared from the *make_model* and *fit_model* R functions, respectively, from the AICcPermanova v0.0.2 R package (Corcoran, 2023). Multivariate analysis was conducted *via* PERMANOVAs using the *vegan* R package v2.6-4 (Oksanen et al., 2020). Where relevant, pairwise comparisons between groups of interest were computed using *pairwiseAdonis2* function from the *pairwiseAdonis* v0.4.1 R package whilst accounting for the effects of covariates identified by the AICc method (Martinez Arbizu, 2017). To identify the cytokines of interest between the treated and control biopsies, three methods were combined: PLS-DA, a moderated t-test model, and a model on the covariate-adjusted residuals. First, the PLS-DA identified the cytokines that contributed the most to the discrimination between treated and control biopsies using the *mixOmics* v6.24.0 R package (Rohart et al., 2017, Welham et al., 2023). These cytokines were selected based on VIP (Variable important projection) being > 1. However, since PLS-DA tends to overfit the data, this was combined with a linear model comparing the treated and control biopsies with covariate adjustment identified from the AICc model. The linear model was fitted for the effect of treatments whilst controlling for covariates using the *Limma* v3.56.2

R package (Ritchie et al., 2015). The effect of treatment on the cytokine expression wvisualisedsed using the *EnhancedVolcano* v1.18.0 R package (Blighe et al., 2020).

Third, the univariate analysis and selection of the important cytokines was triple-checked using a model of the treatment effect on the residuals of the covariate effects and compared by repeated Student-t-tests with p-value adjustment for multiple tests. These models wevisualisedsed using the *sjPlot* v2.8.15 R package (Lüdecke, 2023). Effect sizes were calculated using the *effectsize* v0.8.6 R package based on R2 and ETA2 values and interpreted according to Cohen (1988) and Cohen (1992), respectively (Ben-Shachar et al., 2020, Cohen, 1988, Cohen, 1992).

4.4.2 Data structure and pre-processing

A substantial proportion of the dataset consists of zero values, indicating the absence of cytokine expression after normalisation to reference loading controls **(Figure 4.19 A)**. While these zeros represent true biological values, their presence skews the data distribution, limiting the applicability of parametric statistical tests. This skewness is confirmed by the quantile-quantile (Q-Q) plot, which illustrates deviations from a normal distribution **(Figure 4.19 B)**.

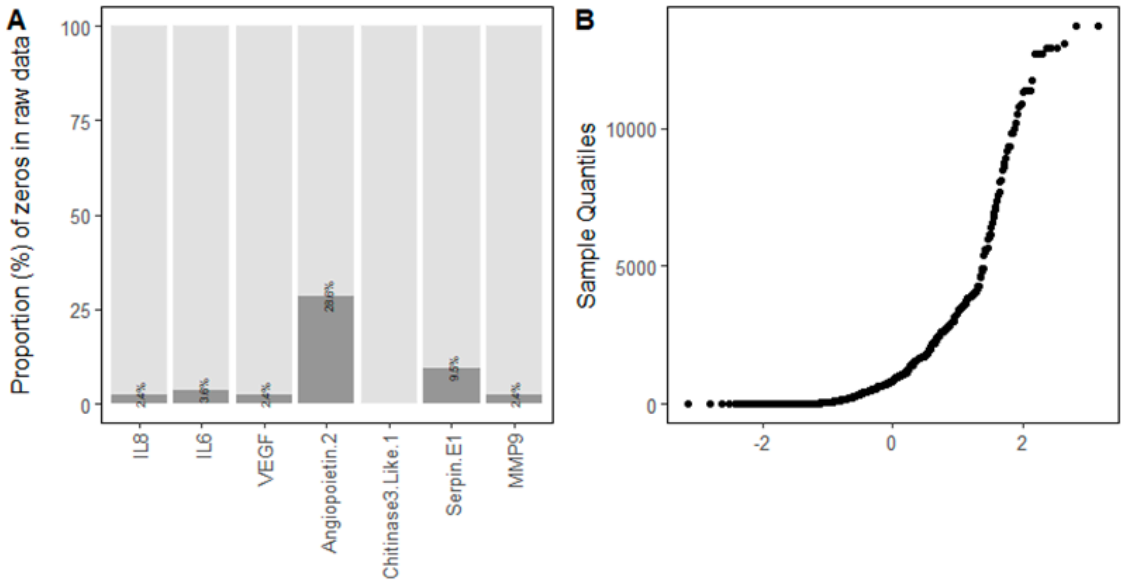

Figure 4.19: Profile of the raw data.

A) Graph showing the proportion of zeros in the data for 7 most important cytokines. B) Data normalisation and variable fitting makes the data suitable for parametric tests.

To address this issue, data scaling and normalisation were applied using MetaboAnalystR**,** which transformed the dataset into a more parametric-like distribution **(Figure 4.20)**. This transformation particularly improved the variance structure of cytokine expression, making the dataset more suitable for statistical comparisons of variables of interest**.**

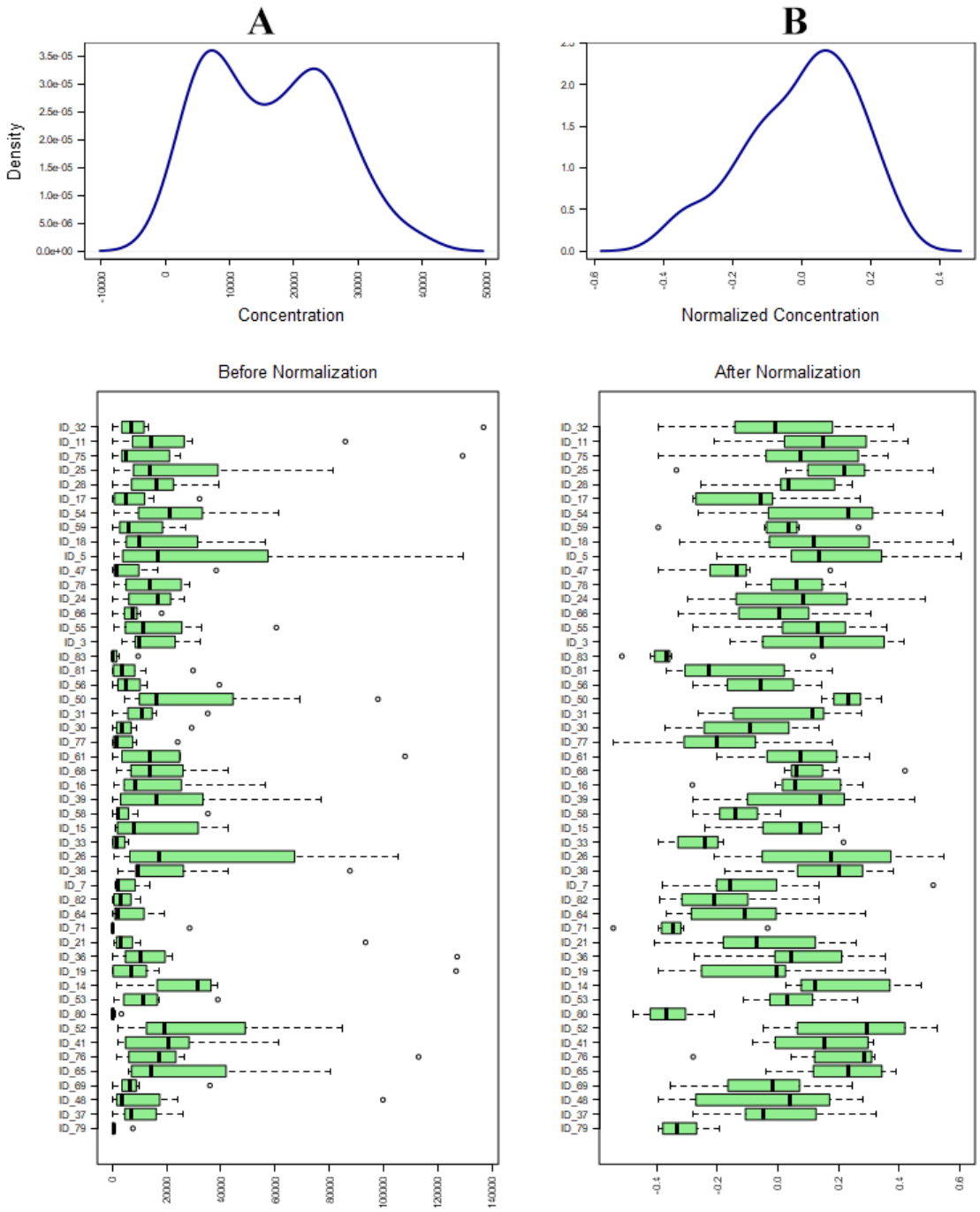
A
B
Density
Concentration
Normalized Concentration
Before Normalization
After Normalization

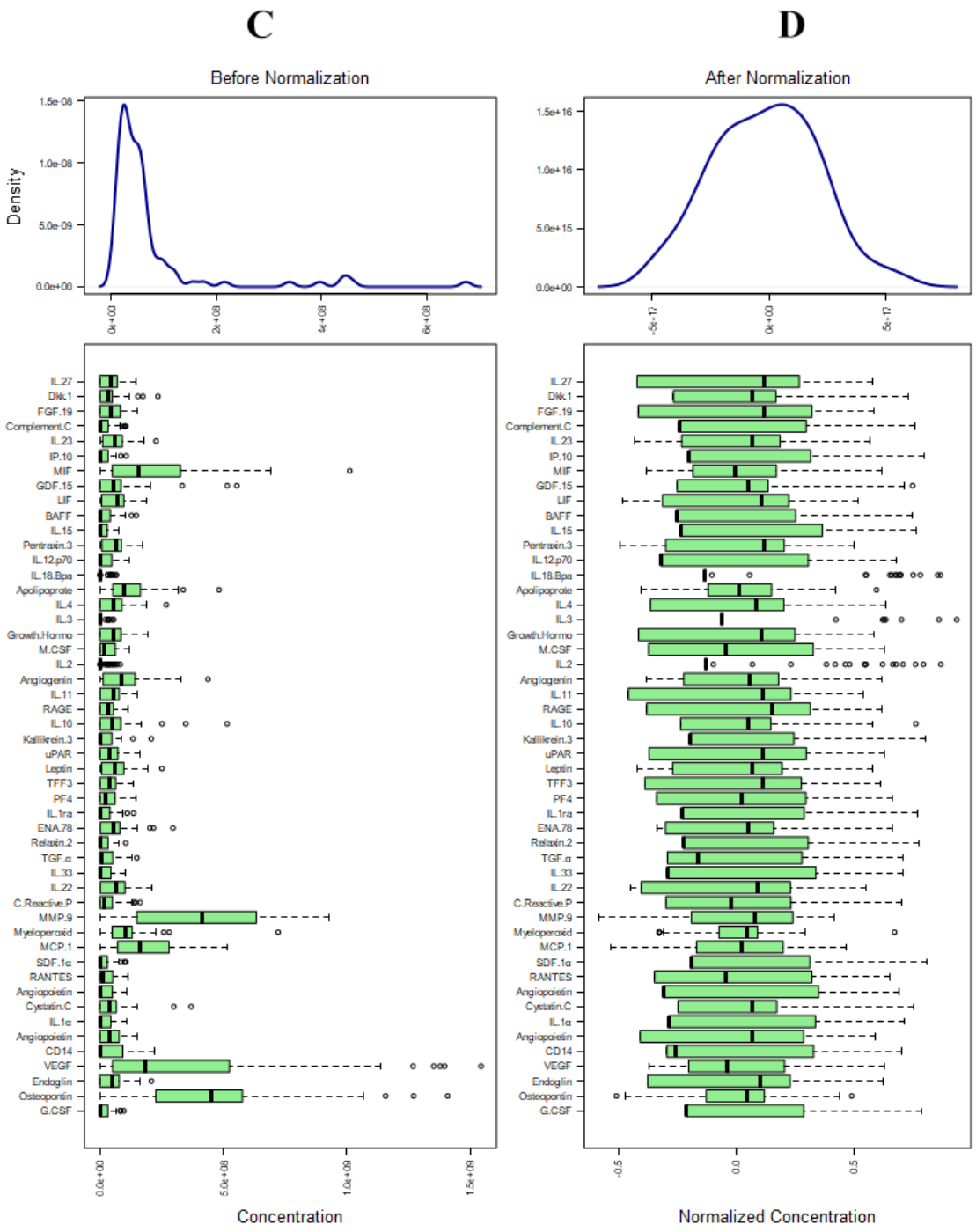

Figure 4.20: ***Profile of the data before and after normalisation and scaling in MetaboAnalyst.*** *Sample view before (A) and after (B) normalisation. Feature view (C) and after (D)normalisation.*

The dataset was screened for outliers using the Mahalanobis distance **(Figure 4.24)**. Due to large number of response variables, outlier detection was performed using the first two principal components from a spectral decomposition analysis. This statistical approach was complemented by a visual inspection based on the 95% CI of PCA. The results indicated that no samples were classified as outliers according to both Henze-Zirkler's multivariate normality test and the Mahalanobis distance when considering the 95% CI. Following this screening process, the final dataset retained cytokine expression data for 84 samples. The effluent samples include the 13 patients X 2 groups (control and treatment) X 3 main time points (48, 96,192 hrs) in additional to the 3 patients that had extended incubation time to 288 hrs (3 X2), making it 84 samples.

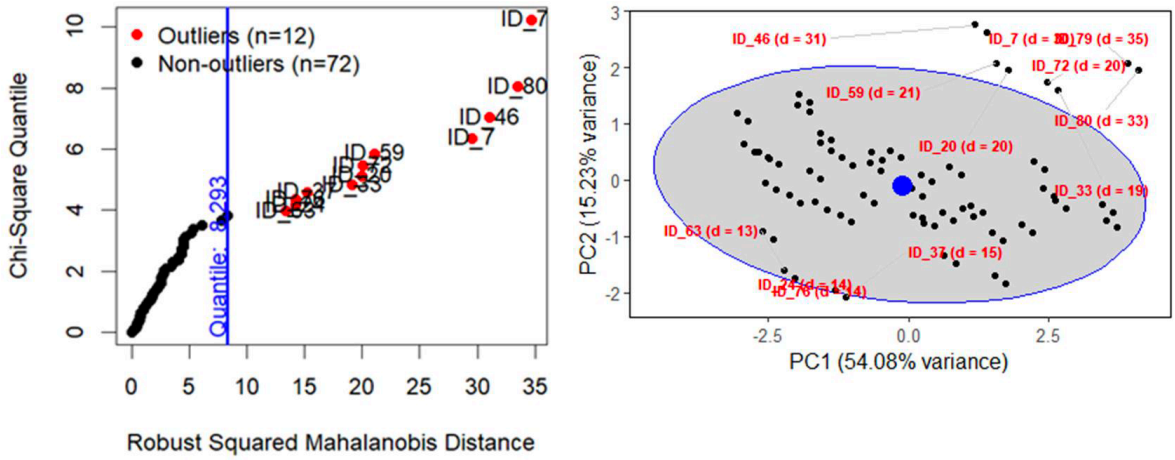

Figure 4.21: Detection of outliers.
Left: Adjusted χ2 quantile-quantile plot for detection of outliers using the statistical method from a Henze-Zirkler's test on the Mahalanobis Distance. Right: visual method showing the 95% confidence interval (ellipse) around the centroid (large blue point).

The processed data was generally normally distributed (p = 0.0506), with most cytokines following a normal distribution, with only two cytokines showed slight deviations **(Figure 4.22)**. Importantly, data transformation did not alter the relationship between raw and processed values, ensuring that the biological patterns remained consistent **(Figure 4.23)**. Additionally, variance in cytokine expression was comparable between treatment groups, as confirmed by Levene's test (p = 0.938). This consistency was observed for both the overall dataset and individual cytokines **(Figure 4.24)**. Together, these results confirm that the processed dataset meets the statistical assumptions necessary for subsequent stages of data analysis.

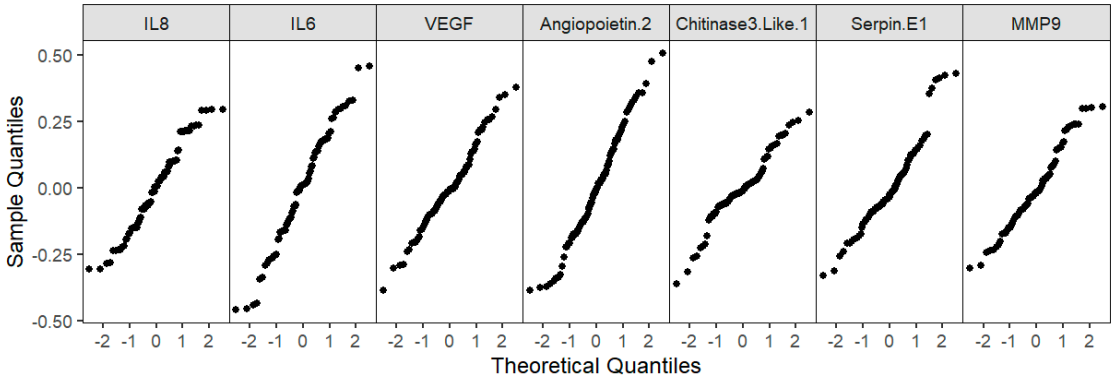

Figure 4.22: Quantile-Quantile plot of processed data per cytokine.

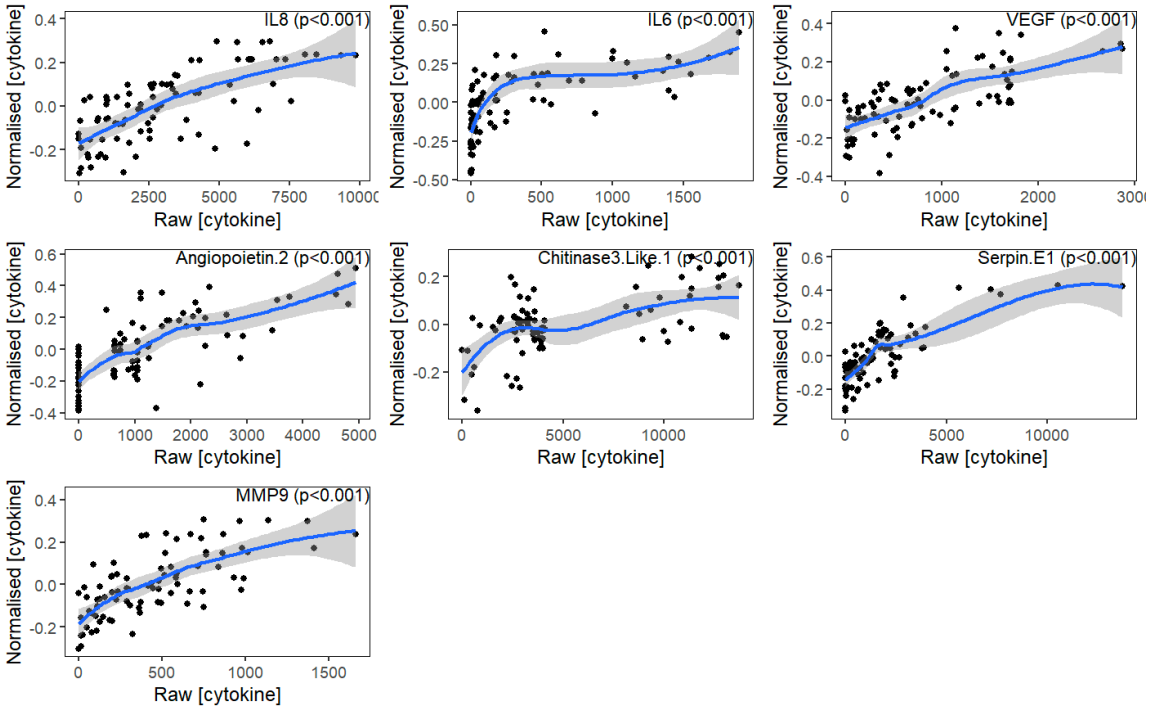

Figure 4.23: Relationship between raw and transformed data.
The variance was comparable between treatments overall according to a Levene's test ($p = 0.938$), which was verified for each individual cytokine.

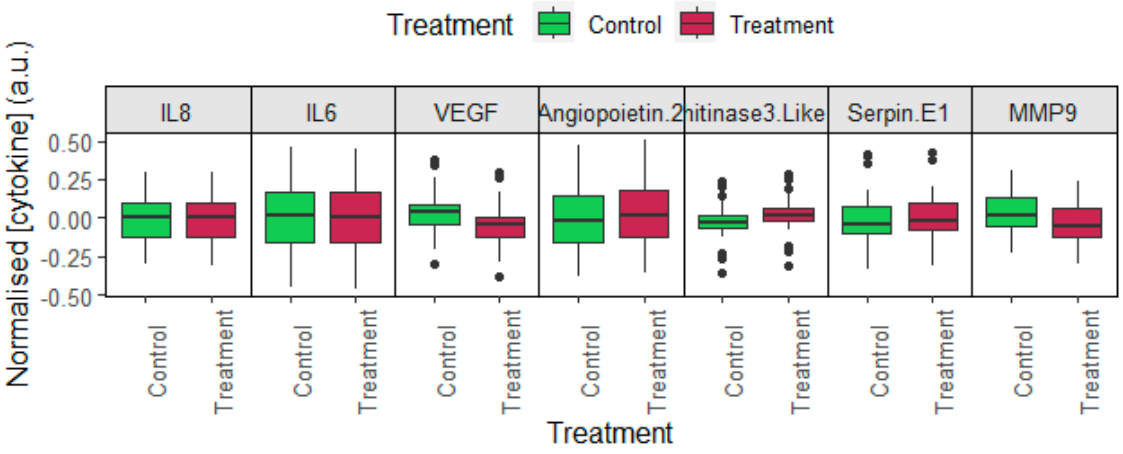

Figure 4.24: Cytokine levels show similar variance between treatments.

In summary, the cytokine dataset underwent preprocessing and validation to ensure its suitability for subsequent statistical analysis. Issues of skewness and zero inflation were addressed through normalization and transformation, while key analytical assumptions were confirmed through checks for normality, variance homogeneity, and outlier identification. Advanced statistical modeling, incorporating covariate adjustments and multiple complementary methods, enabled the reliable detection of cytokines responsive to treatment. These collective steps strengthen the validity of subsequent findings and established a solid foundation for interpreting the biological significance of the treatment effects. The following section will build upon this framework to explore specific patterns of cytokine changes and it's analysis.

4.4.3 Multivariate analysis for all 7 cytokines

A multivariate analysis was conducted using data from seven cytokines to assess the influence of key predictors. The analysis aimed to identify the best predictors among the primary variables of interest **(**treatment and time) while also accounting for relevant covariates, including MGMT status**,** survival at six months, recurrence status, age, and gender.

4.4.3.1 Assumptions

Before conducting the multivariate analysis, key statistical assumptions were evaluated to ensure the validity of the results. The assumption of independent response variables was not met, as cytokines are a group of related biomarkers that tend to be correlated. A correlation matrix confirmed the presence of significant correlations between multiple cytokines, indicating a presence of multicollinearity **(Figure 4.25)**. The histogram of *p*-values from correlation tests further illustrates that most cytokine pairs exhibit significant associations, with the majority falling below the $p < 0.05$ threshold.

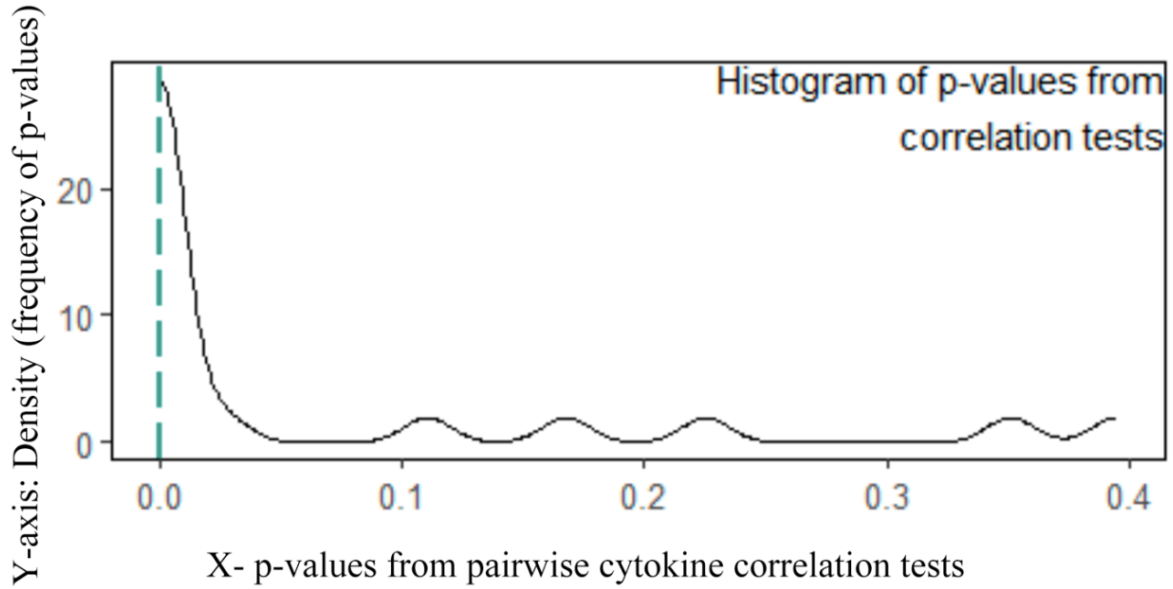

Figure 4.25: Histogram of distribution of p-values from correlation tests between cytokines. *The green line shows the median value below p < 0.05; indicating that most cytokines are correlated with at least one other selected factor.*

The dataset satisfied the adequate sample size assumption, as the number of samples (n = 84) was greater than the number of response variables (n = 7). Additionally, the assumption of multivariate normality was largely respected, though two individual cytokines exhibited slight deviations from a normal distribution.

The assumption of equal variance (homogeneity) was not fully met, particularly for the time factor, as shown by the beta-dispersion analysis **(Table 4.12)**. There were no significant differences in variance between treatment groups (F = 0.0, p = 1.0) or in the interaction between treatment and time (F = 1.37, p = 0.23). However, significant variance differences were found across time points (F = 3.31, p = 0.02). This means that for treatment, any differences found in PERMANOVA are likely due to real changes in cytokine levels, not random variability. In contrast, for time, the observed differences might be due to either real changes in cytokine profiles or just differences in variance.

Table 4.12: Summary of dispersion tests.

Variable	Model	Df	Sum Sq	Mean Sq	F	N permutations	Pr (>F)
Treatment	Treatment	1	0.00	0.00	0.00	9999.00	1.00
Residuals	Treatment	82	1.93	0.02	NA	NA	NA
Time	Time	3	0.14	0.05	3.31	9999.00	**0.02**
Residuals	Time	80	1.11	0.01	NA	NA	NA
Time: Treatment	Groups	7	0.14	0.02	1.37	9999.00	0.23
Residuals2	Groups	76	1.15	0.02	NA	NA	NA

Permutation tests on beta-dispersion tests. "Group" represents the time × _Treatment subsets. Df: degree of freedom. Sq: square.

4.4.3.2 Model selection

To determine the best-fitting model for explaining cytokine expression, multiple models were compared while considering treatment as the primary variable of interest. The results provided strong evidence that all covariates should be included in the model, with the optimal model comprising Time + Treatment + Age + Gender + Recurrence Status + MGMT Status + Survival Status

There was no evidence supporting the inclusion of an interaction term between treatment and time. The additive model (*Treatment + Time + Covariates*) demonstrated a significantly better fit than the interaction model (*Treatment × Time + Covariates*), with ΔAICc > 2 (ΔAICc = 8.19). This indicates that the effect of treatment on cytokine expression is independent of time, meaning that treatment differences can be analysed without accounting for time-dependent interactions. See Table 7.6 in Appendix 7.6.

4.4.3.3 Model summary

There was strong statistical evidence that treatment significantly influenced cytokine expression **(**$F = 4.94$, $p = 0.004$**) (Table 4.13)**. Additionally, all covariates had a highly significant impact on cytokine expression, further emphasising their role in shaping cytokine profiles.

Table 4.13: Summary of the model with all covariates.

Term	Df	SumOfSqs	R^2	F	Pr(>F)
Treatment	1	0.32	0.02	4.94	**0.0048**
Time in hrs	3	4.25	0.25	21.94	**0.0001**
Gender	1	2.02	0.12	31.39	**0.0001**
Age (years)	1	2.67	0.16	41.39	**0.0001**
Recurrence status	1	0.94	0.05	14.59	**0.0001**
MGMT status	1	0.84	0.05	12.97	**0.0001**
Survival at 6 months	1	1.33	0.08	20.67	**0.0001**
Residual	74	4.77	0.28	NA	NA
Total	83	17.14	1.00	NA	NA

4.4.3.4 Visualisation of treatment effect

PCA was performed to visualise the factors identified in the PERMANOVA. While the first two principal components did not show a clear distinction between treatment groups, a more noticeable separation was observed between the second and third principal components. It would mean that the majority of cytokine are not defined by treatment, since no difference of PC1) but nevertheless there exist some changes (PC3 being different). The fact the differences are only visible on the third component makes sense since because there are lots of covariate effects, so the treatment effect is "hidden". Here this shows the importance of combining univariate (limma) and multivariate tests **(Figure 4.26).**

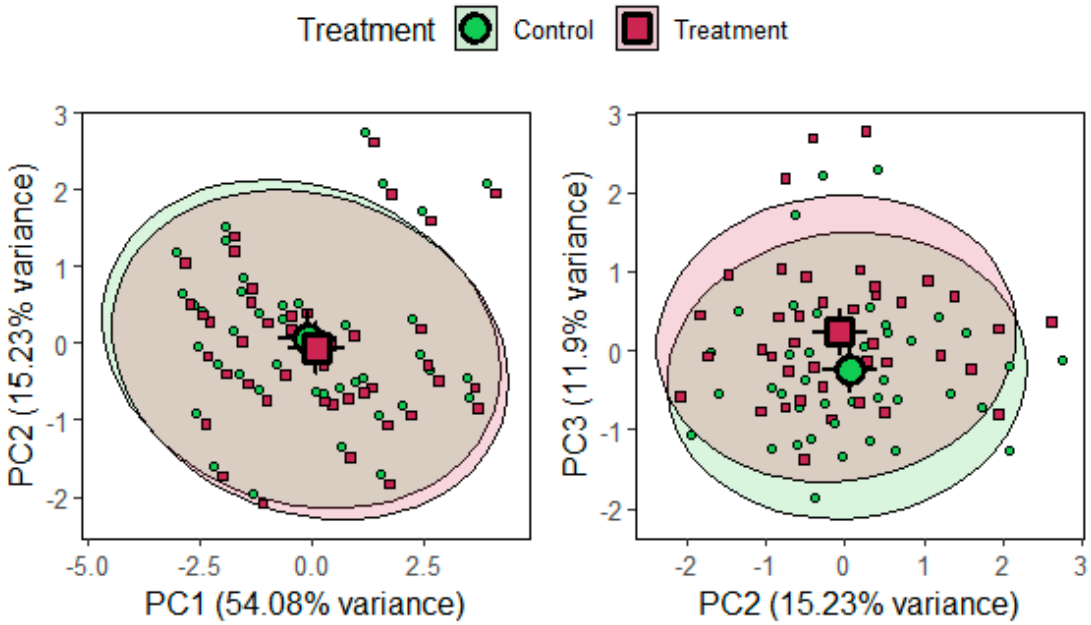

Figure 4.26: 2D PCA of treatment effect for all cytokines.
Left: PC2 vs PC1 plot. Right: PC3 vs PC2 axes. Large shapes show the centroids (± 95% confidence intervals). Small shapes show individual data points. Ellipses show the 95% confidence intervals. Polygons show the maximal dispersion between outermost points for each group.

4.4.3.5 Covariate effects

The PCA revealed distinct clustering patterns based on key covariates, including Time, Age, Gender, Recurrence, and MGMT status, aligning with the findings from PERMANOVA **(Figure 4.27)** To enhance visualisation, age was categorised into two groups (<60 and ≥60 years), which demonstrated noticeable differences in cytokine expression profiles **(Figure 7.1 in the appendix 7.6)**.

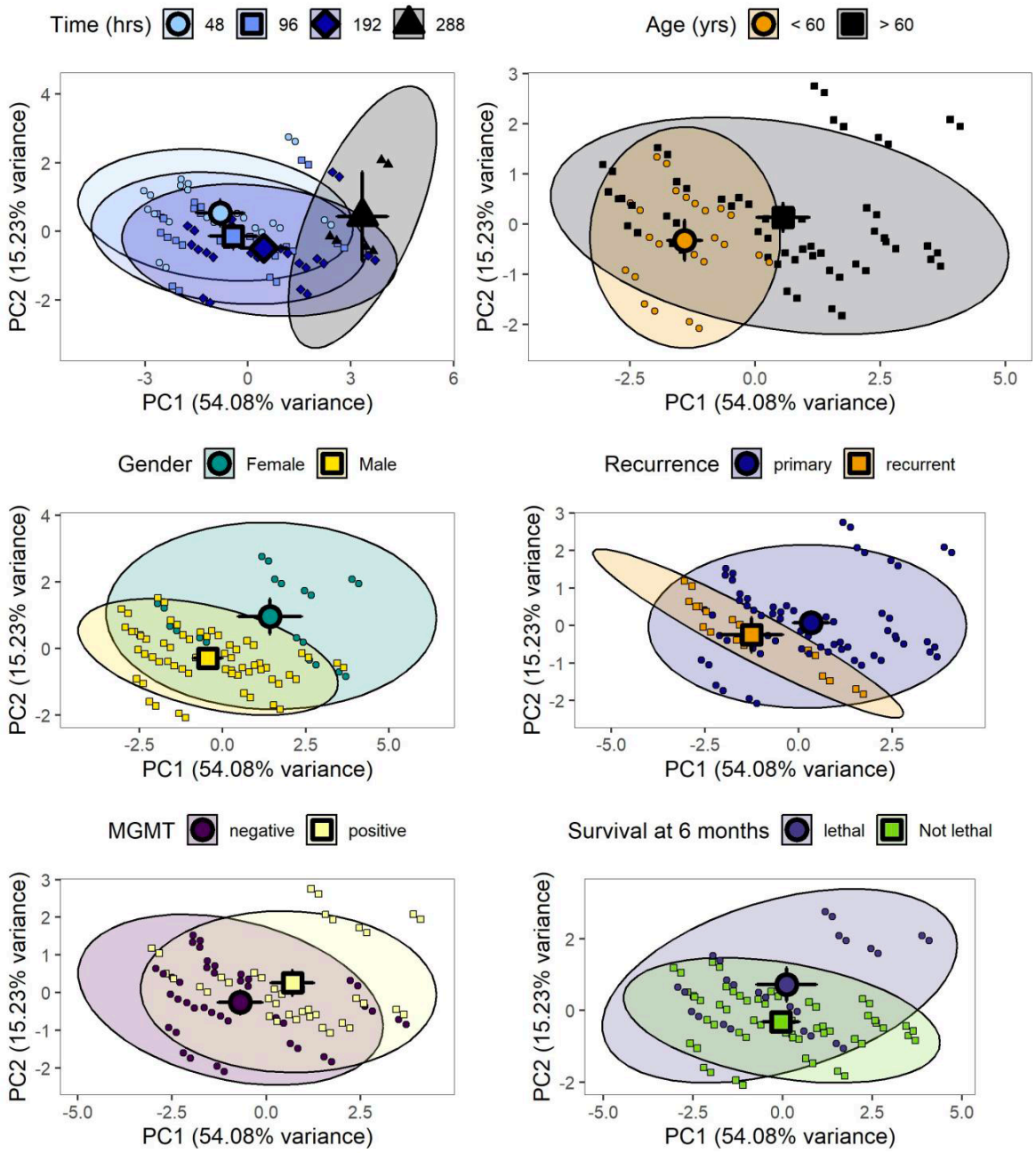

Figure 4.27: 2D PCA of covariate effects for all cytokines (PC1 and PC2).
Large shapes show the centroids (± 95% confidence intervals). Small shapes show individual data points. Ellipses show the 95% confidence intervals. Polygons show the maximal dispersion between outermost points for each group.

The pairwise PERMANOVA analysis showed significant differences in cytokine levels across all time points **(Table 4.14)**, highlighting the effect of time. In general, cytokine levels decreased as time progressed (Figure 7.2 in the appendix 7.6).

Table 4.14: Summary of pairwise PERMANOVAs for the time effect.

Comparison	Df	SumOfSqs	R^2	F	*P*	Evidence	R^2	ETA2
48 vs_288 hr	1	2.81	0.38	38.26	**0.0001**	Very strong	substantial	large
96 vs 288 hr	1	2.20	0.33	29.97	**0.0001**	Very strong	substantial	large
192 vs 288 hr	1	1.28	0.22	17.37	**0.0001**	Very strong	moderate	medium
48 vs 192 hr	1	1.69	0.17	24.89	**0.0001**	Very strong	moderate	medium
96 vs 192 hr	1	0.66	0.07	9.66	**0.0001**	Very strong	weak	small
48 vs 96 hr	1	0.64	0.07	9.43	**0.0004**	Very strong	weak	small

The significant differences between time groups are shown in bold. The pairwise PERMANOVAs are corrected for the effect of covariates. Evidence" reflects the strength of statistical significance based on the p-value (e.g., $p < 0.001$ = very strong evidence). "ETA²" (Eta-squared) represents the effect size, indicating how much of the variation in cytokine expression is explained by differences between time points. It is interpreted as: small (0.01), medium (0.06), and large (0.14), following Cohen's guidelines (Ben-Shachar et al., 2020, Cohen, 1988, Cohen, 1992).

4.4.4 Identification of important cytokines

Building on the multivariate analysis from the previous section, which showed that combined treatment significantly influenced overall cytokine expression, the aim was to identify the specific cytokines most affected by treatment. Identifying these key cytokines would help improve understanding of the molecular mechanisms underlying the treatment response and may reveal potential biomarkers for prognostic expectation and therapeutic targeting. To achieve this, a combination of PLS-DA and moderated t-tests was applied.

4.4.4.1 Univariate analysis of cytokines in function of treatment

PLS-DA identified three cytokines: (VEGF, CHI3L1, and MMP9) as the most significant in distinguishing between treatment groups VIP > 1) **(Figure 7.3 in Appendix 7.6).** Furthermore, analysis using Limma, with a linear model incorporating treatment, time, and covariates (MGMT status, survival at 6 months, recurrence status, age, and gender), confirmed that these three cytokines were significantly influenced by treatment after adjusting for multiple testing **(Figure 4.28, Table 4.15, Table 4.16)**. Finally, student t-tests on covariate-adjusted data also supported the treatment-induced changes in all three factors. The consistent results across all three methods strengthen the importance of the role these cytokines play in response to treatment **(Figure 4.29).**

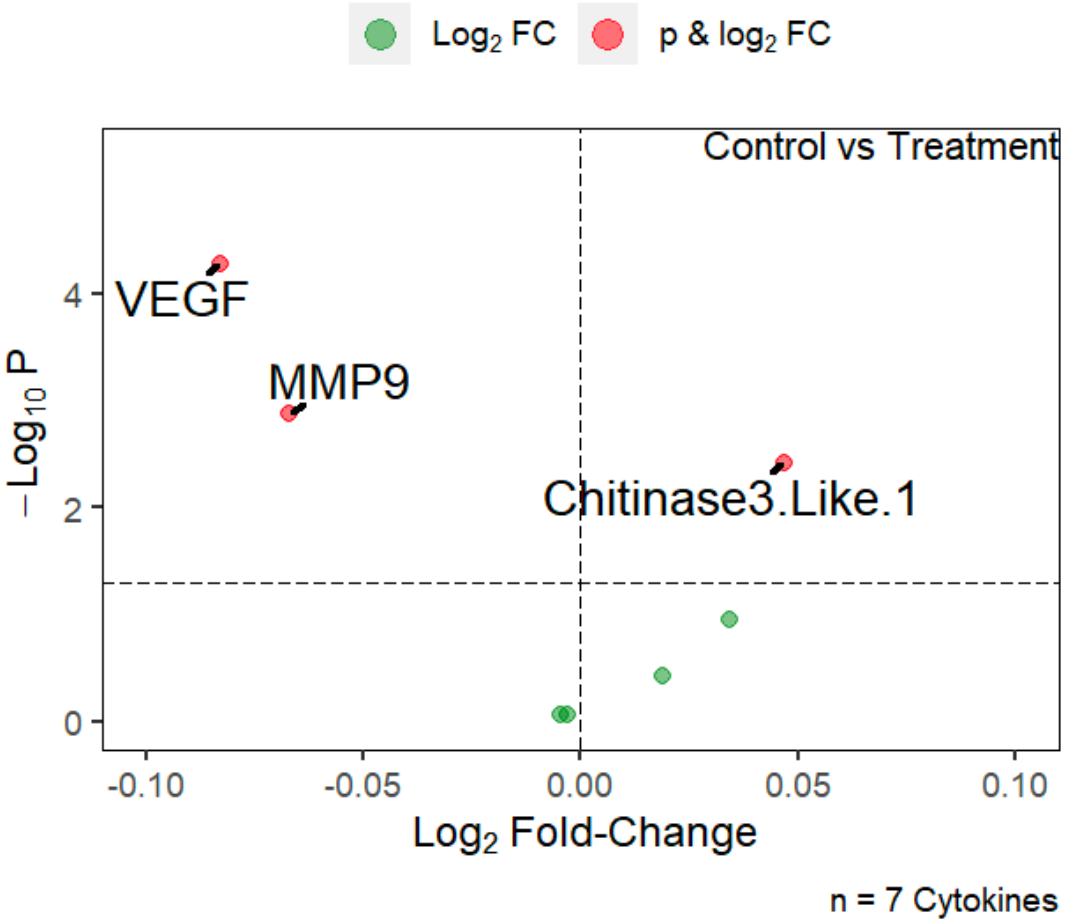

Figure 4.28: ***Volcano plot of the cytokine expression between treated and control biopsies.*** *The expression is adjusted for the covariates. Raw p-values are shown. Annotated points show the significant cytokines with raw p-values < 0.05.*

Table 4.15: Differential cytokine expression between treated and control GBM biopsies based on ELISA validation.

Cytokine	logFC	AveExpr	B	t	P.Value	adj.P.Val
VEGF	**-0.08**	0.00	1.66	**-4.25**	0.0001	**0.0004**
MMP9	**-0.07**	0.00	-1.33	**-3.32**	0.0013	**0.0046**
CHI3L1	**0.05**	0.00	-2.28	**2.97**	0.0038	**0.0088**
Angiopoietin 2	0.03	0.00	-5.19	1.60	0.1129	0.1976
Serpin E1	0.02	0.00	-6.05	0.88	0.3814	0.5340
IL6	0.00	0.00	-6.42	-0.17	0.8620	0.8752
IL8	0.00	0.00	-6.42	-0.16	0.8752	0.8752

Cytokine expression was compared between treated and control biopsies whilst adjusting for covariates. Significant cytokines after p-value correction are shown in bold. logFC = log10-fold change in treated biopsies relative to control. adj.P.Val = adjusted p-value.

Table 4.16: Comparison of covariate-adjusted residuals between treated and control groups using Student's t-test.

Cytokine	T	P	P-adj
VEGF	4.4859	0.0000	**0.0002**
MMP9	3.4712	0.0008	**0.0029**
CHI3L1	-3.3385	0.0013	**0.0030**
Angiopoietin 2	-1.6565	0.1015	0.1775
Serpin E1	-0.9091	0.3660	0.5124
IL6	0.1750	0.8615	0.8655
IL8	0.1699	0.8655	0.8655

Cytokine expression was compared between treated and control biopsies whilst adjusting for covariates. Significant cytokines after p-value correction are shown in bold. P-adj = adjusted p-value. A model is fitted to the covariates and the residuals are extracted. This removed the effects of covariates and looks only at the treatment effect. It is similar to the limma test but just an alternative method to ensure similar results across methods were found.

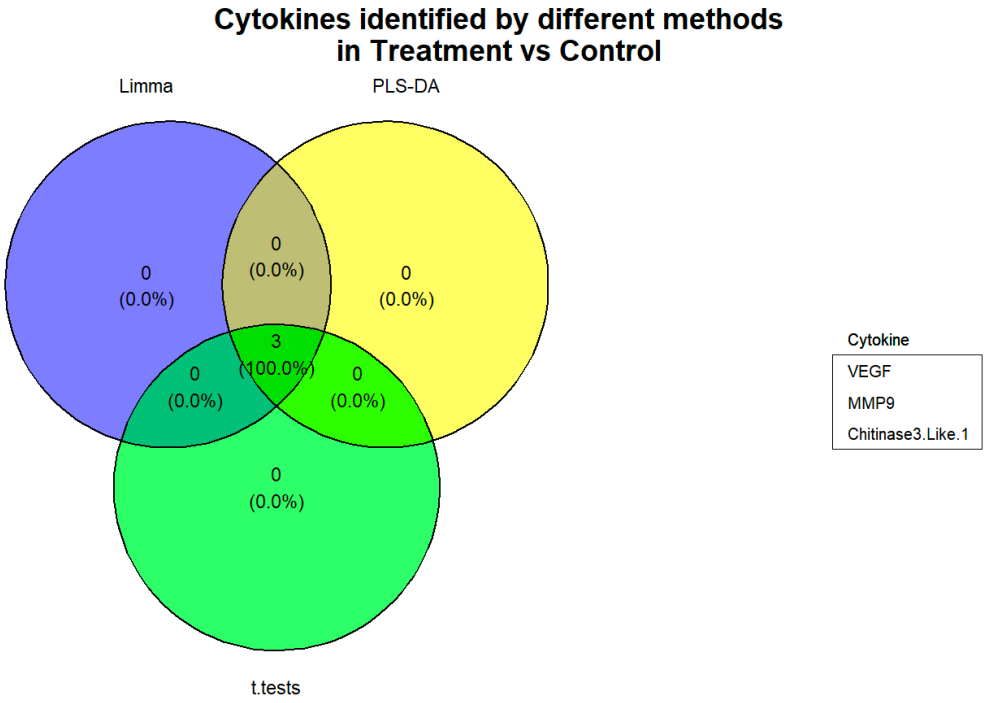

Figure 4.29: Cytokines influenced by treatment identified by Student's t-tests, a PLS-DA, and Limma moderated t-tests methods.

In summary, the production of three cytokines (VEGF, MMP9 and CHI3L1) is significantly changed in response to treatment whichever statistical method was applied (PLS-DA, Limma linear modelling and covariate-adjusted student's t-tests), confirming the robustness of the observed findings. While VGEF and MMP9 were significantly downregulated, CHI3L1 was upregulated under the effect of treatment.

4.4.4.2 Multivariate analysis of cytokines altered by treatment

To further examine the treatment effect on the most responsive cytokines, a PERMANOVA analysis was conducted, focusing specifically on VEGF, CHI3L1, and MMP9. Compared to the initial PERMANOVA, which included all seven cytokines, this targeted analysis demonstrated a stronger treatment effect, as reflected by a higher F value (**Figure 4.17**). Additionally, the separation between treated and control biopsies became more pronounced in the PCA when considering only these three cytokines, highlighting their significance as key markers of treatment response **(Figure 4.30).**

Table 4.17: Summary of PERMANOVA using only the three most contributing cytokines.

Term	Df	SumOfSqs	R^2	F	Pr (>F)
Treatment	**1**	**0.29**	**0.05**	**13.41**	**0.0001**
Time hrs	**3**	**0.99**	**0.19**	**15.56**	**0.0001**
Gender	**1**	**0.81**	**0.16**	**38.12**	**0.0001**
Age (years)	**1**	**0.99**	**0.19**	**46.35**	**0.0001**
Recurrence status	1	0.07	0.01	3.22	0.0342
MGMT status	**1**	**0.13**	**0.02**	**5.92**	**0.0031**
Survival at 6 months	**1**	**0.37**	**0.07**	**17.25**	**0.0001**
Residual	74	1.58	0.30	NA	NA
Total	83	5.22	1.00	NA	NA

Significant terms are shown in bold.

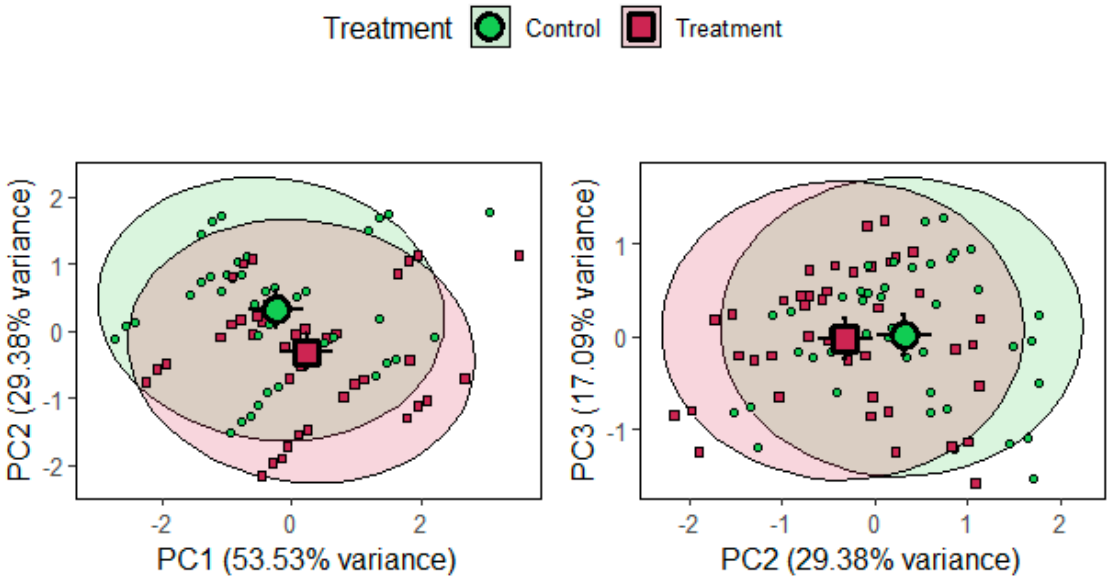

Figure 4.30: Principal Component Analysis of the effect of treatments for all times for cytokines of interest.

Large shapes show the centroids (± 95% confidence intervals). Small shapes show individual data points. Ellipses show the 95% confidence intervals.

4.4.5 Data validation: ELISA vs profiler

To verify the accuracy and reliability of the cytokine expression data, a validation study was conducted by comparing results from the semi-quantitative proteome profiler assay with quantitative ELISA measurements. This comparison was essential to ensure that the observed changes in cytokine levels were consistent across different analytical methods, thereby increasing confidence in the findings. A comparison of processed data (**Figure 4.31**) revealed significant positive correlations for four of the chosen seven cytokines**:** IL-8, VEGF, CHI3L1, and MMP9 ($p < 0.001$), indicating strong agreement between platforms after normalization. When comparing the raw, unprocessed values **(Figure 4.32),** five cytokines our of seven (IL-8, IL-6, VEGF, CHI3L1, and MMP9) showed statistically significant correlations ($p < 0.001$), reinforcing the consistency and biological relevance of these targets across analytical methods. Conversely, Angiopoietin-2 and Serpin E1 demonstrated weaker or nonsignificant correlations in both comparisons, suggesting potential technical limitations or lower sensitivity for these cytokines in one or both assays. Overall, the strong harmony observed for the majority of examined cytokines, proves the validity of the proteome profiler findings and confirms the robustness of key cytokine measurements.

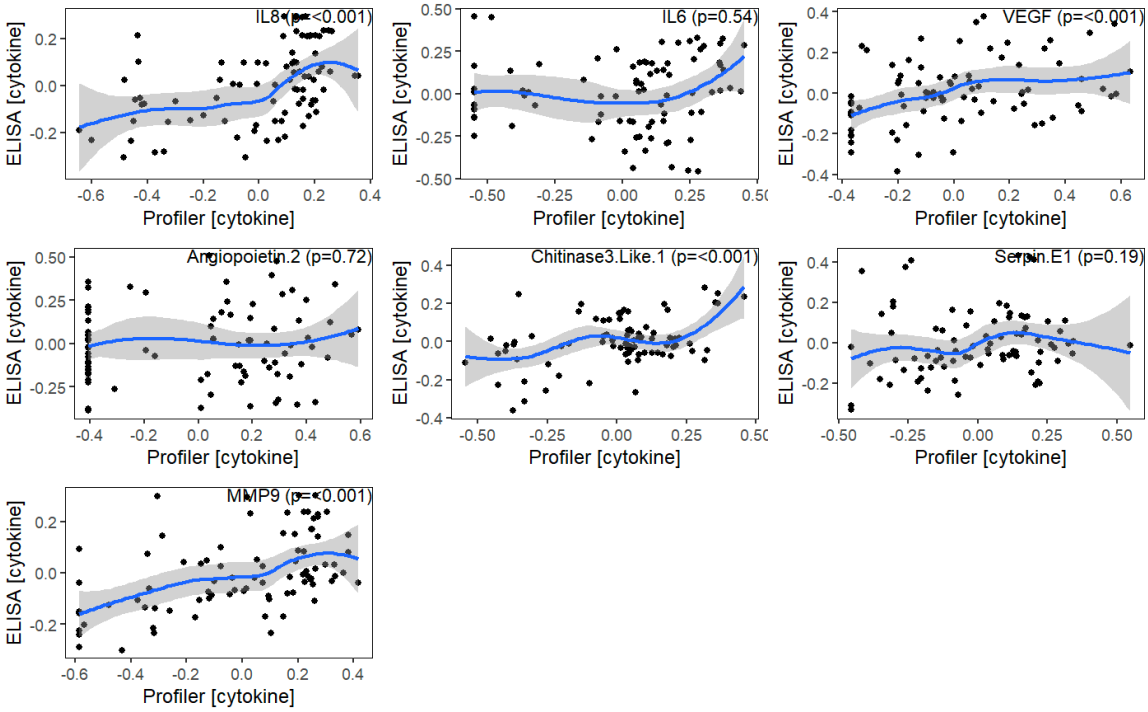

Figure 4.31: Correlation between the processed profiler data and processed ELISA data for the target cytokines.

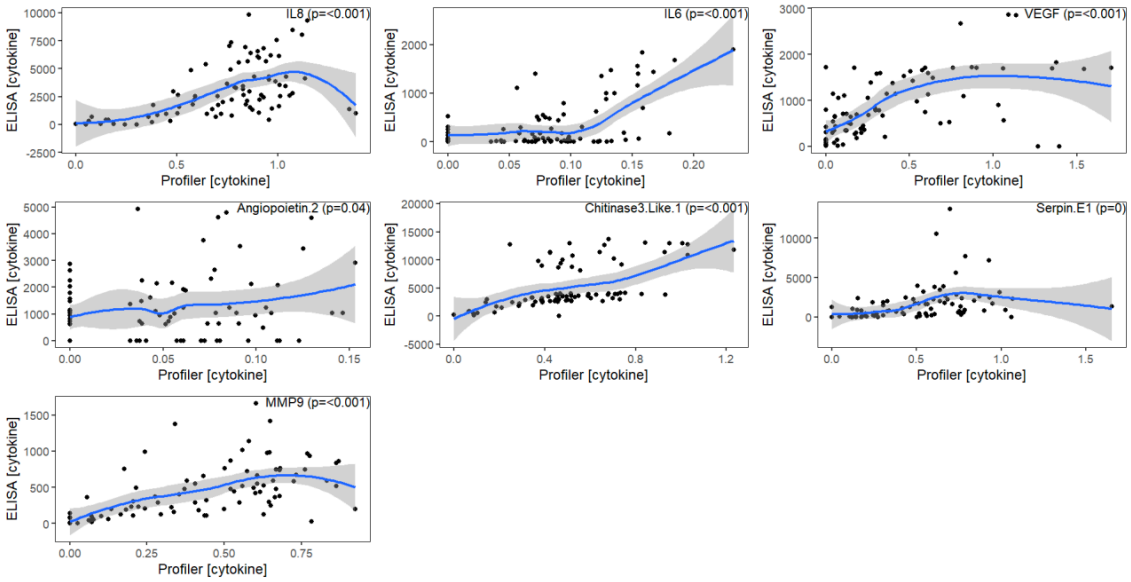

Figure 4.32: Correlation between the raw profiler data and raw ELISA data for the target cytokines.

5 Discussion

5.1 Overview of Study & Major Findings

GBM remains one of the most lethal brain malignancies, with limited therapeutic progress over the past 20 years despite advances in surgical and medical techniques. Resistance to the current standard chemoradiotherapy regimen that includes TMZ, is a core driver of treatment failure and disease progression. This phenomenon urges a dual need: first, to develop novel therapeutics that operate through mechanisms distinct from TMZ, and second, to deepen the biological understanding of how TMZ resistance develops. Achieving either goal requires translationally relevant experimental models that reflect the profound heterogeneity of GBM and its dynamic microenvironment.

New models must function over sufficient time to observe meaningful biological responses to treatment and mirror the *in vivo* environment as closely as possible. In this context, the current study created a novel microfluidic platform capable of keeping patient-derived GBM tissue viable *ex vivo* for up to 12 days, thereby enabling both longitudinal drug testing and temporal cytokine profiling. To the author's knowledge, this is the most extended duration reported for maintaining viable GBM patient tissues in a flow-based 3D platform, and it represents an important step toward bridging preclinical studies with clinically practical insights while respecting personalised and precision medicine.

Using this PMMA-based device, cytokine secretion profiles were determined under the effect of TMZ and a PRMT inhibitor using a proteome profiler, that could detect 105 human cytokines simultaneously. Following this initial screen individual ELISA analysis of seven consistently detectable cytokines was undertaken. The key findings were:

- **Model Viability and Feasibility:** The platform successfully maintained tumour viability and cytokine output, supporting its application for studying GBM biology and pharmacologic response in a patient-specific manner.
- **Temporal and Treatment-Related Trends:** Time-course analysis revealed shifts in cytokine expression, i.e. VEGF, MMP-9, and CHI3L1 in response to a combination of TMZ and the PRMT inhibitor GSK3368715.

- **The novelty of patient-specific factors on cytokine expression:** Multivariate analysis identified significant influences of age and gender on cytokine levels. The cytokine secretion observed was higher in females and patients under the age of 60. It declined over time spent on chip. This is the first study to report such demographic influences using a microfluidic GBM model, which can be considered a step further towards potential personalised medicine, although this should be interpreted with caution due to the relatively small sample size.

The most important methodological facet of the microfluidic system used in this study was that it maintained the biopsy in a viable state, so that hopefully it would respond as it would have if treated *in vivo*, i.e. preserving the tumour microenvironment. The system enables the study of tissue behaviour over time, the effects of drugs within an environment where the flow pressure, shear stress, substance transport and drug effects can all be controlled (Barry et al., 2023b, Hosni et al., 2023, Zhang et al., 2017, Jarrah et al., 2023). Below, is a discussion of the microfluidic device materials and related brain tumour research using different platforms, the biological effects observed from the tissue and specifically changes in three key cytokines (VEGF, MMP9 and CHI3L1).

5.2 Materials used in microfluidic platform

Many different materials are used in microfluidic manufacturing. These includes inorganic materials (silicon and glass), polyurethane methacrylate, PDMS, elastomers and thermoplastic material such as thermosetting polyester, and polycarbonate, PMMA and polystyrene (Ding et al., 2020). PDMS is the most widely used material for fabricating tumour-on-a-chip devices because of its optical transparency, biocompatibility, low cost, and ease of use, which enables a real-time assessment of cell behaviour and response to treatment with continuous microscopic observation of tumour tissue (Toepke and Beebe, 2006). PDMS is the material of choice for most laboratory-based studies. Despite this, the hydrophobicity characteristics represent the major drawbacks of this material, which limits its application in drug screening, because of non-standardised absorption of hydrophobic molecules (Auner et al., 2019).

Kang's group developed one of the first tissue on chip devices using PMMA, which is impermeable to small lipophilic molecules (Nguyen et al., 2019). They compared human lung adenocarcinoma cells cultured on PMMA and PDMS devices, and showed more reliable responses regarding the cytotoxicity caused after the addition of vincristine in the former material (Nguyen et al., 2019). A further advantage of PMMA is that it is recyclable and reusable after simple sterilisation, making it an environmentally friendly choice (Wan et al., 2017). PMMA material-based microfluidic devices offer additional advantages. They have excellent optical transparency and are cost-effective, particularly when scaled up for automated manufacture. (Matellan and del Río Hernández, 2018,

Zheng et al., 2014, Ma et al., 2020). Two recent studies from the Hull laboratory both used PMMA based microfluidic devices. The first one demonstrated a successful small Interfering RNA (siRNA)-mediated knockdown of genes in GBM spheroids (U 87 cells) cultured using the same microfluidic device employed in the current study. Gene expression was measured by quantitative-PCR(q-PCR)(Hosni et al., 2023). In the other study patient GBM tissue was successfully maintained in a viable condition for eight days post-surgical resection and was analysed principally by immunohistochemistry. Moreover they did drug testing experiments of GBM tissue using PRMT inhibitors demonstrating that there was crosstalk between different types of arginine methylation which had been observed in clinical samples after treatment (Barry et al., 2023b).

However, PMMA has some drawbacks, such as moisture absorption properties and low cell adhesion alongside manufacturing issues such as dimensional inaccuracy during laser micromachining, which can lead to rough or uneven microchannel shapes. (Rega et al., 2019, Mecozzi et al., 2016, Sharifi et al., 2020, Sözmen and Arslan Yildiz, 2021). In addition to PDMS and PMMA base materials, various natural biomaterials can be added to modify the microfluidic model. These include Matrigel™, collagen, hyaluronic acid and hydrogels, which all promote and stimulate the cellular matrix's composition and structure, with the aim of better modelling the *in vivo* situation. However, these materials may limit microfluidic reproducibility and reliability due to their variable composition, potential contaminants with undesired soluble components, rapid degradation, and variability between batches (Barbosa et al., 2021).

5.3 *In vitro* GBM models: tissue, spheroids, and organoid approaches

5.3.1 Patient tissue based GBM models

In a recent review Liu et al. (2022) have stated that microfluidic devices now represent reliable systems for the maintenance and the study of tumour tissues extracted from patients, enabling a continuous flow of nutrients and removal of waste offering an *ex-vivo* tumour microenvironment mimicking that of the original tumour (Liu et al., 2022). Various microfluidic models have been used in prior studies to preserve and study normal and tumour tissues extracted from various cancer types, including ovarian (Astolfi et al., 2016), lung (Yang et al., 2018), rectal (Rodriguez et al., 2020), thyroid(Riley et al., 2021), head and neck (Green et al., 2012), and brain (Cho et al., 2021).

Most of the microfluidic applications on brain tumours studied glioma as it is the most common and deadly brain tumour. An early study by (Liu et al., 2010) developed a microfluidic device consisting of four parallel chambers to study the response of C6 glioma rat cells to colchicine. They found that increasing colchicine concentration or treatment time induced significant changes in cell morphology and increased death rate. (Fan et al., 2016) used a 3D brain tumour microchip fabricated

from Polyethylene Glycol Diacrylate (PEGDA), a hydrogel, with top and bottom cover glass for high-throughput drug screening (Pitavastatin and Irinotecan combination) using U87 GBM spheroids. Spheroids were grown for 7 days, until 300-400 μm in diameter before being tested with various, clinically relevant, drug combinations for another 7 days. In a novel study, (Xiao et al., 2019) developed a vascularized microfluidic model to investigate the behaviour of brain tumour stem-like cells (BTSCs) within a perivascular niche like environment. They used dissociated BTSCs derived from 10 primary IDH-wildtype GBM patients, and co-cultured them in a commercial AIM Biotech microfluidic device made of PDMS. This device consists of a central hydrogel channel containing green fluorescent protein (GFP)-labelled human umbilical vein endothelial cells (HUVECs) and red-stained BTSCs, along with two lateral media channels, with nutrient delivery maintained by gravity flow. After 48 hrs of culture, live confocal microscopy was performed for an additional 20 hrs, capturing images every 30 minutes to monitor BTSC behaviour. The authors observed that BTSCs displayed heterogeneous behaviour; some cells remained quiescent near microvessels, while others exhibited active migration along vascular tracks, mimicking *in vivo* infiltration **(Figure 5.1 A).** The first microfluidic device to utilise intact patient-derived GBM tissue was developed by the Hull laboratory (Olubajo et al., 2020). They used 128 tissue biopsies from 33 patients (average weight of 10-15mg) and demonstrated that GBM tissue can be maintained viable in the microfluidic chip made of PDMS with a glass cover for about 72 hrs using a flow rate of 4 μL/ min **(Figure 5.1 B).** (Wong et al., 2021a) developed a microfluidic platform called **MAqCI** (Microfluidic Assay for Quantification of Cell Invasion), which aims to mimic the GBM invasion of brain tissue. The device contains Y-shaped microchannels that progressively narrow from 20 μm to 10 μm and finally to 3 μm**,** allowing precise tracking of how far tumour cells can migrate. Primary GBM cells were freshly isolated from surgical resections of treatment-naïve patients**,** briefly cultured and seeded into the device on laminin-coated channels, which simulate the native brain extracellular matrix. Migration was monitored via 24-hour live-cell imaging, and proliferation was measured using Kiel-67 protein (Ki-67) staining. The assay categorized 28 patients into short- and long-term progression-free survival groups with an accuracy of 86%**,** and also predicted time to recurrence. Moreover, it prospectively and correctly predicted survival classification in five additional patients. The combined MAqCI score based on migratory and proliferative behaviour outperformed traditional prognostic markers, including IDH1 mutation status and total Ki-67 expression, offering a rapid, low-cost, and clinically informative assay for glioblastoma prognosis **(Figure 5.1 C).** Lastly, the microfluidic device used in this study has also been used recently for successful maintenance and drug testing on GBM tissues for 8 days (Barry et al., 2023b)**(Figure 5.1 D).**

In the present work, GBM tissue (average weight of 20 mg/biopsy) was maintained in a device for an extended duration of 12 days, using a perfusion-based GBM tissue platform, using a syringe pump at a flow rate of 3 µL/min. The viable state was demonstrated by the combination of biochemical assays (LDH activity), histological analysis (H&E staining and IHC for apoptotic markers), and sustained cytokine release (Proteome profiler and ELISA assays). This platform has been successfully adopted by several other groups nationally (Academic Surgical Unit, Leeds University; Quadram Institute: UK Health Security Agency (UK-HSA), Porton Down) and internationally (Head & Neck Oncology, All India Institute of Medical Sciences) demonstrating the expanding utility of this technology. Collaborative work with the UK-HSA and Quadram Institute developed a dual-flow gut–brain microphysiological system (MPS) fabricated in PMMA investigating epithelial-to-neuronal translocation. This system enables off-chip pre-culture and employs continuous perfusion via a syringe pump at a controlled flow rate of 2.94 µl/min, mimicking systemic circulation. Colonic epithelial cells were cultured off-chip for 5–6 days and SH-SY5Y neuronal cells were differentiated for 18 days (including 8 days on-chip). The assembled chips were perfused and maintained under flow for 24 hrs before fixation and imaging. They assessed neuronal-specific cytotoxicity and mitochondrial toxicity caused by the translocation of 1-methyl-4-phenylpyridinium (MPP^+), a neurotoxic metabolite that selectively targets dopaminergic neurons, from gut to brain. This revealed significant neuronal death and mitochondrial fragmentation after 24 h of perfusion (Jones et al., 2024) **(Figure 5.1 E).**

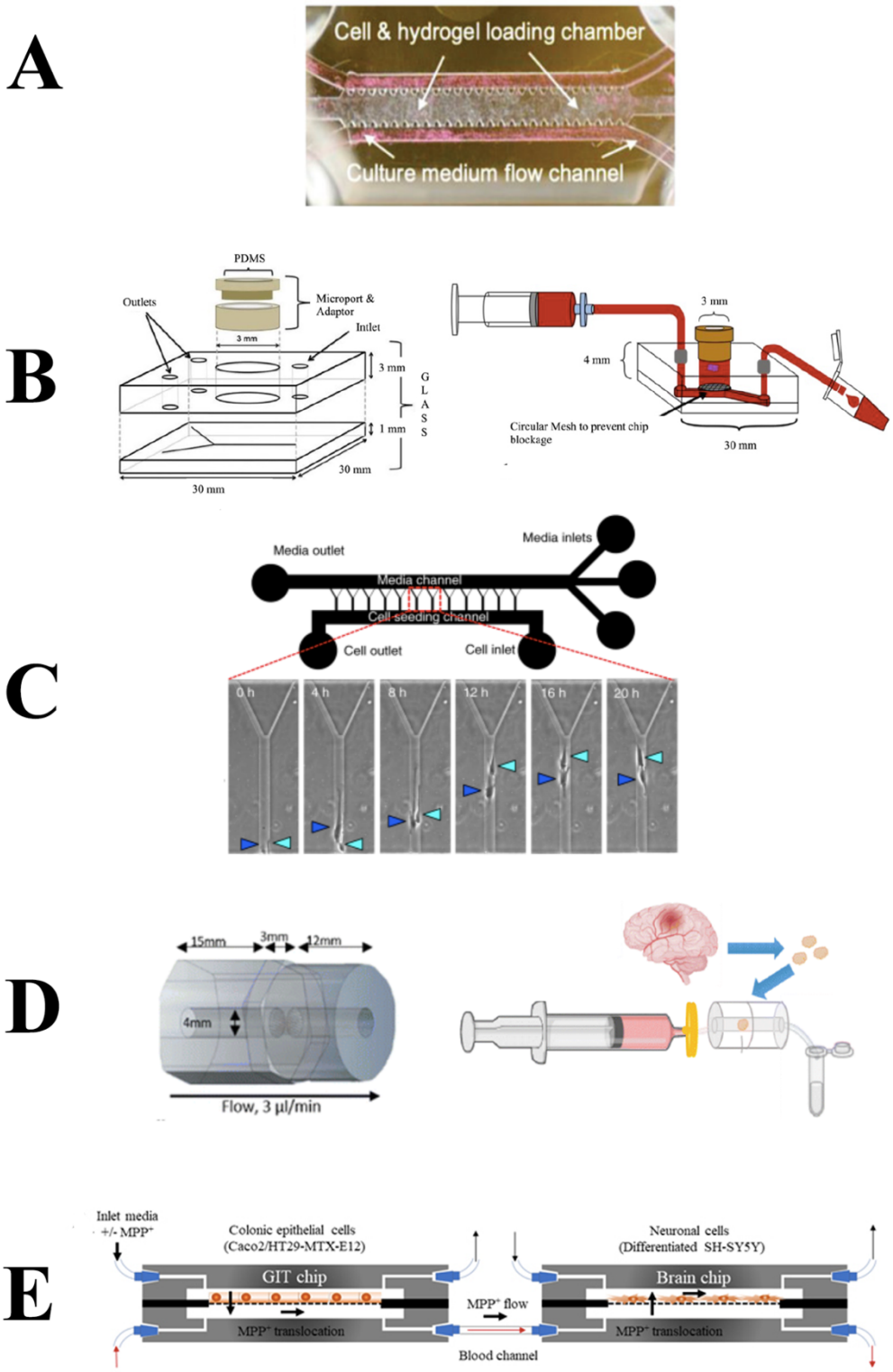

Figure 5.1: Different microfluidic GBM based models.

A. BTSC-incorporated microvasculature-on-a- PDMS chip (Xiao et al., 2019).
B. PDMS microfluidic with glass cover (Olubajo et al., 2020).
C. Microfluidic Assay for Quantification of Cell Invasion with Y-shaped microchannels . (Wong et al., 2021a).
D.PMMA single lumen microfluid chip .(Barry et al., 2023a)
E. Dual-flow gut–brain microphysiological system (Jones et al., 2024).

Microfluidic chips offer a cost-effective and physiologically relevant environment for studying glioma by replicating *in vivo*-like perfusion and reducing sample and reagent use. They are particularly valuable for personalized medicine, enabling real-time testing of patient-derived cells under controlled, continuous conditions. The microfluidic model used here, and all other models, still have limitations that need to be considered. The relatively short duration of time culture is compared to clinical reality, where the patient received more than 6 months of chemotherapy postoperatively(Stupp et al., 2009). It lacks the dynamic interaction with surrounding normal brain tissue. Given the limited amount of GBM tissue dedicated to the microfluidic chip, the study model is limited in high throughput screening potential. Collectively, despite advances in microfluidic platform technology, it does not fully mimic the complex GBM TME, and therefore, further development is required (Xie et al., 2023b).

5.3.2 Spheroid-Based GBM Models

Intact GBM patient tissue is not the only source of GBM cells that can be used in 3D microfluidic devices**,** spheroids and organoids are also commonly studied (Figure 5.2). Looking first at spheroid-based microfluidic platforms: (Akay et al., 2018a) developed a microfluidic *chip* that cultured 3D spheroids from patient-derived primary GBM cells obtained from three surgical specimens. Over a 14-day total period (7 days to grow the spheroid plus 7 days of drug testing)**,** spheroids were formed and then exposed to TMZ and BVZ via diffusion-based microfluidic channels. Drug efficacy was evaluated through spheroid volume reduction and trypan blue exclusion assays on day 7 post-treatment, revealing variable patient-specific responses. Notably, combination therapy (TMZ + BVZ) was more effective than monotherapy across all samples. This low-cost device was made of hydrogel layers between upper and lower cover glass slides, offers the potential for rapid, **personalised, drug screening**. However, the authors acknowledged limitations in spheroid viability when using freshly dissociated cells directly and the challenge of replicating the whole tumour microenvironment *in vitro*. (Ko et al., 2019) developed a 3D tumour spheroid on a chip platform named (Spheroid-based *In vitro* MicroPhysiological Angiogenesis and Cancer Testing) (Sphero-IMPACT), using U87MG glioblastoma cells in a 96-well plate design, fabricated from polystyrene. U87-derived spheroids (500–600 μm in diameter) were co-cultured with endothelial cells, and imaging was performed over 4 days. The system successfully modelled tumour behaviours such as invasion, migration, and angiogenesis, enabling pharmacological testing. Following Tumour necrosis factor-alpha (TNF-α) and TGF-β1 exposure, U87 cells exhibited increased invasive and migratory activity within 48 hrs. Furthermore, angiogenesis and drug screening assays confirmed that anti-angiogenic agents (bevacizumab, sunitinib) significantly reduced vascular area, sprouting length, and vessel number. More recently, (Hosni et al., 2023) which was mentioned before, demonstrated a U87

spheroid-based microfluidic system allowing gene knockdown using siRNA under continuous perfusion 2 μL/min, showing downregulation of cell adhesion genes, suggesting a potential shift toward a more invasive phenotype. Functional assays demonstrated effective knockdown of target genes PRMT2 and Ras-related protein Rab-21(RAB21).

Although spheroid-based models provide a 3D architecture that better resembles *in vivo* tumour structure compared to 2D cultures, above studies all have highlighted differences. (Akay et al., 2018a) emphasized that these models often lack vascular perfusion, and native extracellular matrix organization. Hosni et al. (2023) demonstrated that static spheroid cultures show reduced proliferation and altered gene expression compared to those under flow conditions. (Ko et al., 2019) further stressed that spheroid models fail to recapitulate essential *in vivo* features such as vascularization, shear stress, and dynamic cell–ECM interactions. Collectively, these findings suggest that while useful, spheroid-only systems are insufficient to fully replicate the glioblastoma microenvironment and may benefit from integration with perfused or vascularized microfluidic platforms. Taking all these factors together, at present they are major limits in their translational relevance for modelling patient-specific GBM biology.

5.3.3 Organoid-Based GBM Models

On the other hand, organoid-based microfluidic platforms represent an advanced model for studying GBM, as they can mimic the tumour's cytoarchitecture, cell diversity, and patient-specific features more effectively than spheroids (Figure 5.2). Two examples of organoids; those derived from induced pluripotent stem cells (iPSCs) or disaggregated patient tumour biopsies are described for comparison. For example, Hwang et al. (2020) developed a GBM model using iPSCs, which are adult somatic cells reprogrammed to a pluripotent state capable of generating any cell type. In this study, stem cells were derived from a patient carrying a c-MET mutation and cultured as aggregates over a long-term period of 90 days, allowing them to differentiate into neuronal-like organoids spontaneously. These organoids expressed many hallmarks of GBM as confirmed through immunostaining, gene expression profiling, and electron microscopy. To evaluate drug response, the organoids were treated with TMZ for 5 days at 700 μmol/well. Caspase-3 immunostaining was used to assess apoptosis, which revealed that the c-MET-mutated organoids were more sensitive to TMZ than control organoids, demonstrating the potential of this iPSC-derived organoid model as a personalised platform for GBM research and drug testing. However, this model is technically more complex and requires extended culture time, with the associated risks of infection. Additionally, like almost all models they lack the vasculature and immune cells, which are critical components in the GBM microenvironment (Hwang et al., 2020). Another organoid model established by Jacob et al. (2020) established a glioblastoma organoid (GBO) model using intact tumour tissue from patients

without enzymatic dissociation. Small tumour fragments (~1 mm) were cultured, allowing organoids to form within 1–2 weeks. The GBO retained the original tumours' cellular heterogeneity and genetic profile and could be maintained for 48 weeks in culture. To evaluate treatment response, organoids were exposed to temozolomide (50 µM) for one week with single 10 Gy radiation**,** and the effect was measured using Ki-67 immunostaining, a cell proliferation marker. A decrease in Ki-67 positive cells indicated reduced tumour proliferation, reflecting sensitivity to treatment. Despite its advantages, the model has limitations, including reduced vascular and immune components over time and relatively lower success rates in IDH1-mutant tumours (66.7%) (Jacob et al., 2020).

On of the most recent study which does not fall under classical microfluidic, spheroid, or organoid models, is that by (Posthoorn-Verheul et al., 2025) who used a hybrid approach. They established glioma stem-like cell (GSC) cultures from 114 GBM patients, using both single-cell-derived and 3D fragment-derived tissue processing. After 5–8 days in initial suspension culture cells were transferred into Culture Basement Membrane Extract (BME)-coated flasks, enriched for adhesion and growth. This protocol successfully enabled personalized drug screening on 16 of 18 samples within 3 weeks using 21 different anti-cancer drugs including TMZ. They demonstrated sustained molecular heterogeneity and genomic stability across multiple passages during culture process. This method shortens the interval between surgical resection operation and functional assays establishment. This can be a potential robust platform for GBM patient tissue.

Each model offers distinct advantages: spheroids for simplicity and relatively high throughput, organoids for longevity and incorporation of multiple cell types, and intact tissue-on-chip (the model used in this thesis) for immediate translation and preservation of tumour complexity. In future consideration for the choice of platform, it must be aligned with the specific research question and availability of cell sources and lab facilities.

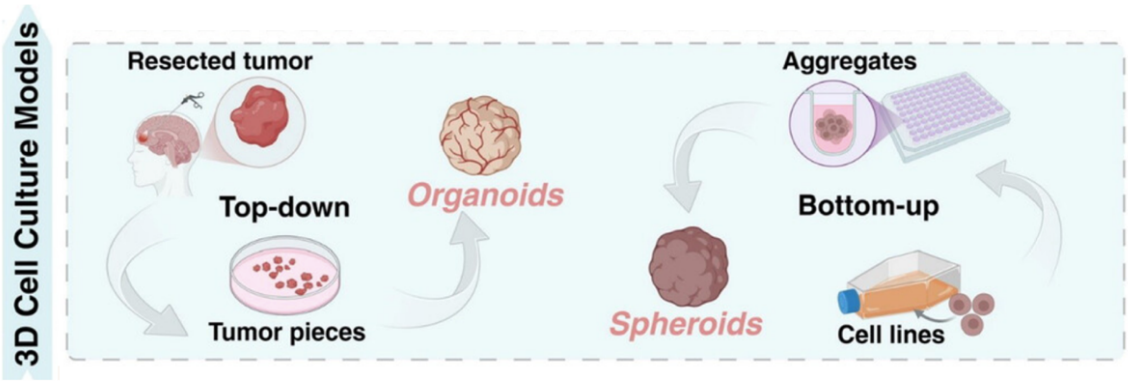

Figure 5.2: 3D cell culture models (Tissue, organoids ,spheroids)

Adapted from (Liu et al., 2025)

5.4 Overall effect of TMZ on cytokines

The current work used a PMMA-based microfluidic platform continually delivering the combined treatment (1 μM GSK3368715 and 10 μM TMZ) showed no significant effect on cytokine levels ($p = 0.1977$) during the 12-day duration. However, looking at different platforms that examined the effect of TMZ on GBM in culture, Zhang and colleagues found no significant impact of TMZ (300 μM) on U87 GBM cell line monolayer viability using Calcein-AM/PI double staining assay in a PDMS-based chip following a 6 hour exposure (Zhang et al., 2020c). Interestingly, Samiei et al. (2020) demonstrated that GBM cells (U87 and U251) were significantly less sensitive to TMZ in a 3D PDMS microfluidic model than in conventional 2D cultures. Over 72 hrs, TMZ (0–500 μM) combined with simvastatin led to a dose-dependent reduction in cell viability and invasion and increased apoptosis, with more pronounced effects in 2D than 3D. Considering the duration of exposure to TMZ, the study of Ozturk et al showed initial tumour regression and decreased metabolic activity followed by regrowth (using second-generation mesoscopic fluorescence molecular tomography+ wide-field fluorescence microscopy imaging) under the effect of 100 μM TMZ over 70 days using Patient-derived GBM spheroids loaded on a 3D bioprinted model (Ozturk et al., 2020).Those above studies have differences in the method used which could be attributed to differences in platform materials, cell sources, treatment duration, drug combinations, TMZ dosage, evaluation methods, and the specific cell lines or patient tissues used. Given the methodological differences, it is unsurprising that direct comparisons cannot be made. To mimic the clinical administration of TMZ in GBM patients, the optimal model needs to allow a longer treatment duration in order to better reflect the 6-month time frame of Stupp protocol.

5.5 Effects on VEGF following treatment

VEGF is a well-known therapeutic target in GBM due to its central role in angiogenesis (Lukas et al., 2019). In this thesis, it was shown that VEGF cytokine expression was significantly downregulated under the effect of treatment (TMZ + PRMT inhibitor; $p = .0004$). Interestingly, VEGF was detected in 83.3% of all effluent samples with a mean relative expression of 0.41 (on a scale of 0 to 1), suggesting a common and essential role in tumour maintenance. (Shin et al., 2025) used a vascularised PDMS microfluidic model that incorporated GBM spheroid with HUVECs spheroid, which led to endothelial sprouting and penetration, replicating the angiogenesis. They detected high VEGF levels after 48 hrs, which significantly reduced when treated with Bevacizumab loaded in the chip ($p < 0.01$) using both ELISA and quantitative Reverse Transcription Polymerase Chain Reaction (RT-PCR). Similarly, Lee et al., found that VEGF expression in U-87 GBM 2D monolayer cells cultured in a PDMS microfluidic chip was significantly reduced after 16 hrs of treatment with isolinderalactone, a Chinese natural product,

(P<0.001) which measured at both the transcript and protein levels using RT-PCR and Western blot respectively (Lee et al., 2022b). While no studies exactly mirrored this work microfluidic set-up, a common observation is a reduction in VEGF under the treatment effect. This supports the usage of VEGF as a reliable and sensitive biomarker for evaluating therapeutic effects of different drugs across different microfluidic platforms.

5.6 Effects on MMP9 following treatment

MMP9 secretion is known to be enhanced by VEGF signalling, leading to ECM degradation, allowing endothelial cells to invade the surrounding tissue and form new vascular structures (Ahir et al., 2020). In the current study, MMP9 followed a similar response to VEGF expression, with significant downregulation under the effect of treatment with TMZ and PRMT inhibitor. MMP9 was detected in 91.7% of all this work effluent samples with an average relative expression of 0.45, placing it among the top five highly expressed cytokines across the cohort. Similarly, (Mirabdaly et al., 2020) reported that MMP9 and VEGF expression and activity were decreased in the U87 MG cell line cultured in RPMI1640 medium under the effect of escalating dose of TMZ (15, 30, 60 μg/ml) over 1–3 days as measured by by RT-PCR and flow cytometry. ELISA and zymography also assessed MMP9 protein expression and activity. These studies consistently report that both VEGF and MMP9 expression are reduced by TMZ, despite differences between the two GBM models described above. Surprisingly, in contrast, Thanh et al. detected significant upregulation of MMP9 in specific GBM cell lines (U343 and U87MG) after 48 hrs in DMEM culture with 500 μM TMZ. y. MMP9 expression was measured by detecting protein (western blotting) and mRNA (quantitative RT-PCR). Although Thanh's findings of a transcriptional increase, they only detected low MMP9 enzyme activity using gelatine zymography in U343, U87, and GL261 cells, but activity was elevated in T98G, T98G-R (TMZ-resistant), and U251 cells (Thanh et al., 2024) .This discrepancy between the TMZ - MMP9 effect can suggest a dual relationship, where TMZ effectively kill GBM cells that secrete MMP9, resulting in a low expression level. Still, at the same time, survived or resistant cells increase MMP9 expression level as a survival mechanism. More studies are needed to clarify the nature of the connection between MMP and TMZ resistance in GBM.

5.7 Effects on CHI3L1 following treatment

CHI3L1, which was the most frequent cytokine present in 98.8% of all effluents and the third in most expressed cytokine (mean relative expression .52) regardless of time point or treatment. This is consistent with Kamniska et al preprint and Lie and colleagues, where CHI3L1 mRNA expression in GBM was nearly 60-fold higher than in normal brain tissue, using the Gene Expression Profiling Interactive Analysis (GEPIA) online platform (Li et al., 2023) (Kaminska et al., 2023). The prevalence of CHI3L1 was further supported by Nimbalkar et al. (2022) who showed that CHI3L1 mRNA was significantly higher in the GBM tissue of 34 patients when compared to 20 patients with non-neoplastic brain tissue ($P < .0001$). There is a consistent finding that CH13sL1 is a highly specific marker expressed abundantly in GBM, supporting its potential diagnostic biomarker role.

The work of this thesis also found that CHI3L1 was the only cytokine significantly upregulated with treatment (TMZ and PRMT inhibitor) **(**p=.0088). Aligning with this finding, Junker et al. found that CHI3L1level increased dramatically in glioma U87 cells under stress conditions caused by a single dose of ionising radiation (0,2,5,10 or 20 Gy or hypoxia (0.1% oxygen) when cultured in 2D monolayers for 48 hrs. The CHI3L1 level was measured at mRNA level (Northern blot analysis) and protein (ELISA) (Junker et al., 2005). Taking into consideration that Janker et al used relevant ionising radiation doses that were still different from what GBM patients received in the clinical world (2 Gy per day for 6 weeks except for weekends as per Stupp protocol), taken together with the work in this thesis suggests that an increase in CHI3L1 expression acts as a stress response of GBM to different treatment methods (chemotherapy, radiation, or hypoxia) and may contribute to tumour resistance and survival.

5.8 A summary of the strengths and limitations of the current study

5.8.1 Strengths:

- **Novel Microfluidic Platform:** The use of a microfluidic platform for maintaining patient-derived GBM tissue with all the microenvironment components, is a significant strength of this study. The maximum duration was 12 days in the laboratory. This approach allows for precise control over the tumour microenvironment and enables real-time monitoring of cytokine secretion.
- **Comprehensive Cytokine Profiling in patient-derived GBM tissue:** In this study a proteome profiler assay was used to screen 105 human cytokines simultaneously, providing a comprehensive overview of the cytokine landscape in GBM patient tissue. No past studies have screened this number of cytokines in a single GBM tissue sample.
- **Validation with ELISA:** Quantification using ELISA confirmed the findings from the

proteome profiler, thereby strengthening the reliability of the results and supporting the validity of both platforms for cytokine detection.

- **Patient-Specific Factors**: Considering patient-specific factors such as age, gender, and MGMT status, survival at 6 months is a strength of this study, as it highlights the importance of personalised medicine approaches in GBM treatment.
- **CHL31** is under-researched cytokine in GBM which was analysed in this study. It is the only cytokine that significantly upregulated against treatment which may refer to resistant mechanism. Further dedicated studies are required to characterize this cytokine in relation to treatment.

5.8.2 Limitations:

- The sample size of 13 patients limits the generalizability, meaning the findings should be considered as preliminary.
- Lack of solo TMZ treatment and solo PMRT inhibitor in addition to combination, to isolate the effect of each drug separately and compared to combined treatment and control; this was not possible due to the lack of tissue.
- Only three out of thirteen patients had tissue maintained for the full 12-day duration (set up in duplicate with control and treatment arms), while the remaining cases were limited to 8 days. A larger sample size is needed to more confidently validate the platform's ability to sustain GBM tissue for extended periods.
- Microfluidic platform effluent analysis was performed at selected time points over a 12-day period rather than daily. In future studies, daily cytokine measurements would provide a more detailed profile.
- Logistical considerations are critical. Due to the need for access to viable surgical specimens, a close proximity between the operating theatre and the laboratory is essential. This requirement may present significant challenges for replicating the model in other centres.

5.9 What is the potential impact of the project on neurosurgery clinical practice?

This study has several potential implications for neurosurgery clinical practice:

- **Personalised Medicine:** The influence of patient-specific factors such as age and gender on cytokine profiles can be measured and observed for their responses to treatment. It can be considerable factors to determine individual patient characteristics in GBM treatment strategies.
- **Drug Development:** The microfluidic platform used in this study could be used to screen other new drugs and drug combinations for GBM. This approach may allow rapid and cost-effective assessment of drug responses in patient-derived tissue in the future, with the added benefit of

reducing animal experimentation.

- **Therapeutic Targets:** The identification of specific cytokines that are responsive to treatment, as well as those that are consistently highly expressed, may provide potential therapeutic targets for GBM. For example, specific inhibitors or antibodies could target VEGF, MMP9, and CHI3L1, alone or in combination.
- **Prognostic Markers:** The cytokine profiles could potentially be used as a tool to predict patient outcomes and guide treatment decisions. However, this will require larger patient groups and comparative studies to validate their clinical utility.

5.10 Future Directions

Building on the current findings, future research should explore several key directions to enhance the clinical relevance and therapeutic insight of GBM-on-chip platforms. First, incorporating a wider range of drug combinations could better reflect the multi-resistance mechanisms of GBM and help identify synergistic treatment strategy. Second, patient samples could be stratified based on clinical response (e.g., lethal vs. non-lethal outcomes, or TMZ-responsive vs. TMZ-resistant cases). Having different patient groups based on their clinical characteristics and retrospective analysis of their cytokine profile, can lead to predict the biomarkers or specific cytokine signature linked to them. Third, the analysis of cytokines should extend beyond the protein level to include transcriptional profiling via RT-PCR, offering a deeper and more robust analysis. Finally, I aim to gradually extend the duration of microfluidic culture to better mimic the timescale of standard clinical treatments, allowing for more clinically relevant data, whilst looking to disseminate to other units to allow widespread adoption of the technology.

Conclusion

This study demonstrates the feasibility of maintaining patient-derived GBM tissue on a PMMA-based microfluidic platform for up to 12 days, enabling real-time cytokine profiling and treatment testing. The system preserved tissue viability, showed consistent downregulation of VEGF and MMP9, and highlighted CHI3L1 as potential markers of treatment resistance. Compared to spheroid and organoid models, this intact tissue-on-chip more closely replicates the tumour microenvironment. Future studies should expand drug testing, link cytokine patterns to clinical outcomes, and explore longer-term cultures to support personalised therapy in GBM.

6 Reference list / Bibliography

Abels, E. R., Maas, S. L., Tai, E., Ting, D. T., Broekman, M. L., Breakefield, X. O. & El Khoury, J. 2020. GlioM&M: Web-based tool for studying circulating and infiltrating monocytes and macrophages in glioma. *Scientific Reports,* 10**,** 1-11.

Ah-Pine, F., Khettab, M., Bedoui, Y., Slama, Y., Daniel, M., Doray, B. & Gasque, P. 2023. On the origin and development of glioblastoma: multifaceted role of perivascular mesenchymal stromal cells. *Acta Neuropathologica Communications,* 11**,** 104.

Ahir, B. K., Engelhard, H. H. & Lakka, S. S. 2020. Tumor Development and Angiogenesis in Adult Brain Tumor: Glioblastoma. *Molecular Neurobiology,* 57**,** 2461-2478.

Ajami, B., Bennett, J. L., Krieger, C., Tetzlaff, W. & Rossi, F. M. 2007. Local self-renewal can sustain CNS microglia maintenance and function throughout adult life. *Nature neuroscience,* 10**,** 1538-1543.

Akay, M., Hite, J., Avci, N. G., Fan, Y., Akay, Y., Lu, G. & Zhu, J.-J. 2018a. Drug Screening of Human GBM Spheroids in Brain Cancer Chip. *Scientific Reports,* 8**,** 15423.

Akay, M., Hite, J., Avci, N. G., Fan, Y., Akay, Y., Lu, G. & Zhu, J. J. 2018b. Drug Screening of Human GBM Spheroids in Brain Cancer Chip. *Sci Rep,* 8**,** 15423.

Akhil, A., Raj, D., Raj, M., Bhat, S., Akshay, V., Bhowmik, S., Ramanathan, S. & Ahmed, S. 2016. Vaporized solvent bonding of polymethyl methacrylate. *Journal of Adhesion Science and Technology,* 30**,** 826-841.

Al-Okaili, R. N., Krejza, J., Woo, J. H., Wolf, R. L., O'Rourke, D. M., Judy, K. D., Poptani, H. & Melhem, E. R. 2007. Intraaxial brain masses: MR imaging-based diagnostic strategy--initial experience. *Radiology,* 243**,** 539-50.

Alghamdi, M., Gumbleton, M. & Newland, B. 2021. Local delivery to malignant brain tumors: potential biomaterial-based therapeutic/adjuvant strategies. *Biomaterials Science,* 9**,** 6037-6051.

Alves, A. H., Nucci, M. P., Mamani, J. B., Valle, N. M. E., Ribeiro, E. F., Rego, G. N. A., Oliveira, F. A., Theinel, M. H., Santos, R. S. & Gamarra, L. F. 2022. The Advances in Glioblastoma On-a-Chip for Therapy Approaches. *Cancers,* 14**,** 869.

Andersen, C., Astrup, J. & Gyldensted, C. Quantitation of peritumoural oedema and the effect of steroids using NMR-relaxation time imaging and blood-brain barrier analysis. Brain Edema IX: Proceedings of the Ninth International Symposium Tokyo, May 16–19, 1993, 1994. Springer, 413-415.

Astolfi, M., Péant, B., Lateef, M. A., Rousset, N., Kendall-Dupont, J., Carmona, E., Monet, F., Saad, F., Provencher, D., Mes-Masson, A. M. & Gervais, T. 2016. Micro-dissected tumor tissues on chip: an ex vivo method for drug testing and personalized therapy. *Lab Chip,* 16**,** 312-25.

Auner, A. W., Tasneem, K. M., Markov, D. A., McCawley, L. J. & Hutson, M. S. 2019. Chemical-PDMS binding kinetics and implications for bioavailability in microfluidic devices. *Lab on a Chip,* 19**,** 864-874.

Banasavadi-Siddegowda, Y. K., Namagiri, S., Otani, Y., Sur, H., Rivas, S., Bryant, J.-P., Shellbourn, A., Rock, M., Chowdhury, A. & Lewis, C. T. 2022. Targeting protein arginine methyltransferase 5 sensitizes glioblastoma to trametinib. *Neuro-Oncology Advances,* 4**,** vdac095.

Banasavadi-Siddegowda, Y. K., Russell, L., Frair, E., Karkhanis, V. A., Relation, T., Yoo, J. Y., Zhang, J., Sif, S., Imitola, J., Baiocchi, R. & Kaur, B. 2017. PRMT5–PTEN molecular pathway regulates senescence and self-renewal of primary glioblastoma neurosphere cells. *Oncogene,* 36**,** 263-274.

Barbosa, M. A., Xavier, C. P., Pereira, R. F., Petrikaitė, V. & Vasconcelos, M. H. 2021. 3D cell culture models as recapitulators of the tumor microenvironment for the screening of anti-cancer drugs. *Cancers,* 14**,** 190.

Barnett, A. E., Ozair, A., Bamashmos, A. S., Li, H., Bosler, D. S., Yeaney, G., Ali, A., Peereboom, D. M., Lathia, J. D. & Ahluwalia, M. S. 2024. MGMT Methylation and Differential Survival Impact by Sex in Glioblastoma. *Cancers,* 16**,** 1374.

Barry, A., Samuel, S. F., Hosni, I., Moursi, A., Feugere, L., Sennett, C. J., Deepak, S., Achawal, S., Rajaraman, C. & Iles, A. 2023a. Investigating the effects of arginine methylation inhibitors on microdissected brain tumour biopsies maintained in a miniaturised perfusion system. *Lab on a Chip,* 23**,** 2664-2682.

Barry, A., Samuel, S. F., Hosni, I., Moursi, A., Feugere, L., Sennett, C. J., Deepak, S., Achawal, S., Rajaraman, C., Iles, A., Wollenberg Valero, K. C., Scott, I. S., Green, V., Stead, L. F., Greenman, J., Wade, M. A. & Beltran-Alvarez, P. 2023b. Investigating the effects of arginine methylation inhibitors on microdissected brain tumour biopsies maintained in a miniaturised perfusion system. *Lab Chip,* 23**,** 2664-2682.

Bassi, G., Grimaudo, M. A., Panseri, S. & Montesi, M. 2021. Advanced Multi-Dimensional Cellular Models as Emerging Reality to Reproduce In Vitro the Human Body Complexity. *International Journal of Molecular Sciences,* 22**,** 1195.

Begagić, E., Pugonja, R., Bečulić, H., Čeliković, A., Lihić, L. T., Samra Kadić, V., Čejvan, L., Skomorac, R., Selimović, E., Jaganjac, B., Juković-Bihorac, F., Jusić, A. & Mirza, P. 2023. Molecular Targeted Therapies in Glioblastoma Multiforme: A Systematic Overview of Global Trends and Findings. *Brain Sciences,* 13**,** 1602.

Beltzig, L., Stratenwerth, B. & Kaina, B. 2021. Accumulation of Temozolomide-Induced Apoptosis, Senescence and DNA Damage by Metronomic Dose Schedule: A Proof-of-Principle Study with Glioblastoma Cells. *Cancers,* 13**,** 6287.

Ben-Shachar, M. S., Lüdecke, D. & Makowski, D. 2020. effectsize: Estimation of effect size indices and standardized parameters. *Journal of open source software,* 5**,** 2815.

Berro, A., Assi, A., Farhat, M., Hatoum, L., Saad, J.-P., Mohanna, R., Bechara, A. M. A., Prince, G., Hachem, M. C. R., Zalaquett, Z. & Kourie, H.-R. 2024. Unlocking Hope: Anti-VEGFR inhibitors and their potential in glioblastoma treatment. *Critical Reviews in Oncology/Hematology,* 198**,** 104365.

Bhuta, S. 2011. Glioblastoma NOS (with diffusion tensor imaging). *Radiopaedia.org*.

Bi, J., Chowdhry, S., Wu, S., Zhang, W., Masui, K. & Mischel, P. S. 2020. Altered cellular metabolism in gliomas—An emerging landscape of actionable co-dependency targets. *Nature Reviews Cancer,* 20**,** 57-70.

Bischof, J., Westhoff, M.-A., Wagner, J. E., Halatsch, M.-E., Trentmann, S., Knippschild, U., Wirtz, C. R. & Burster, T. 2017. Cancer stem cells: The potential role of autophagy, proteolysis, and cathepsins in glioblastoma stem cells. *Tumor Biology,* 39**,** 1010428317692227.

Blighe, K., Rana, S. & Lewis, M. 2020. *EnhancedVolcano: Publication-ready volcano plots with enhanced colouring and labeling* [Online]. Available: **https://github.com/kevinblighe/EnhancedVolcano** [Accessed March 11 2025].

Bonosi, L., Marrone, S., Benigno, U. E., Buscemi, F., Musso, S., Porzio, M., Silven, M. P., Torregrossa, F. & Grasso, G. 2023. Maximal Safe Resection in Glioblastoma Surgery: A Systematic Review of Advanced Intraoperative Image-Guided Techniques. *Brain Sciences,* 13**,** 216.

Borók, A., Laboda, K. & Bonyár, A. 2021. PDMS bonding technologies for microfluidic applications: A review. *Biosensors,* 11**,** 292.

Bou Zerdan, M. & Assi, H. I. 2021. Oligodendroglioma: A Review of Management and Pathways. *Front Mol Neurosci,* 14**,** 722396.

Brat, D. J., Aldape, K., Colman, H., Holland, E. C., Louis, D. N., Jenkins, R. B., Kleinschmidt-DeMasters, B., Perry, A., Reifenberger, G. & Stupp, R. 2018. cIMPACT-NOW update 3: recommended diagnostic criteria for "Diffuse astrocytic glioma, IDH-wildtype, with molecular features of glioblastoma, WHO grade IV". *Acta neuropathologica,* 136**,** 805-810.

Bressenot, A., Marchal, S., Bezdetnaya, L., Garrier, J., Guillemin, F. & Plénat, F. 2009. Assessment of apoptosis by immunohistochemistry to active caspase-3, active caspase-7, or cleaved PARP

in monolayer cells and spheroid and subcutaneous xenografts of human carcinoma. *J Histochem Cytochem,* 57**,** 289-300.
Brodbelt, A., Greenberg, D., Winters, T., Williams, M., Vernon, S. & Collins, V. P. 2015a. Glioblastoma in England: 2007-2011. *Eur J Cancer,* 51**,** 533-542.
Brodbelt, A., Greenberg, D., Winters, T., Williams, M., Vernon, S. & Collins, V. P. 2015b. Glioblastoma in England: 2007–2011. *European Journal of Cancer,* 51**,** 533-542.
Bryant, J.-P., Heiss, J. & Banasavadi-Siddegowda, Y. K. 2021a. Arginine Methylation in Brain Tumors: Tumor Biology and Therapeutic Strategies. *Cells,* 10**,** 124.
Bryant, J. P., Heiss, J. & Banasavadi-Siddegowda, Y. K. 2021b. Arginine Methylation in Brain Tumors: Tumor Biology and Therapeutic Strategies. *Cells,* 10.
Bulik, M., Kazda, T., Slampa, P. & Jancalek, R. 2015. The Diagnostic Ability of Follow-Up Imaging Biomarkers after Treatment of Glioblastoma in the Temozolomide Era: Implications from Proton MR Spectroscopy and Apparent Diffusion Coefficient Mapping. *Biomed Res Int,* 2015**,** 641023.
Caballero, D., Reis, R. L. & Kundu, S. C. 2020. Engineering Patient-on-a-Chip Models for Personalized Cancer Medicine. *In:* OLIVEIRA, J. M. & REIS, R. L. (eds.) *Biomaterials- and Microfluidics-Based Tissue Engineered 3D Models.* Cham: Springer International Publishing.
Cai, X., Briggs, R. G., Homburg, H. B., Young, I. M., Davis, E. J., Lin, Y.-H., Battiste, J. D. & Sughrue, M. E. 2020a. Application of microfluidic devices for glioblastoma study: current status and future directions. *Biomedical Microdevices,* 22**,** 60.
Cai, X., Briggs, R. G., Homburg, H. B., Young, I. M., Davis, E. J., Lin, Y. H., Battiste, J. D. & Sughrue, M. E. 2020b. Application of microfluidic devices for glioblastoma study: current status and future directions. *Biomed Microdevices,* 22**,** 60.
Caldwell, C., Johnson, C. E., Balaji, V. N., Balaji, G. A., Hammer, R. D. & Kannan, R. 2017. Identification and Validation of a PD-L1 Binding Peptide for Determination of PDL1 Expression in Tumors. *Scientific Reports,* 7**,** 13682.
Cao, U. M., Zhang, Y., Chen, J., Sayson, D., Pillai, S. & Tran, S. D. 2023. Microfluidic organ-on-a-chip: a guide to biomaterial choice and fabrication. *International Journal of Molecular Sciences,* 24**,** 3232.
Cauli, E., Polidoro, M. A., Marzorati, S., Bernardi, C., Rasponi, M. & Lleo, A. 2023. Cancer-on-chip: a 3D model for the study of the tumor microenvironment. *Journal of Biological Engineering,* 17**,** 53.
Cho, A. N., Jin, Y., An, Y., Kim, J., Choi, Y. S., Lee, J. S., Kim, J., Choi, W. Y., Koo, D. J., Yu, W., Chang, G. E., Kim, D. Y., Jo, S. H., Kim, J., Kim, S. Y., Kim, Y. G., Kim, J. Y., Choi, N., Cheong, E., Kim, Y. J., Je, H. S., Kang, H. C. & Cho, S. W. 2021. Microfluidic device with brain extracellular matrix promotes structural and functional maturation of human brain organoids. *Nat Commun,* 12**,** 4730.
Chong, J. & Xia, J. 2018. MetaboAnalystR: an R package for flexible and reproducible analysis of metabolomics data. *Bioinformatics,* 34**,** 4313-4314.
ClinicalTrials.gov. 2023. *n Open-label, Dose Escalation Study to Investigate the Safety, Pharmacokinetics, Pharmacodynamics and Clinical Activity of GSK3326595 in Participants With Solid Tumors and Non-Hodgkin's Lymphoma (Meteor 1)* [Online]. Available: **https://clinicaltrials.gov/study/NCT02783300** [Accessed 9 August 2024].
ClinicalTrials.gov Updated April 5, 2023. A study of PRT811 in participants with advanced solid tumors, CNS lymphoma and gliomas.
Cohen, J. 1988. *Statistical power analysis for the behavioral sciences,* New York, Routledge Member of the Taylor and Francis Group.
Cohen, J. 1992. A power primer. *Psychol Bull,* 112**,** 155-9.
Coleman, C., Chen, K., Lu, A., Seashore, E., Stoller, S., Davis, T., Braunstein, S., Gupta, N. & Mueller, S. 2023. Interdisciplinary care of children with diffuse midline glioma. *Neoplasia,* 35**,** 100851.

Conarroe, C. A. & Bullock, T. N. J. 2023. Ready for Prime Time? Dendritic Cells in High-Grade Gliomas. *Cancers,* 15**,** 2902.

Corcoran, D. 2023. AICcPermanova: Model Selection of PERMANOVA Models Using AICc. *Zenodo. **https://doi**. org/10.5281/zenodo,* 7816863.

Crowell, C., Mata-Mbemba, D., Bennett, J., Matheson, K., Mackley, M., Perreault, S. & Erker, C. 2022. Systematic review of diffuse hemispheric glioma, H3 G34-mutant: Outcomes and associated clinical factors. *Neurooncol Adv,* 4**,** vdac133.

Cura, V. & Cavarelli, J. 2021. Structure, activity and function of the PRMT2 protein arginine methyltransferase. *Life,* 11**,** 1263.

Danchaivijitr, N., Waldman, A. D., Tozer, D. J., Benton, C. E., Brasil Caseiras, G., Tofts, P. S., Rees, J. H. & Jäger, H. R. 2008. Low-grade gliomas: do changes in rCBV measurements at longitudinal perfusion-weighted MR imaging predict malignant transformation? *Radiology,* 247**,** 170-8.

Daneman, R. & Prat, A. 2015. The blood–brain barrier. *Cold Spring Harbor perspectives in biology,* 7**,** a020412.

Dapash, M., Hou, D., Castro, B., Lee-Chang, C. & Lesniak, M. S. 2021. The Interplay between Glioblastoma and Its Microenvironment. *Cells,* 10**,** 2257.

De Fazio, E., Pittarello, M., Gans, A., Ghosh, B., Slika, H., Alimonti, P. & Tyler, B. 2024. Intrinsic and Microenvironmental Drivers of Glioblastoma Invasion. *International Journal of Molecular Sciences,* 25**,** 2563.

DeCordova, S., Shastri, A., Tsolaki, A. G., Yasmin, H., Klein, L., Singh, S. K. & Kishore, U. 2020. Molecular Heterogeneity and Immunosuppressive Microenvironment in Glioblastoma. *Frontiers in Immunology,* 11.

Del Bianco, P., Pinton, L., Magri, S., Canè, S., Masetto, E., Basso, D., Padovan, M., Volpin, F., d'Avella, D., Lombardi, G., Zagonel, V., Bronte, V., Della Puppa, A. & Mandruzzato, S. 2022. Myeloid Diagnostic and Prognostic Markers of Immune Suppression in the Blood of Glioma Patients. *Frontiers in Immunology,* 12.

Deng, S., Leong, H. C., Datta, A., Gopal, V., Kumar, A. P. & Yap, C. T. 2022. PI3K/AKT Signaling Tips the Balance of Cytoskeletal Forces for Cancer Progression. *Cancers,* 14**,** 1652.

Deng, S., Li, C., Cao, J., Cui, Z., Du, J., Fu, Z., Yang, H. & Chen, P. 2023. Organ-on-a-chip meets artificial intelligence in drug evaluation. *Theranostics,* 13**,** 4526-4558.

DePalma, T. J., Sivakumar, H. & Skardal, A. 2022. Strategies for developing complex multi-component in vitro tumor models: Highlights in glioblastoma. *Advanced drug delivery reviews,* 180**,** 114067.

Ding, C., Chen, X., Kang, Q. & Yan, X. 2020. Biomedical Application of Functional Materials in Organ-on-a-Chip. *Front Bioeng Biotechnol,* 8**,** 823.

Ding, Z., Fan, X., Zhang, Y., Yao, M., Wang, G., Dong, Y., Liu, J. & Song, W. 2023. The glymphatic system: a new perspective on brain diseases. *Frontiers in Aging Neuroscience,* 15.

Dong, F., Li, Q., Yang, C., Huo, D., Wang, X., Ai, C., Kong, Y., Sun, X., Wang, W., Zhou, Y., Liu, X., Li, W., Gao, W., Liu, W., Kang, C. & Wu, X. 2018. PRMT2 links histone H3R8 asymmetric dimethylation to oncogenic activation and tumorigenesis of glioblastoma. *Nature Communications,* 9**,** 4552.

Dong, R., Li, X. & Lai, K.-O. 2021. Activity and Function of the PRMT8 Protein Arginine Methyltransferase in Neurons. *Life,* 11**,** 1132.

Eckel-Passow, J. E., Lachance, D. H., Molinaro, A. M., Walsh, K. M., Decker, P. A., Sicotte, H., Pekmezci, M., Rice, T., Kosel, M. L. & Smirnov, I. V. 2015. Glioma groups based on 1p/19q, IDH, and TERT promoter mutations in tumors. *New England Journal of Medicine,* 372**,** 2499-2508.

Engelhardt, B. 2008. The blood-central nervous system barriers actively control immune cell entry into the central nervous system. *Current pharmaceutical design,* 14**,** 1555-1565.

Erices, J. I., Bizama, C., Niechi, I., Uribe, D., Rosales, A., Fabres, K., Navarro-Martínez, G., Torres, Á., San Martín, R., Roa, J. C. & Quezada-Monrás, C. 2023. Glioblastoma Microenvironment

and Invasiveness: New Insights and Therapeutic Targets. *International Journal of Molecular Sciences,* 24**,** 7047.

Excellence, N. I. f. H. a. C. 2007. *Carmustine implants and temozolomide for the treatment of newly diagnosed high-grade glioma* [Online]. Available: **https://www.nice.org.uk/guidance/ta121** [Accessed 2023].

Excellence, N. i. f. h. a. c. 2021. *Brain tumours (primary) and brain metastases in over 16s NICE guideline Published: 11 July 2018 Last updated: 29 January 2021* [Online]. Available: **https://www.nice.org.uk/guidance/ng99** [Accessed].

Fan, Y., Nguyen, D. T., Akay, Y., Xu, F. & Akay, M. 2016. Engineering a Brain Cancer Chip for High-throughput Drug Screening. *Scientific Reports,* 6**,** 25062.

Fu, M., Zhou, Z., Huang, X., Chen, Z., Zhang, L., Zhang, J., Hua, W. & Mao, Y. 2023a. Use of Bevacizumab in recurrent glioblastoma: a scoping review and evidence map. *BMC Cancer,* 23**,** 544.

Fu, W., Hou, X., Dong, L. & Hou, W. 2023b. Roles of STAT3 in the pathogenesis and treatment of glioblastoma. *Frontiers in cell and developmental biology,* 11**,** 1098482.

Gerritsen, J. K. W., Young, J. S., Chang, S. M., Krieg, S. M., Jungk, C., van den Bent, M. J., Satoer, D. D., Ille, S., Schucht, P., Nahed, B. V., Broekman, M. L. D., Berger, M., De Vleeschouwer, S. & Vincent, A. J. P. E. 2024. SUPRAMAX-study: supramaximal resection versus maximal resection for glioblastoma patients: study protocol for an international multicentre prospective cohort study (ENCRAM 2201). *BMJ Open,* 14**,** e082274.

Gilard, V., Tebani, A., Dabaj, I., Laquerrière, A., Fontanilles, M., Derrey, S., Marret, S. & Bekri, S. 2021. Diagnosis and Management of Glioblastoma: A Comprehensive Perspective. *J Pers Med,* 11.

Gonzalez Castro, L. N. & Wesseling, P. 2021. The cIMPACT-NOW updates and their significance to current neuro-oncology practice. *Neuro-Oncology Practice,* 8**,** 4-10.

Green, V. L., Michno, A., Greenman, J. & Stafford, N. D. 2012. Effect of treatment on systemic cytokines in head and neck squamous cell carcinoma patients. *Results in Immunology,* 2**,** 1-6.

Grochans, S., Cybulska, A. M., Simińska, D., Korbecki, J., Kojder, K., Chlubek, D. & Baranowska-Bosiacka, I. 2022. Epidemiology of Glioblastoma Multiforme–Literature Review. *Cancers,* 14**,** 2412.

Group, G. M.-a. T. G. 2002. Chemotherapy in adult high-grade glioma: a systematic review and meta-analysis of individual patient data from 12 randomised trials. *The Lancet,* 359**,** 1011-1018.

Habanjar, O., Diab-Assaf, M., Caldefie-Chezet, F. & Delort, L. 2021. 3D Cell Culture Systems: Tumor Application, Advantages, and Disadvantages. *International Journal of Molecular Sciences,* 22**,** 12200.

Hammond, L. A., Eckardt, J. R., Baker, S. D., Eckhardt, S. G., Dugan, M., Forral, K., Reidenberg, P., Statkevich, P., Weiss, G. R. & Rinaldi, D. A. 1999. Phase I and pharmacokinetic study of temozolomide on a daily-for-5-days schedule in patients with advanced solid malignancies. *Journal of Clinical Oncology,* 17**,** 2604-2604.

Harada, Y., Murayama, Y., Takamatsu, T., Otsuji, E. & Tanaka, H. 2022. 5-Aminolevulinic Acid-Induced Protoporphyrin IX Fluorescence Imaging for Tumor Detection: Recent Advances and Challenges. *International Journal of Molecular Sciences,* 23**,** 6478.

Hattersley, S. M., Dyer, C. E., Greenman, J. & Haswell, S. J. 2008. Development of a microfluidic device for the maintenance and interrogation of viable tissue biopsies. *Lab on a Chip,* 8**,** 1842-1846.

Hawly, J., Murcar, M. G., Schcolnik-Cabrera, A. & Issa, M. E. 2024. Glioblastoma stem cell metabolism and immunity. *Cancer and Metastasis Reviews,* 43**,** 1015-1035.

He, X., Wang, B., Meng, J., Zhang, S. & Wang, S. 2021. How to Prevent Bubbles in Microfluidic Channels. *Langmuir,* 37**,** 2187-2194.

Hegi, M. E., Liu, L., Herman, J. G., Stupp, R., Wick, W., Weller, M., Mehta, M. P. & Gilbert, M. R. 2008. Correlation of O6-methylguanine methyltransferase (MGMT) promoter methylation

with clinical outcomes in glioblastoma and clinical strategies to modulate MGMT activity. *Journal of clinical oncology,* 26**,** 4189-4199.

Henssen, D., Meijer, F. J., Verburg, F. A. & Smits, M. 2022. Challenges and opportunities for advanced neuroimaging of glioblastoma. *Br J Radiol***,** 20211232.

Hersh, A. M., Gaitsch, H., Alomari, S., Lubelski, D. & Tyler, B. M. 2022. Molecular Pathways and Genomic Landscape of Glioblastoma Stem Cells: Opportunities for Targeted Therapy. *Cancers (Basel),* 14.

Holst, C. B., Christensen, I. J., Vitting-Seerup, K., Skjøth-Rasmussen, J., Hamerlik, P., Poulsen, H. S. & Johansen, J. S. 2021. Plasma IL-8 and ICOSLG as prognostic biomarkers in glioblastoma. *Neuro-Oncology Advances,* 3.

Horbinski, C., Ligon, K. L., Brastianos, P., Huse, J. T., Venere, M., Chang, S., Buckner, J., Cloughesy, T., Jenkins, R. B. & Giannini, C. 2019. The medical necessity of advanced molecular testing in the diagnosis and treatment of brain tumor patients. *Neuro-oncology,* 21**,** 1498-1508.

Hosni, I., Iles, A., Greenman, J. & Wade, M. A. 2023. A robust, flow-based, microfluidic device for siRNA-mediated gene knockdown in glioblastoma spheroids. *Innovation and Emerging Technologies,* 10**,** 2340005.

Hu, G., Yan, C., Xie, P., Cao, Y., Shao, J. & Ge, J. 2020a. PRMT2 accelerates tumorigenesis of hepatocellular carcinoma by activating Bcl2 via histone H3R8 methylation. *Experimental Cell Research,* 394**,** 112152.

Hu, X., Deng, Q., Ma, L., Li, Q., Chen, Y., Liao, Y., Zhou, F., Zhang, C., Shao, L. & Feng, J. 2020b. Meningeal lymphatic vessels regulate brain tumor drainage and immunity. *Cell research,* 30**,** 229-243.

Hwang, J. W., Loisel-Duwattez, J., Desterke, C., Latsis, T., Pagliaro, S., Griscelli, F., Bennaceur-Griscelli, A. & Turhan, A. G. 2020. A novel neuronal organoid model mimicking glioblastoma (GBM) features from induced pluripotent stem cells (iPSC). *Biochim Biophys Acta Gen Subj,* 1864**,** 129540.

IdealEyes. 2024. *QuickSpots™ – Sample Spotting for Membranes* [Online]. IdealEyes. Available: **https://idealeyes.com/products/QuickSpots/** [Accessed 2025 May 19].

Ismailov, A., Spallone, A., Belogurov Jr, A., Herbert, A. & Poptsova, M. 2025. Molecular biology of the deadliest cancer–glioblastoma: what do we know? *Frontiers in Immunology,* 16**,** 1530305.

Ius, T., Pignotti, F., Della Pepa, G. M., La Rocca, G., Somma, T., Isola, M., Battistella, C., Gaudino, S., Polano, M., Dal Bo, M., Bagatto, D., Pegolo, E., Chiesa, S., Arcicasa, M., Olivi, A., Skrap, M. & Sabatino, G. 2020. A Novel Comprehensive Clinical Stratification Model to Refine Prognosis of Glioblastoma Patients Undergoing Surgical Resection. *Cancers,* 12**,** 386.

Izumikawa, K., Ishikawa, H., Simpson, R. J. & Takahashi, N. 2018. Modulating the expression of Chtop, a versatile regulator of gene-specific transcription and mRNA export. *RNA biology,* 15**,** 849-855.

Jacob, F., Salinas, R. D., Zhang, D. Y., Nguyen, P. T. T., Schnoll, J. G., Wong, S. Z. H., Thokala, R., Sheikh, S., Saxena, D., Prokop, S., Liu, D.-a., Qian, X., Petrov, D., Lucas, T., Chen, H. I., Dorsey, J. F., Christian, K. M., Binder, Z. A., Nasrallah, M., Brem, S., O'Rourke, D. M., Ming, G.-l. & Song, H. 2020. A Patient-Derived Glioblastoma Organoid Model and Biobank Recapitulates Inter- and Intra-tumoral Heterogeneity. *Cell,* 180**,** 188-204.e22.

Jarmuzek, P., Defort, P., Kot, M., Wawrzyniak-Gramacka, E., Morawin, B. & Zembron-Lacny, A. 2023. Cytokine Profile in Development of Glioblastoma in Relation to Healthy Individuals. *International Journal of Molecular Sciences,* 24**,** 16206.

Jarrah, R., Nathani, K. R., Bhandarkar, S., Ezeudu, C. S., Nguyen, R. T., Amare, A., Aljameey, U. A., Jarrah, S. I., Bhandarkar, A. R. & Fiani, B. 2023. Microfluidic 'Brain-on Chip'Systems to Supplement Neurological Practice: Development, Applications and Considerations. *Regenerative Medicine,* 18**,** 413-423.

Jensen, C. & Teng, Y. 2020. Is It Time to Start Transitioning From 2D to 3D Cell Culture? *Frontiers in Molecular Biosciences,* 7.

Jie, M., Mao, S., Liu, H., He, Z., Li, H. F. & Lin, J. M. 2017. Evaluation of drug combination for glioblastoma based on an intestine-liver metabolic model on microchip. *Analyst,* 142**,** 3629-3638.

Jones, E. J., Skinner, B. M., Parker, A., Baldwin, L. R., Greenman, J., Carding, S. R. & Funnell, S. G. P. 2024. An in vitro multi-organ microphysiological system (MPS) to investigate the gut-to-brain translocation of neurotoxins. *Biomicrofluidics,* 18.

Junker, N., Johansen, J. S., Hansen, L. T., Lund, E. L. & Kristjansen, P. E. 2005. Regulation of YKL‐40 expression during genotoxic or microenvironmental stress in human glioblastoma cells. *Cancer science,* 96**,** 183-190.

Kaja, S., Payne, A. J., Naumchuk, Y. & Koulen, P. 2017. Quantification of Lactate Dehydrogenase for Cell Viability Testing Using Cell Lines and Primary Cultured Astrocytes. *Curr Protoc Toxicol,* 72**,** 2.26.1-2.26.10.

Kaminska, B., Cyranowski, S., Ghosh, M., Wojtas, B., Zawadzka, M., Baluszek, S., Swatler, J., Wojnicki, K. & Gielniewski, B. 2023. Depletion of chitinase-3-like protein 1 (CHI3L1) in glioma cells restraints tumor growth and affects neovasculature in intracranial murine gliomas.

Kaminska, B., Czapski, B., Guzik, R., Król, S. K. & Gielniewski, B. 2019. Consequences of IDH1/2 mutations in gliomas and an assessment of inhibitors targeting mutated IDH proteins. *Molecules,* 24**,** 968.

Karschnia, P., Young, J. S., Dono, A., Häni, L., Sciortino, T., Bruno, F., Juenger, S. T., Teske, N., Morshed, R. A., Haddad, A. F., Zhang, Y., Stoecklein, S., Weller, M., Vogelbaum, M. A., Beck, J., Tandon, N., Hervey-Jumper, S., Molinaro, A. M., Rudà, R., Bello, L., Schnell, O., Esquenazi, Y., Ruge, M. I., Grau, S. J., Berger, M. S., Chang, S. M., van den Bent, M. & Tonn, J.-C. 2022. Prognostic validation of a new classification system for extent of resection in glioblastoma: A report of the RANO resect group. *Neuro-Oncology,* 25**,** 940-954.

Kassambara, A. 2020. *ggpubr: 'ggplot2' Based Publication Ready Plots* [Online]. Available: **https://CRAN.R-project.org/package=ggpubr** [Accessed March 11 2025].

Kassambara, A. 2023. *Pipe-Friendly Framework for Basic Statistical Tests* [Online]. Available: **https://CRAN.R-project.org/package=rstatix** [Accessed March 4 2025].

Kaur, M. & Thomas, R. 2023. Brain Edema and Corticosteroid Toxicity. *In:* MOHILE, N. A. & THOMAS, A. A. (eds.) *Brain Tumors: A Pocket Guide.* Cham: Springer International Publishing.

Kennedy, B. C., Showers, C. R., Anderson, D. E., Anderson, L., Canoll, P., Bruce, J. N. & Anderson, R. C. 2013. Tumor-associated macrophages in glioma: friend or foe? *Journal of oncology,* 2013.

Kim, H., Lee, J. M., Park, J. S., Jo, S. A., Kim, Y.-O., Kim, C.-W. & Jo, I. 2008. Dexamethasone coordinately regulates angiopoietin-1 and VEGF: a mechanism of glucocorticoid-induced stabilization of blood–brain barrier. *Biochemical and biophysical research communications,* 372**,** 243-248.

Kim, H. & Ronai, Z. A. 2020. PRMT5 function and targeting in cancer. *Cell Stress,* 4**,** 199-215.

Kim, J., Cho, H., Kim, J., Park, J. S. & Han, K.-H. 2021. A disposable smart microfluidic platform integrated with on-chip flow sensors. *Biosensors and Bioelectronics,* 176**,** 112897.

Kircher, M. F., De La Zerda, A., Jokerst, J. V., Zavaleta, C. L., Kempen, P. J., Mittra, E., Pitter, K., Huang, R., Campos, C. & Habte, F. 2012. A brain tumor molecular imaging strategy using a new triple-modality MRI-photoacoustic-Raman nanoparticle. *Nature medicine,* 18**,** 829-834.

Klemm, F., Maas, R. R., Bowman, R. L., Kornete, M., Soukup, K., Nassiri, S., Brouland, J.-P., Iacobuzio-Donahue, C. A., Brennan, C. & Tabar, V. 2020. Interrogation of the microenvironmental landscape in brain tumors reveals disease-specific alterations of immune cells. *Cell,* 181**,** 1643-1660. e17.

Ko, J., Ahn, J., Kim, S., Lee, Y., Lee, J., Park, D. & Jeon, N. L. 2019. Tumor spheroid-on-a-chip: a standardized microfluidic culture platform for investigating tumor angiogenesis. *Lab on a Chip,* 19**,** 2822-2833.

Ko, J., Park, D., Lee, S., Gumuscu, B. & Jeon, N. L. 2022. Engineering Organ-on-a-Chip to Accelerate Translational Research. *Micromachines,* 13**,** 1200.

Komai, T., Inoue, M., Okamura, T., Morita, K., Iwasaki, Y., Sumitomo, S., Shoda, H., Yamamoto, K. & Fujio, K. 2018. Transforming growth factor-β and interleukin-10 synergistically regulate humoral immunity via modulating metabolic signals. *Frontiers in immunology,* 9**,** 1364.

Korkmaz, S., Göksülük, D. & Zararsiz, G. 2014. MVN: An R package for assessing multivariate normality. *R journal,* 6.

Kotsarini, C., Griffiths, P. D., Wilkinson, I. D. & Hoggard, N. 2010. A systematic review of the literature on the effects of dexamethasone on the brain from in vivo human-based studies: implications for physiological brain imaging of patients with intracranial tumors. *Neurosurgery,* 67**,** 1799-1815.

Laigle-Donadey, F., Metellus, P., Guyotat, J., Menei, P., Proust, F., Dufour, H., Chinot, O., Honnorat, J., Faillot, T., Paquis, P., Peruzzi, P., Emery, E., Guillamo, J.-S., Carpentier, A., Wager, M., Lebbah, S., Hajage, D., Delattre, J.-Y. & Cornu, P. 2023. Surgery for glioblastomas in the elderly: an Association des Neuro-oncologues d'Expression Française (ANOCEF) trial. *Journal of Neurosurgery,* 138**,** 1199-1205.

Lakshmanachetty, S., Cruz-Cruz, J., Hoffmeyer, E., Cole, A. P. & Mitra, S. S. 2021. New Insights into the Multifaceted Role of Myeloid-Derived Suppressor Cells (MDSCs) in High-Grade Gliomas: From Metabolic Reprograming, Immunosuppression, and Therapeutic Resistance to Current Strategies for Targeting MDSCs. *Cells,* 10**,** 893.

Lamberti, A., Marasso, S. L. & Cocuzza, M. 2014. PDMS membranes with tunable gas permeability for microfluidic applications. *Rsc Advances,* 4**,** 61415-61419.

Le Calvez, K., Mauricaite, R., Treasure, P., Booth, T. C., Price, S. J., Brodbelt, A., Gregory, J. J., Dadhania, S., Pakzad-Shahabi, L., Dumba, M., Oberg, I., Vernon, S., Basharat, J. & Williams, M. 2025. Adult glioblastoma in England: Incidence, treatment, and outcomes with novel population-based strata. *Cancer Epidemiology,* 97**,** 102811.

Le Rhun, E., Weller, M., Brandsma, D., Van den Bent, M., De Azambuja, E., Henriksson, R., Boulanger, T., Peters, S., Watts, C. & Wick, W. 2017. EANO–ESMO Clinical Practice Guidelines for diagnosis, treatment and follow-up of patients with leptomeningeal metastasis from solid tumours. *Annals of oncology,* 28**,** iv84-iv99.

Lee, E. Q. & Wen, P. Y. 2016. Corticosteroids for peritumoral edema: time to overcome our addiction? : Oxford University Press US.

Lee, J., Kay, K., Troike, K., Ahluwalia, M. S. & Lathia, J. D. 2022a. Sex Differences in Glioblastoma Immunotherapy Response. *NeuroMolecular Medicine,* 24**,** 50-55.

Lee, S. Y., Park, J. H., Cho, K. H., Kim, H. & Shin, H. K. 2022b. Isolinderalactone inhibits glioblastoma cell supernatant-induced angiogenesis. *Oncol Lett,* 24**,** 328.

Levivier, M., Goldman, S., Pirotte, B., Brucher, J. M., Balériaux, D., Luxen, A., Hildebrand, J. & Brotchi, J. 1995. Diagnostic yield of stereotactic brain biopsy guided by positron emission tomography with [18F]fluorodeoxyglucose. *J Neurosurg,* 82**,** 445-52.

Li, F., Liu, A., Zhao, M. & Luo, L. 2023. Astrocytic Chitinase-3-like protein 1 in neurological diseases: Potential roles and future perspectives. *Journal of Neurochemistry,* 165**,** 772-790.

Liao, Y., Luo, Z., Lin, Y., Chen, H., Chen, T., Xu, L., Orgurek, S., Berry, K., Dzieciatkowska, M., Reisz, J. A., D'Alessandro, A., Zhou, W. & Lu, Q. R. 2022. PRMT3 drives glioblastoma progression by enhancing HIF1A and glycolytic metabolism. *Cell Death Dis,* 13**,** 943.

Lim-Fat, M. J., Bi, W. L., Lo, J., Lee, E. Q., Ahluwalia, M. S., Batchelor, T. T., Chang, S. M., Chiocca, E. A., Chukwueke, U. & Cloughesy, T. F. 2019a. when less is more: dexamethasone dosing for brain tumors. *Neurosurgery,* 85**,** E607.

Lim-Fat, M. J., Bi, W. L., Lo, J., Lee, E. Q., Ahluwalia, M. S., Batchelor, T. T., Chang, S. M., Chiocca, E. A., Chukwueke, U., Cloughesy, T. F., Colman, H., Deangelis, L. M., Galanis, E., Gilbert, M. R., De Groot, J. F., Lassman, A. B., Liau, L. M., Mason, W., McFaline-Figueroa, J. R., Mehta, M. P., Mellinghoff, I. K., Nabors, L. B., Nayak, L., Reardon, D. A. & Wen, P. Y.

2019b. Letter: When Less is More: Dexamethasone Dosing for Brain Tumors. *Neurosurgery,* 85.

Liu, S., Gong, Z., Zhou, D., Ayala‐Nunez, V., Xu, T. & Wick, P. 2025. Bridging the Gap: How Organ‐on‐a‐Chip Technology Facilitates the Battle against Glioma. *Small Science***,** 2500154.

Liu, W., Sun, P., Yang, L., Wang, J., Li, L. & Wang, J. 2010. Assay of glioma cell responses to an anticancer drug in a cell-based microfluidic device. *Microfluidics and Nanofluidics,* 9**,** 717-725.

Liu, X., Su, Q., Zhang, X., Yang, W., Ning, J., Jia, K., Xin, J., Li, H., Yu, L., Liao, Y. & Zhang, D. 2022. Recent Advances of Organ-on-a-Chip in Cancer Modeling Research. *Biosensors,* 12**,** 1045.

Lopez-Muñoz, G. A., Mughal, S. & Ramón-Azcón, J. 2022. Sensors and Biosensors in Organs-on-a-Chip Platforms. *In:* CABALLERO, D., KUNDU, S. C. & REIS, R. L. (eds.) *Microfluidics and Biosensors in Cancer Research: Applications in Cancer Modeling and Theranostics.* Cham: Springer International Publishing.

Lou, C., Yang, H., Hou, Y., Huang, H., Qiu, J., Wang, C., Sang, Y., Liu, H. & Han, L. 2024. Microfluidic Platforms for Real‐Time In Situ Monitoring of Biomarkers for Cellular Processes. *Advanced Materials,* 36**,** 2307051.

Louis, D. N., Aldape, K., Brat, D. J., Capper, D., Ellison, D. W., Hawkins, C., Paulus, W., Perry, A., Reifenberger, G. & Figarella-Branger, D. 2017. Announcing cIMPACT-NOW: the consortium to inform molecular and practical approaches to CNS tumor taxonomy. Springer.

Louis, D. N., Ohgaki, H., Wiestler, O. D., Cavenee, W. K., Burger, P. C., Jouvet, A., Scheithauer, B. W. & Kleihues, P. 2007. The 2007 WHO classification of tumours of the central nervous system. *Acta neuropathologica,* 114**,** 97-109.

Louis, D. N., Perry, A., Reifenberger, G., Von Deimling, A., Figarella-Branger, D., Cavenee, W. K., Ohgaki, H., Wiestler, O. D., Kleihues, P. & Ellison, D. W. 2016. The 2016 World Health Organization classification of tumors of the central nervous system: a summary. *Acta neuropathologica,* 131**,** 803-820.

Louis, D. N., Perry, A., Wesseling, P., Brat, D. J., Cree, I. A., Figarella-Branger, D., Hawkins, C., Ng, H., Pfister, S. M. & Reifenberger, G. 2021a. The 2021 WHO classification of tumors of the central nervous system: a summary. *Neuro-oncology,* 23**,** 1231-1251.

Louis, D. N., Perry, A., Wesseling, P., Brat, D. J., Cree, I. A., Figarella-Branger, D., Hawkins, C., Ng, H. K., Pfister, S. M., Reifenberger, G., Soffietti, R., von Deimling, A. & Ellison, D. W. 2021b. The 2021 WHO Classification of Tumors of the Central Nervous System: a summary. *Neuro Oncol,* 23**,** 1231-1251.

Louveau, A., Smirnov, I., Keyes, T. J., Eccles, J. D., Rouhani, S. J., Peske, J. D., Derecki, N. C., Castle, D., Mandell, J. W. & Lee, K. S. 2015. Structural and functional features of central nervous system lymphatic vessels. *Nature,* 523**,** 337-341.

Lucas, C.-H. G., Mueller, S., Reddy, A., Taylor, J. W., Oberheim Bush, N. A., Clarke, J. L., Chang, S. M., Gupta, N., Berger, M. S., Perry, A., Phillips, J. J. & Solomon, D. A. 2021. Diffuse hemispheric glioma, H3 G34-mutant: Genomic landscape of a new tumor entity and prospects for targeted therapy. *Neuro-Oncology,* 23**,** 1974-1976.

Lüdecke, D. 2023. *sjPlot: Data Visualization for Statistics in Social Science* [Online]. Available: **https://cran.r-project.org/web/packages/sjPlot/sjPlot.pdf** [Accessed March 11 2025].

Lund, H., Pieber, M., Parsa, R., Han, J., Grommisch, D., Ewing, E., Kular, L., Needhamsen, M., Espinosa, A. & Nilsson, E. 2018. Competitive repopulation of an empty microglial niche yields functionally distinct subsets of microglia-like cells. *Nature communications,* 9**,** 4845.

Ma, C., Peng, Y., Li, H. & Chen, W. 2021. Organ-on-a-chip: a new paradigm for drug development. *Trends in pharmacological sciences,* 42**,** 119-133.

Ma, X., Li, R., Jin, Z., Fan, Y., Zhou, X. & Zhang, Y. 2020. Injection molding and characterization of PMMA-based microfluidic devices. *Microsystem Technologies,* 26**,** 1317-1324.

Maccari, M., Baek, C., Caccese, M., Mandruzzato, S., Fiorentino, A., Internò, V., Bosio, A., Cerretti, G., Padovan, M., Idbaih, A. & Lombardi, G. 2023. Present and Future of Immunotherapy in Patients With Glioblastoma: Limitations and Opportunities. *The Oncologist,* 29**,** 289-302.

Mair, D. B., Williams, M. A. C., Chen, J. F., Goldstein, A., Wu, A., Lee, P. H. U., Sniadecki, N. J. & Kim, D.-H. 2022. PDMS–PEG Block Copolymer and Pretreatment for Arresting Drug Absorption in Microphysiological Devices. *ACS Applied Materials & Interfaces,* 14**,** 38541-38549.

Mariappan, A., Goranci-Buzhala, G., Ricci-Vitiani, L., Pallini, R. & Gopalakrishnan, J. 2021. Trends and challenges in modeling glioma using 3D human brain organoids. *Cell Death & Differentiation,* 28**,** 15-23.

Martinez Arbizu, P. 2017. *pairwiseAdonis: Pairwise Multilevel Comparison using Adonis* [Online]. Available: **https://github.com/pmartinezarbizu/pairwiseAdonis** [Accessed March 11 2025].

Martins, C., Pacheco, C. & Sarmento, B. 2023. Chapter 30 - The effect of glioblastoma microenvironment on therapeutic, diagnostic, or theranostic systems. *In:* VITORINO, C., BALAñA, C. & CABRAL, C. (eds.) *New Insights Into Glioblastoma.* Academic Press.

Masood, A., Kayani, M. & Batool, S. 2020. Targetting Interleukins Involved in Glioblastoma – A New Pharmacological Approach. *Journal of Life and Bio Sciences Research,* 1**,** 82 - 88.

Matellan, C. & del Río Hernández, A. E. 2018. Cost-effective rapid prototyping and assembly of poly (methyl methacrylate) microfluidic devices. *Scientific reports,* 8**,** 6971.

Matias, D., Balça-Silva, J., da Graça, G. C., Wanjiru, C. M., Macharia, L. W., Nascimento, C. P., Roque, N. R., Coelho-Aguiar, J. M., Pereira, C. M. & Dos Santos, M. F. 2018. Microglia/astrocytes–glioblastoma crosstalk: crucial molecular mechanisms and microenvironmental factors. *Frontiers in cellular neuroscience,* 12**,** 235.

McCornack, C., Woodiwiss, T., Hardi, A., Yano, H. & Kim, A. H. 2023. The function of histone methylation and acetylation regulators in GBM pathophysiology. *Frontiers in Oncology,* 13**,** 1144184.

McCoy, M. G., Nyanyo, D., Hung, C. K., Goerger, J. P., R. Zipfel, W., Williams, R. M., Nishimura, N. & Fischbach, C. 2019. Endothelial cells promote 3D invasion of GBM by IL-8-dependent induction of cancer stem cell properties. *Scientific Reports,* 9**,** 9069.

McKinnon, C., Nandhabalan, M., Murray, S. A. & Plaha, P. 2021. Glioblastoma: clinical presentation, diagnosis, and management. *Bmj,* 374**,** n1560.

Mecozzi, L., Gennari, O., Rega, R., Grilli, S., Bhowmick, S., Gioffrè, M., Coppola, G. & Ferraro, P. 2016. Spiral formation at the microscale by μ-pyro-electrospinning. *Soft matter,* 12**,** 5542-5550.

Meghani, N., Kim, K. H., Kim, S. H., Lee, S. H. & Choi, K. H. 2020. Evaluation and live monitoring of pH-responsive HSA-ZnO nanoparticles using a lung-on-a-chip model. *Archives of Pharmacal Research,* 43**,** 503-513.

Mellinghoff, I. K., Wang, M. Y., Vivanco, I., Haas-Kogan, D. A., Zhu, S., Dia, E. Q., Lu, K. V., Yoshimoto, K., Huang, J. H. & Chute, D. J. 2005. Molecular determinants of the response of glioblastomas to EGFR kinase inhibitors. *New England Journal of Medicine,* 353**,** 2012-2024.

Miller, K. D., Ostrom, Q. T., Kruchko, C., Patil, N., Tihan, T., Cioffi, G., Fuchs, H. E., Waite, K. A., Jemal, A., Siegel, R. L. & Barnholtz-Sloan, J. S. 2021. Brain and other central nervous system tumor statistics, 2021. *CA Cancer J Clin,* 71**,** 381-406.

Mirabdaly, S., Elieh Ali Komi, D., Shakiba, Y., Moini, A. & Kiani, A. 2020. Effects of temozolomide on U87MG glioblastoma cell expression of CXCR4, MMP2, MMP9, VEGF, anti-proliferatory cytotoxic and apoptotic properties. *Molecular Biology Reports,* 47**,** 1187-1197.

Mishra, S., Mondal, G. & Kumarasamy, M. 2025. Development of Low-Cost CNC-Milled PMMA Microfluidic Chips as a Prototype for Organ-on-a-Chip and Neurospheroid Applications. *Organoids,* 4**,** 13.

Mohile, N. A., Messersmith, H., Gatson, N. T., Hottinger, A. F., Lassman, A., Morton, J., Ney, D., Nghiemphu, P. L., Olar, A., Olson, J., Perry, J., Portnow, J., Schiff, D., Shannon, A., Shih, H.

A., Strowd, R., van den Bent, M., Ziu, M. & Blakeley, J. 2022. Therapy for Diffuse Astrocytic and Oligodendroglial Tumors in Adults: ASCO-SNO Guideline. *J Clin Oncol,* 40**,** 403-426.

Mondesir, J., Willekens, C., Touat, M. & de Botton, S. 2016. IDH1 and IDH2 mutations as novel therapeutic targets: current perspectives. *Journal of blood medicine***,** 171-180.

Mondragon-Soto, M., Rodríguez-Hernández, L. A., Moreno Jiménez, S., Gómez Amador, J. L., Gutierrez-Aceves, A., Montano-Tello, H., Reyes-Moreno, I., Santos-Zambrano, J., Castro-Martinez, E. & Gonzalez-Aguilar, A. 2022. Clinical, Therapeutic, and Prognostic Experience in Patients With Glioblastoma. *Cureus,* 14**,** e29856.

Monga, V., Johanns, T. M., Stupp, R., Chandra, S., Falchook, G. S., Giglio, P., Philipovskiy, A., Alnahhas, I., Babbar, N., Sun, W. & McKean, M. 2023. A phase 1 study of the protein arginine methyltransferase 5 (PRMT5) brain-penetrant inhibitor PRT811 in patients (pts) with recurrent high-grade glioma or uveal melanoma (UM). *Journal of Clinical Oncology,* 41**,** 3008-3008.

Mor, V., Laliberte, L., Morris, J. N. & Wiemann, M. 1984. The Karnofsky performance status scale: an examination of its reliability and validity in a research setting. *Cancer,* 53**,** 2002-2007.

Mormino, A. & Garofalo, S. 2022. Dialogue among Lymphocytes and Microglia in Glioblastoma Microenvironment. *Cancers (Basel),* 14.

Mosteiro, A., Pedrosa, L., Ferrés, A., Diao, D., Sierra, À. & González, J. J. 2022. The Vascular Microenvironment in Glioblastoma: A Comprehensive Review. *Biomedicines,* 10**,** 1285.

Mostofa, A. G. M., Punganuru, S. R., Madala, H. R., Al-Obaide, M. & Srivenugopal, K. S. 2017. The Process and Regulatory Components of Inflammation in Brain Oncogenesis. *Biomolecules,* 7**,** 34.

Nakada, M., Kita, D., Watanabe, T., Hayashi, Y., Teng, L., Pyko, I. V. & Hamada, J.-I. 2011. Aberrant Signaling Pathways in Glioma. *Cancers,* 3**,** 3242-3278.

Nemzek, J. A., Siddiqui, J. & Remick, D. G. 2001. Development and optimization of cytokine ELISAs using commercial antibody pairs. *Journal of Immunological Methods,* 255**,** 149-157.

Newlands, E., Stevens, M., Wedge, S., Wheelhouse, R. & Brock, C. 1997. Temozolomide: a review of its discovery, chemical properties, pre-clinical development and clinical trials. *Cancer treatment reviews,* 23**,** 35-61.

Nguyen, T., Jung, S. H., Lee, M. S., Park, T.-E., Ahn, S.-k. & Kang, J. H. 2019. Robust chemical bonding of PMMA microfluidic devices to porous PETE membranes for reliable cytotoxicity testing of drugs. *Lab on a Chip,* 19**,** 3706-3713.

Nice 2021. Brain tumours (primary) and brain metastases in over 16s: diagnosis and management. *NICE guideline [NG99]*.

Noorani, B., Bhalerao, A., Raut, S., Nozohouri, E., Bickel, U. & Cucullo, L. 2021. A Quasi-Physiological Microfluidic Blood-Brain Barrier Model for Brain Permeability Studies. *Pharmaceutics,* 13**,** 1474.

Oksanen, J., Blanchet, F. G., Friendly, M., Kindt, R., Legendre, P., McGlinn, D. & al., e. 2020. *vegan: Community Ecology Package* [Online]. Available: **https://CRAN.R-project.org/package=vegan** [Accessed March 11 2025].

Oksanen, J., Simpson, G. L., Blanchet, F. G., Kindt, R., Legendre, P., Minchin, P. R. & al., e. 2022. *vegan: Community Ecology Package* [Online]. Available: **https://CRAN.R-project.org/package=vegan** [Accessed March 11 2025].

Olubajo, F., Achawal, S. & Greenman, J. 2020. Development of a Microfluidic Culture Paradigm for Ex Vivo Maintenance of Human Glioblastoma Tissue: A New Glioblastoma Model? *Translational Oncology,* 13**,** 1-10.

OncLive. 2023. *Early trials of PRMT5 inhibitors leave much to be desired, but optimism remains* [Online]. Available: **https://www.onclive.com/view/early-trials-of-prmt5-inhibitors-leave-much-to-be-desired-but-optimism-remains** [Accessed 9 August 2024].

Ortiz, R., Perazzoli, G., Cabeza, L., Jiménez-Luna, C., Luque, R., Prados, J. & Melguizo, C. 2021. Temozolomide: an updated overview of resistance mechanisms, nanotechnology advances and clinical applications. *Current neuropharmacology,* 19**,** 513-537.

Ostrom, Q. T., Cioffi, G., Gittleman, H., Patil, N., Waite, K., Kruchko, C. & Barnholtz-Sloan, J. S. 2019. CBTRUS statistical report: primary brain and other central nervous system tumors diagnosed in the United States in 2012–2016. *Neuro-oncology,* 21**,** v1-v100.

Ostrom, Q. T., Patil, N., Cioffi, G., Waite, K., Kruchko, C. & Barnholtz-Sloan, J. S. 2020. CBTRUS Statistical Report: Primary Brain and Other Central Nervous System Tumors Diagnosed in the United States in 2013-2017. *Neuro Oncol,* 22**,** iv1-iv96.

Ou, A., Ott, M., Fang, D. & Heimberger, A. B. 2021. The role and therapeutic targeting of JAK/STAT signaling in glioblastoma. *Cancers,* 13**,** 437.

Ozturk, M. S., Lee, V. K., Zou, H., Friedel, R. H., Intes, X. & Dai, G. 2020. High-resolution tomographic analysis of in vitro 3D glioblastoma tumor model under long-term drug treatment. *Sci Adv,* 6**,** eaay7513.

Pachocki, C. J. & Hol, E. M. 2022. Current perspectives on diffuse midline glioma and a different role for the immune microenvironment compared to glioblastoma. *J Neuroinflammation,* 19**,** 276.

Pang, Z., Chong, J., Li, S. & Xia, J. 2020. MetaboAnalystR 3.0: toward an optimized workflow for global metabolomics. *Metabolites,* 10**,** 186.

Pang, Z., Lu, Y., Zhou, G., Hui, F., Xu, L., Viau, C., Spigelman, A. F., MacDonald, P. E., Wishart, D. S. & Li, S. 2024. MetaboAnalyst 6.0: towards a unified platform for metabolomics data processing, analysis and interpretation. *Nucleic acids research,* 52**,** W398-W406.

Park, J. H. & Lee, H. K. 2022. Current Understanding of Hypoxia in Glioblastoma Multiforme and Its Response to Immunotherapy. *Cancers,* 14**,** 1176.

Pereiro, I., Fomitcheva Khartchenko, A., Petrini, L. & Kaigala, G. V. 2019. Nip the bubble in the bud: a guide to avoid gas nucleation in microfluidics. *Lab on a Chip,* 19**,** 2296-2314.

Philips, A., Henshaw, D. L., Lamburn, G. & O'Carroll, M. J. 2018a. Brain Tumours: Rise in Glioblastoma Multiforme Incidence in England 1995-2015 Suggests an Adverse Environmental or Lifestyle Factor. *J Environ Public Health,* 2018**,** 7910754.

Philips, A., Henshaw, D. L., Lamburn, G. & O'Carroll, M. J. 2018b. Brain Tumours: Rise in Glioblastoma Multiforme Incidence in England 1995–2015 Suggests an Adverse Environmental or Lifestyle Factor. *Journal of Environmental and Public Health,* 2018**,** 7910754.

Pichardo-Rojas, P. S., Pichardo-Rojas, D., Marín-Castañeda, L. A., Palacios-Cruz, M., Rivas-Torres, Y. I., Calderón-Magdaleno, L. F., Sánchez-Serrano, C. D., Chandra, A., Dono, A., Karschnia, P., Tonn, J.-C. & Esquenazi, Y. 2024. Prognostic value of surgical resection over biopsy in elderly patients with glioblastoma: a meta-analysis. *Journal of Neuro-Oncology,* 169**,** 469-487.

Pirotte, B. J., Levivier, M., Goldman, S., Massager, N., Wikler, D., Dewitte, O., Bruneau, M., Rorive, S., David, P. & Brotchi, J. 2009. Positron emission tomography-guided volumetric resection of supratentorial high-grade gliomas: a survival analysis in 66 consecutive patients. *Neurosurgery,* 64**,** 471-81; discussion 481.

Pombo Antunes, A. R., Scheyltjens, I., Lodi, F., Messiaen, J., Antoranz, A., Duerinck, J., Kancheva, D., Martens, L., De Vlaminck, K. & Van Hove, H. 2021. Single-cell profiling of myeloid cells in glioblastoma across species and disease stage reveals macrophage competition and specialization. *Nature neuroscience,* 24**,** 595-610.

Posthoorn-Verheul, C., Fabro, F., Ntafoulis, I., den Hollander, C., Verploegh, I. S. C., Balvers, R., Kers, T. V., Hoogeveen, J., van der Burg, J., Eussen, B., de Klein, A., Feller, K. J., Chien, M.-P., Dirven, C. M. F., Leenstra, S. & Lamfers, M. L. M. 2025. Optimized culturing yields high success rates and preserves molecular heterogeneity, enabling personalized screening for high-grade gliomas. *npj Precision Oncology,* 9**,** 156.

Price, M., Ballard, C., Benedetti, J., Neff, C., Cioffi, G., Waite, K. A., Kruchko, C., Barnholtz-Sloan, J. S. & Ostrom, Q. T. 2024. CBTRUS Statistical Report: Primary Brain and Other Central Nervous System Tumors Diagnosed in the United States in 2017–2021. *Neuro-Oncology,* 26**,** vi1-vi85.

Price, S. J., Jena, R., Burnet, N. G., Hutchinson, P. J., Dean, A. F., Peña, A., Pickard, J. D., Carpenter, T. A. & Gillard, J. H. 2006. Improved delineation of glioma margins and regions of infiltration with the use of diffusion tensor imaging: an image-guided biopsy study. *AJNR Am J Neuroradiol,* 27**,** 1969-74.

Quartuccio, N., Laudicella, R., Vento, A., Pignata, S., Mattoli, M. V., Filice, R., Comis, A. D., Arnone, A., Baldari, S., Cabria, M. & Cistaro, A. 2020. The Additional Value of (18)F-FDG PET and MRI in Patients with Glioma: A Review of the Literature from 2015 to 2020. *Diagnostics (Basel),* 10.

Raman, R., Prabhu, V., Kumar, P. & Mani, N. K. 2024. Advancements in Microfluidic Platforms for Glioblastoma Research. *Chemistry,* 6**,** 1039-1062.

Rega, R., Gennari, O., Mecozzi, L., Pagliarulo, V., Mugnano, M., Oleandro, E., Nazzaro, F., Ferraro, P. & Grilli, S. 2019. Pyro-Electrification of Freestanding Polymer Sheets: A New Tool for Cation-Free Manipulation of Cell Adhesion in vitro. *Frontiers in Chemistry,* Volume 7 - 2019.

Regmi, S., Poudel, C., Adhikari, R. & Luo, K. Q. 2022. Applications of Microfluidics and Organ-on-a-Chip in Cancer Research. *Biosensors,* 12**,** 459.

Riley, A., Jones, H., England, J., Kuvshinov, D., Green, V. & Greenman, J. 2021. Identification of soluble tissue-derived biomarkers from human thyroid tissue explants maintained on a microfluidic device. *Oncology Letters,* 22**,** 780.

Ritchie, M. E., Phipson, B., Wu, D., Hu, Y., Law, C. W., Shi, W. & Smyth, G. K. 2015. limma powers differential expression analyses for RNA-sequencing and microarray studies. *Nucleic acids research,* 43**,** e47-e47.

Rivera, A. L., Pelloski, C. E., Gilbert, M. R., Colman, H., De La Cruz, C., Sulman, E. P., Bekele, B. N. & Aldape, K. D. 2009. MGMT promoter methylation is predictive of response to radiotherapy and prognostic in the absence of adjuvant alkylating chemotherapy for glioblastoma. *Neuro-Oncology,* 12**,** 116-121.

Rodriguez, A. D., Horowitz, L. F., Castro, K., Kenerson, H., Bhattacharjee, N., Gandhe, G., Raman, A., Monnat, R. J., Yeung, R., Rostomily, R. C. & Folch, A. 2020. A microfluidic platform for functional testing of cancer drugs on intact tumor slices. *Lab on a Chip,* 20**,** 1658-1675.

Rohart, F., Gautier, B., Singh, A. & Lê Cao, K.-A. 2017. mixOmics: An R package for 'omics feature selection and multiple data integration. *PLoS computational biology,* 13**,** e1005752.

Roos, W., Batista, L. F. Z., Naumann, S., Wick, W., Weller, M., Menck, C. F. M. & Kaina, B. 2007. Apoptosis in malignant glioma cells triggered by the temozolomide-induced DNA lesion O6-methylguanine. *Oncogene,* 26**,** 186-197.

Rosenthal, M., Clement, P. M., Campone, M., Gil-Gil, M. J., DeGroot, J., Chinot, O., Idbaih, A., Gan, H., Raizer, J., Wen, P. Y., Pineda, E., Donnet, V., Mills, D., El-Hashimy, M. & Mason, W. 2020. Buparlisib plus carboplatin or lomustine in patients with recurrent glioblastoma: a phase Ib/II, open-label, multicentre, randomised study. *ESMO Open,* 5.

Roy, E., Pallandre, A., Zribi, B., Horny, M. C., Delapierre, F. D., Cattoni, A., Gamby, J. & Haghiri-Gosnet, A. M. 2016. Overview of materials for microfluidic applications. *Advances in microfluidics-new applications in biology, energy, and materials Sciences,* 335.

Ryan, R., Booth, S. & Price, S. 2012. Corticosteroid-use in primary and secondary brain tumour patients: a review. *Journal of Neuro-oncology,* 106**,** 449-459.

Sachamitr, P., Ho, J. C., Ciamponi, F. E., Ba-Alawi, W., Coutinho, F. J., Guilhamon, P., Kushida, M. M., Cavalli, F. M. G., Lee, L., Rastegar, N., Vu, V., Sánchez-Osuna, M., Coulombe-Huntington, J., Kanshin, E., Whetstone, H., Durand, M., Thibault, P., Hart, K., Mangos, M., Veyhl, J., Chen, W., Tran, N., Duong, B.-C., Aman, A. M., Che, X., Lan, X., Whitley, O., Zaslaver, O., Barsyte-Lovejoy, D., Richards, L. M., Restall, I., Caudy, A., Röst, H. L., Bonday, Z. Q., Bernstein, M., Das, S., Cusimano, M. D., Spears, J., Bader, G. D., Pugh, T. J., Tyers, M., Lupien, M., Haibe-Kains, B., Artee Luchman, H., Weiss, S., Massirer, K. B., Prinos, P., Arrowsmith, C. H. & Dirks, P. B. 2021. PRMT5 inhibition disrupts splicing and stemness in glioblastoma. *Nature Communications,* 12**,** 979.

Saha, S., Sachdev, M. & Mitra, S. K. 2023. Recent advances in label-free optical, electrochemical, and electronic biosensors for glioma biomarkers. *Biomicrofluidics,* 17**,** 011502.

Samiei, E., Seyfoori, A., Toyota, B., Ghavami, S. & Akbari, M. 2020. Investigating Programmed Cell Death and Tumor Invasion in a Three-Dimensional (3D) Microfluidic Model of Glioblastoma. *Int J Mol Sci,* 21.

Sampson, J. H., Maus, M. V. & June, C. H. 2017. Immunotherapy for brain tumors. *Journal of Clinical Oncology,* 35**,** 2450-2456.

Samuel, S. F., Barry, A., Greenman, J. & Beltran-Alvarez, P. 2021. Arginine methylation: the promise of a 'silver bullet' for brain tumours? *Amino Acids,* 53**,** 489-506.

Sareen, H., Ma, Y., Becker, T. M., Roberts, T. L., de Souza, P. & Powter, B. 2022. Molecular Biomarkers in Glioblastoma: A Systematic Review and Meta-Analysis. *Int J Mol Sci,* 23.

Shakeri, A., Khan, S. & Didar, T. F. 2021. Conventional and emerging strategies for the fabrication and functionalization of PDMS-based microfluidic devices. *Lab on a Chip,* 21**,** 3053-3075.

Shan, Y., He, X., Song, W., Han, D., Niu, J. & Wang, J. 2015. Role of IL-6 in the invasiveness and prognosis of glioma. *Int J Clin Exp Med,* 8**,** 9114-20.

Sharifi, R., Mahmoudzadeh, S., Islam, M. M., Koza, D., Dohlman, C. H., Chodosh, J. & Gonzalez-Andrades, M. 2020. Covalent Functionalization of PMMA Surface with L-3,4-Dihydroxyphenylalanine (L-DOPA) to Enhance its Biocompatibility and Adhesion to Corneal Tissue. *Advanced Materials Interfaces,* 7**,** 1900767.

Sharma, N., Mallela, A. N., Shi, D. D., Tang, L. W., Abou-Al-Shaar, H., Gersey, Z. C., Zhang, X., McBrayer, S. K. & Abdullah, K. G. 2023a. Isocitrate dehydrogenase mutations in gliomas: A review of current understanding and trials. *Neurooncol Adv,* 5**,** vdad053.

Sharma, P., Aaroe, A., Liang, J. & Puduvalli, V. K. 2023b. Tumor microenvironment in glioblastoma: Current and emerging concepts. *Neurooncol Adv,* 5**,** vdad009.

Shi, T., Zhu, J., Zhang, X. & Mao, X. 2023a. The Role of Hypoxia and Cancer Stem Cells in Development of Glioblastoma. *Cancers,* 15**,** 2613.

Shi, Y., He, X., Wang, H., Dai, J., Fang, J., He, Y., Chen, X., Hong, Z. & Chai, Y. 2023b. Construction of a novel blood brain barrier-glioma microfluidic chip model: Applications in the evaluation of permeability and anti-glioma activity of traditional Chinese medicine components. *Talanta,* 253**,** 123971.

Shin, S., Choi, Y., Jang, W., Ulziituya, B., Ha, G., Kang, R., Park, S., Kim, M., Zhang, Y. S., Kim, H. J. & Lee, J. 2025. A vascularized tumors-on-a-chip model for studying tumor-angiogenesis interplay, heterogeneity and drug responses. *Mater Today Bio,* 32**,** 101741.

Shukla, G., Alexander, G. S., Bakas, S., Nikam, R., Talekar, K., Palmer, J. D. & Shi, W. 2017. Advanced magnetic resonance imaging in glioblastoma: a review. *Chinese Clinical Oncology,* 6**,** 40.

Simandi, Z., Czipa, E., Horvath, A., Koszeghy, A., Bordas, C., Póliska, S., Juhász, I., Imre, L., Szabó, G., Dezso, B., Barta, E., Sauer, S., Karolyi, K., Kovacs, I., Hutóczki, G., Bognár, L., Klekner, Á., Szucs, P., Bálint, B. L. & Nagy, L. 2015. PRMT1 and PRMT8 Regulate Retinoic Acid-Dependent Neuronal Differentiation with Implications to Neuropathology. *Stem Cells,* 33**,** 726-741.

Skardelly, M., Kaltenstadler, M., Behling, F., Mäurer, I., Schittenhelm, J., Bender, B., Paulsen, F., Hedderich, J., Renovanz, M. & Gempt, J. 2021. A continuous correlation between residual tumor volume and survival recommends maximal safe resection in glioblastoma patients: a nomogram for clinical decision making and reference for non-randomized trials. *Frontiers in Oncology***,** 5092.

Slavkov, D., Hadzhiyanev, A. & Slavkova, S. 2023. Tumor treating fields: a new treatment for glioblastoma. *Biotechnology & Biotechnological Equipment,* 37**,** 58-63.

Slika, H., Karimov, Z., Alimonti, P., Abou-Mrad, T., De Fazio, E., Alomari, S. & Tyler, B. 2023. Preclinical Models and Technologies in Glioblastoma Research: Evolution, Current State, and Future Avenues. *International Journal of Molecular Sciences,* 24**,** 16316.

Smittenaar, C. R., Petersen, K. A., Stewart, K. & Moitt, N. 2016. Cancer incidence and mortality projections in the UK until 2035. *Br J Cancer,* 115**,** 1147-1155.

Smolenschi, C., Rassy, E., Pallud, J., Dezamis, E., Copaciu, R., Parker, F., Garcia, G., Lezghed, N., Colomba, E., Khettab, M., Ammari, S., Fekhi, M., Martanovschi, L., Benadhou, L., Knafo, S., Guyon, D., Cheaib, B., Dhermain, F. & Dumont, S. N. 2023. Bevacizumab in real-life patients with recurrent glioblastoma: benefit or futility? *Journal of Neurology,* 270**,** 2702-2714.

Solomou, G., Finch, A., Asghar, A. & Bardella, C. 2023. Mutant IDH in Gliomas: Role in Cancer and Treatment Options. *Cancers (Basel),* 15.

Song, E., Mao, T., Dong, H., Boisserand, L. S. B., Antila, S., Bosenberg, M., Alitalo, K., Thomas, J.-L. & Iwasaki, A. 2020. VEGF-C-driven lymphatic drainage enables immunosurveillance of brain tumours. *Nature,* 577**,** 689-694.

Sønstevold, L., Czerkies, M., Escobedo-Cousin, E., Blonski, S. & Vereshchagina, E. 2023. Application of Polymethylpentene, an Oxygen Permeable Thermoplastic, for Long-Term on-a-Chip Cell Culture and Organ-on-a-Chip Devices. *Micromachines,* 14**,** 532.

Sözmen, A. B. & Arslan Yildiz, A. 2021. Cost-effective and rapid prototyping of PMMA microfluidic device via polymer-assisted bonding. *Microfluidics and Nanofluidics,* 25**,** 66.

Staub-Bartelt, F., Suresh Babu, M. P., Szelényi, A., Rapp, M. & Sabel, M. 2024. Establishment of Different Intraoperative Monitoring and Mapping Techniques and Their Impact on Survival, Extent of Resection, and Clinical Outcome in Patients with High-Grade Gliomas—A Series of 631 Patients in 14 Years. *Cancers,* 16**,** 926.

Stitzlein, L. M., Adams, J. T., Stitzlein, E. N., Dudley, R. W. & Chandra, J. 2024. Current and future therapeutic strategies for high-grade gliomas leveraging the interplay between epigenetic regulators and kinase signaling networks. *Journal of Experimental & Clinical Cancer Research,* 43**,** 12.

Straehla, J. P., Hajal, C., Safford, H. C., Offeddu, G. S., Boehnke, N., Dacoba, T. G., Wyckoff, J., Kamm, R. D. & Hammond, P. T. 2022. A predictive microfluidic model of human glioblastoma to assess trafficking of blood-brain barrier-penetrant nanoparticles. *Proc Natl Acad Sci U S A,* 119**,** e2118697119.

Strepkos, D., Markouli, M., Klonou, A., Piperi, C. & Papavassiliou, A. G. 2020. Insights in the immunobiology of glioblastoma. *Journal of Molecular Medicine,* 98**,** 1-10.

Stummer, W., Pichlmeier, U., Meinel, T., Wiestler, O. D., Zanella, F. & Reulen, H.-J. 2006. Fluorescence-guided surgery with 5-aminolevulinic acid for resection of malignant glioma: a randomised controlled multicentre phase III trial. *The lancet oncology,* 7**,** 392-401.

Stupp, R., Hegi, M. E., Mason, W. P., Van Den Bent, M. J., Taphoorn, M. J., Janzer, R. C., Ludwin, S. K., Allgeier, A., Fisher, B. & Belanger, K. 2009. Effects of radiotherapy with concomitant and adjuvant temozolomide versus radiotherapy alone on survival in glioblastoma in a randomised phase III study: 5-year analysis of the EORTC-NCIC trial. *The lancet oncology,* 10**,** 459-466.

Stupp, R., Mason, W. P., van den Bent, M. J., Weller, M., Fisher, B., Taphoorn, M. J., Belanger, K., Brandes, A. A., Marosi, C., Bogdahn, U., Curschmann, J., Janzer, R. C., Ludwin, S. K., Gorlia, T., Allgeier, A., Lacombe, D., Cairncross, J. G., Eisenhauer, E. & Mirimanoff, R. O. 2005. Radiotherapy plus concomitant and adjuvant temozolomide for glioblastoma. *N Engl J Med,* 352**,** 987-96.

Stupp, R., Taillibert, S., Kanner, A. A., Kesari, S., Steinberg, D. M., Toms, S. A., Taylor, L. P., Lieberman, F., Silvani, A. & Fink, K. L. 2015. Maintenance therapy with tumor-treating fields plus temozolomide vs temozolomide alone for glioblastoma: a randomized clinical trial. *Jama,* 314**,** 2535-2543.

Suero Molina, E., Schipmann, S. & Stummer, W. 2019. Maximizing safe resections: the roles of 5-aminolevulinic acid and intraoperative MR imaging in glioma surgery—review of the literature. *Neurosurgical review,* 42**,** 197-208.

Systems, R. D. 2024. *Proteome Profiler Array Protocols* [Online]. R&D Systems. Available: **https://www.rndsystems.com/protocol-types/proteome-profiler-arrays** [Accessed 2025 May 19].

Takai, H., Masuda, K., Sato, T., Sakaguchi, Y., Suzuki, T., Suzuki, T., Koyama-Nasu, R., Nasu-Nishimura, Y., Katou, Y. & Ogawa, H. 2014. 5-Hydroxymethylcytosine plays a critical role in glioblastomagenesis by recruiting the CHTOP-methylosome complex. *Cell reports,* 9**,** 48-60.

Tamai, S., Ichinose, T., Tsutsui, T., Tanaka, S., Garaeva, F., Sabit, H. & Nakada, M. 2022. Tumor Microenvironment in Glioma Invasion. *Brain Sciences,* 12**,** 505.

Tan, A. C., Ashley, D. M., López, G. Y., Malinzak, M., Friedman, H. S. & Khasraw, M. 2020. Management of glioblastoma: State of the art and future directions. *CA Cancer J Clin,* 70**,** 299-312.

Tang, M., Xie, Q., Gimple, R. C., Zhong, Z., Tam, T., Tian, J., Kidwell, R. L., Wu, Q., Prager, B. C. & Qiu, Z. 2020. Three-dimensional bioprinted glioblastoma microenvironments model cellular dependencies and immune interactions. *Cell research,* 30**,** 833-853.

Technologies, A. 2024. *BioTek Synergy HTX Multi-Mode Reader* [Online]. Agilent Technologies. Available: **https://www.agilent.com/en/product/microplate-instrumentation/microplate-readers/multimode-microplate-readers/biotek-synergy-htx-multimode-reader-1623207** [Accessed 2025 May 19].

Testa, E., Palazzo, C., Mastrantonio, R. & Viscomi, M. T. 2022. Dynamic Interactions between Tumor Cells and Brain Microvascular Endothelial Cells in Glioblastoma. *Cancers,* 14**,** 3128.

Thanh, H. D., Lee, S., Nguyen, T. T., Huu, T. N., Ahn, E.-J., Cho, S.-H., Kim, M. S., Moon, K.-S. & Jung, C. 2024. Temozolomide promotes matrix metalloproteinase 9 expression through p38 MAPK and JNK pathways in glioblastoma cells. *Scientific Reports,* 14**,** 14341.

Thenuwara, G., Javed, B., Singh, B. & Tian, F. 2024. Biosensor-Enhanced Organ-on-a-Chip Models for Investigating Glioblastoma Tumor Microenvironment Dynamics. *Sensors,* 24**,** 2865.

Thomas, R. P., Recht, L. & Nagpal, S. 2012. Advances in the management of glioblastoma: the role of temozolomide and MGMT testing. *Clinical pharmacology: advances and applications***,** 1-9.

Timmermann, C. 2013. 'Just give me the best quality of life questionnaire': the Karnofsky scale and the history of quality of life measurements in cancer trials. *Chronic Illn,* 9**,** 179-90.

Tiwari, S. & Han, Z. 2024. Immunotherapy: Advancing glioblastoma treatment—A narrative review of scientific studies. *Cancer Reports,* 7**,** e1947.

Toepke, M. W. & Beebe, D. J. 2006. PDMS absorption of small molecules and consequences in microfluidic applications. *Lab Chip,* 6**,** 1484-6.

Torrisi, F., Alberghina, C., D'Aprile, S., Pavone, A. M., Longhitano, L., Giallongo, S., Tibullo, D., Di Rosa, M., Zappalà, A., Cammarata, F. P., Russo, G., Ippolito, M., Cuttone, G., Li Volti, G., Vicario, N. & Parenti, R. 2022. The Hallmarks of Glioblastoma: Heterogeneity, Intercellular Crosstalk and Molecular Signature of Invasiveness and Progression. *Biomedicines,* 10**,** 806.

Tournier, J. D., Mori, S. & Leemans, A. 2011. Diffusion tensor imaging and beyond. *Magn Reson Med,* 65**,** 1532-56.

Traylor, J. I., Pernik, M. N., Sternisha, A. C., McBrayer, S. K. & Abdullah, K. G. 2021. Molecular and metabolic mechanisms underlying selective 5-aminolevulinic acid-induced fluorescence in gliomas. *Cancers,* 13**,** 580.

Trevisi, G. & Mangiola, A. 2023. Current Knowledge about the Peritumoral Microenvironment in Glioblastoma. *Cancers (Basel),* 15.

Tripathy, D. K., Panda, L. P., Biswal, S. & Barhwal, K. 2024. Insights into the glioblastoma tumor microenvironment: current and emerging therapeutic approaches. *Frontiers in Pharmacology,* 15.

UK, C. R. 2024. *Brain, other CNS and intracranial tumours statistics* [Online]. Available: **https://www.cancerresearchuk.org/health-professional/cancer-statistics/statistics-by-cancer-type/brain-other-cns-and-intracranial-tumours** [Accessed 17 August 2024].

van den Bent, M. J., Tesileanu, C. M. S., Wick, W., Sanson, M., Brandes, A. A., Clement, P. M., Erridge, S., Vogelbaum, M. A., Nowak, A. K. & Baurain, J. F. 2021. Adjuvant and concurrent temozolomide for 1p/19q non-co-deleted anaplastic glioma (CATNON; EORTC study 26053-22054): second interim analysis of a randomised, open-label, phase 3 study. *The Lancet Oncology,* 22**,** 813-823.

Vatankhahan, H., Esteki, F., Jabalameli, M. A., Kiani, P., Ehtiati, S., Movahedpour, A., Vakili, O. & Khatami, S. H. 2024. Electrochemical biosensors for early diagnosis of glioblastoma. *Clinica Chimica Acta,* 557**,** 117878.

Verdugo, E., Puerto, I. & Medina, M. Á. 2022. An update on the molecular biology of glioblastoma, with clinical implications and progress in its treatment. *Cancer Communications,* 42**,** 1083-1111.

Verhaak, R. G., Hoadley, K. A., Purdom, E., Wang, V., Qi, Y., Wilkerson, M. D., Miller, C. R., Ding, L., Golub, T. & Mesirov, J. P. 2010. Integrated genomic analysis identifies clinically relevant subtypes of glioblastoma characterized by abnormalities in PDGFRA, IDH1, EGFR, and NF1. *Cancer cell,* 17**,** 98-110.

Wach, J., Vychopen, M., Kühnapfel, A., Seidel, C. & Güresir, E. 2023. A Systematic Review and Meta-Analysis of Supramarginal Resection versus Gross Total Resection in Glioblastoma: Can We Enhance Progression-Free Survival Time and Preserve Postoperative Safety? *Cancers,* 15**,** 1772.

Wan, A. M. D., Devadas, D. & Young, E. W. K. 2017. Recycled polymethylmethacrylate (PMMA) microfluidic devices. *Sensors and Actuators B: Chemical,* 253**,** 738-744.

Wang, G., Zhong, K., Wang, Z., Zhang, Z., Tang, X., Tong, A. & Zhou, L. 2022. Tumor-associated microglia and macrophages in glioblastoma: From basic insights to therapeutic opportunities. *Frontiers in Immunology,* 13.

Wanichthanarak, K., Jeamsripong, S., Pornputtapong, N. & Khoomrung, S. 2019. Accounting for biological variation with linear mixed-effects modelling improves the quality of clinical metabolomics data. *Computational and structural biotechnology journal,* 17**,** 611-618.

Wanis, H. A., Møller, H., Ashkan, K. & Davies, E. A. 2021. The incidence of major subtypes of primary brain tumors in adults in England 1995-2017. *Neuro-Oncology,* 23**,** 1371-1382.

Wei, T. & Simko, V. 2021. *R package "corrplot": Visualization of a Correlation Matrix* [Online]. Available: **https://github.com/taiyun/corrplot** [Accessed March 11 2025].

Welham, Z., Déjean, S. & KA, L. C. 2023. Multivariate Analysis with the R Package mixOmics. *Methods Mol Biol,* 2426**,** 333-359.

Welham, Z., Déjean, S. & Lê Cao, K.-A. 2012. Multivariate analysis with the R package mixOmics. *Statistical Analysis of Proteomic Data: Methods and Tools.* Springer.

Weller, M., van den Bent, M., Preusser, M., Le Rhun, E., Tonn, J. C., Minniti, G., Bendszus, M., Balana, C., Chinot, O. & Dirven, L. 2021. EANO guidelines on the diagnosis and treatment of diffuse gliomas of adulthood. *Nature reviews Clinical oncology,* 18**,** 170-186.

Weller, M., van den Bent, M., Preusser, M., Le Rhun, E., Tonn, J. C., Minniti, G., Bendszus, M., Balana, C., Chinot, O. & Dirven, L. 2022. Author Correction: EANO guidelines on the diagnosis and treatment of diffuse gliomas of adulthood. *Nature Reviews Clinical Oncology,* 19**,** 357-358.

Wen, P. Y., Weller, M., Lee, E. Q., Alexander, B. M., Barnholtz-Sloan, J. S., Barthel, F. P., Batchelor, T. T., Bindra, R. S., Chang, S. M. & Chiocca, E. A. 2020. Glioblastoma in adults: a Society for Neuro-Oncology (SNO) and European Society of Neuro-Oncology (EANO) consensus review on current management and future directions. *Neuro-oncology,* 22**,** 1073-1113.

Wick, W., Platten, M., Meisner, C., Felsberg, J., Tabatabai, G., Simon, M., Nikkhah, G., Papsdorf, K., Steinbach, J. P. & Sabel, M. 2012. Temozolomide chemotherapy alone versus

radiotherapy alone for malignant astrocytoma in the elderly: the NOA-08 randomised, phase 3 trial. *The lancet oncology,* 13**,** 707-715.

Wolburg, H., Noell, S., Mack, A., Wolburg-Buchholz, K. & Fallier-Becker, P. 2009. Brain endothelial cells and the glio-vascular complex. *Cell and tissue research,* 335**,** 75-96.

Wong, B. S., Shah, S. R., Yankaskas, C. L., Bajpai, V. K., Wu, P.-H., Chin, D., Ifemembi, B., ReFaey, K., Schiapparelli, P., Zheng, X., Martin, S. S., Fan, C.-M., Quiñones-Hinojosa, A. & Konstantopoulos, K. 2021a. A microfluidic cell-migration assay for the prediction of progression-free survival and recurrence time of patients with glioblastoma. *Nature Biomedical Engineering,* 5**,** 26-40.

Wong, B. S., Shah, S. R., Yankaskas, C. L., Bajpai, V. K., Wu, P. H., Chin, D., Ifemembi, B., ReFaey, K., Schiapparelli, P., Zheng, X., Martin, S. S., Fan, C. M., Quiñones-Hinojosa, A. & Konstantopoulos, K. 2021b. A microfluidic cell-migration assay for the prediction of progression-free survival and recurrence time of patients with glioblastoma. *Nat Biomed Eng,* 5**,** 26-40.

Wu, L. & Qu, X. 2015. Cancer biomarker detection: recent achievements and challenges. *Chem Soc Rev,* 44**,** 2963-97.

Xiao, Y., Kim, D., Dura, B., Zhang, K., Yan, R., Li, H., Han, E., Ip, J., Zou, P., Liu, J., Chen, A. T., Vortmeyer, A. O., Zhou, J. & Fan, R. 2019. Ex vivo Dynamics of Human Glioblastoma Cells in a Microvasculature-on-a-Chip System Correlates with Tumor Heterogeneity and Subtypes. *Advanced Science,* 6**,** 1801531.

Xie, X., Bao, S., Zhao, H., Li, L. & Fu, X. 2023a. Efficacy and Safety of Bevacizumab for Treating Glioblastoma: A Systematic Review and Meta-Analysis of Phase II and III Randomized Controlled Trials. *Cancer Investigation,* 41**,** 305-317.

Xie, Z., Chen, M., Lian, J., Wang, H. & Ma, J. 2023b. Glioblastoma-on-a-chip construction and therapeutic applications. *Frontiers in Oncology,* 13.

Yang, X., Li, K., Zhang, X., Liu, C., Guo, B., Wen, W. & Gao, X. 2018. Nanofiber membrane supported lung-on-a-chip microdevice for anti-cancer drug testing. *Lab on a Chip,* 18**,** 486-495.

Yeo, E. C., Brown, M. P., Gargett, T. & Ebert, L. M. 2021. The role of cytokines and chemokines in shaping the immune microenvironment of glioblastoma: implications for immunotherapy. *Cells,* 10**,** 607.

Yuk, N. & Jung, H. J. 2024. Inhibition of PRMT1 Suppresses the Growth of U87MG-Derived Glioblastoma Stem Cells by Blocking the STAT3 Signaling Pathway. *International Journal of Molecular Sciences,* 25**,** 2950.

Zakharova, M., Palma do Carmo, M. A., van der Helm, M. W., Le-The, H., de Graaf, M. N. S., Orlova, V., van den Berg, A., van der Meer, A. D., Broersen, K. & Segerink, L. I. 2020. Multiplexed blood–brain barrier organ-on-chip. *Lab on a Chip,* 20**,** 3132-3143.

Zhang, A. B., Mozaffari, K., Aguirre, B., Li, V., Kubba, R., Desai, N. C., Wei, D., Yang, I. & Wadehra, M. 2023. Exploring the Past, Present, and Future of Anti-Angiogenic Therapy in Glioblastoma. *Cancers,* 15**,** 830.

Zhang, F., Wang, H., Wang, X., Jiang, G., Liu, H., Zhang, G., Wang, H., Fang, R., Bu, X. & Cai, S. 2016. TGF-β induces M2-like macrophage polarization via SNAIL-mediated suppression of a pro-inflammatory phenotype. *Oncotarget,* 7**,** 52294.

Zhang, J. J., Lee, K. S., Voisin, M. R., Hervey-Jumper, S. L., Berger, M. S. & Zadeh, G. 2020a. Awake craniotomy for resection of supratentorial glioblastoma: a systematic review and meta-analysis. *Neuro-oncology advances,* 2**,** vdaa111.

Zhang, P., Xia, Q., Liu, L., Li, S. & Dong, L. 2020b. Current Opinion on Molecular Characterization for GBM Classification in Guiding Clinical Diagnosis, Prognosis, and Therapy. *Front Mol Biosci,* 7**,** 562798.

Zhang, Q., Mao, S., Li, W., Huang, Q., Feng, S., Hong, Z. & Lin, J.-M. 2020c. Microfluidic adhesion analysis of single glioma cells for evaluating the effect of drugs. *Science China Chemistry,* 63**,** 865-870.

Zhang, Y. S., Zhang, Y.-N. & Zhang, W. 2017. Cancer-on-a-chip systems at the frontier of nanomedicine. *Drug Discovery Today,* 22**,** 1392-1399.
Zhao, X., Gao, W., Yin, J., Fan, W., Wang, Z., Hu, K., Mai, Y., Luan, A., Xu, B. & Jin, Q. 2021. A high-precision thermometry microfluidic chip for real-time monitoring of the physiological process of live tumour cells. *Talanta,* 226**,** 122101.
Zhao, X., Ma, C., Park, D. S., Soper, S. A. & Murphy, M. C. 2022. Air bubble removal: Wettability contrast enabled microfluidic interconnects. *Sensors and Actuators B: Chemical,* 361**,** 131687.
Zheng, G.-X., Zhang, X.-M., Yang, Y.-S., Zeng, S.-R., Wei, J.-F., Wang, Y.-H. & Li, Y.-J. 2014. An integrated microfludic device for culturing and screening of Giardia lamblia. *Experimental Parasitology,* 137**,** 1-7.

Appendices

Appendix 7.1 Ethical approval

NHS
Health Research Authority

Yorkshire & The Humber - South Yorkshire Research Ethics Committee

NHSBT Newcastle Blood Donor Centre
Holland Drive
Newcastle upon Tyne
NE2 4NQ

Tel: 0207 104 8079

Please note: This is the favourable opinion of the REC only and does not allow the amendment to be implemented at NHS sites in England until the outcome of the HRA assessment has been confirmed.

18 March 2021

Professor John Greenman
University of Hull
Hardy Building
Cottingham Road
Hull
HU6 7RX

Dear Professor Greenman

Study title:	**Application of microfluidics system for evaluating the biology of Glioblastoma multiforme tissues and testing their response to chemotherapy**
REC reference:	**13/YH/0238**
Protocol number:	**N/A**
Amendment number:	**Amendment 5**
Amendment date:	**01 February 2021**
IRAS project ID:	**131630**

The above amendment was reviewed by the Sub-Committee in correspondence.

Ethical opinion

The members of the Committee taking part in the review gave a favourable ethical opinion of the amendment on the basis described in the notice of amendment form and supporting documentation.

Approved documents

The documents reviewed and approved at the meeting were:

Document	*Version*	*Date*
Completed Amendment Tool [plication of microfluidics in Glioblastoma multiforme]	1	01 February 2021

A Research Ethics Committee established by the Health Research Authority

Participant consent form [Consent Form]	5.1, highlighted	12 March 2021
Participant information sheet (PIS) [Participant Information Sheet]	5.1, highlighted	12 March 2021

Membership of the Committee

The members of the Committee who took part in the review are listed on the attached sheet.

Working with NHS Care Organisations

Sponsors should ensure that they notify the R&D office for the relevant NHS care organisation of this amendment in line with the terms detailed in the categorisation email issued by the lead nation for the study.

Amendments related to COVID-19

We will update your research summary for the above study on the research summaries section of our website. During this public health emergency, it is vital that everyone can promptly identify all relevant research related to COVID-19 that is taking place globally. If you have not already done so, please register your study on a public registry as soon as possible and provide the HRA with the registration detail, which will be posted alongside other information relating to your project.

Statement of compliance

The Committee is constituted in accordance with the Governance Arrangements for Research Ethics Committees and complies fully with the Standard Operating Procedures for Research Ethics Committees in the UK.

HRA Learning

We are pleased to welcome researchers and research staff to our HRA Learning Events and online learning opportunities– see details at: https://www.hra.nhs.uk/planning-and-improving-research/learning/

IRAS Project ID - 131630:	**Please quote this number on all correspondence**

Yours sincerely
Pp

Dr Max Huxham
Chair

E-mail: southyorks.rec@hra.nhs.uk

Enclosures: *List of names and professions of members who took part in the review*

Appendix 7.2 Patient information sheet (Version 5)

UNIVERSITY OF Hull

NHS Hull University Teaching Hospitals NHS Trust

Research Participant Information Sheet

Application of microfluidics system for evaluating the biology of Brain Tumour tissues and testing their response to treatment

Invitation

We would like to invite you to take part in a research study. Before you decide, you need to understand why the research is being undertaken and what would be required of you. Please take the time to read the following information carefully. Talk to others about the study if you wish; ask us if there is anything that is not clear or if you would like more information.

Purpose of the study

The ultimate aim is to develop a system that could be used to understand why and how certain treatments work on one individual and not on others, and in doing so, help us to personalise treatments in the future. This study forms the basis of a Medical Doctorate and a PhD project. The University of Hull has developed a method to keep a small piece of tissue functioning for a number of days out of the body on a miniaturised analysis device (often referred to as a 'Lab on a Chip'). We will investigate the effects of treatments (e.g. testing different known or potential chemotherapy drugs, or radiotherapy) on this tissue to give us better information as to how these treatments work on tissues within the body. We will also look for changes in proteins and genes (we call these biomarkers) to identify new factors that would help us treat brain tumours better.

Why have I been chosen?

We are inviting you to take part in the study as you are undergoing a procedure that will involve the removal of a brain tumour, or you are having the removal of small pieces of tissue (a diagnostic biopsy) for diagnostic purposes.

Do I have to take part?

It is your decision whether you wish to take part. We will describe the study and go through this information sheet with you. You can keep this information sheet and use it to help you decide. If you decide to be a part of the study, we will ask you to sign a consent form to show you have agreed to take part.

Am I free to withdraw at any time?

You are free to withdraw at any time without giving a reason for your withdrawal. This will not affect the standard of care you receive. However, samples already collected before your withdrawal will continue to be stored and any information gained from these may be used in the study. We would not access any information about your

clinical progress.

What will happen to me if I take part?

If you agree to take part in the study and if you are undergoing tumour resection, a small (2 cubic millimetres) sample of tissue will be taken from the specimen removed. If you are undergoing a diagnostic biopsy, a small part (2 cubic millimetres) of the sample tissue (surplus tissue) will be used if available. We would also ask for you consent to donate an additional blood sample (4 ml), which would be taken during your routine blood tests. Samples will be taken before your surgery, as well as during your follow-up care. Once your samples are taken they will only be identifiable by a number; non-clinical laboratory staff will not have any access to your personal details. Information regarding your response to treatment and outcome (if applicable) will be accessed by the clinical staff involved with your treatment and possibly communicated with the research staff. You will not be contacted by the research team after today.

Expenses and payment

You should not incur any expenses during participation. There will not be any financial benefit if this research leads to the development of a new treatment or test.

What are the possible risks of taking part?

There are no risks to you or your treatment if you take part.

What are the benefits of taking part?

There will be no direct benefit to you for taking part, but the information we obtain by studying your sample will potentially help the development of treatments for other patients in the future.

There is a very small chance that something will be discovered in the genetic study that would be relevant for staff managing your current treatment; if this happens the consultant in charge of your care at this time will be informed and will act with the clinical team as appropriate.

What do I do if I have a complaint?

Any complaint about the way you have been dealt with during the study can be addressed to **Mr. Achawal, Consultant Neurosurgeon on (01482) 605338.** Alternatively, you can contact the patient advice and liaison service (PALS) on (01482) 623065.

Will my role in the study be kept confidential?

Yes. We will follow best ethical and legal practice and all information about you will be handled in confidence. Your sample will be identifiable by a number that can only be linked back to personal details via your clinical team e.g. Mr. Achawal.

What will happen to the samples I give?

The samples will be taken to the research laboratory at the University of Hull where we will investigate the effect of treatments (chemotherapy and/or radiotherapy) on them. Following completion of the study, excess samples will remain stored in liquid nitrogen, securely and anonymously for possible use in future research. In this instance, new research ethical approval will be sought prior to commencing a study.

What will happen to the results of the research study?

The results of the study may be published in a scientific journal. At no time will you be identifiable to the reader. No feedback will be given to you unless specifically requested, in which instance the research team will be happy to discuss the general findings.

Who is organising and funding the research?

The University of Hull will be organising and conducting research in their laboratories. A joint University of Hull / Hull Neurosurgery Department research account is held at the University of Hull and this will be used to fund the research, along with a grant from the Yorkshire Brain Tumour Charity.

Who has reviewed the study?

To protect your interests, all research in the NHS is reviewed and authorised by an independent group of people called a Research Ethics Committee. This study has been reviewed and authorised by a relevant National Local Research Ethics Committee.

Further information

If you require any further information on the research, advice on whether to take part, or if you're at all unhappy, please contact Mr. Achawal on (01482) 605338. Thank you for taking time to read this information sheet.

Consent

If you decide to take part in this study, we will provide you with a copy of the information sheet and ask you to sign a Consent Form.
Should you be unable to, but have been considered by the neurosurgical multidisciplinary team to proceed with surgical treatment, your next of kin can sign on your behalf.

Appendix 7.3 Consent form version 5

IVERSITY OF Hull

NHS
Hull University Teaching Hospitals
NHS Trust

Centre Number: **Study Number:**

Patient Identification Number:

CONSENT FORM

Application of microfluidics system for evaluating the biology of Brain Tumour tissues and testing their response to treatment

- I confirm that I have read and understood the information sheet dated 12.03.21 (version 5.1) for the above study. I have had the opportunity to consider the information, ask questions and have had these answered satisfactorily. ☐
- I understand my participation is voluntary and that I am free to withdraw at any time without giving a reason, without my medical care or legal rights being affected. If I do withdraw, samples already obtained may still be used. ☐
- I understand that I am under no obligation to take part and that, in agreeing to take part, I am free to change my mind at any time. ☐
- I understand that I will not benefit financially if this research leads to the development of a new treatment or test. ☐
- I give permission for a sample of tissue taken during my operation/diagnostic biopsy to be used for this research. ☐
- I give permission for blood samples to be taken before my operation and during follow-up care to be used for this research. ☐
- I give permission for my blood and tissue samples to be analysed to search for new protein and genetic biomarkers relevant to brain tumour research. ☐
- I agree that any abnormal results from my blood samples will be assessed by a clinical professional and shared with your GP. ☐
- I agree that any samples not used in this study may be stored and used in future research of a similar nature pending ethical approval. ☐
- I understand that these samples will be stored anonymously and I consent to the information derived from them to be analysed. ☐
- I understand that relevant sections of my medical notes and data collected during the study may be looked at by individuals from the University of Hull, from regulatory authorities or from the NHS Trust, where it is relevant to me taking part in this research. I give permission for these individuals to have access to my records. ☐
- I hereby freely give my consent to take part in this study. ☐

Version 5.1 12th March 2021

Name of Volunteer/next of kin	Date	Signature

Consented by	Date	Signature

Version 5.1 12th March 2021

Appendix 7.4 The cytokine detected by proteome profiler

Table 7.1: Panel of 105 Human Cytokines Detected by Proteome Profiler Human XL Cytokine Array (Catalog #: ARY022B)

Simultaneously detect the levels of these cytokines and acute phase proteins in a single sample.		
Adiponectin/Acrp30	IFN-gamma	CCL2/MCP-1
Angiogenin	IGFBP-2	CCL7/MCP-3
Angiopoietin-1	IGFBP-3	M-CSF
Angiopoietin-2	IL-1 alpha/IL-1F1	MIF
Apolipoprotein A1	IL-1 beta/IL-1F2	CXCL9/MIG
BAFF/BLyS/TNFSF13B	IL-1ra/IL-1F3	CCL3/CCL4 MIP-1 alpha/beta
BDNF	IL-2	CCL20/MIP-3 alpha
CD14	IL-3	CCL19/MIP-3 beta
CD30	IL-4	MMP-9
CD31/PECAM-1	IL-5	Myeloperoxidase
CD40 Ligand/TNFSF5	IL-6	Osteopontin (OPN)
Chitinase 3-like	IL-8	PDGF-AA
Complement Component C5/C5a	IL-10	PDGF-AB/BB
Complement Factor D	IL-11	Pentraxin 3/TSF-14
C-Reactive Protein/CRP	IL-12 p70	CXCL4/PF4
Cripto-1	IL-13	RAGE
Cystatin C	IL-15	CCL5/RANTES
Dkk-1	IL-16	RBP4
DPPIV/CD26	IL-17A	Relaxin-2
EGF	IL-18 BPa	Resistin

CXCL5/ENA-78	IL-19	CXCL12/SDF-1 alpha
Endoglin/CD105	IL-22	Serpin E1/PAI-1
EMMPRIN	IL-23	SHBG
Fas Ligand	IL-24	ST2/IL1 R4
FGF basic	IL-27	CCL17/TARC
KGF/FGF-7	IL-31	TFF3
FGF-19	IL-32 alpha/beta/gamma	TfR
Flt-3 Ligand	IL-33	TGF-alpha
G-CSF	IL-34	Thrombospondin-1
GDF-15	CXCL10/IP-10	TIM-1
GM-CSF	CXCL11/I-TAC	TNF-alpha
CXCL1/GRO alpha	Kallikrein 3/PSA	uPAR
Growth Hormone (GH)	Leptin	VCAM-1
HGF	LIF	VEGF
ICAM-1/CD54	Lipocalin-2/NGAL	Vitamin D BP

Appendix 7.5 Preparation of Reagents Used in ELISA Protocols

7.2 Solutions in DuoSet Ancillary Reagent Kit (R&D Systems, DY008)

Solution	Preparation (if necessary)
PBS: 137 mM NaCl, 2.7 mM KCl, 8.1 mM Na2HPO4, 1.5 mM KH2PO4, 0.2 µm filtered (DY006)	N/A
Wash buffer: 0.05% Tween 20 in PBS (WA126)	20 mL of wash buffer concentrate to 480 mL deionised/distilled water
Reagent diluent: 1% BSA in PBS, 0.2 um filtered (DY995)	5 mL reagent diluent in 45 mL deionised water
Substrate solution: 1:1 mixture of H2O2 and Tetramethylbenzidine (DY999)	5 mL H2O2 mixed with 5 mL Tetramethylbenzidine (use within 15 minutes of Preparation, avoid sunlight)
Stop solution: 2 N H2SO4 (DY994)	N/A
Streptavidin-HRP	270 µL Streptavidin-HRP with 10530 µL reagent diluent

7.3 Preparation of In-House Reagents Used in ELISA Assays

Solution (in house)	Preparation
Reagent diluent	Suspend 5 mL of 10% BSA (in PBS) in 45 mL PBS, filter and dilute with 450 mL deionised water.
Substrate solution: Calbiochem Tetramethylbenzidine Solution (MilliporeSigma, 613544100ML)	N/A

Appendix 7.6: Supplementary Tables and Figures of Cytokine Analysis Results

Table 7.4 :Outliers Detected by Henze-Zirkler's Test via Mahalanobis Distance.

Treatment	Subgroup	Patient	Gender	Age. years	Recurrence.status	MGMT status	Survival (6 m)	Membrane
Treatment	GSK_48	SD0057	Female	73	primary	positive	lethal	B526
Treatment	GSK_96	SD0057	Female	73	primary	positive	lethal	B528
Treatment	GSK_192	SD0057	Female	73	primary	positive	lethal	B014
Control	DMSO_48	SD0057	Female	73	primary	positive	lethal	B525
Control	DMSO_96	SD0057	Female	73	primary	positive	lethal	B527
Control	DMSO_192	SD0057	Female	73	primary	positive	lethal	B013
Control	DMSO_288	SD0057	Female	73	primary	positive	lethal	B0615
Treatment	GSK_288	SD0057	Female	73	primary	positive	lethal	T0742
Treatment	GSK_96	SD0066	Male	58	primary	negative	Not lethal	M336
Treatment	GSK_192	SD0066	Male	58	primary	negative	Not lethal	M236
Control	DMSO_96	SD0066	Male	58	primary	negative	Not lethal	M365
Control	DMSO_192	SD0066	Male	58	primary	negative	Not lethal	M235

List of patient-membrane data points identified as multivariate outliers during normality testing.

Table 7.5: Shapiro-Wilk Test Statistics for Raw Cytokine Values.

Cytokine	variable	statistic	p
IL8	Raw values	0,92	7,9E-05
IL6	Raw values	0,72	2,1E-11
VEGF	Raw values	0,91	2,3E-05
Angiopoietin.2	Raw values	0,85	7,9E-08
Chitinase3.Like.1	Raw values	0,82	9,4E-09
Serpin.E1	Raw values	0,67	1,6E-12
MMP9	Raw values	0,92	5,8E-05

Normality assessment for cytokine expression data prior to transformation.

Table 7.6: AICc-Based Model Selection for Cytokine Predictors.

Formula	AICc	Δ AICc
Treatment + Time + Gender + Age + Recurrence + MGMT + Survival	-217.9	0.0
Treatment * Time + Gender + Age + Recurrence + MGMT + Survival	-209.7	8.2
Treatment + Time + Gender + Age + MGMT + Survival	-208.1	9.7
Treatment + Time + Gender + Age + Recurrence + Survival	-207.2	10.7
Treatment * Time + Gender + Age + MGMT + Survival	-200.2	17.7
Treatment + Time + Gender + Age + Recurrence + MGMT	-199.8	18.1
Treatment * Time + Gender + Age + Recurrence + Survival	-199.2	18.7
Treatment + Time + Gender + Age + Survival	-196.7	21.2
Treatment + Time + Gender + Age + MGMT	-192.7	25.2
Treatment * Time + Gender + Age + Recurrence + MGMT	-191.8	26.1
Treatment + Time + Age + Recurrence + MGMT + Survival	-191.6	26.3
Treatment + Time + Gender + Age + Recurrence	-191.5	26.4
Treatment * Time + Gender + Age + Survival	-188.9	28.9
Treatment + Time + Age + Recurrence + Survival	-186.5	31.4
Treatment * Time + Gender + Age + MGMT	-184.9	33.0
Treatment * Time + Gender + Age + Recurrence	-183.8	34.1
Treatment * Time + Age + Recurrence + MGMT + Survival	-183.7	34.2
Treatment + Time + Gender + Age	-183.3	34.6
Treatment + Time + Age + Recurrence + MGMT	-180.4	37.5
Treatment * Time + Age + Recurrence + Survival	-178.8	39.1
Treatment + Time + Gender + Recurrence + MGMT + Survival	-178.7	39.2
Treatment + Time + Age + MGMT + Survival	-178.4	39.5
Treatment + Time + Age + Recurrence	-176.4	41.5
Treatment + Time + Gender + MGMT + Survival	-175.8	42.1
Treatment * Time + Gender + Age	-175.7	42.2
Treatment + Time + Gender + Recurrence + MGMT	-175.4	42.5
Treatment + Time + Age + Survival	-172.9	45.0

Formula	AICc	Δ AICc
Treatment + Time + Gender + MGMT	-172.8	45.1
Treatment * Time + Age + Recurrence + MGMT	-172.6	45.3
Treatment * Time + Gender + Recurrence + MGMT + Survival	-170.7	47.2
Treatment * Time + Age + MGMT + Survival	-170.6	47.3
Treatment + Time + Age + MGMT	-169.8	48.1
Treatment * Time + Age + Recurrence	-168.9	49.0
Treatment * Time + Gender + MGMT + Survival	-168.1	49.8
Treatment * Time + Gender + Recurrence + MGMT	-167.6	50.3
Treatment + Time + Gender + Recurrence + Survival	-166.9	51.0
Treatment * Time + Age + Survival	-165.3	52.6
Treatment * Time + Gender + MGMT	-165.2	52.7
Treatment + Time + Age	-165.1	52.8
Treatment + Time + Gender + Recurrence	-164.6	53.3
Treatment + Time + Gender + Survival	-163.3	54.6
Treatment * Time + Age + MGMT	-162.2	55.6
Treatment + Time + Recurrence + MGMT + Survival	-162.1	55.8
Treatment + Time + Gender	-161.2	56.7
Treatment + Time + Recurrence + MGMT	-159.7	58.2
Treatment * Time + Gender + Recurrence + Survival	-159.2	58.7
Treatment * Time + Age	-157.8	60.1
Treatment + Time + MGMT + Survival	-157.1	60.8
Treatment * Time + Gender + Recurrence	-157.0	60.9
Treatment + Time + Recurrence + Survival	-156.3	61.6
Treatment * Time + Gender + Survival	-155.7	62.2
Treatment + Time + MGMT	-155.1	62.8
Treatment * Time + Recurrence + MGMT + Survival	-154.3	63.6
Treatment + Time + Recurrence	-154.3	63.6
Treatment * Time + Gender	-153.8	64.1
Treatment * Time + Recurrence + MGMT	-152.2	65.7
Treatment + Time + Survival	-150.3	67.5
Treatment * Time + MGMT + Survival	-149.5	68.4
Treatment + Time	-148.7	69.2
Treatment + Time + 1	-148.7	69.2
Treatment * Time + Recurrence + Survival	-148.7	69.2
Treatment * Time + MGMT	-147.7	70.1
Treatment * Time + Recurrence	-146.9	71.0
Treatment * Time + Survival	-143.0	74.9
Treatment * Time	-141.6	76.3
Treatment * Time + 1	-141.6	76.3

Comparison of multiple linear models including treatment, time, and patient covariates to determine optimal fit.

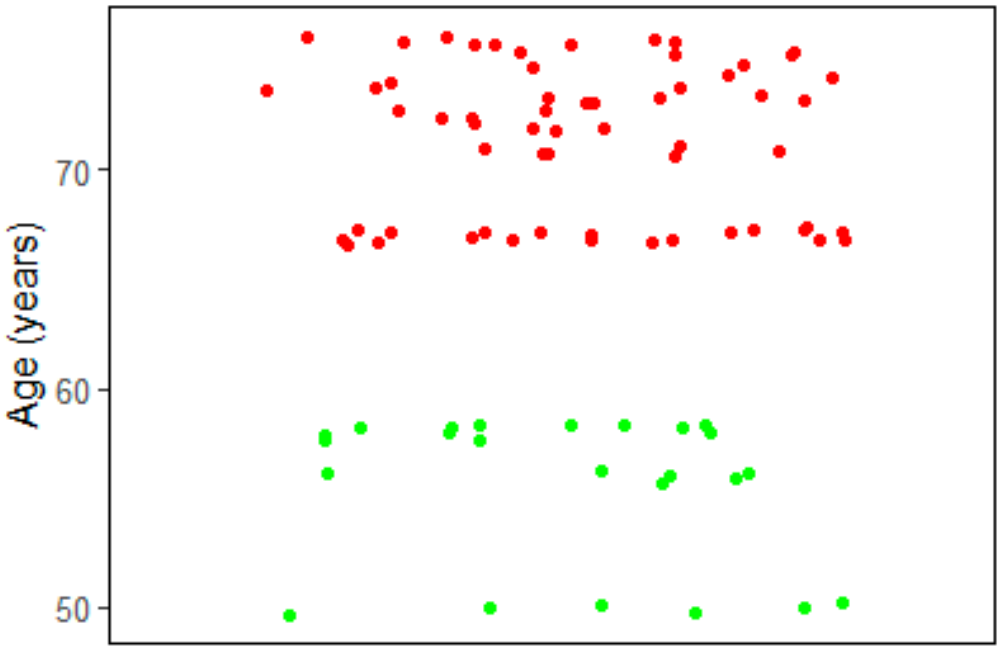

Figure 7.1: Age Stratification of Patients (<60 vs ≥60 Years)
Age can be divided into two groups based on the age variable.

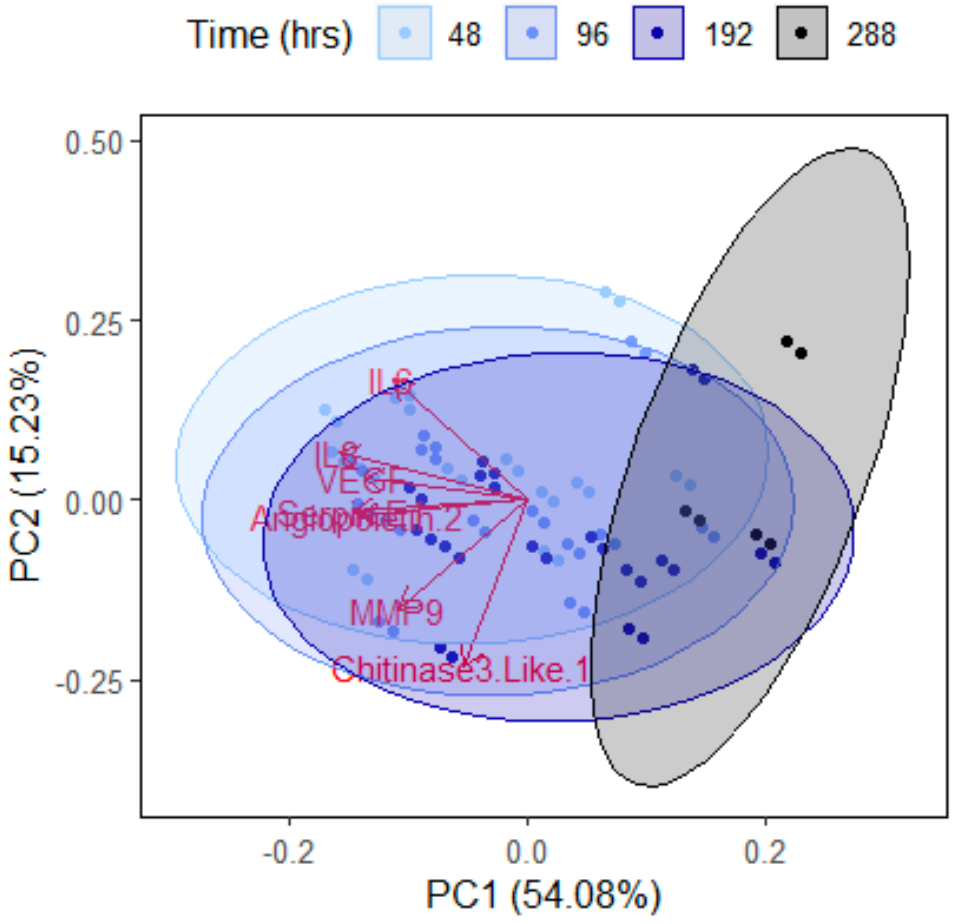

Figure 7.2: Cytokine profile with time showing the reduced expression with time.

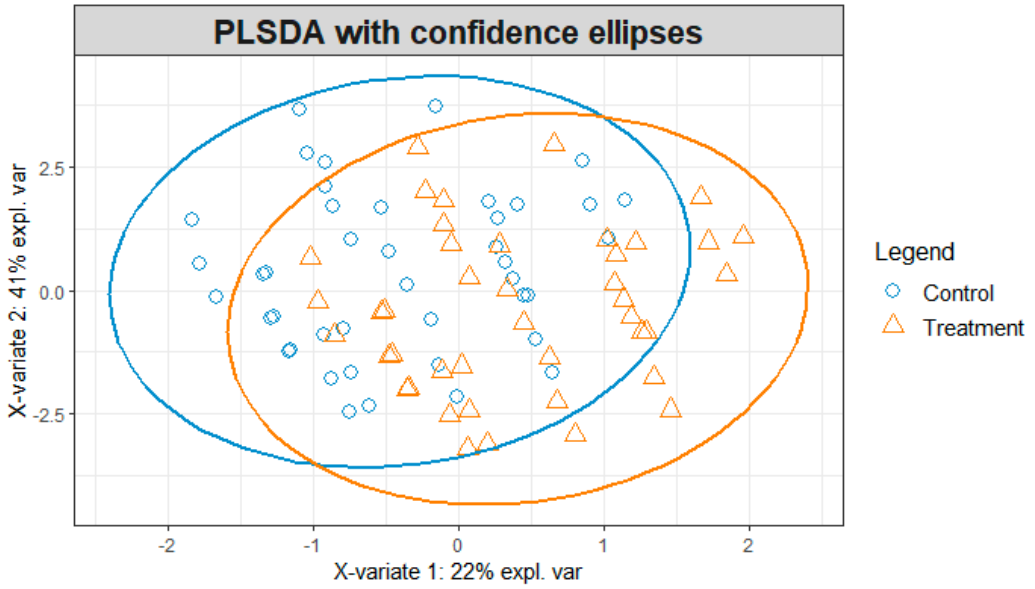

Figure 7.3: PLS-DA analysis of treatment vs control.

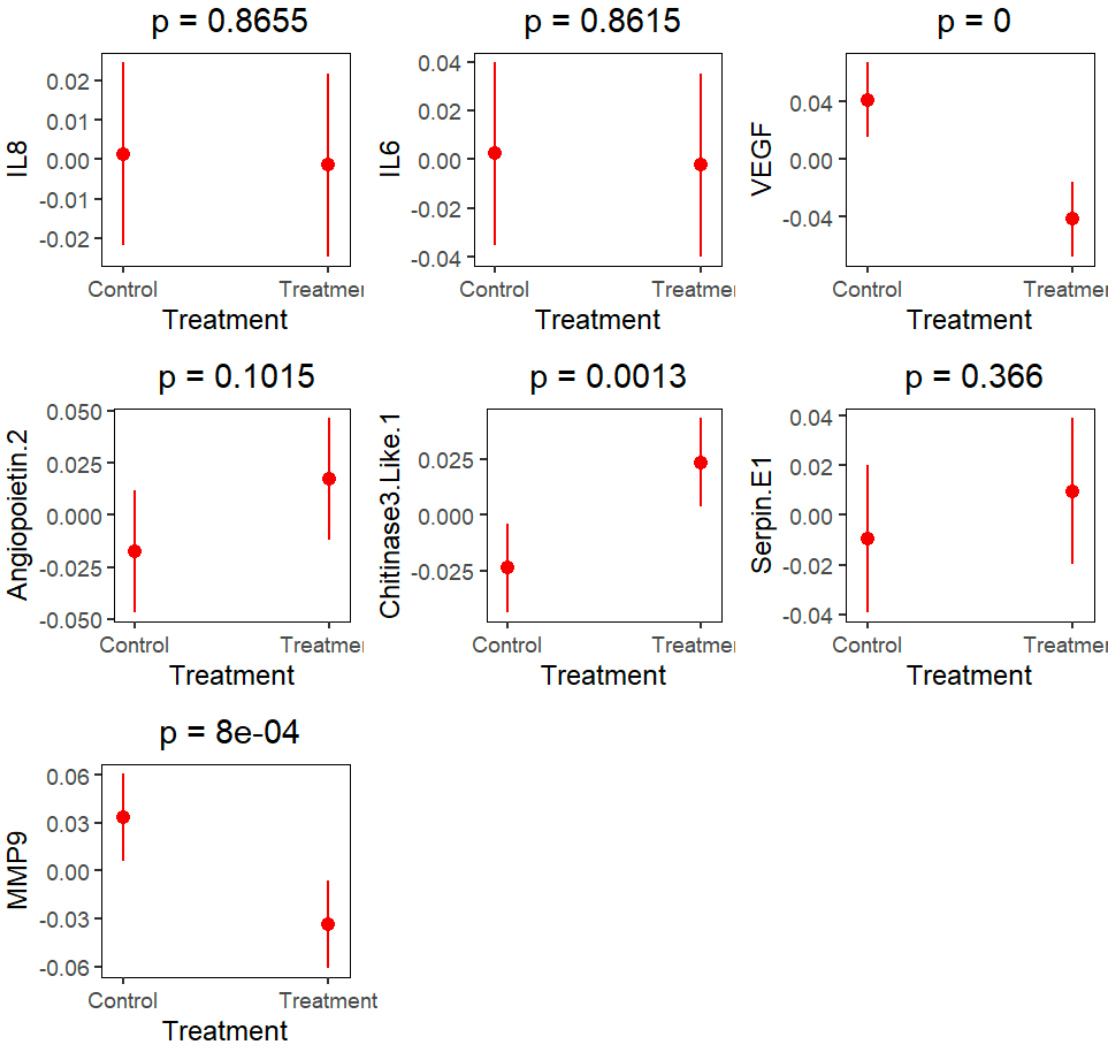

Figure 7.4: Validation of significant cytokines from the comparison of covariate-residuals between treatment and control.

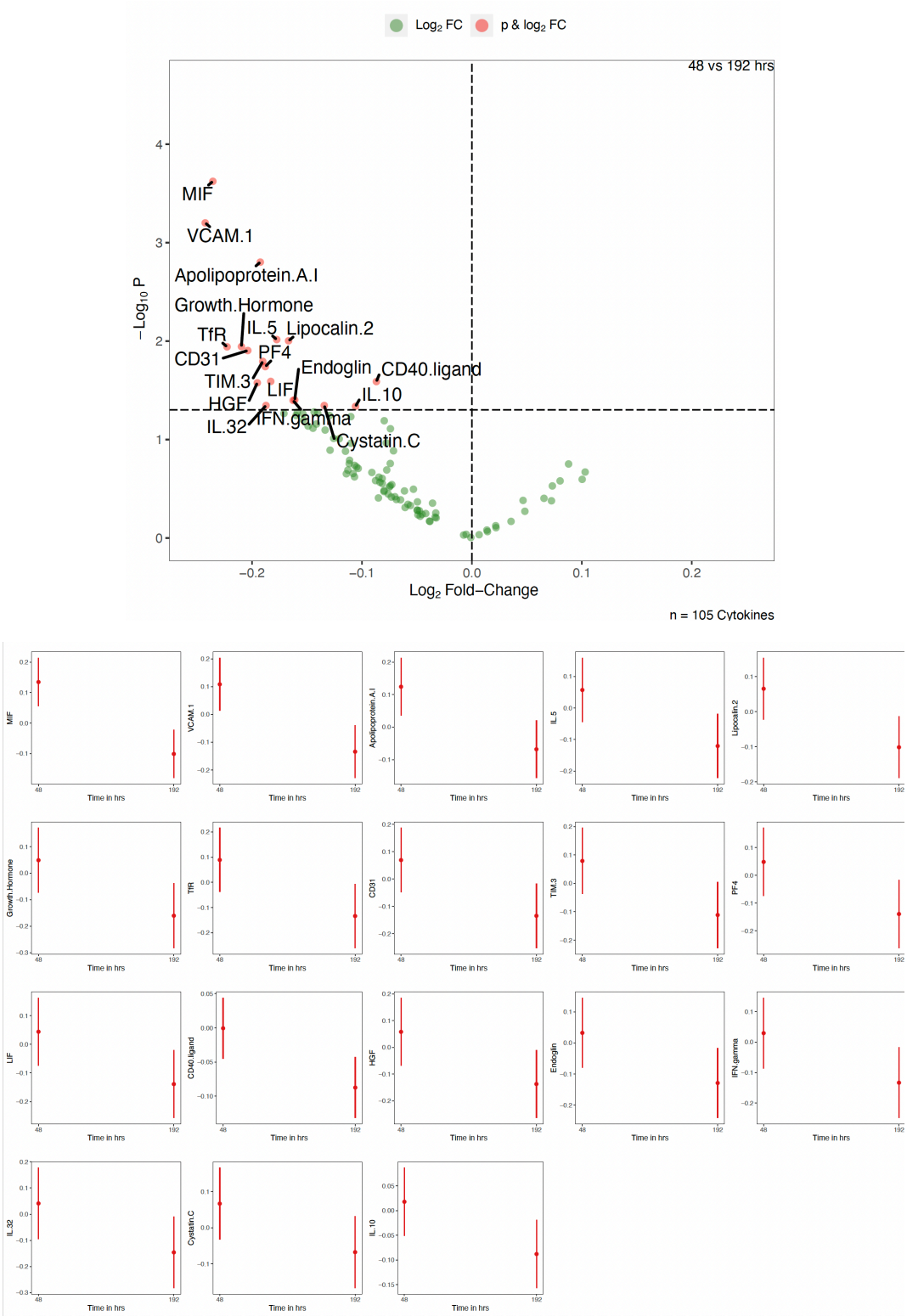

Figure 7.5: Cytokine expression downregulated with Time (48 vs 192) enhanced volcano figures and plots.

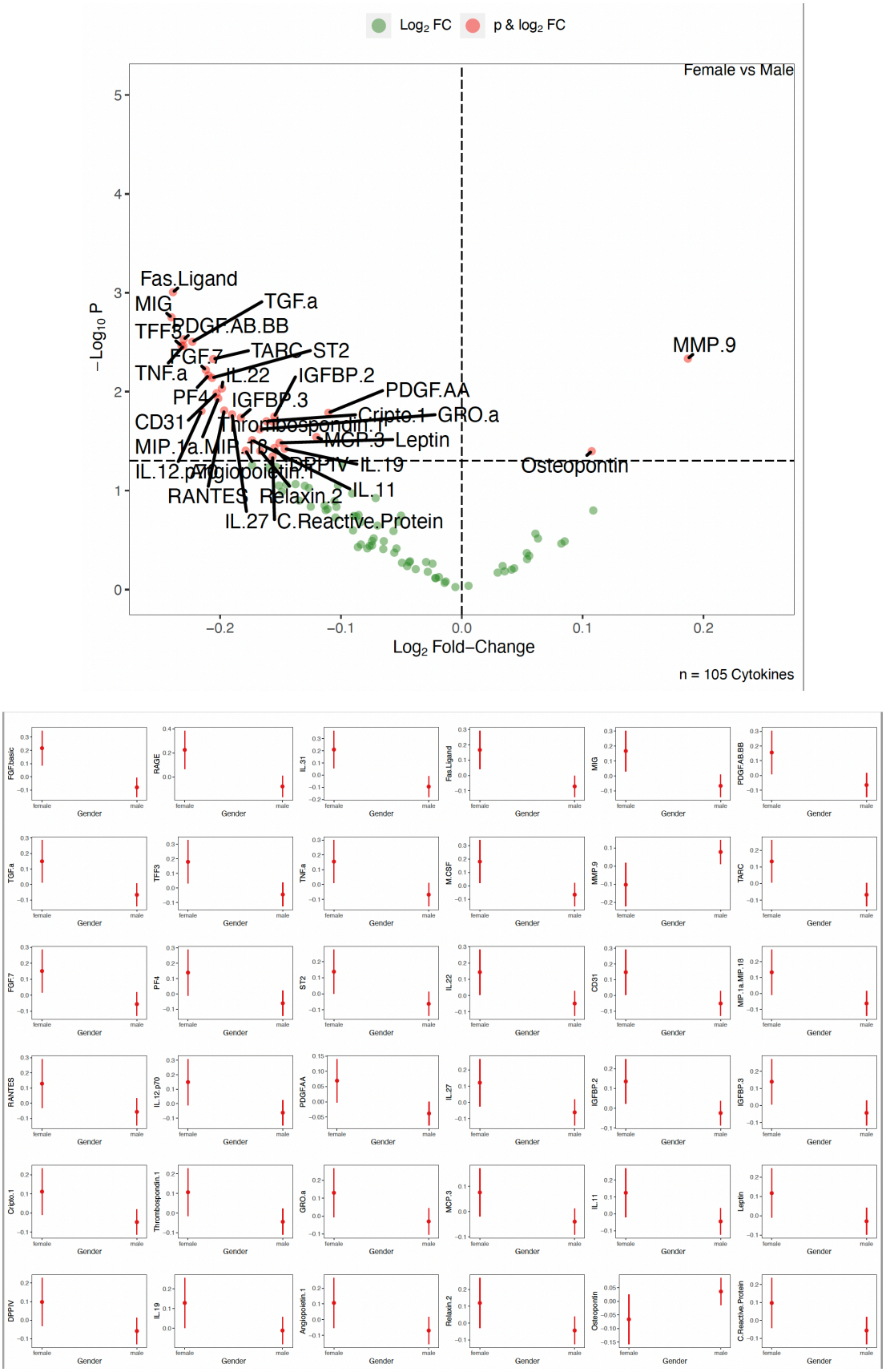

Figure 7.6: Sex-Based Cytokine Expression Differences

Cytokine expression upregulated in Female vs Male except MMP9 and Osteopontin.

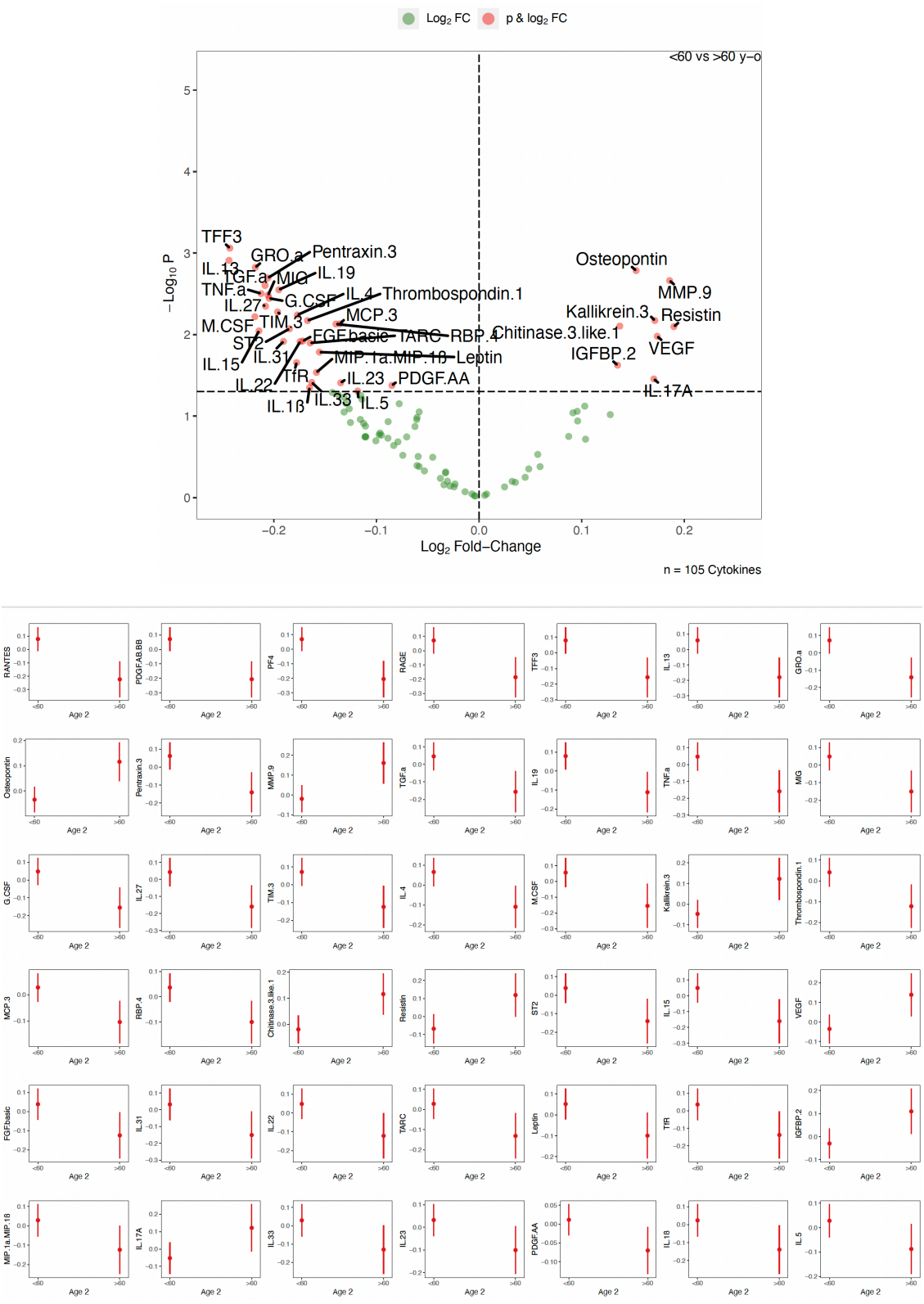

Figure 7.7: Age-Based Cytokine Expression Differences.

Patients <60 years showed elevated cytokine levels, except for 8 cytokines(Osteopontin, MMP9, Kallilkein.3, Chitinase 3 like 1, Resistin, VGEF, Insulin-Like Growth Factor Binding Protein (IGFBP-2), IL17-A)..